

EFFECTS OF TURBULENT MAGNETIC FIELDS ON THE
TRANSPORT AND ACCELERATION OF ENERGETIC
CHARGED PARTICLES: NUMERICAL SIMULATIONS WITH
APPLICATION TO HELIOSPHERIC PHYSICS

by

Fan Guo

A Dissertation Submitted to the Faculty of the
DEPARTMENT OF PLANETARY SCIENCES

In Partial Fulfillment of the Requirements
For the Degree of

DOCTOR OF PHILOSOPHY

In the Graduate College

THE UNIVERSITY OF ARIZONA

2012

THE UNIVERSITY OF ARIZONA
GRADUATE COLLEGE

As members of the Dissertation Committee, we certify that we have read the dissertation prepared by Fan Guo entitled Effects of Turbulent Magnetic Fields on the Transport and Acceleration of Energetic Charged Particles: Numerical Simulations with Application to Heliospheric Physics and recommend that it be accepted as fulfilling the dissertation requirement for the Degree of Doctor of Philosophy.

Joe Giacalone

Date: 22 August 2012

J. R. Jokipii

Date: 22 August 2012

Roger Yelle

Date: 22 August 2012

Jozsef Kota

Date: 22 August 2012

Ke Chiang Hsieh

Date: 22 August 2012

Final approval and acceptance of this dissertation is contingent upon the candidate's submission of the final copies of the dissertation to the Graduate College.

I hereby certify that I have read this dissertation prepared under my direction and recommend that it be accepted as fulfilling the dissertation requirement.

Dissertation Director: Joe Giacalone

Date: 22 August 2012

STATEMENT BY AUTHOR

This dissertation has been submitted in partial fulfillment of requirements for an advanced degree at the University of Arizona and is deposited in the University Library to be made available to borrowers under rules of the Library.

Brief quotations from this dissertation are allowable without special permission, provided that accurate acknowledgment of source is made. Requests for permission for extended quotation from or reproduction of this manuscript in whole or in part may be granted by the head of the major department or the Dean of the Graduate College when in his or her judgment the proposed use of the material is in the interests of scholarship. In all other instances, however, permission must be obtained from the author.

SIGNED: Fan Guo

ACKNOWLEDGEMENTS

First of all, I would like to thank my thesis advisor, Professor Joe Giacalone, for his exceptional guidance and continuous support in the last five years. He has been very patient and spent countless time in discussion with me. He always provides selfless help and allows me to work on the problems I am interested in. Joe is a prototype in my scientific career.

I am very grateful to all other members in my committee. I am glad to work with Professor Randy Jokipii and would like to thank him for his guidance, the numerous sharp comments, and superb suggestions about my research projects. I appreciate Dr. Jozsef Kota for all the precious advice and always being a knowledgeable resource for my questions. I would like to thank Professor Ke Chang Hiesh for his kindness and serving in my thesis committee. I want to thank Professor Roger Yelle, who keeps stimulating me to improve my English and other skills. I am also grateful to Professor Fulvio Melia, who used to be in my committee and introduced me to high-energy Astrophysics (in the well-taught class Astronomy 582).

I would like to acknowledge the help from all the members in our research group, Marcia Neugebauer, Tami Rogers, Federico Fraschetti, Tom Schad, Eric Greenfield, Erica McEvoy, Peng Sun, Eileen Chollet, Huirong Yan, and Chunsheng Pei. I would also like to express my special gratitude to our administrative associate Donita Vanture. She is such a warm-hearted lady and helped a lot to make our work as smooth as possible. My gratitude extends to my classmates, Nikole Lewis, Lissa Ong, Tom Schad, and Devin Schrader. It was great to have you in those classes! I would also like to thank all other graduate students, faculty, and staff in Lunar and Planetary Laboratory. You made LPL such a wonderful place to work! The last five years is such a precious and enjoyable memory.

I would like to thank my colleagues during my visit to Los Alamos National Laboratory, Hui Li, Shengtai Li, Hao Xu, and Wei Liu. It was a great experience and I learned a lot by working with different researchers.

Finally, I deeply appreciate my parents, who give me the most unconditional love and freedom to pursue what I like, and my wife Ting, for her amazing love and all the happiness she brings into my life.

DEDICATION

To Ting.

TABLE OF CONTENTS

LIST OF FIGURES	8
LIST OF TABLES	12
LIST OF ABBREVIATIONS	13
ABSTRACT	14
CHAPTER 1 Introduction and Background	16
1.1 Overview	16
1.2 Charged Particles in the Heliosphere	18
1.3 The Heliospheric Magnetic Field and its Fluctuations	23
1.4 Collisionless Shocks	25
1.5 The Motions of Charged Particles	28
1.6 The Transport and Acceleration of Charged Particles	30
1.7 Summary of the Following Chapters	32
CHAPTER 2 The Effect of Turbulent Magnetic Fields on the Propagation of Solar Energetic Particles in the Inner Heliosphere	35
2.1 Overview of the Transport of Solar Energetic Particles	35
2.2 Numerical Model	43
2.2.1 Turbulent Magnetic Fluctuations	43
2.2.2 Test Particle Simulations	48
2.3 A Numerical Study on the Velocity Dispersion of Solar Energetic Particles	48
2.4 A Numerical Study of Dropouts in Impulsive SEP Events	60
2.5 Summary	66
CHAPTER 3 The Effect of Turbulent Magnetic Fields on the Acceleration of Ions at Collisionless Shocks	72
3.1 Particle Acceleration at Collisionless Shocks: An Overview	72
3.2 The “Injection Problem” (The Acceleration of Low-energy Particles)	74
3.3 A 3-D Hybrid Simulation on Particle Acceleration at Parallel Shocks	77
3.3.1 Numerical Methods	77
3.3.2 Results of Numerical Simulations	82
3.3.3 Summary and Discussion	95

TABLE OF CONTENTS – *Continued*

3.4	Beyond the 1-D Diffusive Shock Acceleration	108
3.5	A Study on Particle Acceleration at Shocks Containing Large-scale Magnetic Variations	111
3.5.1	Basic Considerations and Numerical Model	112
3.5.2	Results of Numerical Simulations	115
3.5.3	Summary and Discussion	125
CHAPTER 4	The Acceleration of Electrons at Collisionless Shocks	129
4.1	Overview	129
4.2	Observations of Energetic Electrons Associated with Shock Waves . .	130
4.3	Review of Previous Theoretical Works	133
4.4	Numerical Method	135
4.5	The Effect of Large-Scale Magnetic Turbulence on the Acceleration of Electrons: Interplanetary Shocks	138
4.5.1	Initial Condition and Parameters	138
4.5.2	Simulation Results for the Acceleration of Electrons	139
4.5.3	Comparison Between the Acceleration of Electrons and That of Ions and its Implication to SEP Events	151
4.5.4	Summary	155
4.6	The Effect of Large-Scale Magnetic Turbulence on the Acceleration of Electrons: Flare Termination Shocks	156
4.6.1	Initial Conditions and Parameters	158
4.6.2	Simulation Results	160
4.7	Discussion and Conclusions	164
4.7.1	Application to Interplanetary Shocks and SEP events	168
4.7.2	Application to Particle Acceleration in Solar Flares	169
CHAPTER 5	Conclusions and Future Work	172
5.1	Summary and Conclusions for the Dissertation	172
5.2	Future Work	175
5.2.1	Effect of Shock Geometry on the Acceleration of Charged Par- ticles in Gradual SEP Events	175
5.2.2	Understanding the Physical Processes in the Acceleration of Low-Energy Particles at Shocks	175
5.2.3	The Application of the Hybrid Simulations in the Heliospheric Plasma Processes	176

LIST OF FIGURES

1.1	The interaction between the interstellar medium and the heliosphere.	17
1.2	The velocity distribution of the solar wind ions and pickup ions . . .	20
1.3	Various types of energetic charged particles in the heliosphere	22
1.4	The spacecraft measurement of the Solar wind turbulence.	25
1.5	The structure of quasi-perpendicular supercritical shocks	27
1.6	The structure of quasi-parallel supercritical shocks	28
2.1	An example of impulsive SEP events that show “dropouts” of energetic particle intensity.	38
2.2	A cartoon that illustrates the effect of meandering magnetic field lines on spacecraft observations of energetic particles.	40
2.3	An example of onset analyses for SEP events.	42
2.4	The turbulent magnetic field lines produced by the foot-point random motion model.	46
2.5	The intensity-time profiles of energetic particles at different energies collected 1 AU normalized using their peak values, in the case of the two-component model.	51
2.6	The intensity-time profiles of energetic particles at different energies collected at 1 AU normalized using their peak values, in the case of the foot-point random motion model.	52
2.7	The intensity-time profiles of energetic particles collected at 1 AU normalized using their peak values, in the case of the two-component model for different variances.	54
2.8	The intensity-time profiles of energetic particles collected at 1 AU normalized using their peak values, in the case of the foot-point random motion model for different variances.	55
2.9	Onset analyses for the two-component model and threshold is 0.001. .	58
2.10	Onset analyses for the two-component model and the magnetic variance is $\sigma^2 = 0.6$	59
2.11	An example of SEP event simulated using the foot-point random motion model for the case of the large source region.	61
2.12	An example of SEP dropouts simulated using the foot-point random motion model for the case of the small source region.	62
2.13	An example of the observed SEP dropouts that show different path lengths observed by ACE/ULEIS detector.	64

LIST OF FIGURES – *Continued*

2.14	Examples of SEP dropouts produced from numerical simulations. The result shows a SEP event that observed by two different observers. The two observations have different apparent path lengths.	65
2.15	The positions of energetic charged particles projected in $x - z$ plane at $t = 12$ hour. The results are from simulations using the foot-point random motion model.	67
2.16	The positions of energetic charged particles projected in $x - z$ plane at $t = 12$ hour. The results are from simulations using the two-component model.	68
2.17	Simulated diffusion coefficient of 1 MeV particles parallel and perpendicular to the mean magnetic field.	69
3.1	A 2-D example for the parallization of hybrid simulation.	80
3.2	1-D profiles of magnetic field component B_x , B_y , and B_z for Run 1 (with a small simulation box in the y and z directions).	83
3.3	1-D representation of magnetic-field magnitude, plasma density, and velocity for Run 1 (with a small simulation box in the y and z directions).	84
3.4	1-D profiles of magnetic field component B_x , B_y , and B_z for Run 2 (with a large simulation box in the y and z directions).	85
3.5	1-D representation of magnetic-field magnitude, plasma density, and velocity for Run 2 (with a large simulation box in the y and z directions).	86
3.6	The cross sections of magnetic-field magnitude and density close to the shock fronts for Run 1 and Run 2.	87
3.7	2-D representation of the magnitude of magnetic field B/B_0 and the velocity in the x -direction V_x/V_{A0} for Run 1 ($L_y = L_z = 10 c/\omega_{pi}$).	89
3.8	2-D representation of the plasma number density n/n_0 and the number density of the accelerated particles for Run 1 ($L_y = L_z = 10 c/\omega_{pi}$).	90
3.9	2-D representation of the magnitude of magnetic field B/B_0 and the velocity in the x -direction V_x/V_{A0} for Run 2 ($L_y = L_z = 40 c/\omega_{pi}$).	91
3.10	2-D representation of the plasma number density n/n_0 and the number density of the accelerated particles for Run 2 ($L_y = L_z = 40 c/\omega_{pi}$).	92
3.11	The magnitude of magnetic field around the shock front for Run 2.	93
3.12	The trajectory of a representative particle accelerated at the shock layer for the case of Run 1.	96
3.13	The trajectory of a representative particle accelerated at the shock layer for the case of Run 2.	97

LIST OF FIGURES – *Continued*

3.14	Three-dimensional plots of representative particle trajectories for Run 1 and Run 2.	98
3.15	1-D averages of the density of the accelerated particles in Run 1 and Run 2	99
3.16	Downstream energy spectra for ions in Run 1 and Run 2	100
3.17	2-D representation of the magnitude of magnetic field B/B_0 and the velocity in the x -direction V_x/V_{A0} for Run 3 (1-D pre-existing fluctuations).	101
3.18	2-D representation of the plasma number density n/n_0 and the number density of the accelerated particles for Run 3 (1-D pre-existing fluctuations).	102
3.19	The trajectory of a representative particle accelerated at the shock layer for Run 3.	103
3.20	2-D representation of the magnitude of magnetic field B/B_0 and the velocity in the x -direction V_x/V_{A0} for Run 4 (3-D isotropic pre-existing fluctuations).	104
3.21	2-D representation of the plasma number density n/n_0 and the number density of the accelerated particles for Run 4 (3-D isotropic pre-existing fluctuations).	105
3.22	The trajectory of a representative particle accelerated at the shock layer in the case of Run 3.	106
3.23	McComas & Schwadron (2006)'s idea on the acceleration of anomalous cosmic rays.	110
3.24	The shock and the magnetic field geometry for an upstream average magnetic field perpendicular to the shock normal.	114
3.25	The representation of density contour of accelerated particles.	117
3.26	The profiles of density of the accelerated particles.	119
3.27	<i>top</i> : The position in the z direction and time when the particle momentum reached $p = 3.0p_0$; <i>bottom</i> : The travel distance in the z direction $ z - z_0 $ and time when the particle momentum reached $p = 3.0p_0$	121
3.28	<i>top</i> : The position in the z direction and time when the particle momentum reached $p = 10.0p_0$; <i>bottom</i> : The travel distance in the z direction $ z - z_0 $ and time when the particle momentum reached $p = 10.0p_0$	122
3.29	The steady state distribution functions at different regions	124

LIST OF FIGURES – *Continued*

3.30	The shock and the magnetic field geometry considered for the case of an average magnetic field is 70° of the shock normal. The blue lines represent the magnetic field lines and red dashed line indicates the position of shock wave. The flow velocities are U_1 (upstream) and U_2 (downstream).	125
3.31	The density contour of accelerated particles for the case of oblique shock and $\delta B/B_0 = 0.5$	126
3.32	A comparison between a spatial profile for the density of energetic particles picked from the numerical simulation and observation made by Voyager 1.	128
4.1	A snapshot of the magnetic field in the z -direction B_z/B_1 represented in color-coded scale	141
4.2	The number of energetic electrons with energies $E > 10E_0$	142
4.3	Trajectory analysis for electron moving between ripples	143
4.4	Energy spectra of energetic electrons for different shock angles	144
4.5	Energy spectra of energetic electrons for an averaged perpendicular shock with different turbulence variances	146
4.6	Energy spectra of energetic electrons for different coherence lengths .	147
4.7	Three turbulent magnetic field lines for different correlation lengths. .	149
4.8	The profiles of the number of energetic electrons across the shock . .	150
4.9	Energy spectra of downstream protons for different shock angles . . .	152
4.10	Energy spectra of downstream protons for an averaged perpendicular shock with different turbulence variances.	153
4.11	Energy spectra of downstream protons for an averaged perpendicular shock with different turbulence correlation lengths	154
4.12	A cartoon illustration of the geometry of flare termination shocks. . .	158
4.13	The color-coded images of magnetic field B_z and ion density n_p	162
4.14	The energy spectra of electrons at the end of the simulation ($\Omega_i t = 130.0$) for runs 1-4.	163
4.15	The energy spectra of electrons at the end of the simulation ($\Omega_i t = 130.0$) for runs 2-7.	165
4.16	The relation between the turbulence amplitude $\delta B^2/B_0^2$ injected in hybrid simulation and the percentage of electrons eventually accelerated to more than 15 keV.	166
4.17	The energy spectra of protons downstream of the shock at the end of the simulation ($\Omega_i t = 130.0$), for runs 2-7	167

LIST OF TABLES

2.1	The parallel mean-free paths and diffusion coefficients calculated from quasi-linear theory.	50
2.2	Results of onset time analyses.	56
3.1	Some parameters for different cases in the 3-D hybrid simulations of parallel shocks: the size of the simulation domain in unit c/ω_{pi} , the variance of injected magnetic fluctuation σ^2 , and the model for the injected magnetic fluctuation.	82
4.1	Some parameters for different simulation runs. The size of the simulation domain, the variance of injected magnetic fluctuation, and the fraction of electrons whose energy is more than 15 keV at the end of simulation.	160

LIST OF ABBREVIATIONS

ACE (spacecraft) - Advanced Composition Explorer
ACR - Anomalous Cosmic Rays
AU - Astronomical Unit
CME - Coronal Mass Ejection
DSA - Diffusive Shock Acceleration
ESP - Energetic Storm Particles
ISEE (spacecraft) - International Sun-Earth Explorer
GCR - Galactic Cosmic Rays
MHD - Magnetohydrodynamics
SDA - Shock Drift Acceleration
SEP - Solar Energetic Particles
SSA - Shock Surfing Acceleration
STEREO (spacecraft) - Solar TERrestrial RELations Observatory

ABSTRACT

Turbulent magnetic fields are ubiquitous in space physics and astrophysics. The influence of magnetic turbulence on the motions of charged particles contains the essential physics of the transport and acceleration of energetic charged particles in the heliosphere, which is to be explored in this thesis. After a brief introduction on the energetic charged particles and magnetic fields in the heliosphere, the rest of this dissertation focuses on three specific topics: 1. the transport of energetic charged particles in the inner heliosphere, 2. the acceleration of ions at collisionless shocks, and 3. the acceleration of electrons at collisionless shocks. We utilize various numerical techniques to study these topics. In Chapter 2 we study the propagation of charged particles in turbulent magnetic fields similar to the propagation of solar energetic particles in the inner heliosphere. The trajectories of energetic charged particles in the turbulent magnetic field are numerically integrated. The turbulence model includes a Kolmogorov-like magnetic field power spectrum containing a broad range of scales from those that lead to large-scale field-line random walk to small scales leading to resonant pitch-angle scattering of energetic particles. We show that small-scale variations in particle intensities (the so-called “dropouts”) and velocity dispersions observed by spacecraft can be reproduced using this method. Our study gives a new constraint on the error of “onset analysis”, which is a technique commonly used to infer information about the initial release of energetic particles. We also find that the dropouts are rarely produced in the simulations using the so-called “two-component” magnetic turbulence model (Matthaeus et al., 1990). The result questions the validity of this model in studying particle transport. In the first part of Chapter 3 we study the acceleration of ions in the existence of turbulent magnetic fields. We use 3-D self-consistent hybrid simulations (kinetic ions and fluid electrons) to investigate the acceleration of low-energy particles (often termed as “injection problem”) at parallel shocks. We find that the accelerated particles always gain the first amount of energy by reflection and acceleration at the shock layer.

The protons can move off their original field lines in the 3-D electric and magnetic fields. The results are consistent with the acceleration mechanism found in previous 1-D and 2-D simulations. In the second part of Chapter 3, we use a stochastic integration method to study diffusive shock acceleration in the existence of large-scale magnetic variations. We show that the 1-D steady state solution of diffusive shock acceleration can be significantly modified in this situation. The results suggest that the observations of anomalous cosmic rays by Voyager spacecraft can be explained by a 2-D shock that includes the large-scale magnetic field variations. In Chapter 4 we study electron acceleration at a shock passing into a turbulent magnetic field by using a combination of hybrid simulations and test-particle electron simulations. We find that the acceleration of electrons is greatly enhanced by including the effect of large-scale magnetic turbulence. Since the electrons mainly follow along the magnetic lines of force, the large-scale braiding of field lines in space allows the fast-moving electrons interacting with the shock front multiple times. Ripples in the shock front occurring at various scales also contribute to the acceleration by mirroring the electrons. Our calculation shows that this process favors electron acceleration at perpendicular shocks. We discuss the application of this process in interplanetary shocks and flare termination shocks. We also discuss the implication of this study to solar energetic particles (SEPs) by comparing the acceleration of electrons with that of protons. The intensity correlation of electrons and ions in SEP events indicates that perpendicular or quasi-perpendicular shocks play an important role in accelerating charged particles. In Chapter 5 we summarize the results of this thesis and discuss possible future work.

CHAPTER 1

Introduction and Background

1.1 Overview

The heliosphere (Figure 1.1) is structured by plasma flows and magnetic fields. As the supersonic “solar wind” (Parker, 1958) expands from the solar atmosphere, it forces plasmas and magnetic fields outward, forming the cavity that interacts with the surrounding interstellar medium. At around 100 AU, the solar wind suddenly slows down and forms the termination shock. The heliosphere is a natural laboratory for physical processes involving charged particles and changing magnetic field. The related physical quantities are continuously measured by spacecraft and ground-based instruments. In particular, the Voyager spacecraft are currently exploring the heliopause, which is the boundary between the heliosphere and the local interstellar medium. It marks the frontier of the solar system and the farthest distance (~ 121 AU at the time of this writing) that man-made instruments have ever reached.

Energetic charged particles are a minor component of space plasmas, but have important and profound effects. They are serious concerns to space weather because of their hazardous effects to astronauts and space satellites. Energetic charged particles propagate at high speeds and carry important information about their source regions and the media they propagate through. Since the early measurements by Victor Hess in 1912, scientists have been measuring energetic particles with energies up to about 10^{21} eV and the electromagnetic radiation they produce.

The acceleration and transport of energetic charged particles are fundamental problems in space physics and astrophysics, in which electric and magnetic fields often play an essential role. From the first principle, the motions of charged particles in electromagnetic fields are governed by the Lorentz force. The large-scale transport and acceleration of energetic charged particles are often described by the

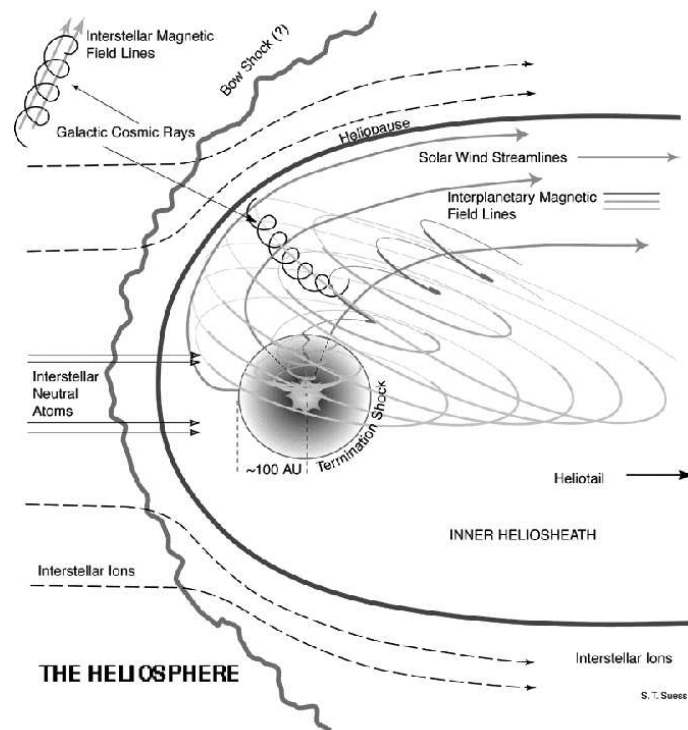


Figure 1.1: The interaction between interstellar medium and the heliosphere. Figure provided courtesy of Steve T. Suess.

Parker’s transport equation (Parker, 1965, see Equation 1.13), and the effect of turbulent magnetic fields is approximated by a large-scale spatial diffusion tensor (Jokipii, 1966, 1971). However, recent studies suggest that the simple spatial diffusion approximation may be oversimplified and the observed behavior of energetic particles is often more complicated. For example, during some solar energetic particle events, the intensity-time profiles often show small-scale sharp variations. In addition, when the velocity distribution of charged particles is highly anisotropic, it cannot be properly described by the transport equation that assumes a quasi-isotropic distribution. It is important to adequately describe this for problems such as the evolution of the velocity distribution of energetic particles during their propagation and the acceleration of low-energy particles at shocks. Understanding this is a challenge to theoretical studies due to the complex nature of particle trajectories in turbulent magnetic fields. Thanks to recent advances in computing capabilities, the acceleration and transport of charged particles can be studied by numerical simulations. This dissertation focuses on understanding the transport and acceleration of energetic charged particles in the existence of turbulent magnetic fields.

1.2 Charged Particles in the Heliosphere

The heliosphere is permeated by charged particles of different origins. There are two important components of charged particles that contribute to the global dynamics inside the heliosphere, i.e., the solar wind and pickup ions. The solar wind is a continuous plasma flow coming from the solar atmosphere (Parker, 1958). It is accelerated to supersonic speeds close to the Sun and propagates outward. The solar wind is often divided into two distinct components, termed as the slow solar wind and fast solar wind. The fast solar wind represents a plasma flow with a temperature about 8×10^5 K and a speed of about 800 km/s, whereas the slow solar wind represents a hotter ($T \sim 1.5 \times 10^6$ K) and denser plasma flow with a slower speed of about 400 km/s (Meyer-Vernet, 2007). The observations of the solar wind at different latitudes by the Ulysses spacecraft have shown that the slow solar

wind is confined to “streamer belt” that is about 20 degrees around the heliospheric current sheet at solar minimum. At the same time the fast solar wind entirely occupies higher latitudes. At solar maximum, the solar wind becomes more mixed and complicated (McComas et al., 2003). Pickup ions are mainly originated from interstellar neutral particles (Axford, 1972; Vasyliunas & Siscoe, 1976; Gloeckler et al., 1995), with minor contributions from inner source pickup ions (Geiss et al., 1995; Gloeckler & Geiss, 1998; Schwadron et al., 2000) and pickup ions from comets (Ipavich et al., 1986; Gloeckler et al., 1986). Interstellar neutral particles can freely penetrate into the heliosphere before they are ionized by charge exchange and/or solar ultraviolet radiation. Once the neutral particles are ionized, they are influenced by electric and magnetic fields (see Section 1.3). As illustrated in Figure 1.2, when the magnetic field vector has a component that is perpendicular to the solar wind velocity vector, the electric and magnetic fields embedded in the solar wind force them to accelerate and make gyro-motions in the frame co-moving with the solar wind. This is the so called “pickup” process. In observer’s frame, the pickup ions have velocities from zero to two times of solar wind speed. After the pickup process, the gyroradii of pickup ions are several times larger than that of the solar wind particles. The gyro-motion forms a ring velocity distribution perpendicular to the ambient magnetic field. The distribution is unstable and expected to generate electromagnetic waves. The “pickup ions” will be scattered into an isotropic distribution by the electromagnetic waves (Wu & Davidson, 1972; Wu et al., 1986) and/or background turbulence. Starting from a heliocentric distance of about 30 AU, the pickup ions play a dominant role in the physics of the outer heliosphere by dominating the pressure of the plasma flow (Richardson & Stone, 2009). It should be noted that neutral particles could also influence the dynamics in the heliosphere, which has been discussed extensively (Zank, 1999, and references therein).

Energetic charged particles are a high-energy, non-thermal component of the plasmas in the heliosphere. They carry large kinetic energies, so their speeds are much faster than background fluid. They have significant effects on space weather and their physics is important to consider. When the energy density of energetic

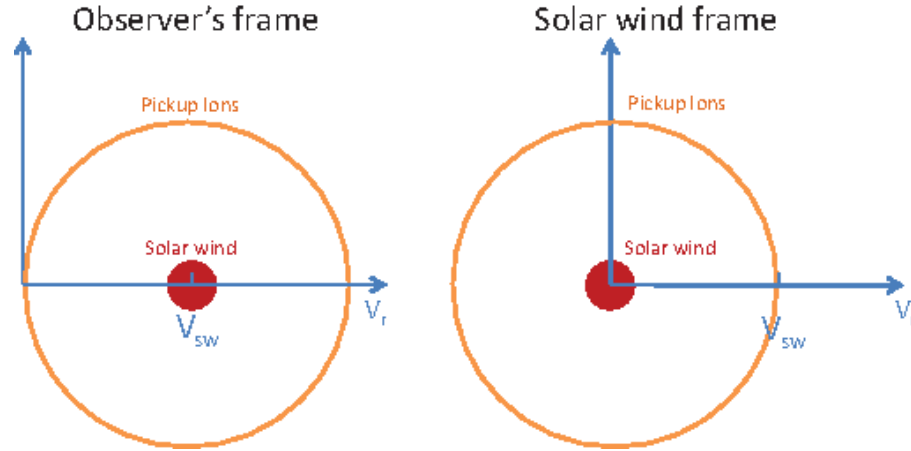


Figure 1.2: The velocity distribution of the solar wind ions and pickup ions in observer's frame and the solar wind frame.

charged particles is large enough, they may even mediate the dynamics of plasma flows (e.g., Florinski et al., 2009). Energetic charged particles in the heliosphere have different components depending on their acceleration sites, energy ranges, charge states, and elemental compositions, etc. Figure 1.3 illustrates various types of charged particles in the heliosphere, their acceleration regions, and their typical energy spectra. In this figure, the solar wind with energies in keV range represents the kinetic energy of the background flow in the heliosphere. Solar energetic particles (SEPs) are usually observed to be from several hundred keV/nucleon to tens of MeV/nucleon for typical events, and even more than 1 GeV/nucleon in extreme events. The SEP events are usually divided into two classes based on the progress made in the last three decades, termed as “impulsive events” and “gradual events” (see Reames, 1999, and references therein). The SEPs associated with impulsive events are thought to be accelerated in solar flares. Impulsive events are characterized by the impulsive peaks in their intensity-time profiles, confined source regions in longitude, high ionization states, and overabundance in isotope ratios such as $^3\text{He}/^4\text{He}$ and Fe/O compared with the values in the solar wind. Energetic particles related to gradual events are thought to be accelerated by collisionless shocks driven by coronal mass ejections (CMEs). The gradual events have extended

intensity-time profiles because of the continuous acceleration at shock fronts. They are also more widely distributed in longitude, indicating a broadened source region (Reames, 1999). Recently, this bi-model picture has been challenged. It has been found that for most events, SEPs appear to have a mixed property of the two classes of events. For example, some large gradual SEP events show a substantially high ionization charge state (Mazur et al., 1999) and enhanced isotope ratios in $^3\text{He}/^4\text{He}$ and Fe/O (Cohen et al., 1999; Mason et al., 1999). In large SEP events, flares and CMEs usually occur together, therefore one may expect that both of the processes play a role. Identifying their relations and contributions to large SEP events is still under hot debate. Energetic storm particles (ESPs) are usually associated with the passage of travelling interplanetary shocks, where the ions can often be accelerated to from several tens of keV/nucleon to MeV/nucleon, and occasionally more than 10 MeV/nucleon. Energetic charged particles associated with corotating interaction regions (CIRs) formed by the interaction between the fast and slow solar wind streams are often observed. These particles appear to have a higher energy range compared to that of ESPs. Anomalous cosmic rays (ACRs) are thought to be originated from pickup ions (Fisk et al., 1974), and are accelerated to energies between several MeV/nucleon to 100 MeV/nucleon at the termination shock (Pesses et al., 1981). Galactic cosmic rays (GCRs) that have energies typically larger than 10 MeV/nucleon are coming from the outside of the heliosphere.

One remarkable feature in Figure 1.3 is that the energy spectra of the accelerated ions are often close to a power law, which indicates a common acceleration process. The acceleration of electrons is also observed, and sometimes accompanies the acceleration of ions. We will discuss the acceleration of electrons in Chapter 4. It is worthwhile to note that many, if not all, of the energetic charged particles are associated with shock waves. For example, it is now established that many SEP events, especially gradual events are associated with CME-driven shocks (Reames, 1999). Energetic particles in impulsive events are accelerated in solar flares. The mechanism for particle acceleration in solar flares is not clear so far. In Chapter 4 we show that collisionless shocks are a possible candidate for the energization of

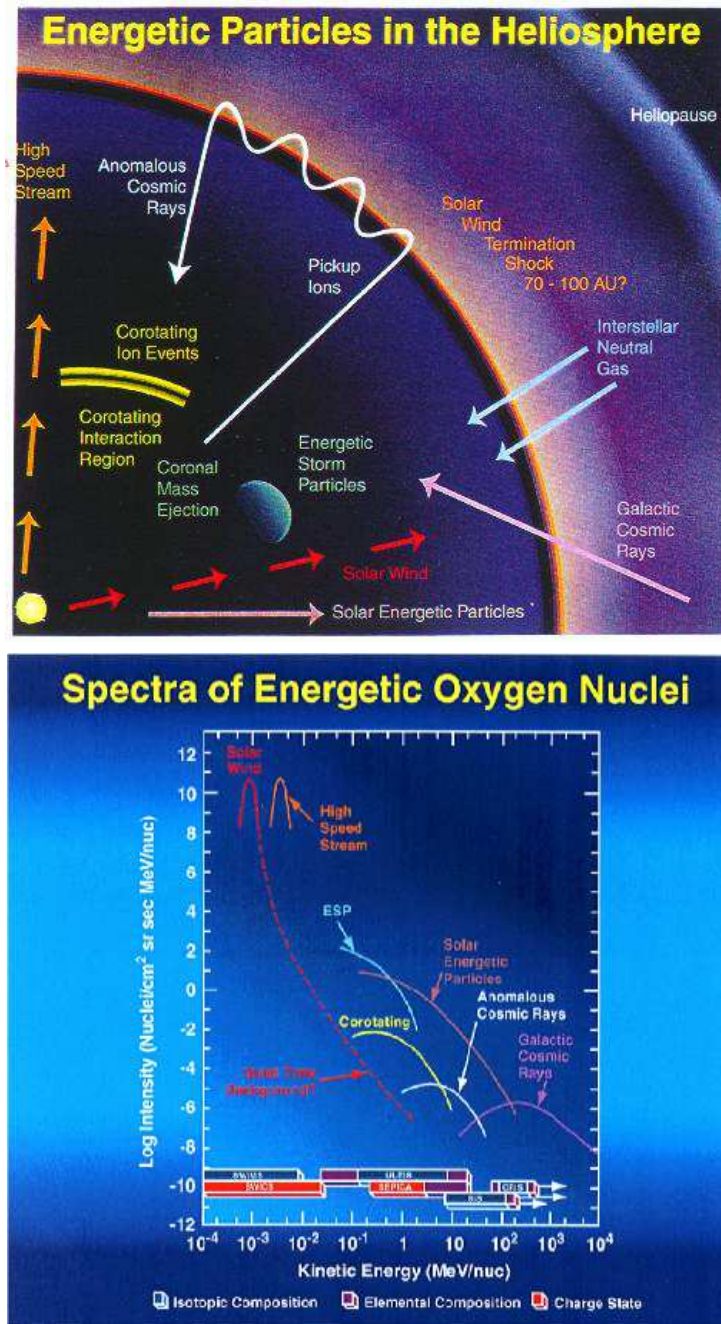


Figure 1.3: Various types of energetic charged particles in the heliosphere. The upper panel indicates related physical processes in different regions of the heliosphere. The bottom panel indicates typical energy spectra of energetic charged particles observed at 1 AU. See text for more details. The pictures are adapted from Stone et al. (1998) with permission by Springer Science + Business Media.

charged particles in solar flare regions. Energetic particles can be accelerated at interplanetary shocks driven by interplanetary CMEs and CIRs. ACRs are thought to be pickup ions accelerated at the solar wind termination shock (Pesses et al., 1981). GCRs are usually thought to be accelerated by astrophysical shocks such as supernova blast waves. Their spectrum is observed as the remarkable power law spectrum of cosmic rays.

After the acceleration, the energetic particles travel in and interact with the heliospheric magnetic field. Understanding the propagation of energetic particles is difficult since, in general, the motion of charged particles in a turbulent magnetic field is very complicated. The transport of energetic particles in heliospheric magnetic field is usually considered to be a diffusion process (Jokipii, 1966, 1971). In principle, if the motion of energetic particles is well understood, they can be used as a tracer of magnetic field structure in the heliosphere.

1.3 The Heliospheric Magnetic Field and its Fluctuations

Since plasma flows in the heliosphere are highly electrically conductive, the heliospheric magnetic field is frozen in the background fluid to a high degree. It can be inferred from the generalized Ohm's law that the only macroscopic electric field in this situation is due to the motional electric field $\mathbf{E} = -\mathbf{U}_{flow} \times \mathbf{B}/c$ (see, e.g., Krall & Trivelpiece, 1973), where \mathbf{U}_{flow} is the background flow speed, \mathbf{B} is magnetic field vector, and c is the speed of light in *vacuum*. The supersonic solar wind carries the magnetic field to many AU. Because of solar rotation, the magnetic field lines of force have a spiral shape termed as the Parker spiral (Parker, 1958; Hundhausen, 1972). In spherical coordinates (radial heliocentric distance \hat{r} , polar angle $\hat{\theta}$, and azimuthal angle $\hat{\phi}$), the average magnetic field is given by

$$\mathbf{B} = B_r \hat{r} + B_\phi \hat{\phi} = B_s \frac{R_s^2}{r^2} \left[\hat{r} - \frac{r \Omega_s \sin \theta}{V_{SW}} \left(1 - \frac{R_s^2}{r^2} \right) \hat{\phi} \right], \quad (1.1)$$

where B_r and B_ϕ are the magnetic fields in the \hat{r} and $\hat{\phi}$ direction respectively, B_s is the radial magnetic field close to the Sun at heliocentric distance R_s , V_{SW} is the

speed of the solar wind, and Ω_s is the angular frequency of the solar rotation. In this steady-state model, B_s , V_{SW} , and Ω_s are assumed to be constants.

At a low heliocentric latitude and a distance of 1 AU, the average angle between the direction of magnetic fields and the orientation of the solar wind flow at low latitude is about 45 degrees. In the outer heliosphere, the plasma almost flows transverse to the mean magnetic field. At high latitude regions ($\sin \theta \sim 0$), the azimuthal component of the Parker spiral magnetic field is small. However, it is expected that at a large heliocentric distance, the transverse perturbation of magnetic field lines of force dominates since it decays as $B_{tp} \propto 1/r$. The distant magnetic field almost always transverses to the radial direction while the average magnetic field is still the Parker spiral magnetic field (Jokipii & Kota, 1989). The inferred large scale fluctuations have been observed by the Ulysses spacecraft (Jokipii et al., 1995; Balogh et al., 1995).

Magnetic fields in the heliosphere are turbulent (Tu & Marsch, 1995; Goldstein et al., 1995). It is often convenient to write the magnetic field as a summation of an average component and a turbulent component $\mathbf{B} = \mathbf{B}_0 + \delta\mathbf{B}$. In the solar wind, the magnetic fluctuations are observed to be highly Alfvénic (Belcher & Davis, 1971, Figure 1.4), i.e., the magnetic fluctuation vector is highly correlated with the velocity fluctuation vector. Observations show that the power of turbulent magnetic field P_B versus spatial wave number k is close to a Kolmogorov law $P_B \propto k^{-5/3}$ (Coleman, 1968, Figure 1.4). The power spectrum suggests that most power of the fluctuations is in large spatial scales, and cascades into smaller and smaller spatial scales until dissipation effects are important. The correlation length is observed to be on the order of 10^6 km at 1 AU and increases in the outer heliosphere (Matthaeus & Goldstein, 1982). Recent theories, numerical simulations, and observations have revealed that the solar wind magnetic turbulence is anisotropic. In other words, most of the fluctuations have wave vectors transverse to the mean magnetic field (e.g., Matthaeus et al., 1990; Goldreich & Sridhar, 1995; Matthaeus et al., 1996).

Electric and magnetic fluctuations can also be produced by plasma instabilities. For example, freshly created pickup ions can have a ring distribution and excite

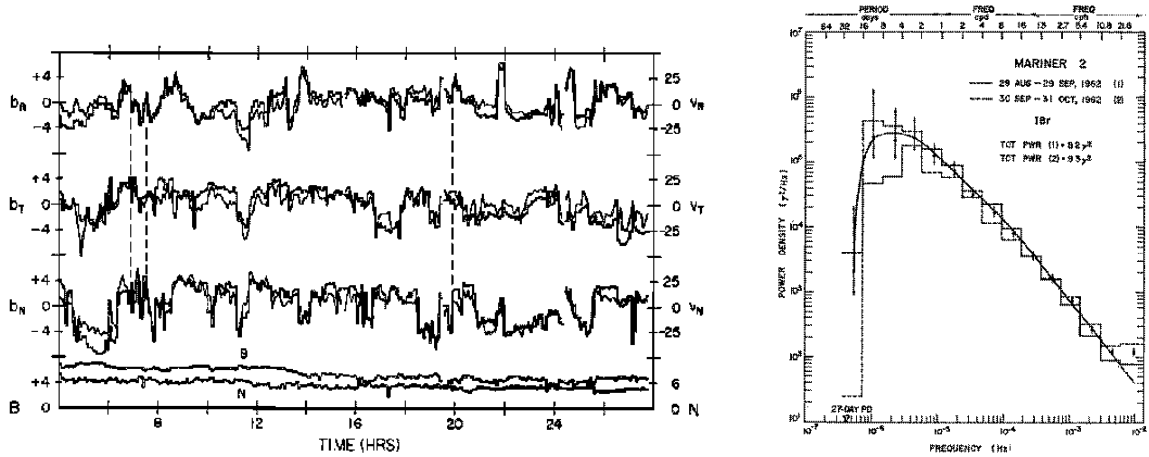


Figure 1.4: The spacecraft measurement of the Solar wind turbulence. Left: An example of magnetic field and velocity measurements in the solar wind (adapted from Belcher & Davis, 1971). Right: An example of power spectrum of magnetic field component measured in the solar wind fluctuations (Figure 6 in Coleman, 1968). The figure is reproduced by permission of the AAS.

ion-cyclotron waves (Wu & Davidson, 1972; Wu et al., 1986). In the upstream medium of a collisionless shock, the streaming of energetic particles may excite electromagnetic fluctuations (Lee, 1982, 1983). The fluctuation may be important for particle acceleration at quasi-parallel shocks.

1.4 Collisionless Shocks

Collisionless shocks are believed to be important accelerators for charged particles in the heliosphere. In this section we introduce the basic concepts of collisionless shocks. The acceleration of charged particles will be discussed in Chapter 3 and Chapter 4.

Shocks are characterized by sharp transitions in the physical quantities of medium such as flow speed, density, magnetic field, and temperature, etc. Since Coulomb collisions are too infrequent in space plasmas, the kinetic energy of plasma flow is dissipated at shocks through other mechanisms such as the interaction between particles and plasma waves. The shocks are termed as collisionless shocks. Dependent on the angle between upstream magnetic field vector and shock normal

θ_{Bn} , collisionless shocks can be divided into quasi-perpendicular shocks ($\theta_{Bn} > 45^\circ$) and quasi-parallel shocks ($\theta_{Bn} < 45^\circ$). In the limit of ideal magnetohydrodynamics (MHD), shocks are a kind of discontinuities. One can relate upstream and downstream medium using MHD conservation laws and Maxwell equations. The result gives the well-known jump conditions for MHD discontinuities (e.g., Burgess, 1995):

$$B_{1n} = B_{2n} \quad (1.2)$$

$$U_{1n}B_{1t} = U_{2n}B_{2t} \quad (1.3)$$

$$\rho_1 U_{1n} = \rho_2 U_{2n} \quad (1.4)$$

$$\rho_1 U_{1n}^2 + P_1 + \frac{B_1^2}{8\pi} = \rho_2 U_{2n}^2 + P_2 + \frac{B_2^2}{8\pi} \quad (1.5)$$

$$\rho_1 U_{1n}U_{1t} - \frac{B_{1n}B_{1t}}{4\pi} = \rho_2 U_{2n}U_{2t} - \frac{B_{2n}B_{2t}}{4\pi} \quad (1.6)$$

$$\begin{aligned} \rho_1 U_{1n} \left(\frac{1}{2} U_1^2 + \frac{\gamma}{\gamma-1} \frac{P_1}{\rho_1} \right) + U_{1n} \frac{B_1^2}{4\pi} - (\mathbf{U}_1 \cdot \mathbf{B}_1) \frac{B_{1n}}{4\pi} &= \rho_2 U_{2n} \left(\frac{1}{2} U_2^2 + \right. \\ \left. \frac{\gamma}{\gamma-1} \frac{P_2}{\rho_2} \right) + U_{2n} \frac{B_2^2}{4\pi} - (\mathbf{U}_2 \cdot \mathbf{B}_2) \frac{B_{2n}}{4\pi} &\quad (1.7) \end{aligned}$$

where B , U , ρ , and P represent magnetic field, flow speed, density, and pressure, the subscript “1” and “2” specify physical quantities in upstream and downstream media, and the subscripts “n” and “t” mean the normal components and transverse components, respectively.

The shock solutions of the jump conditions have three possibilities: slow shocks, intermediate shocks, and fast shocks, which correspond to three modes of waves in MHD. In this thesis we only discuss fast shocks. At a fast-mode shock, the flow is decelerated and compressed. The transverse component of magnetic field increases as the magnetic field get compressed at the shock. Fast shocks are most frequently observed shocks in the heliosphere, including planetary bow shocks, CME-driven shocks, most of interplanetary shocks, and the solar wind termination shock.

Strong shocks in the heliosphere are usually supercritical shocks where the shock Mach numbers $M_A > M_{critical}$ and $M_{critical} \leq 2.76$ depends on the shock normal angle and the plasma beta, etc (Stone & Tsurutani, 1985). In these shocks a fraction

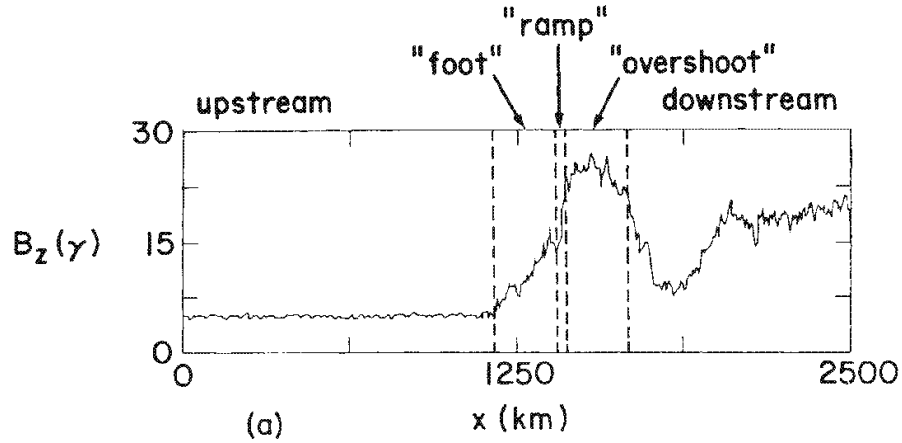


Figure 1.5: The structure of quasi-perpendicular supercritical shocks. The picture is adapted from (Wu et al., 1984) with permission by Springer Science + Business Media.

of ions get reflected at the shock front, which provide an additional dissipation mechanism as resistivity cannot provide enough dissipation (Tidman & Krall, 1971). At small spatial scales, shocks have microscopic structures and the structures are often distinct dependent on the shock normal angle θ_{Bn} . For quasi-perpendicular supercritical shocks, the shock structure is relatively well-defined. Since magnetic field vector is mainly perpendicular to the shock normal vector, after ions first encounter the shock, their gyro-motions are confined to the vicinity of the shock front. The quasi-perpendicular shocks are featured by the “foot-ramp-overshoot” structure, as shown in Figure 1.5 (Leroy et al., 1982). For quasi-parallel shocks, their micro-structures are less clear than that of perpendicular shocks. The micro-structure for quasi-parallel supercritical shocks is shown in Figure 1.6. Since the background magnetic field is mainly along the shock normal, the reflected ions can travel far upstream. It forms ion beams that excite ion-scale low-frequency waves. These waves grow in amplitude and is shortened in wavelength as they approach the shock. The structures are so called SLAMS (stands for Short Large Amplitude Magnetic Structures).

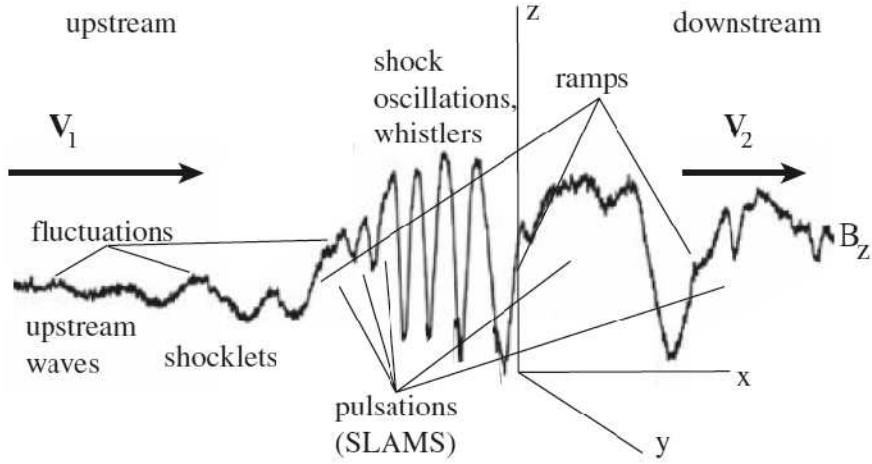


Figure 1.6: The structure of quasi-parallel supercritical shocks. The picture is adapted from (Treumann, 2009) with permission by Springer Science + Business Media.

1.5 The Motions of Charged Particles

The heliosphere provides a natural laboratory to study the physics of charged particles. In this section we discuss the motions of charged particles influenced by a variety of effects. For energetic charged particles in the heliosphere, their motions are completely dominated by the Lorentz force.

When the kinetic energy density of charged particles for the problem of interest is much less than the background field, the motion of charged particles has virtually no feedback to the background field and can be approximated as test particles. The major forces acting on a charged object include electromagnetic force and gravity. In spherical coordinates with radial heliocentric distance \hat{r} , according to Newton's second law, we have

$$F_{total} = \frac{d\mathbf{p}}{dt} = q(\mathbf{E} + \frac{1}{c}\mathbf{v} \times \mathbf{B}) - \frac{GM_s m}{r^2}\hat{r} + \text{other forces}, \quad (1.8)$$

where \mathbf{E} and \mathbf{B} are electric and magnetic field vectors, \mathbf{p} , \mathbf{v} , q , and m are the momentum vector, velocity vector, electric charge, and mass of a particle, respectively, c is the speed of light in *vacuum*, G is the gravitation constant, and M_s is the mass

of the Sun.

It is easy to show that for energetic charged particles such as ions and electrons in the heliosphere, their motion is dominated by the Lorentz force. For larger particles, such as charged dust grains, other effects like radiation pressure and Poynting-Robertson drag, etc. may also be important dependent on their charge and mass. In this dissertation we focus on energetic charged particles. Their motions in electromagnetic field can be described by

$$F_{EM} = \frac{d\mathbf{p}}{dt} = q\mathbf{E} + \frac{q}{c}\mathbf{v} \times \mathbf{B}. \quad (1.9)$$

In the simplest case with constant magnetic field $\mathbf{B} = B_0\hat{z}$ and no electric field, the equation has the solution that describes a gyro-motion around a magnetic line of force:

$$\begin{aligned} v_x &= v_\perp \cos(\Omega t + \phi_0) \\ v_y &= -v_\perp \sin(\Omega t + \phi_0) \end{aligned} \quad (1.10)$$

$$\begin{aligned} v_z &= v_\parallel \\ x &= \frac{v_\perp}{\Omega} \sin(\Omega t + \phi_0) + x_0 \\ y &= \frac{v_\perp}{\Omega} \cos(\Omega t + \phi_0) + y_0 \\ z &= v_\parallel t + z_0, \end{aligned} \quad (1.11)$$

where v_\perp and v_\parallel are velocity components perpendicular and parallel to the magnetic field, respectively. The gyrofrequency $\Omega = qB/mc$. ϕ_0 , x_0 , y_0 and z_0 are constant.

When charged particles are moving in electric and magnetic fields that are spatially and temporally dependent, the motions of energetic charged particles are very complicated in general. An important approximation is when the particle moves in a slowly varying electric and magnetic field on spatial and temporal scales much larger than the scale of gyro-motions. In this case the motion of a charged particle can be expressed as a summation of a gyro-motion and a drift motion of the guiding center. In a static electric and magnetic field, the guiding-center motion of charged particles can be expressed as (Boyd & Sanderson, 2003):

$$\mathbf{v}_{gc} = \left[v_{\parallel} + \frac{cW_{\perp}}{qB^3} \mathbf{B} \cdot (\nabla \times \mathbf{B}) \right] \frac{\mathbf{B}}{B} + \mathbf{U}_{flow\perp} + \frac{cW_{\perp}}{qB^3} \mathbf{B} \times \nabla B + \frac{2cW_{\parallel}}{qB^4} \mathbf{B} \times (\mathbf{B} \cdot \nabla) \mathbf{B}, \quad (1.12)$$

where $W_{\perp} = mv_{\perp}^2/2$ and $W_{\parallel} = mv_{\parallel}^2/2$ are the components of particle kinetic energy perpendicular and parallel to the magnetic field, and $\mathbf{U}_{flow\perp}$ is the background flow speed component that is perpendicular to the magnetic field. The first two terms describe the particle motion parallel to the magnetic field including the original velocity parallel to the magnetic field and a small modification caused by parallel drift. The remaining terms are drift motion transverse to a magnetic field line caused by drift in the motional electric field, gradient B drift, and curvature B drift.

Magnetic fluctuations have profound influences on the behavior of energetic charged particles. One important effect is pitch-angle scattering by resonant interactions between charged particles and magnetic fluctuations. When the resonant condition $k_{\parallel}v_{\parallel} - \omega - \Omega = 0$ is satisfied, the particle can strongly interact with magnetic fluctuations and the pitch-angles of charged particles may be changed. Here k_{\parallel} and ω are the wave number parallel to the magnetic field and angular frequency of the wave, and v_{\parallel} is the parallel velocity of the particle. The resonant wave-particle interaction results in the evolution of distribution function that can be described by a pitch-angle diffusion.

1.6 The Transport and Acceleration of Charged Particles

Particle transport and acceleration are fundamental problems in space physics and astrophysics. This section gives an overview of this subject. The large-scale behavior of energetic charged particles is usually approximated by a diffusion process, given the fact that the scattering time is short compared to the time scale of interest. For particles moving in a compression/expansion flow, energetic particles experience an increase/decrease in energy. A complete equation that describes the evolution of a nearly isotropic distribution of energetic charged particles is the well-known Parker transport equation (Parker, 1965). The equation describes the large-scale evolution

of the distribution function $f(x_i, p, t)$ of the energetic particles with momentum p dependent on the position x_i and time t including effects of diffusion, convection, drift, acceleration and source particles:

$$\frac{\partial f}{\partial t} = \frac{\partial}{\partial x_i} \left[\kappa_{ij} \frac{\partial f}{\partial x_j} \right] - U_i \frac{\partial f}{\partial x_i} - V_{d,i} \frac{\partial f}{\partial x_i} + \frac{1}{3} \frac{\partial U_i}{\partial x_i} \left[\frac{\partial f}{\partial \ln p} \right] + Q, \quad (1.13)$$

where κ_{ij} is the symmetric part of the diffusion coefficient tensor, U_i is the velocity of plasma fluid, and Q is a local source. The drift velocity can be formally derived from the drift motion for a single particle in guiding center approximation (Equation 1.12) by assuming a quasi-isotropic distribution function (Isenberg & Jokipii, 1979). It is given by $\mathbf{V}_{d,i} = (p_i c w_i / 3 q_i) \nabla \times (\mathbf{B} / B^2)$, where w_i is the velocity of the particles, c is the speed of light in *vacuum*, and q_i is the electric charge of the particles. The drift can be included in the diffusion tensor as an anti-symmetric part

$$\kappa_A = p_i c w_i / 3 q_i B. \quad (1.14)$$

The motions of energetic charged particles parallel and perpendicular to magnetic field directions are generally quite distinct. The spatial transport coefficient along the mean magnetic field can be related to the pitch-angle diffusion coefficient $D_{\mu\mu}$ (Jokipii, 1966). The diffusion of energetic particles transverse to the mean magnetic field is less understood. Recent test-particle simulation has shown that the perpendicular diffusion coefficient κ_{\perp} can be a few percent of the parallel diffusion coefficient κ_{\parallel} (Giacalone & Jokipii, 1999). The symmetric part of the spatial diffusion tensor can be related by the magnetic field vector B_i and diffusion coefficient parallel and perpendicular to the magnetic field:

$$\kappa_{ij} = \kappa_{\perp} \delta_{ij} - \frac{(\kappa_{\perp} - \kappa_{\parallel}) B_i B_j}{B^2}. \quad (1.15)$$

The Parker's transport equation also describes the acceleration (deceleration) of charged particles. This equation states that the first-order energy change is due to the compression (expansion) of plasma flows. It has been shown by a series papers (Krymsky, 1977; Axford et al., 1977; Bell, 1978; Blandford & Ostriker, 1978) that

collisionless shocks are the acceleration sites of charged particles because of the sharp compressions. It should also be noted that particle acceleration may also happen in MHD turbulence (e.g., Petrosian & Liu, 2004), reconnection regions (e.g., Drake et al., 2010), and parallel electric fields due to non-ideal MHD effects (Damiano & Wright, 2005). These processes will not be discussed in this dissertation.

1.7 Summary of the Following Chapters

In this dissertation, we study the acceleration and transport of charged particles, focusing on the effect of fluctuating magnetic fields. The importance of turbulent magnetic fields has been recognized in many previous works. However, the previous studies often treat the effect of magnetic field as a rather simplified process. For example, the propagation of energetic particles in space is often assumed to be a simple spatial diffusion, and the particle acceleration at collisionless shock has often been considered as a process in a 1-D planar shock, etc. While these simplified approximations were successful in describing the physical processes, these theories have been facing some difficulties in understanding the physical processes and explaining observations.

Recently, there have been a few observations that begin to challenge this picture. For example, some spacecraft have observed SEP events in great details (Mazur et al., 2000). The observations of impulsive SEP events show fine structures in intensity-time plots on small temporal scales (hours) that are not described by a large-scale spatial diffusion (Mazur et al., 2000; Chollet et al., 2007; Chollet & Giacalone, 2008). The Voyager spacecraft crossed the solar wind termination shock but did not observe a saturated energy spectrum of ACRs, which is predicted by the 1-D, time-steady shock theory. As we will show in this dissertation, many features in the observations of energetic particles can be explained by considering the turbulent nature of magnetic fields. Moreover, we also discuss situations that the transport of charged particles cannot be described by the Parker's equation. An example is the process related to low-energy particles or other charged particles with high

anisotropies. Since the Parker’s equation only concerns a quasi-isotropic distribution of charged particles, their physical processes can not be appropriately described by the equation. Using numerical simulations, we study the transport of energetic particles with high anisotropies and the acceleration of low-energy particles.

In Chapter 2 we study the propagation of charged particles in a turbulent magnetic field, which is similar to the propagation of impulsive SEPs in the inner heliosphere. The trajectories of energetic charged particles in the turbulent magnetic field are numerically integrated. The charged particles reached 1 AU are collected to mimic spacecraft observations. We show that small-scale variations in the observed particle intensity (the so-called “dropouts”) and velocity dispersion observed by spacecraft can be well reproduced using this method. Our study also gives a new constraint on the error of “onset analysis”, which is a technique commonly used to study the propagation of energetic particle and infer the information of the initial injection of energetic particles. We also find that the dropouts are rarely produced in the simulations using the so-called “two-component” magnetic turbulence model (Matthaeus et al., 1990). The result questions the validity of this model in studying particle transport. In Chapter 3 we study the acceleration of ions in the existence of turbulent magnetic fields. We use 3-D hybrid simulations (kinetic ions and fluid electron) to study the acceleration of low-energy particles at parallel shocks. This gives new results for the initial acceleration of particles at shocks in fully three-dimensional electric and magnetic fields. We also use a stochastic integration method to study diffusive shock acceleration in the existence of large-scale magnetic variation. The results show that the observations by Voyager spacecraft can be explained by a 2-D shock that includes the large-scale magnetic field variation. In Chapter 4 we study the electron acceleration at a shock passing into a turbulent magnetic field by using a combination of hybrid simulations and test-particle electron simulations. We found that the acceleration of electrons is enhanced by including this effect. We discuss the application of this process in interplanetary shocks and flare termination shocks. We also discuss the implication of this process for SEP events. The correlation of electrons and ions in SEP events indicates that perpendicular or quasi-perpendicular

shocks play an important role in accelerating charged particles. In Chapter 5 we summarize the results and discuss the future work.

CHAPTER 2

The Effect of Turbulent Magnetic Fields on the Propagation of Solar Energetic Particles in the Inner Heliosphere

2.1 Overview of the Transport of Solar Energetic Particles

One of the most important tasks in the study of solar energetic particles (SEPs) is to understand their propagation in the heliospheric magnetic field. The large-scale transport of SEPs in the solar wind is usually studied by solving the transport equation (Equation 1.13) first derived by Parker (1965). The spatial diffusion tensor (Equation 1.15) can be studied by considering the statistical properties of magnetic turbulence (Jokipii, 1966, 1971; Giacalone & Jokipii, 1999; Matthaeus et al., 2003). The transport equation has been routinely used to fit the intensity-time profiles of SEP events for several decades (e.g., Burlaga, 1967). For gradual SEP events (see Section 1.2), it has been realized that the profiles of the SEPs cannot be described by a simple spatial diffusion process since the energetic particles are continuously accelerated at the shock front, meaning that there must be at least energy changes (Kahler et al., 1984). For impulsive SEP events (see Chapter 1.2), energetic particles are usually released from a confined region in a short duration, which provides a relatively simple case to study the transport of energetic particles in space. A long standing problem related to the transport of energetic particles is that the mean-free paths inferred from SEP events are usually much longer than those derived from the quasi-linear theory (Palmer, 1982; Bieber et al., 1994), which assumes that the trajectories of charged particles are weakly perturbed by magnetic fluctuations. The discrepancy between the observations and the theories is still not well resolved. Another problem that requires further investigation is the large-scale transport of charged particles normal to the magnetic field. Some analyses give a rather small cross-field diffusion so the ratio of the perpendicular diffusion coefficient to the

parallel diffusion coefficient is $\kappa_{\perp}/\kappa_{\parallel} \sim 10^{-4}$ or smaller (Roelof et al., 1983). Recent numerical simulations and analytical studies give a larger value of $\kappa_{\perp}/\kappa_{\parallel} \sim 0.02$ or larger for energetic particles moving in the heliospheric magnetic field at 1 AU (Giacalone & Jokipii, 1999; Qin et al., 2002; Matthaeus et al., 2003).

Recently, there have been several observations of SEP events that reveal some new characteristics of particle transport. For example, Mazur et al. (2000) reported that the intensity of impulsive SEP events often shows small-scale sharp variations, alternatively called the “dropouts” of SEPs (see Figure 2.1). These dropouts are commonly seen in impulsive SEP events and the typical convected distance between the dropouts is about 0.03 AU, similar to the spatial scale of the correlation length of the solar wind turbulence. The occurrence of the dropouts does not seem to be associated with the rapid magnetic field changes as one can see from Figure 2.1, meaning that it is more associated with some large-scale transport effects. The phenomena indicate that the diffusion of energetic particles transverse to the local magnetic field is very small (see also, Chollet & Giacalone, 2011), and the transport of energetic particles in the solar wind is not a simple diffusion process as described by the Parker’s transport equation (1.13). However, Some spacecraft measurements indicate that the ratio between perpendicular to parallel diffusion coefficient $\kappa_{\perp}/\kappa_{\parallel}$ can reach values of 0.2 or even larger (Dwyer et al., 1997; Zhang et al., 2003), which is unexpectedly large compared to those obtained from numerical simulations (Giacalone & Jokipii, 1999). Newly available data shows that impulsive SEP events are occasionally seen by all three spacecraft (STEREO A/B and ACE) with a more than 100-degree longitudinal separation (Wiedenbeck et al., 2010). Giacalone & Jokipii (2012)’s numerical simulations suggest that the perpendicular diffusion has to be as large as a few percent to explain these multi-spacecraft observations. It should be noted that the motions of energetic charged particles transverse to magnetic field can be considered to consist of two parts: 1. the actual particle motion across the local magnetic field due to drift or scattering; and 2. the particle motions along meandering magnetic field lines but normal to the mean magnetic field. The observed SEP “dropouts” may be interpreted as that the motions of particles across

the local magnetic field is small, but a large part of the perpendicular diffusion can be contributed by field-line random walk. These new observations have provided an excellent opportunity to examine and constrain the relative contributions from these two effects to the large-scale perpendicular transport.

Using numerical simulations that contain large-scale turbulent magnetic fields, Giacalone et al. (2000) have demonstrated that the dropouts can be reproduced when energetic particles are released in a small source region near the Sun. The idea of the model can be illustrated by Figure 2.2. When the source region of a SEP event is small, it just releases energetic particles into a small volume in space so that only some magnetic flux tubes are filled by energetic particles. When the field lines of force are meandering, the magnetic flux tubes will convect through spacecraft at 1 AU with a mixture of those filled by energetic particles and those that are not. The spacecraft that observe the passage of these flux tubes will see “dropouts” of the SEP intensity. It should be noted that this model is consistent with magnetic turbulence models that allow a large perpendicular diffusion with a value of $\kappa_{\perp}/\kappa_{\parallel} \sim 0.02$ or larger due to field line random walk (Giacalone & Jokipii, 1999). The time duration between the numerically produced dropouts is several hours, which is similar to that observed in the impulsive SEP events. It also naturally reproduces the feature that the typical spatial scale for the convected distance between the dropouts is the same as the correlation scale in the solar wind turbulence (Mazur et al., 2000). Based on the so-called “two-component” model (see Section 2.2), Ruffolo et al. (2003) and Chuychai et al. (2007) proposed a somewhat different idea. They argued that some magnetic field lines in the solar wind can have very restricted random walk. The corresponding magnetic flux tubes connecting to the source regions are concentrated by energetic particles; For magnetic field lines that are meandering in space, the energetic particles in the associated flux tubes will diffuse away. However, this effect depends on the “two-component” magnetic field model they use (a composition of a two-dimensional fluctuation and a one-dimensional fluctuation) and the motions of charged particles during the trapping are not explored by numerical simulations. Although previous numerical simulations that contain large-scale field-line random

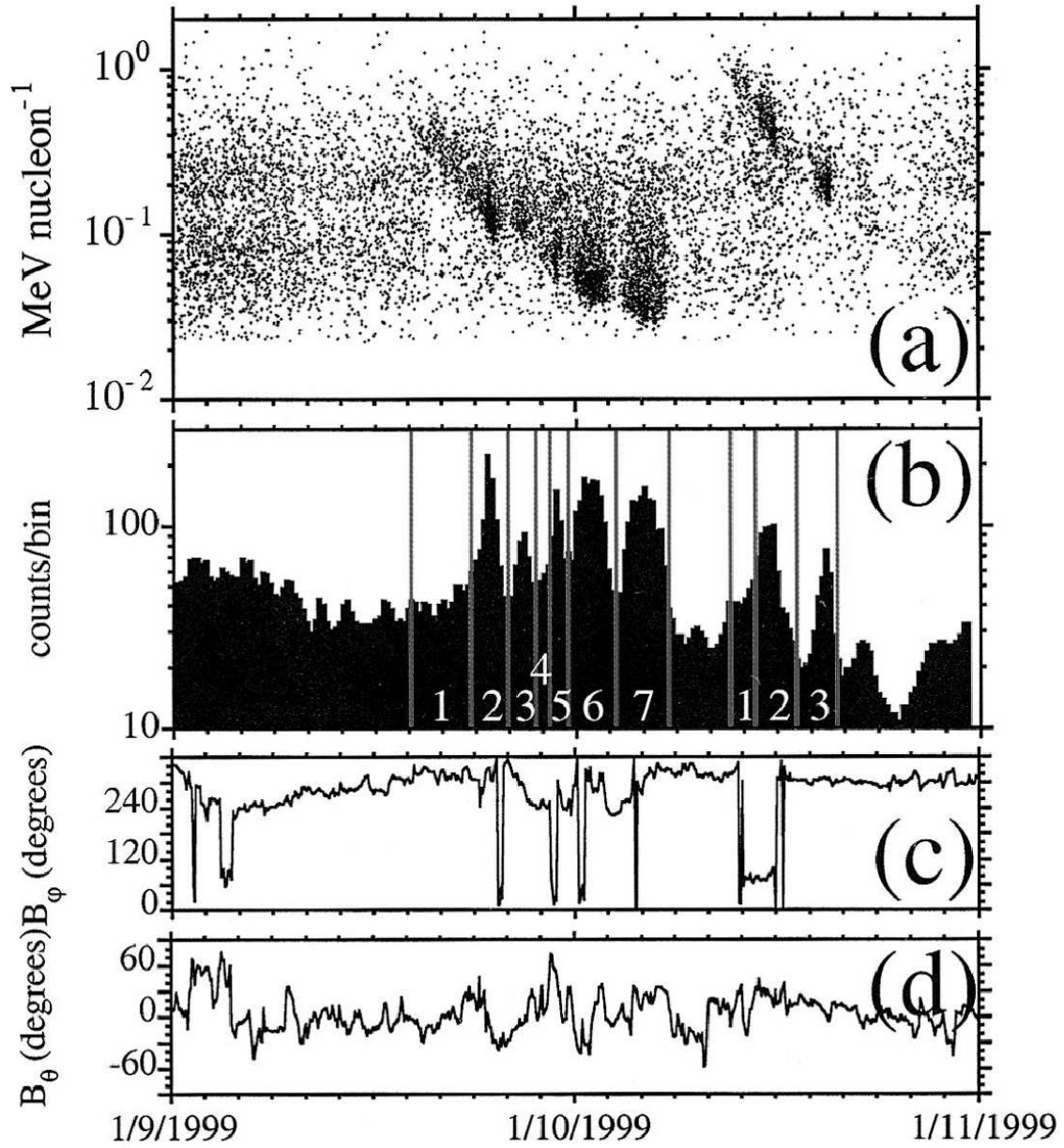


Figure 2.1: An example of impulsive SEP events that show “dropouts” of energetic particle intensity (Figure 1 in Mazur et al., 2000). The figure is reproduced by permission of the AAS.

walk has successfully produced SEP “dropouts” (Giacalone et al., 2000), this model assumed an *ad hoc* pitch-angle scattering that is not realistic. Physically, the pitch-angle scattering should be caused by small-scale magnetic fluctuations, which was not present in the Giacalone et al. (2000) model. One main purpose of this study is to include the effect of small-scale magnetic turbulence and examine the propagation of SEPs in a turbulent magnetic field that has a power spectrum similar to that derived from observations. The current numerical simulations directly solve the equations of motion for charged particles in turbulent magnetic fields generated by magnetic turbulence models. The results (Section 2.4) give some new insight for the transport of energetic particles in the heliospheric magnetic fields.

Another important issue on the transport of SEPs in interplanetary space is whether we can relate the *in-situ* spacecraft observation of a particular SEP event at 1 AU to the initial release of energetic particles in the solar atmosphere (time and/or location). Since the energetic particles suffer from spatial diffusion, they gradually lose the information about the source regions and injection times after they are released. A popular way to get the information about the location of source regions and release time is to analyse the onsets of SEP events, namely, the earliest arriving particles at a given energy (Krucker & Lin, 2000; Tylka et al., 2003; Mewaldt et al., 2003; Kahler & Ragot, 2006; Chollet, 2008; Hill et al., 2009; Reames, 2009). Those particles have experienced the least scattering during propagation. One can obtain the apparent propagation path length L and the apparent release time $t_{release}$ of SEP events by linearly fitting the onsets of the first arriving particles based on the formula

$$t - t_{release} = L/v, \quad (2.1)$$

where t is the arriving time for first-arriving particles at a given energy and v is the velocity corresponding to the energy. The assumptions implicitly made in these studies are that the first-arriving particles are released impulsively and have

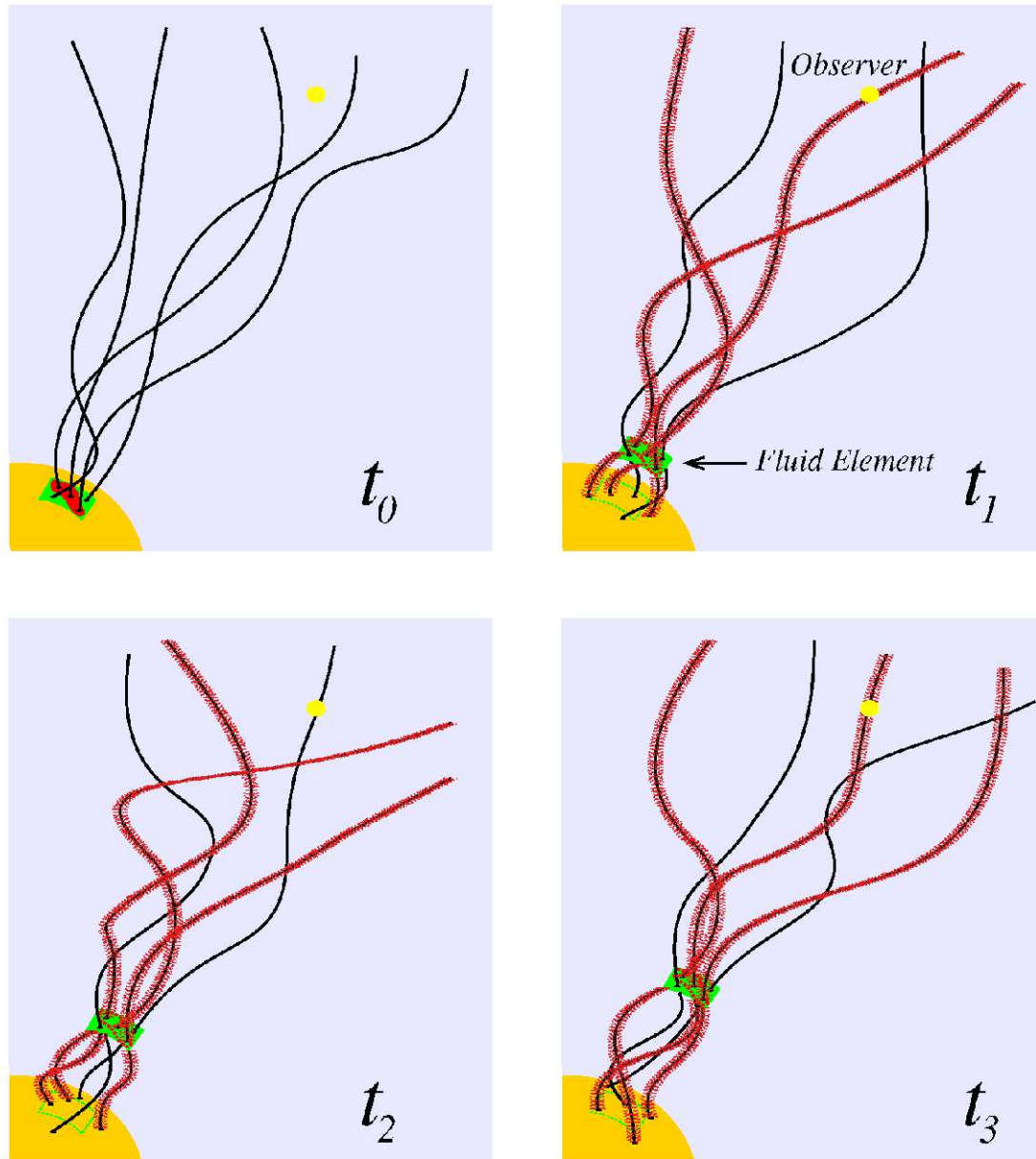


Figure 2.2: A cartoon that illustrates the effect of meandering magnetic field lines on the observations of energetic particles. The SEP dropouts can be seen when different field lines pass by the observer. Figure provided courtesy Joe Giacalone, University of Arizona.

experienced no scattering or energy change and that they have travelled exactly along the magnetic field lines with pitch-angle cosines $\mu = 1$. A main criticism of this method is that the assumption is inconsistent with the fact that the mean-free paths of energetic particles in the inner heliosphere are usually less than 1 AU. Moreover, the mean-free path is usually energy dependent. Nevertheless, some onset analyses do show a good linear relation. In Figure 2.3 we show an example for the onset analysis to a SEP event, which is adapted from (Figure 8 in Reames, 2009). One can see that the linear relation in the “onset time” versus c/v plot is quite good for the energy range they use (> 1 MeV/nucleon). However, the apparent path length is larger than typical length of Parker spiral (1.1-1.2 AU). The feature that the fitted path length is different from the Parker spiral magnetic field lines has been found by a few authors (Krucker & Lin, 2000; Tylka et al., 2003; Mewaldt et al., 2003; Kahler & Ragot, 2006; Chollet, 2008). Pei et al. (2006) have demonstrated that the effect of large-scale field line meandering can significantly change the arrival times for energetic particles, and when some of the field lines are straightened radially, the energetic particles can arrive at 1 AU faster than particles travel along the Parker spiral. This is the issue that will be further explored in this chapter. Lintunen & Vainio (2004), Sáiz et al. (2005) and Diaz et al. (2011) have used more sophisticated particle transport models to examine the validity of the velocity dispersion analysis and they estimate the errors contained in these analyses could be on the order of several minutes or even an hour for typical parameters at 1 AU. However, none of these works considers the propagation of energetic particles in a turbulent magnetic field that has a power spectrum that extends to small resonant scales similar to Giacalone & Jokipii (1999).

In this study, we use two different types of 3-D magnetic field turbulence models often used in studying the transport of energetic particles in space. The generated fluctuating magnetic field has a Kolmogorov-like power spectrum with wavelengths from just larger than the correlation scale, leading to large-scale field-line random walk, down through very small scales that lead to resonant pitch-angle scattering of the particles. In Section 2.2 we describe the magnetic turbulence models and

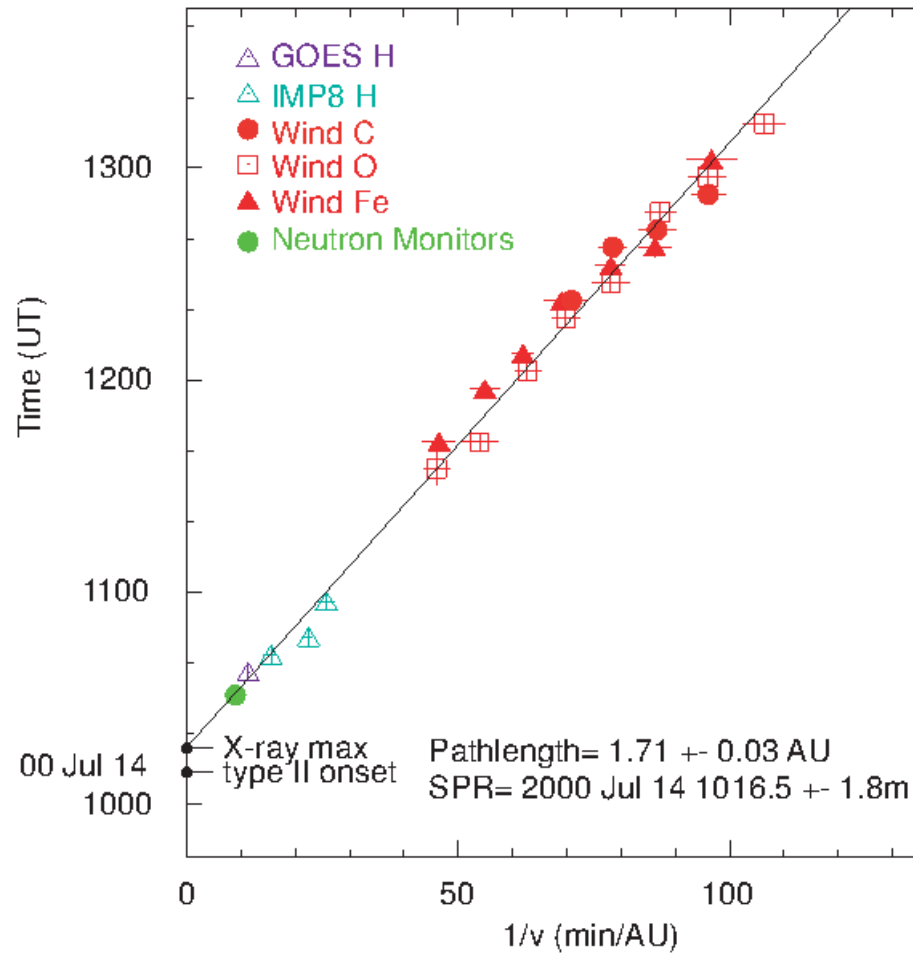


Figure 2.3: An example of onset analyses for SEP events. The plot is adapted from (Figure 8 in Reames, 2009). The figure is reproduced by permission of the AAS.

numerical methods we use to study the propagation of energetic particles. In Section 2.3 we use the magnetic turbulence models to study the first-arriving particles and test the validity of the velocity dispersion analysis. We estimate the errors in this technique in a variety of cases with different magnetic fluctuation amplitudes and thresholds for the onset. In Section 2.4, we use the magnetic turbulence models to study the propagation of SEPs. We show that the “dropouts” of impulsive SEPs can be produced using the foot-point random motion model when the source region is small. However, for the two-component model, we find that the “dropouts” are rarely seen for the parameters we use. The results of this chapter will be summarized in Section 2.5.

2.2 Numerical Model

In this study we consider the propagation of energetic particles from a spatially compact and instantaneous source in turbulent magnetic fields. We primarily use two magnetic field turbulence models that capture the main observations of magnetic field fluctuation in the solar wind: the so-called “two-component” model (Matthaeus et al., 1990) and the foot-point random motion model (e.g., Jokipii & Parker, 1969; Jokipii & Kota, 1989; Giacalone et al., 2006). This section gives a mathematical description of the turbulent magnetic field models and the numerical method for integrating the trajectories of energetic charged particles.

2.2.1 Turbulent Magnetic Fluctuations

In a three-dimensional Cartesian geometry (x, y, z) , the turbulent magnetic field can be expressed as

$$\begin{aligned} \mathbf{B} &= \mathbf{B}_0 + \delta\mathbf{B} \\ &= B_0\hat{z} + \delta B_x(x, y, z, t)\hat{x} + \delta B_y(x, y, z, t)\hat{y} + \delta B_z(x, y, z, t)\hat{z}. \end{aligned} \quad (2.2)$$

This expression assumes a globally uniform background magnetic field \mathbf{B}_0 and a fluctuating magnetic field component $\delta\mathbf{B}$.

The two-component model is a quasi-static model for the wave-vector spectrum of magnetic fluctuation based on observations of the solar wind turbulence (Matthaeus et al., 1990). In this model, the fluctuating magnetic field is expressed as the sum of two parts: a slab component $\delta\mathbf{B}^s = (B_x^s(z), B_y^s(z), 0)$ and a two-dimensional component $\delta\mathbf{B}^{2D} = (B_x^{2D}(x, y), B_y^{2D}(x, y), 0)$. The slab component is a one-dimensional fluctuating magnetic field with all wave vectors along the direction of the uniform magnetic field \hat{z} , and the two-dimensional component only consists of magnetic fluctuation with wave vectors along the transverse direction \hat{x} and \hat{y} . It has been observed that the magnetic field fluctuation has components with wave vectors nearly parallel or perpendicular to the magnetic field, with more wave power concentrated in the perpendicular directions (usually about 80% in the solar wind). This model captures the anisotropic characteristic of the solar wind turbulence but neglects any turbulence component that propagates obliquely to the magnetic field \mathbf{B}_0 .

Another often used model for magnetic turbulence is based on the idea that magnetic fluctuations can be generated by foot-point random motions (Jokipii & Parker, 1969; Jokipii & Kota, 1989; Giacalone et al., 2006). One can consider a Cartesian geometry with the uniform magnetic field \mathbf{B}_0 along the z direction and the source surface lying in the x - y plane at $z = 0$. Since the magnetic field lines are frozen in the surface velocity field, the magnetic field fluctuation can be produced by foot-point motions in the form of Equation 2.2. We assume that the surface foot-point motion is described by $\mathbf{v}_{fp}(x, y, t) = \nabla \times \Psi(x, y, t)$, where Ψ is an arbitrary stream function. The fluctuating component of the magnetic field anywhere is given by

$$\delta\mathbf{B}^{fp} = \frac{B_0}{U} \mathbf{v}_{fp}(x, y, t - z/U). \quad (2.3)$$

The magnetic field at $z > 0$ is assumed to have no dynamical variation but continuously dragged outward by a background fluid (the solar wind) with a convective speed U . When the magnetic field is evaluated at a certain time, the magnetic field

is fully three-dimensional with dependences on x , y , and z .

In both of these two magnetic fluctuation models the magnetic field are variable in three spatial dimensions. As demonstrated by Jokipii et al. (1993) and Jones et al. (1998), it is important to consider particle transport in a fully three-dimensional magnetic field since particles tie on their original field lines in one-dimensional or two-dimensional magnetic field due to the presence of at least one ignorable spatial coordinate. The magnetic fluctuations can be constructed by the random phase approximation (e.g., Giacalone & Jokipii, 1999) and assuming a power spectrum of magnetic field. This power spectrum can be determined from spacecraft observations. The slab component $\delta\mathbf{B}^s$, two-dimensional component $\delta\mathbf{B}^{2D}$, and fluctuating magnetic field produced by the foot-point random motion $\delta\mathbf{B}^{fp}$ can be expressed as

$$\delta\mathbf{B}^s = \sum_{n=1}^{N_m} A_n [\cos \alpha_n (\cos \phi_n \hat{x} + \sin \phi_n \hat{y}) + i \sin \alpha_n (-\sin \phi_n \hat{x} + \cos \phi_n \hat{y})] \times \exp(ik_n z + i\beta_n), \quad (2.4)$$

$$\delta\mathbf{B}^{2D} = \sum_{n=1}^{N_m} A_n i (-\sin \phi_n \hat{x} + \cos \phi_n \hat{y}) \times \exp[ik_n (\cos \phi_n x + \sin \phi_n y) + i\beta_n], \quad (2.5)$$

$$\delta\mathbf{B}^{fp} = (\hat{x} \frac{\partial}{\partial y} - \hat{y} \frac{\partial}{\partial x}) \times \left[\sum_{n=1}^{N_m} \left(-\frac{1}{k_n} \right) A_n e^{ik_n (\cos \phi_n x + \sin \phi_n y) + i\omega_n (t-z/U) + i\beta_n} \right] \quad (2.6)$$

where β_n is the phase of each wave mode, A_n is its amplitude, ω_n is its frequency, α_n is polarization angle, and ϕ_n determines spatial direction of the k -vector in the x - y plane. β_n , α_n , and ϕ_n are random numbers between 0 and 2π . The frequency is taken to be $\omega_n = 0.1Uk_n$. All the forms of fluctuating magnetic field satisfy the condition $\nabla \cdot \delta\mathbf{B} = 0$.

The amplitude of magnetic fluctuation at wave number k_n is assumed to follow a Kolomogorov-like power law:

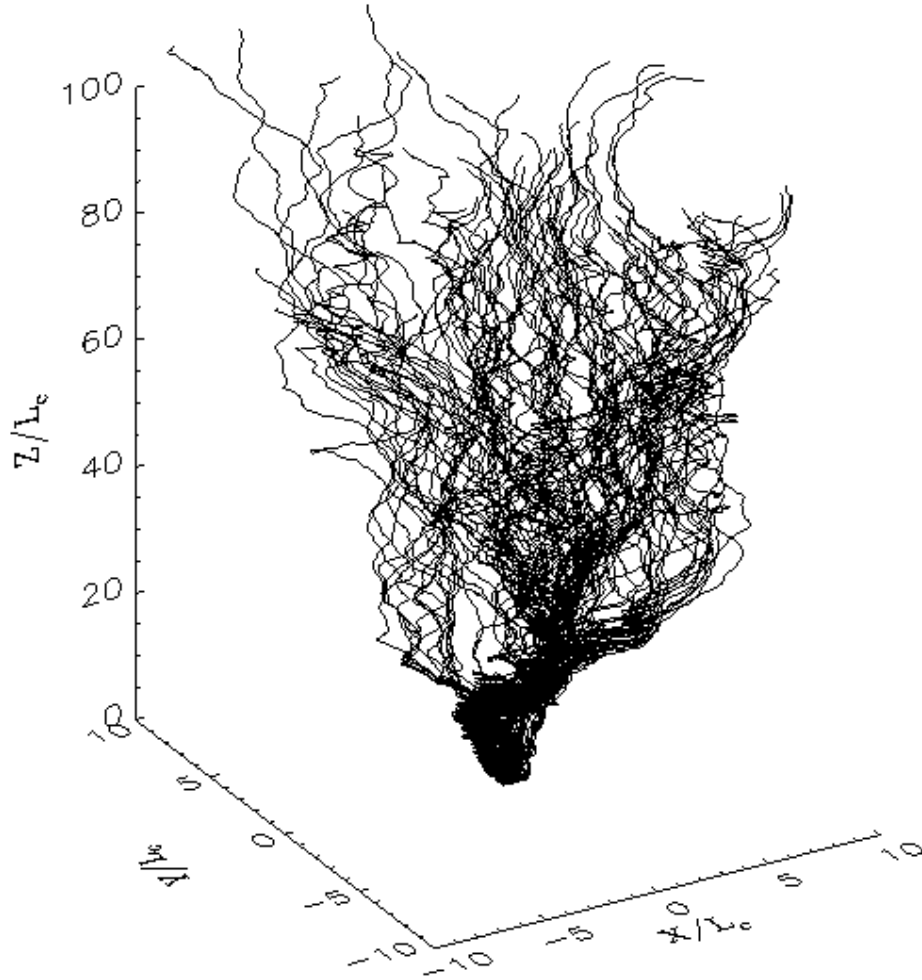


Figure 2.4: The turbulent magnetic field lines produced by the foot-point random motion model originated from $-L_c < x < L_c$ and $-L_c < y < L_c$ at $t = 0$. See the text in Section 2.2.1 for description and parameters.

$$A_n^2 = \sigma^2 \frac{\Delta V_n}{1 + (k_n L_c)^\gamma} \left[\sum_{n=1}^{N_m} \frac{\Delta V_n}{1 + (k_n L_c)^\gamma} \right]^{-1}, \quad (2.7)$$

where $\sigma^2 = \langle \delta B^2 \rangle / B_0^2$ is the total magnetic variance and ΔV is a normalization factor. In one-dimensional, two-dimensional, and three-dimensional omnidirectional spectra, $\Delta V_n = \Delta k_n$, $2\pi k_n \Delta k_n$, and, $4\pi k_n^2 \Delta k_n$ and $\gamma = 5/3$, $8/3$, and $11/3$, respectively.

It has been pointed out by Giacalone et al. (2006) that these two models are closely related and the two-component model can be reproduced using the foot-point random motion model by choosing a particular set of fluctuating velocity field. It should be noted that both of these two simplified models assume a quasi-static field that may not be appropriate for describing magnetic turbulence. Nonlinear structures of the magnetic turbulence, such as current sheets that could have important effects are not included. Nevertheless, these two models are very useful in studying the transport of energetic charged particles in magnetic turbulence and explaining the observations of SEP events. We also note that since these models assume a uniform solar wind speed in Cartesian coordinates, they do not include the effects of an expanding solar wind in spherical coordinates such as adiabatic cooling and adiabatic focusing.

In the simulations we generally use parameters similar to what is observed in the solar wind at 1 AU. The minimum and maximum wavelengths λ_{min} and λ_{max} are taken to be 10^{-4} - 10^{-5} AU and 1 AU. The mean magnetic field B_0 is typically taken to be 5 nT. The convection velocity of the solar wind U is set to be 400 km/s. The correlation length is assumed to be $L_c = 0.01$ AU. In figure 2.4 we illustrate 100 turbulent magnetic field lines origin from a surface region within $-L_c < x < L_c$ and $-L_c < y < L_c$ at $z = 0$ at time $t = 0$ produced by foot-point random motion. It is clear that the magnetic field lines are meandering in large scales. The meandering field lines originated from the compact region can have large displacements in the x and y directions.

2.2.2 Test Particle Simulations

In order to study the propagation of energetic particles in the heliospheric magnetic field, we numerically integrate the trajectories of energetic particles in magnetic fields generated from the magnetic turbulence models described previously. In each time step, the magnetic field is calculated at the position of a charged particle. The numerical technique used to integrate the trajectories of energetic particles is the so-called Bulirsch-Stoer method, which is described in detail by Press et al. (1986). It is highly accurate and conserves energy well. The algorithm uses an adjustable time-step method that is based on the evaluation of the local truncation error. The time step is increased if the local truncation error is smaller than 10^{-6} for several consecutive time steps. In the case of no electric field, the energy of a single particle in the fluctuating magnetic field is conserved to a high degree with total changes smaller than 0.01% during the simulation.

2.3 A Numerical Study on the Velocity Dispersion of Solar Energetic Particles

In this section we use both of the magnetic turbulence models described in Section 2.2.1 to study the velocity dispersions of energetic particles in the heliospheric magnetic field. The velocity dispersion is due to the fact that faster particles are detected earlier than slow particles if they are released at the same time and location. The parameters are chosen to match the magnetic field observed at 1 AU. Protons are released impulsively at $z = 0$ with random pitch angles $\mu = v_z/v$ between 0 and 1. This injected pitch-angle distribution is different than previous studies (Sáiz et al., 2005), which assume that the initial pitch angles for all the particles are $\mu = 1$. The trajectories of the charged particles are integrated until they reach the boundaries at $z = 1.2$ AU and $z = -0.1$ AU. The area of the source region is taken to be $L_x \times L_y = 5L_c \times 5L_c$, which is chosen to be larger than the correlation length in order to obtain the statistical meaningful results. It is also possible that the source regions are small and the transport of SEPs released from those regions are only affected by the field lines connecting to the source regions. The effect is

unpredictable and requires a demanding computing resource. Here we only discuss the situation that the source regions are fairly large. The energies for the released protons are 100, 9.4671, 3.3057, 1.6649, and 1 MeV, which correspond to the values of $1/v$ (converted to hour/AU): 0.3, 0.976, 1.65, 2.33, and 3.00, respectively. The magnetic variances used in the simulations are varied from $\sigma^2 = 0.01$ to $\sigma^2 = 0.6$. The mean-free paths and parallel diffusion coefficients calculated from the quasi-linear theory (Jokipii, 1966; Giacalone & Jokipii, 1999) are listed in Table 2.1. In each case, we numerically simulate the intensity-time profiles for test particles arrived at 1 AU using the magnetic field generated from four different realizations. Each realization is delineated using a new set of random phases, polarizations, and propagation angles, etc. The onset times for different thresholds are recorded when the values of the intensity reach the thresholds 0.1, 0.01, and 0.001 of the peak values, respectively.

Figure 2.5 illustrates the intensity-time profiles of energetic particles normalized using the peak values in the case of the two-component model. In this plot the red solid line represents the profile for particles with the energy of 9.4671 MeV, the green solid line represents the profile for particles with the energy of 3.3057 MeV, and the blue solid line represents the profile for particles with the energy of 1.6649 MeV. The thresholds for 0.001, 0.01 and 0.1 of the peak value are labelled using dashed lines. Figure 2.6 displays a similar plot for the case of the foot-point random motion model. The feature of velocity dispersion can be clearly seen from these two plots. The propagation of energetic particles along the z -direction depends on their pitch-angles and the scattering they experienced, therefore the energetic particles arrive at 1 AU at different times. The intensity-time profile usually has a sharp increase when the particles start to reach 1 AU. For particles with lower energies, the increases are slower compared to the cases for higher energies, presumably because charged particles with lower energies have smaller mean-free paths. However, as we will show below, for the energy range we simulate (1 - 100 MeV), this usually does not introduce a large error in analysing the injection time for energetic particle events under the situations that we study.

Energy (MeV)	1/v (hour/AU)	$\sigma^2 = \delta B^2/B_0^2$	λ_{\parallel} (AU)	κ_{\parallel} (10^{20} cm ² /s)
100	0.3	0.6	0.046	31.7
100	0.3	0.3	0.092	63.4
100	0.3	0.1	0.276	190.2
100	0.3	0.03	0.92	634
100	0.3	0.01	2.76	1902
9.4671	0.976	0.6	0.03	6.54
9.4671	0.976	0.3	0.06	13.08
9.4671	0.976	0.1	0.18	39.24
9.4671	0.976	0.03	0.6	130.8
9.4671	0.976	0.01	1.8	392.4
3.3057	1.65	0.6	0.026	3.24
3.3057	1.65	0.3	0.052	6.48
3.3057	1.65	0.1	0.156	19.44
3.3057	1.65	0.03	0.52	64.8
3.3057	1.65	0.01	1.56	194.4
1.6649	2.33	0.6	0.023	2.05
1.6649	2.33	0.3	0.046	4.1
1.6649	2.33	0.1	0.138	12.3
1.6649	2.33	0.03	0.46	41
1.6649	2.33	0.01	1.38	123
1	3.00	0.6	0.021	1.46
1	3.00	0.3	0.042	2.92
1	3.00	0.1	0.126	9.76
1	3.00	0.03	0.42	29.2
1	3.00	0.01	1.26	97.6

Table 2.1: The parallel mean-free paths and diffusion coefficients calculated from quasi-linear theory (Giocalone & Jokipii, 1999) for particle energies and magnetic variances used in this study.

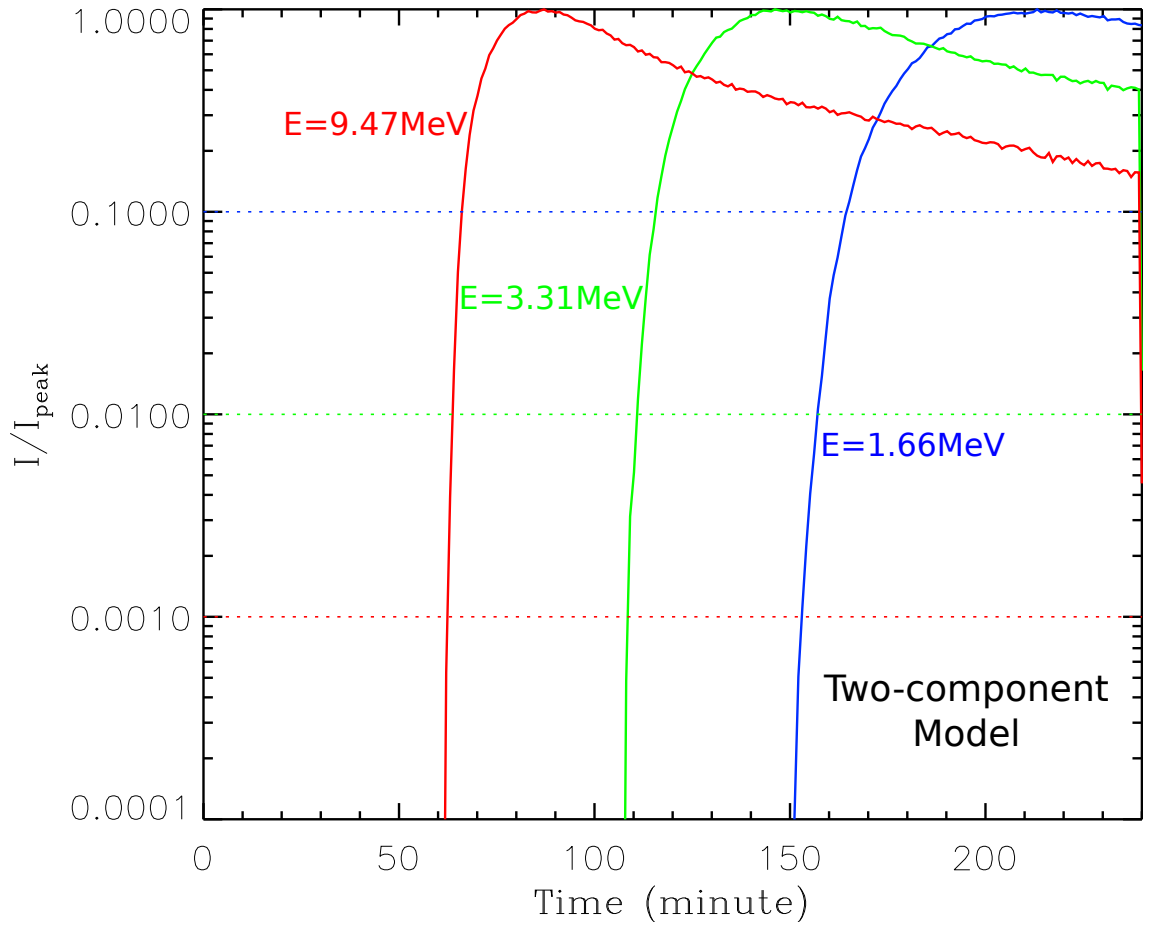


Figure 2.5: The intensity-time profiles of energetic particles collected at 1 AU normalized by their peak values at energies of 9.4671 MeV (the red solid line), 3.3057 MeV (the green solid line) and 1.6649 MeV (the blue solid line). The magnetic field turbulence is generated from the two-component model and the total variance is $\sigma^2 = 0.3$.

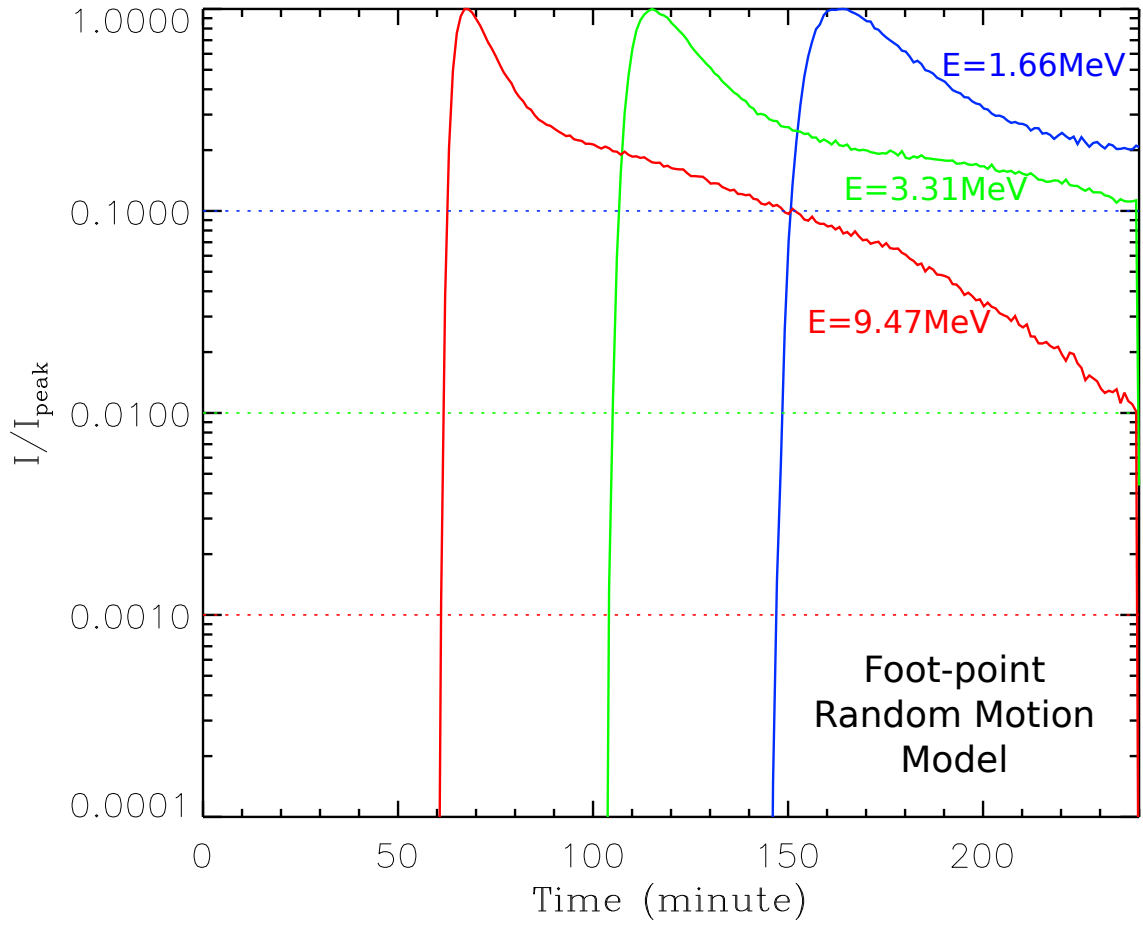


Figure 2.6: The intensity-time profiles of energetic particles collected at 1 AU normalized by their peak values at energies of 9.4671 MeV (the red solid line), 3.3057 MeV (the green solid line) and 1.6649 MeV (the blue solid line). The magnetic field turbulence is generated from the foot-point random motion and the total variance is $\sigma^2 = 0.3$.

Figure 2.7 displays the intensity-time profiles of energetic particles at 9.4671 MeV normalized using their peak values in the case of the two-component model. In this plot the magnetic variances are $\sigma^2 = 0.6$ (the blue solid line), $\sigma^2 = 0.3$ (the green solid line), and $\sigma^2 = 0.1$ (the red solid line). Figure 2.8 displays a similar plot in the case of the foot-point random motion model. It can be seen that in the case of larger magnetic variances, the arriving times for the onsets of energetic particles at 1 AU are delayed. The delays may be due to two effects: 1. The first-arriving particles experience more pitch-angle scattering during the propagation and 2. the lengths of turbulent magnetic field lines are larger in the cases of larger magnetic variances. Since we study the propagation of particles in a Cartesian geometry, the larger magnetic variances only result in longer lengths of magnetic field lines of force. This is different than the field lines of force in a spherical geometry, where the Parker's spiral field lines can be straightened and therefore shortened by the effect of large-scale magnetic turbulence (Pei et al., 2006). The decays of the intensities of charged particles after the peaks are also different. In the case of larger magnetic variances, the decay is slower because of the enhanced scattering during the propagation.

After obtained the onsets for the intensity-time profiles of energetic particles at all selected energies, we linearly fit the onset time t and $1/v$ based on Equation 2.1 and get the values of fitted path length L and release time $t_{release}$. This is similar to the method used to analyse the onsets of SEP events. Since we release particles at $t = 0$, the fitted release times actually represent the errors of the onset analyses. Two examples of these analyses are given in Figure 2.9 and Figure 2.10. In Figure 2.9 we present the results of the onset analyses for the two-component model, with different magnetic variances varying from $\sigma^2 = 0.01$ to $\sigma^2 = 0.6$ and the thresholds for intensity onsets are taken to be 0.001 of the peak values. Figure 2.10 shows a similar plot for the onset analyses for the cases that the magnetic variance is $\sigma^2 = 0.6$ and the threshold for intensity onset is varied from 0.001 of the peak value to 0.1 of the peak value. One can see that the onset analyses usually have a good linear relation. For a larger magnetic variance and/or a larger threshold value, the onset analyses give relatively large path lengths and more significant

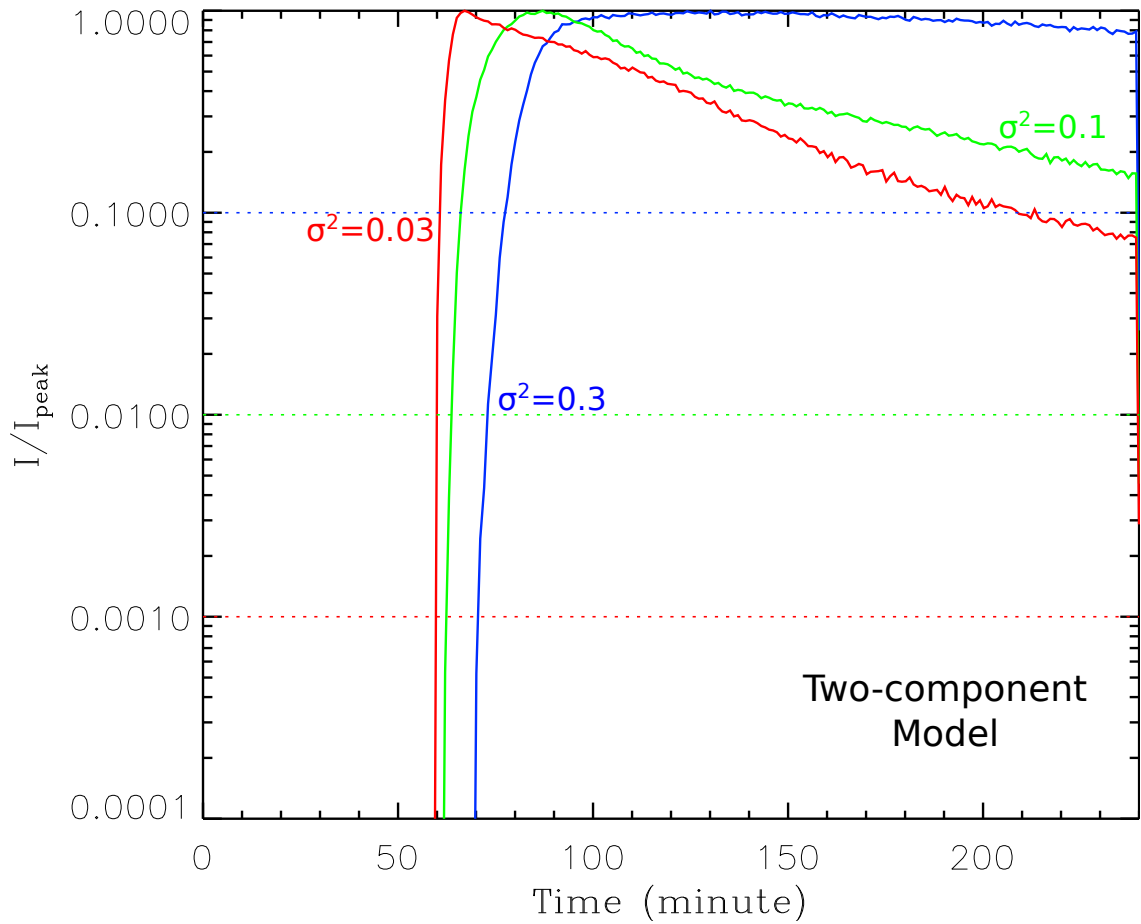


Figure 2.7: The intensity-time profiles of energetic particles collected at 1 AU normalized by their peak values at the energy of 9.4671 MeV. The magnetic field turbulence is generated from the two-component model and the total variance is $\sigma^2 = 0.3$ (the blue solid line), $\sigma^2 = 0.1$ (the green solid line), and $\sigma^2 = 0.03$ (the red solid line). It is shown that the effect of larger magnetic variance results in delayed onsets in the SEP events.

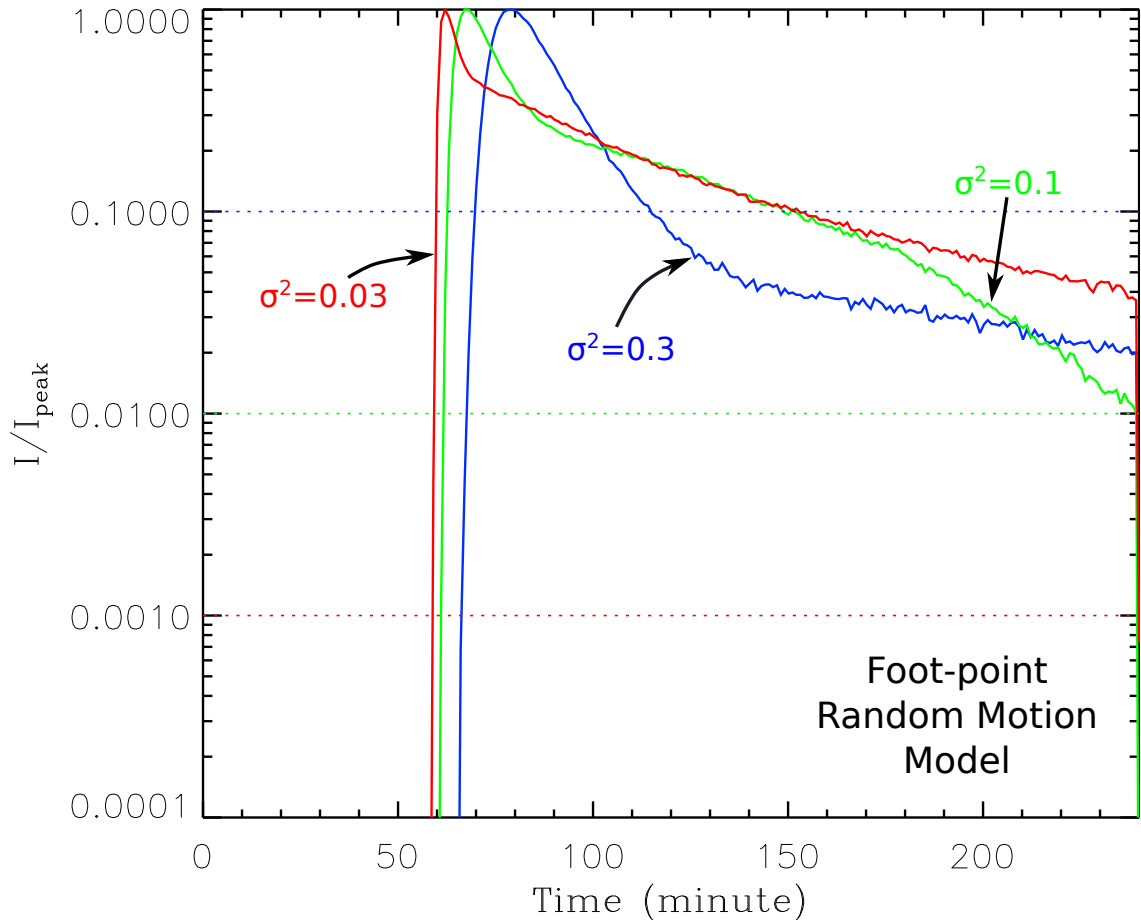


Figure 2.8: The intensity-time profiles of energetic particles collected at 1 AU normalized by their peak values at the energy of 9.4671 MeV. The magnetic field turbulence is generated from the foot-point random motion model and the total variances are $\sigma^2 = 0.3$ (the blue solid line), $\sigma^2 = 0.1$ (the green solid line), and $\sigma^2 = 0.03$ (the red solid line). It is shown that the effect of larger magnetic variance results in delayed onsets in the SEP events.

Model	$\delta B^2/B_0^2$	Threshold/Peak	Path Length (AU)	$T_{release}$ (min)
two-component	0.01	0.001	1.010	-0.38
two-component	0.01	0.01	1.012	-0.3
two-component	0.01	0.1	1.018	-0.19
two-component	0.03	0.001	1.031	-0.80
two-component	0.03	0.01	1.042	-0.69
two-component	0.03	0.1	1.068	-1.16
two-component	0.1	0.001	1.12	-2.33
two-component	0.1	0.01	1.15	-2.73
two-component	0.1	0.1	1.21	-3.63
two-component	0.3	0.001	1.29	-4.23
two-component	0.3	0.01	1.33	-4.36
two-component	0.3	0.1	1.42	-4.52
two-component	0.6	0.001	1.50	5.67
two-component	0.6	0.01	1.65	8.89
two-component	0.6	0.1	2.21	-24.64
foot-point	0.01	0.001	1.008	-0.22
foot-point	0.01	0.01	1.009	-0.08
foot-point	0.01	0.1	1.011	-0.07
foot-point	0.03	0.001	1.018	-0.42
foot-point	0.03	0.01	1.022	-0.35
foot-point	0.03	0.1	1.028	-0.35
foot-point	0.1	0.001	1.06	-0.98
foot-point	0.1	0.01	1.068	-0.91
foot-point	0.1	0.1	1.08	-0.91
foot-point	0.3	0.001	1.16	-1.45
foot-point	0.3	0.01	1.18	-1.29
foot-point	0.3	0.1	1.21	1.29
foot-point	0.6	0.001	1.26	-1.29
foot-point	0.6	0.01	1.296	-1.48
foot-point	0.6	0.1	1.34	-1.09

Table 2.2: Results of onset time analyses.

errors in the release time $t_{release}$. It has been found that for the case of the foot-point random motion model, the estimated errors for onset analyses are smaller than those of the two-component model. The reason for this result is probably because the parallel diffusion coefficient of particle motion in foot-point random motion model is considerably larger than that in the two-component model. This is illustrated in Figure 2.17 and will be further discussed in Section 2.4. The results of the onset analyses for all cases are listed in Table 2.2. From the table it is shown that the errors for the released times $t_{release}$ are usually within several minutes unless the variance is large $\sigma^2 = 0.6$ and threshold = 0.1. This indicates that although the pitch-angle scattering could play a role, the onset analyses usually have a small error and therefore useful in inferring the release time for energetic particles. However, this method is found to have a relative large error in estimating the path length L for SEP events. The effect of magnetic turbulence on the apparent path lengths is illustrated in Figure 2.9. When a larger value of the magnetic variance is chosen, the slope of the “ $1/v - t$ ” line is steepened so the apparent path lengths get larger. This agrees with SEP observations, which usually get a path length that is deviated from the typical path length of the Parker spiral magnetic field (Krucker & Lin, 2000; Tylka et al., 2003; Mewaldt et al., 2003; Kahler & Ragot, 2006; Chollet, 2008). It should be noted that for a realistic heliospheric magnetic field considering the solar rotation, the lengths of the magnetic field lines can occasionally be shorter than that of the nominal Parker spiral because some magnetic field lines are straighten radially by the effect of the random magnetic field (Pei et al., 2006). It is therefore possible that the onset analyses give a path length L smaller than the lengths of the Parker spiral, as they are seen in some observations (Hilchenbach et al., 2003; Chollet et al., 2007). Although we use a different numerical model to test the validity of the velocity dispersion analysis, the results are qualitatively consistent with previous studies (Lintunen & Vainio, 2004; Sáiz et al., 2005).

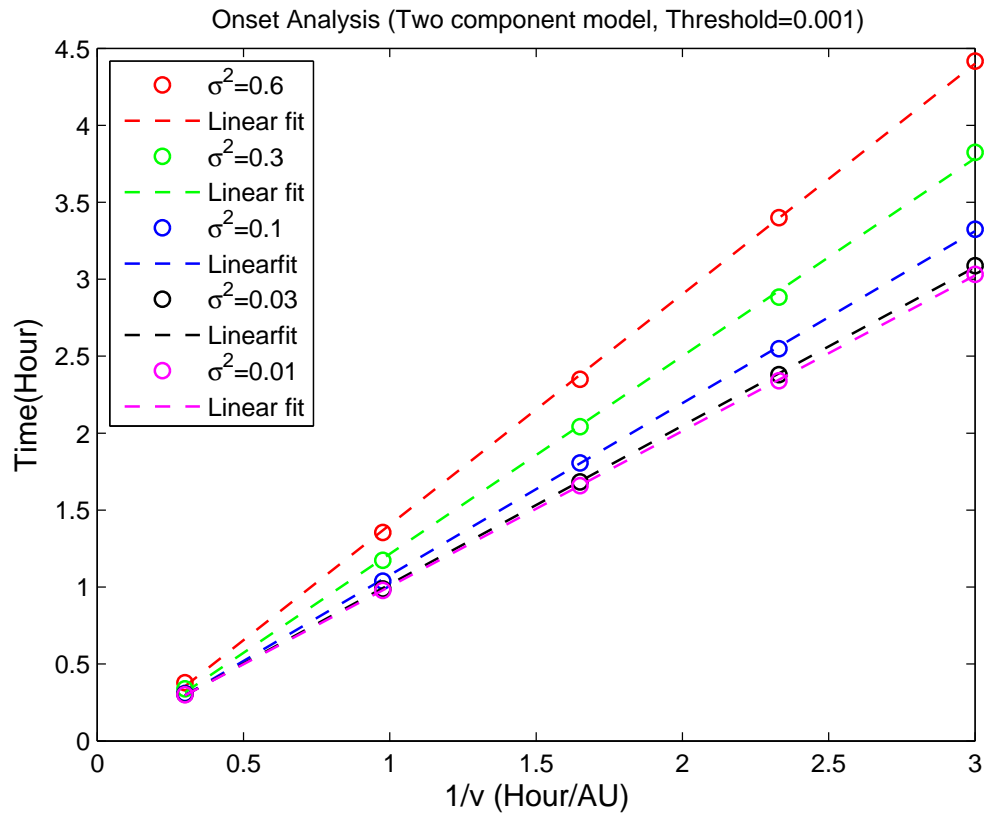


Figure 2.9: Onset analyses for the two-component model and the threshold is 0.001. The different markers represent different magnetic variances σ^2 . It is shown that the effect of larger magnetic variances change the slope (increases the path length L) of the linear fitting in the onset analyses.

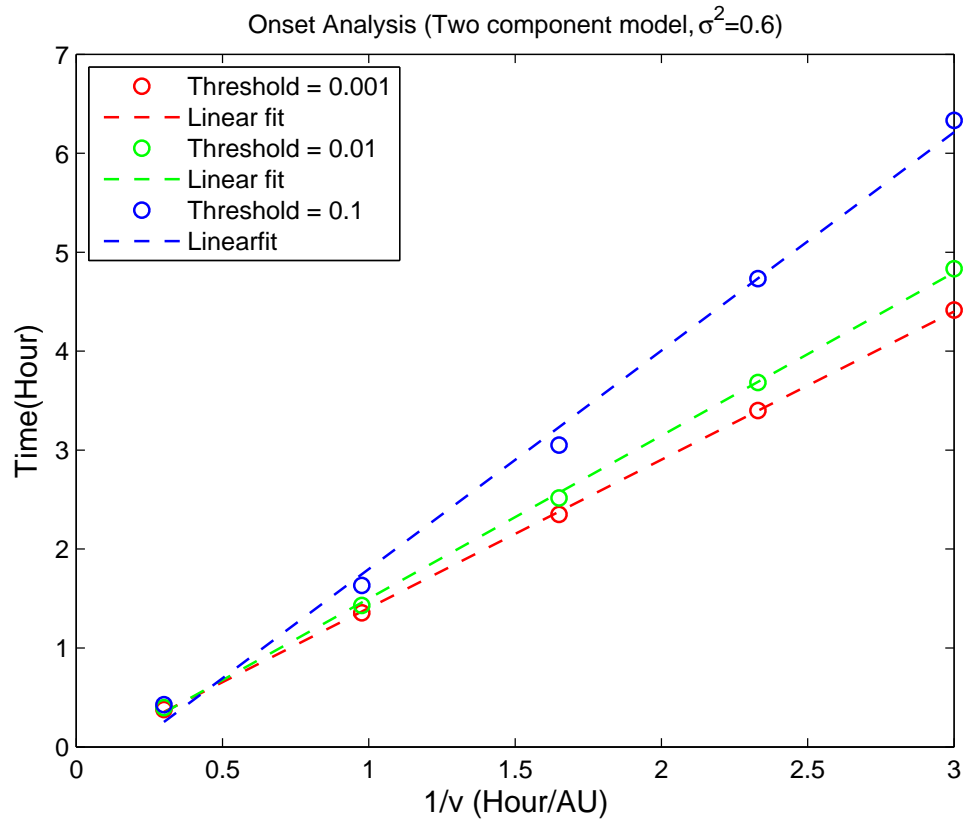


Figure 2.10: Onset analyses for the two-component model and the magnetic variance is $\sigma^2 = 0.6$. The different markers represent different threshold. Their corresponding linear fit are labelled using dashed lines. This result shows that effect of the threshold on onset analyses.

2.4 A Numerical Study of Dropouts in Impulsive SEP Events

In this section we use turbulent magnetic fields generated from the foot-point random motion model and the two-component model to study the SEP “dropouts” observed by spacecraft such as ACE and Wind (Mazur et al., 2000; Chollet & Giacalone, 2008). In our test-particle simulations the charged particles are released impulsively at $z = 0$ and their trajectories are numerically integrated until they reach the boundaries at $z = 1.6$ AU and $z = -0.1$ AU. The spacecraft observations at 1 AU are simulated by collecting particles in windows of a size $L_x \times L_y = L_c \times L_c$ when the particles pass the windows at $z = 1$ AU. The record for each window is plotted as a simulated SEP event observed by spacecraft. The source regions are taken to be a circle at the $z = 0$ plane with a radius of *case 1*: much smaller than the correlation scale ($R_{source} = 0.2L_c$) and *case 2*: much larger than the correlation scale ($R_{source} = 5L_c$). The energy for the released particles ranges from 20 keV to 10 MeV. The velocity distribution of released particles is assumed to follow a power law $f = f_0 v^{-4}$ with random pitch angles between 0 and 1. The magnetic variance used in the simulations is $\sigma^2 = 0.3$. In Figure 2.11 we show a simulated SEP event using the foot-point random motion model for the case of large source region. The upper panel shows the energy-time plot and the lower panel displays the plot of inverse velocity $1/v$ versus the time after the initial release. One can see that in this case the simulated SEP event does not show any dropout. In the small source region case, the dropout can be frequently seen. An example is given in Figure 2.12, which illustrates a simulated SEP event energy-time plot (upper panel) and inverse velocity $1/v$ versus time plot (lower panel). It is shown that two SEP dropouts can be clearly seen at about $t = 13 - 15$ hour and $t = 17.5 - 20.5$ hour, respectively. The time intervals of these dropouts are typically several hours, which is similar to that observed in space (Mazur et al., 2000).

The velocity dispersion of particles seen by observers can be varied as the particles travel along different paths and experience different scattering. This can be illustrated by Figure 2.13, which shows an impulsive SEP event plotted as $1/v$ ver-

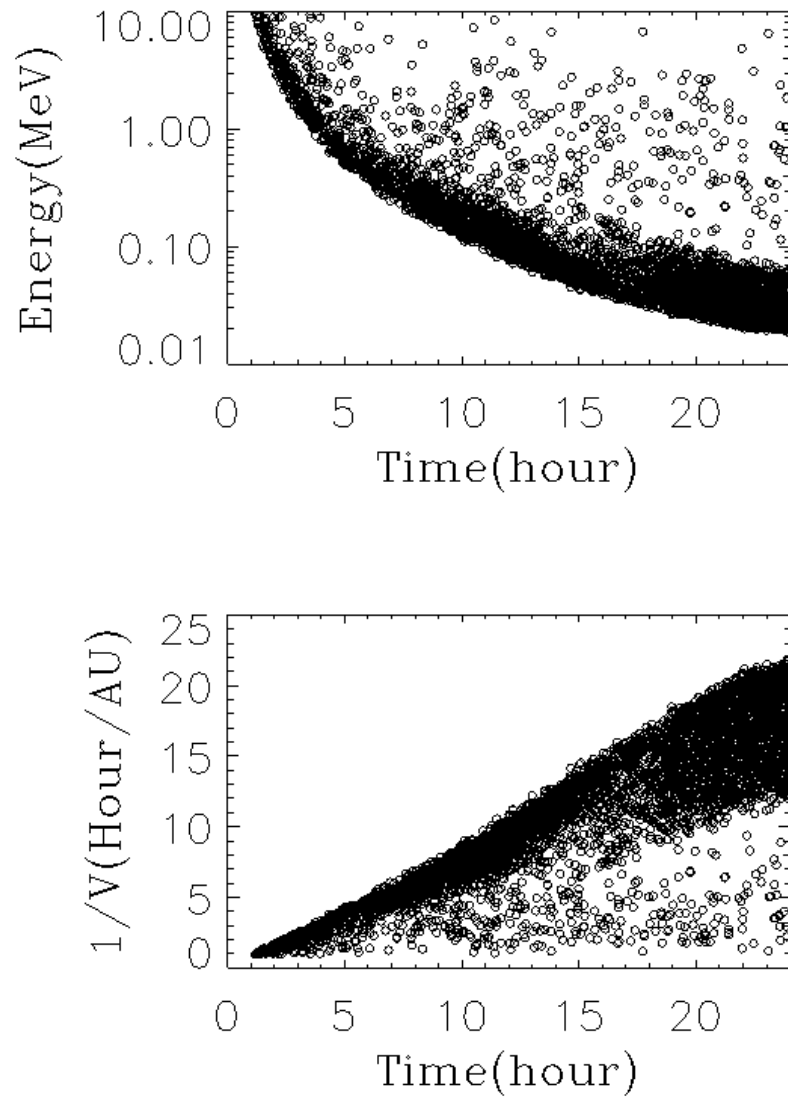


Figure 2.11: An example of SEP event simulated using the foot-point random motion model for the case of the large source region. *Upper panel*: energy-time plot. *Lower panel*: the inverse velocity $1/v$ versus the time after the release. The simulated event does not show SEP “dropouts”.

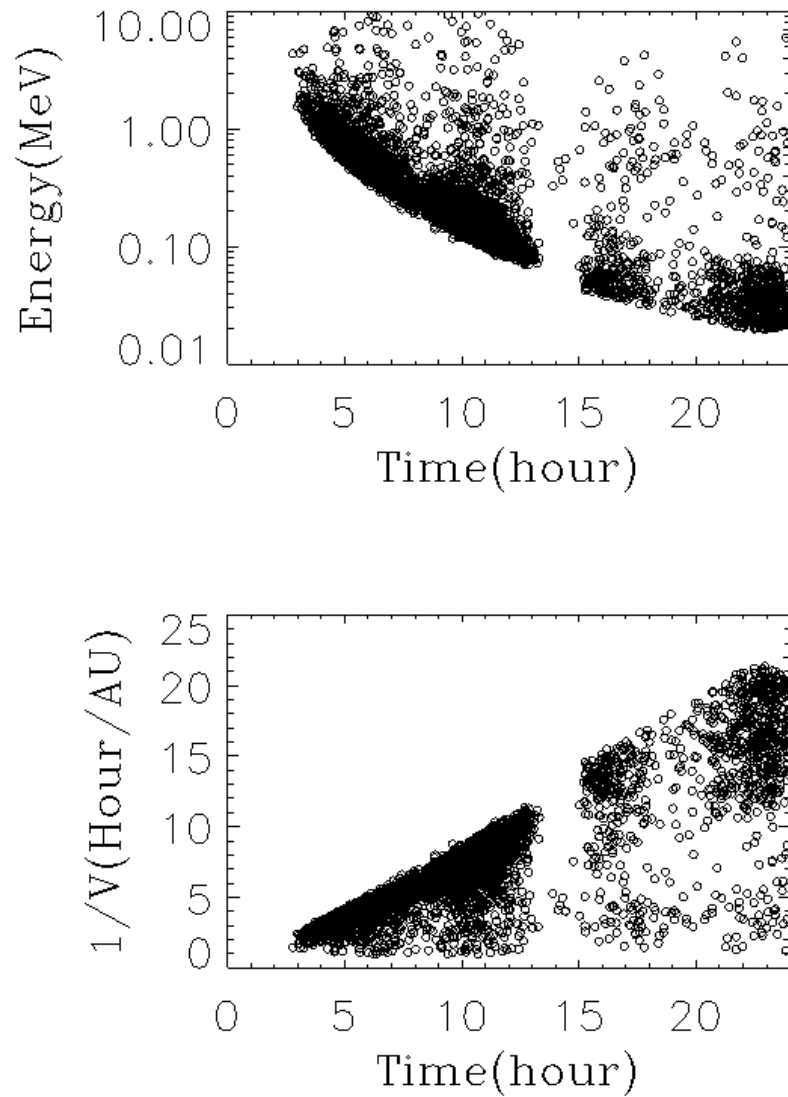


Figure 2.12: An example of SEP dropouts simulated using the foot-point random motion model for the case of the small source region. *Upper panel:* energy-time plot. *Lower panel:* the inverse velocity $1/v$ versus the time after the release. This example clearly shows dropouts.

sus time. The observation was made by observed by ACE/ULEIS detector in 1999. It displays at least two distinct arrival times at 1 AU, which indicates that particles follow at least two distinct field-line lengths. In our simulations, we also find that in some cases the apparent path lengths can be very different. Two examples are presented in Figure 2.14. In these two plots we use blue lines as a reference, which represent the particle travel along a field line with length 1.04 AU with pitch angle $\mu = v_{\parallel}/v = 1$. It can be seen from Figure 2.14 (upper panel) that the edges of the velocity dispersion $t = 15$ hour and $t = 20$ hour indicate particles arriving earlier than that along the blue line. In Figure 2.14 (lower panel) the earliest arrival time for particles at about $t = 15$ hour and $t = 20$ are almost the same as indicated by the blue line. In addition, the slopes of the edges of the velocity dispersions are different.

We have also attempted to use the two-component model to study the SEP dropouts. However, we did *not* find any clear dropout in our simulations. To further resolve this issue, we have prepared two scatter plots that show the positions for energetic particles projected on the $x - z$ plane 12 hours after the initial release. The results are shown in Figure 2.15 for the foot-point random motion model and in Figure 2.16 for the two-component model. It can be clearly seen in Figure 2.15 that the particles follows the braiding magnetic field lines, and they are therefore separated as the field lines doing random walks. However, this feature is not seen in Figure 2.16 for the two-component model. A possible reason is that the two-component model contain a slab component that can more efficiently scatter the energetic particles in pitch-angle. To demonstrate this, we measure the diffusion coefficient by implementing the the technique used by Giacalone & Jokipii (1999). We use the definition of diffusion coefficients $\kappa_{\zeta\zeta} = \langle \zeta^2 \rangle / 2t$, where ζ is the spatial displacement in a given time t . We calculate the perpendicular and parallel diffusion coefficients for 1-MeV protons in the two turbulence models for the same parameters in the simulation. The results are shown in Figure 2.17. For the two-component model, we have $\kappa_{\parallel} = 1.3 \times 10^{21}$ cm²/s and $\kappa_{\perp} = 1.1 \times 10^{19}$ cm²/s. For the foot-point random motion model, we have $\kappa_{\parallel} = 1.5 \times 10^{22}$ cm²/s and $\kappa_{\perp} = 3.1 \times 10^{19}$ cm²/s. It

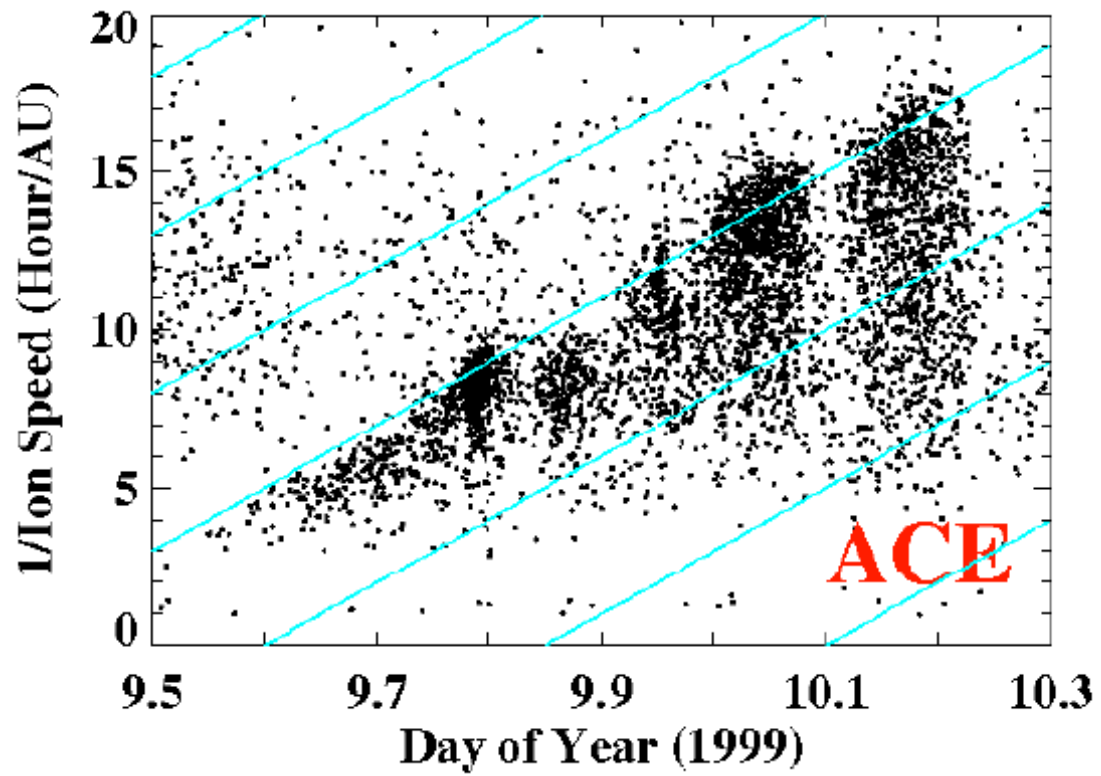


Figure 2.13: An example of the observed SEP dropouts that show different path lengths observed by ACE/ULEIS detector. Figure provided courtesy Joe Mazur, Aerospace Corporation.

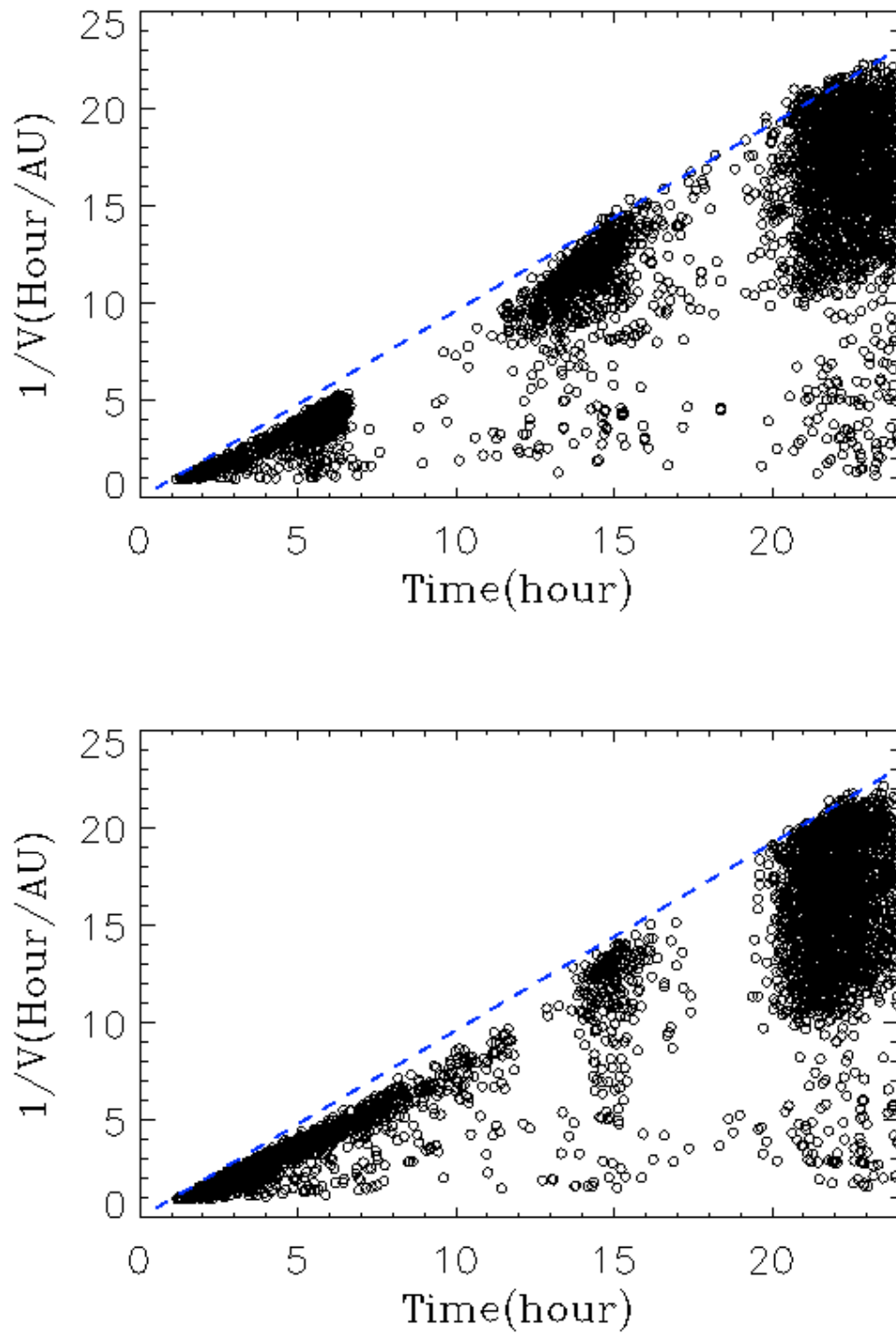


Figure 2.14: Examples of SEP dropouts produced from numerical simulations. The result shows a SEP event that observed by two different observers. The two observations have different apparent path lengths.

is shown that the parallel diffusion coefficient for the two-component model is about one order of magnitude smaller than that for the foot-point random motion model, meaning that particles experience more scattering in the two-component model. The calculation also shows a smaller ratio of $\kappa_{\perp}/\kappa_{\parallel}$ for the foot-point random motion model ($\kappa_{\perp}/\kappa_{\parallel} = 0.002$) compared with that for the two-component model ($\kappa_{\perp}/\kappa_{\parallel} = 0.0085$). The results question the popularly used “two-component” model. If large-scale field line meandering happens to be the explanation for SEP dropouts, pitch-angle scattering due to small-scale scattering should be small so energetic particles can be mostly confined to their field lines of force. When the pitch-angle scattering is large, particles efficiently scatter off their original field lines and observers cannot see the intermittent intensity dropouts. The observational evidence of small scattering has also been shown by Chollet & Giacalone (2011). They inferred the intensity-fall-off lengths at the edges of the dropouts using ACE/ULEIS data and showed that energetic particles rarely scatter off a magnetic field line during the propagation in interplanetary turbulence.

2.5 Summary

In this chapter, we presented numerical simulations for the propagation of SEPs in the inner heliosphere. We numerically integrated the trajectories of energetic charged particles in the turbulent magnetic field generated from the commonly used magnetic turbulence models. The observations of SEP events were simulated by collecting charged particles that reach 1 AU much as a spacecraft detector would.

Since the initial release of SEPs is highly anisotropic, their propagation cannot be well described by the Parker’s transport equation. In Section 2.3 we study the velocity dispersion of SEPs in the turbulent magnetic field and estimate the error involved in the onset analysis commonly used in SEP observations. We find the velocity dispersion can be well produced by this model. For a typical turbulence variation $\delta B^2/B_0^2 \sim 0.1$ observed at 1 AU and a large source region, we find the differences between the apparent release time and the actual release time is less than

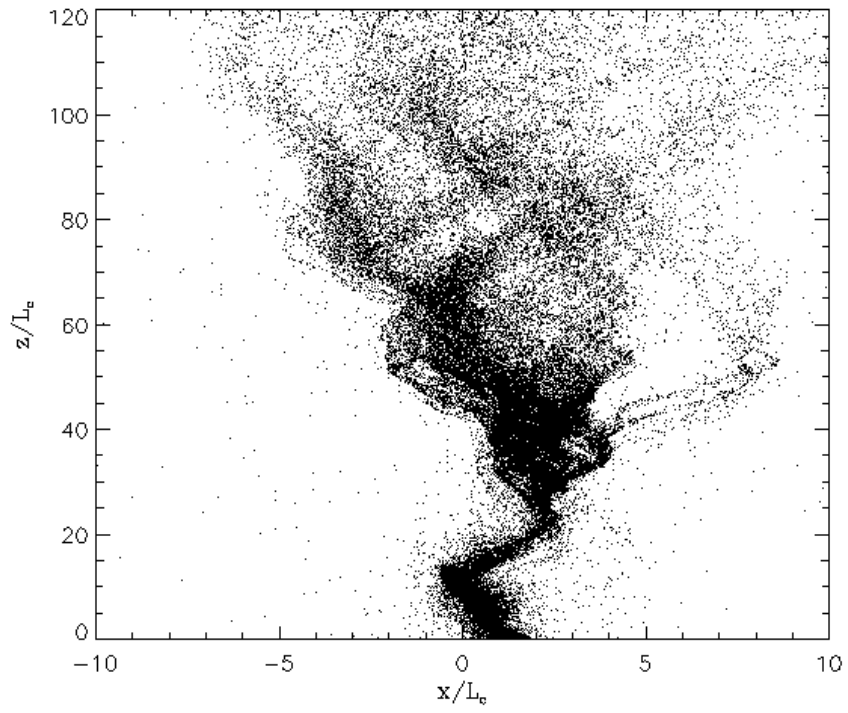


Figure 2.15: The positions of energetic charged particles projected in $x - z$ plane at $t = 12$ hour. The results are from the numerical simulations using the foot-point random motion model. It clearly shows that the particles follows the braiding magnetic field lines similar to the Cartoon in Figure 2.2.

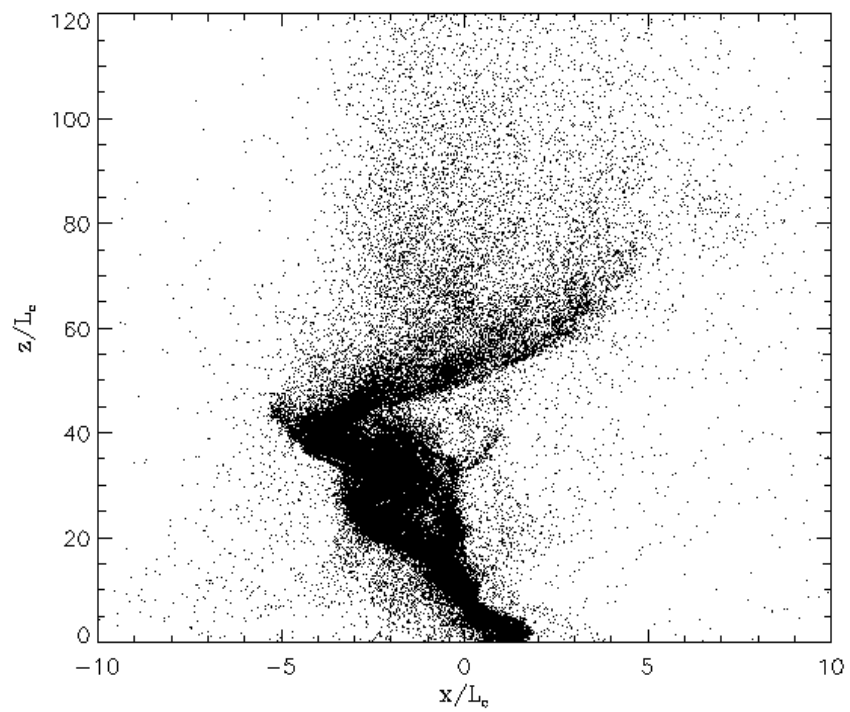


Figure 2.16: The positions of energetic charged particles projected in $x - z$ plane at $t = 12$ hour. The results are from the numerical simulations using the two-component model (slab and two-dimensional components).

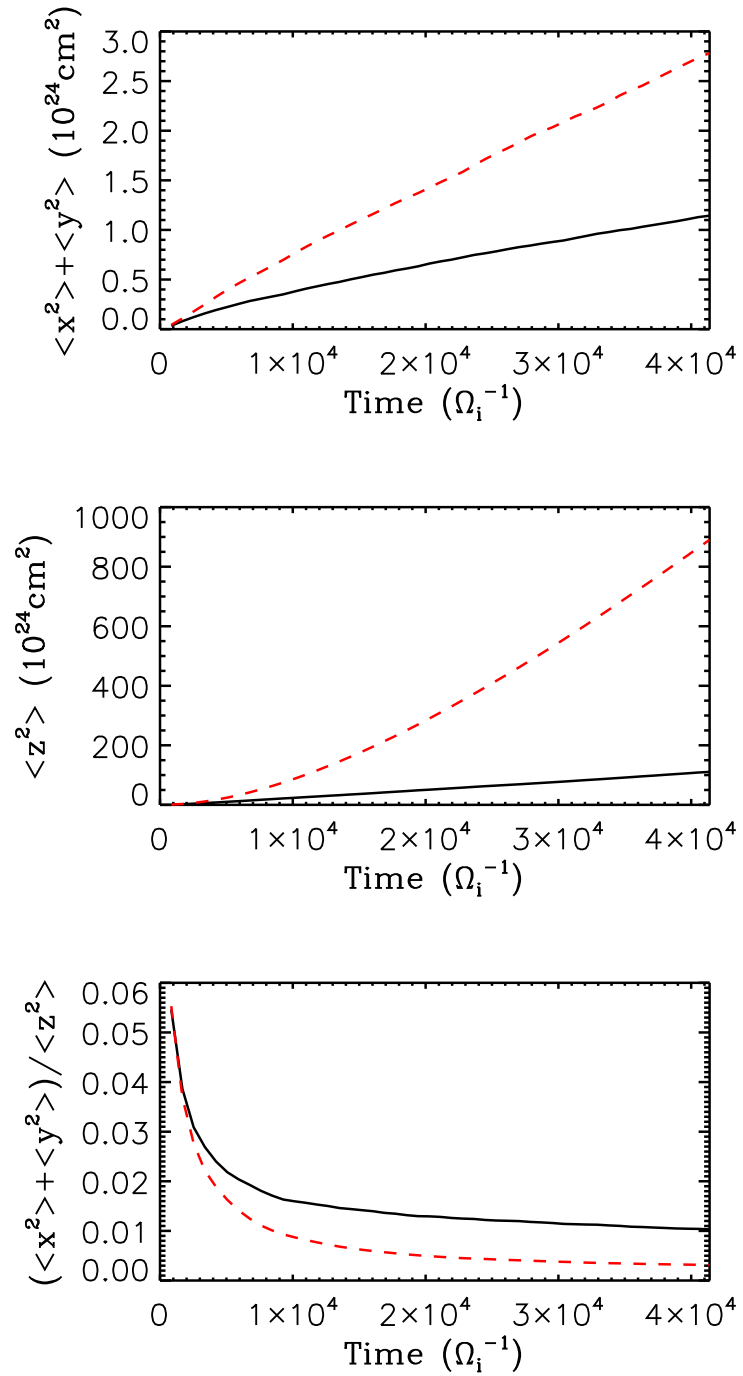


Figure 2.17: Simulated diffusion coefficient of 1 MeV particles parallel (along the z-direction) and perpendicular (along the x- and y-direction) to the mean magnetic field. Black lines represent results from the two-component model and red dashed lines represent results from foot-point random motion model.

a few minutes, but the apparent path lengths can be significantly different than the real path length along the average magnetic field line. For the foot-point random motion model, the error for the inferred release time is smaller than that of the two-component model. This is due to the parallel diffusion coefficient in the foot-point random motion model is considerably larger than that in the two-component model. It should be noted that the energetic particles we study on the onset analysis is fairly energetic (> 1 MeV) and we assume the energetic particles are released in a large source region. In order to increase the statistics, we collect all the particles that reach 1 AU rather than collect particles using a window of a certain size.

We had also reproduced SEP dropouts in the numerical simulations using the foot-point random motion model, assuming the SEP source region is smaller than the correlation scale. The widths of these dropouts are typically several hours, similar to the time scales of dropouts observed in space. The velocity dispersion of the energetic particles appears to have different path lengths, this indicates that the energetic particles travel along different field lines. We have also attempted to use the two-component model to numerically simulate the dropouts of energetic particles. However, we rarely find the evidence of SEP dropouts in our simulation. This is probably because that particle scattering is more efficient in the two-component model compared to that in the foot-point random motion model. This result questions the popular used “two-component model” in that particles in the turbulence model may scatter off field lines too frequently compared to that constrained by the observed dropouts (Mazur et al., 2000). This explanation is also supported by recent observational analysis (Chollet & Giacalone, 2011), which shows that energetic particles are mostly confined to their field lines of forces.

It has been shown that the slab turbulence model gives a mean-free path of energetic particles much smaller than what observed in SEP events (Palmer, 1982). Matthaeus et al. (1990) and Bieber et al. (1996) proposed the two-component model (80% 2D plus 20% slab) that can give a mean-free path several times larger than that given by pure slab model. In this study, we provided the evidence that the mean-free path from the two-component model may be needed to be even larger to

explain the observation of SEP dropouts (Mazur et al., 2000), which is consistent with the observed mean-free path (Palmer, 1982).

CHAPTER 3

The Effect of Turbulent Magnetic Fields on the Acceleration of Ions at
Collisionless Shocks

3.1 Particle Acceleration at Collisionless Shocks: An Overview

Collisionless shocks in space and other astrophysical environments are considered as the main accelerators for energetic charged particles. Diffusive shock acceleration (hereinafter DSA; Krymsky, 1977; Axford et al., 1977; Bell, 1978; Blandford & Ostriker, 1978) is the most accepted theory for the acceleration of charged particles. The basic conclusions of DSA can be drawn from the Parker's transport equation (Equation 1.13, Parker, 1965) by considering a fast shock in a 1-D infinite space and steady state system. In the shock frame, we assume that the plasma comes from upstream ($x < 0$) at a flow speed U_1 , gets compressed and decelerated at the shock ($x = 0$), and flows into downstream ($x > 0$) at a speed of U_2 . For a source function $Q = \delta(p - p_0)\delta(x)$, which represents the injection of low-energy charged particles with momentum p_0 at the shock, the solution of the Parker's equation is

$$\begin{aligned} f(x, p) &= \left(\frac{p}{p_0}\right)^{-\gamma} \exp\left(-\frac{U_1|x|}{\kappa_{xx,1}}\right) & x < 0, p > p_0 \\ &= \left(\frac{p}{p_0}\right)^{-\gamma}, & x > 0, p > p_0 \end{aligned} \quad (3.1)$$

where U_1 is the upstream flow speed in the shock frame and $\kappa_{xx,1}$ is the diffusion coefficient of the charged particles normal to the shock surface. The solution naturally predicts a power-law distribution function $f \propto p^{-\gamma}$ with $\gamma = 3U_1/(U_1 - U_2)$. For strong shocks with compression ratios between 2.0 and 4.0, the slope index of the power law of the distribution function is between 6.0 and 4.0, close to energetic particles observed in many different regions of space. Upstream of the shock front,

DSA predicts an exponential drop as a function of the distance from the shock, similar to some spacecraft observations (e.g., Kennel et al., 1986).

Although DSA has been very successful in explaining the acceleration of charged particles, this theory does have some difficulties. One of the greatest concerns about DSA is how a population of low-energy charged particles gets pre-accelerated at collisionless shocks. Since the Parker’s equation does not consider low-energy particles with high anisotropies, how low-energy particles get accelerated at shocks is unclear. This is often referred to as the “injection problem”. There is no current consensus on this issue. We will discuss the injection problem in more detail in Section 3.2.

Another important problem for DSA is that the observed energetic particles associated with shock waves are irregular and variable, and they are sometimes very different from what is predicted by the 1-D, steady state solution of DSA (Equation 3.1). In contrast, DSA is usually considered to be a simple and robust process. It is important to consider how DSA could explain such observations. In recent years, it has been realized that the effects of shock geometries, seed particles, and spatial and temporal variations, etc. can be important and they are considered to be possible solutions for explaining the observed energetic particles. In Section 3.4 we will discuss these observations and list the possible modifications to the 1-D, steady state solution for DSA to interpret the observations.

There are some other shock-acceleration mechanisms often discussed in the literature. For example, shock drift acceleration (SDA, e.g., Armstrong et al., 1985) and shock surfing acceleration (SSA, Lee et al., 1996; Zank et al., 1996) at quasi-perpendicular or perpendicular shocks. In SDA, charged particles drift because of the gradient of the magnetic field at the shock front. The direction of the drift motion is in the same direction as motional electric field vector $\mathbf{E} = -\mathbf{U} \times \mathbf{B}/c$, and the particles gain energy during this drift motion. In SSA, it is thought that the cross shock potential electric field could reflect ions upstream and the ions gain energy by the gyro-motion along the motional electric field.

SDA and DSA are usually considered to be distinct and their relationship requires

some clarification. It has been demonstrated by Jokipii (1982, 1987) that in a diffusive process, SDA can be unified into DSA by considering the drift term in the Parker’s transport equation. In that case, both drift and diffusion play a role and their relative contributions depend on the shock normal angles. Jokipii (1987) showed that the acceleration rate is greatly enhanced at perpendicular shock or highly oblique shocks since the perpendicular diffusion coefficient is usually much smaller than the parallel diffusion coefficient.

In Section 3.2 we discuss the injection problem of ions for DSA. In Section 3.3 we present a study on the acceleration of thermal ions at parallel shocks using 3-D hybrid simulation (kinetic ions and fluid electron). In Section 3.4 we will discuss a variety of effects that could modify the simple 1-D diffusive shock acceleration model. In Section 3.5 we present a study on particle acceleration at shocks containing large-scale magnetic variations.

3.2 The “Injection Problem” (The Acceleration of Low-energy Particles)

Since the Parker’s transport equation (Equation 1.13, Parker, 1965) assumes a quasi-isotropic distribution of energetic particles, it does not include the pre-acceleration process for low-energy particles known as the “injection problem”. It is usually thought that when the charged particles are energetic enough, they can be efficiently scattered by magnetic turbulence close to the shock and get accelerated in DSA. At present there is no consensus on this issue. However, one can work out the condition for the transport equation to be valid when the anisotropy due to diffusive streaming is small. The absolute value of the streaming anisotropy is (Giagalone & Jokipii, 1999)

$$\xi = \frac{3|S_i|}{vf_0} = \frac{3U_1}{v} \left\{ 1 + \frac{(\kappa_A/\kappa_{\parallel})^2 \sin^2 \theta_{Bn} + (1 - \kappa_{\perp}/\kappa_{\parallel})^2 \sin^2 \theta_{Bn} \cos^2 \theta_{Bn}}{[(\kappa_{\perp}/\kappa_{\parallel}) \sin^2 \theta_{Bn} + \cos^2 \theta_{Bn}]^2} \right\}^{1/2}. \quad (3.2)$$

If we define that the particles can be efficiently accelerated by diffusive shock acceleration when $\xi < 1$, this equation gives an injection velocity

$$v_{inj} > 3U_1 \left\{ 1 + \frac{(\kappa_A/\kappa_{\parallel})^2 \sin^2 \theta_{Bn} + (1 - \kappa_{\perp}/\kappa_{\parallel})^2 \sin^2 \theta_{Bn} \cos^2 \theta_{Bn}}{[(\kappa_{\perp}/\kappa_{\parallel}) \sin^2 \theta_{Bn} + \cos^2 \theta_{Bn}]^2} \right\}^{1/2}. \quad (3.3)$$

For parallel shocks or quasi-parallel shocks, this indicates that $v_{inj} > 3U_1$ and the injection is relatively easy. It is usually thought that Alfvén waves excited by the streaming of high-energy, shock accelerated protons can scatter the pitch angle of the particles. When the fluctuations efficiently interact with the particles, these particles are trapped near the shock and gain energy from the plasma compression across the shock. Ellison (1981) first advocated a model for DSA that includes the injection process, where the particles are assumed to be originated from the shock-heated ions and leak freely from downstream to upstream of the shock. The similar models have been developed and extended by a number of authors (e.g., Ellison et al., 1990; Malkov, 1998; Kang et al., 2012). This is usually referred to as the “thermal leakage” model.

However, a number of researchers (Quest, 1988; Scholer & Terasawa, 1990; Scholer, 1990; Kucharek & Scholer, 1991; Giacalone et al., 1992) have found a different scenario for the initial energization at parallel shocks based on the results of self-consistent hybrid simulations. It is found that the accelerated ions originate from the shock layer rather than via leakage from the plasma. The ions can be accelerated from the incident thermal plasma to high energies while they are making gyro-motions in the electric and magnetic fields at the shock layer. Although the average incident magnetic field is parallel to the shock normal, as the enhanced upstream magnetic fluctuations steepen and convect through the shock layer, the angle between the incident magnetic field and the shock-normal right at the shock front can be quite large. A particle can gain the first amount of energy by drifting and being reflected in this “locally oblique” shock structure (Giacalone et al., 1992). It has been clearly shown by Kucharek & Scholer (1991) that most of the accelerated particles are reflected and gain the first amount of energy at the shock layer. Lyu & Kan (1990) have presented the results of hybrid simulations and they claimed that

the leakage protons dominated the accelerated particles. The reason that they obtained a different result from other researchers may be due to the method they used to drive shocks in their simulations. In their simulations, the shocks are initially assumed to be a hyperbolic tangent function with a thickness of several ion inertial lengths c/ω_{pi} , where c and ω_{pi} are the light speed and proton plasma frequency, respectively. The magnetic fluctuations that are important to reflect ions at shock front are ignored at the beginning of the simulation. It should be noted that previous simulations are restricted to 1-D simulations and occasionally 2-D simulations. In those situations the motions of charged particles are restricted on their original field lines as demonstrated by Jokipii et al. (1993) and Jones et al. (1998). This restriction motivates us to study the acceleration of ions at parallel shocks using 3-D simulations. In Section 3.3 we will present a new study on this problem using 3-D hybrid simulations. The results show that energetic particles can move across field lines but the acceleration mechanism is similar to what is found by previous hybrid simulations (Quest, 1988; Scholer & Terasawa, 1990; Scholer, 1990; Kucharek & Scholer, 1991; Giacalone et al., 1992). Namely, the energetic particles originate in the shock layer and are not due to leakage from downstream.

For perpendicular shocks or quasi-perpendicular shocks, it is thought to be more difficult for particles to be injected into DSA. The required pre-acceleration can be achieved by shock drift acceleration (e.g., Armstrong et al., 1985) or shock surfing acceleration (Lee et al., 1996; Zank et al., 1996). Recent progress has been made to distinguish the relative importance for these two processes. It has been found that in order for shock surfing acceleration to be efficient, the thickness of the shock layer has to be very thin (electron scale), which is different from what is observed in space (Bale et al., 2003) and in numerical simulations (Leroy et al., 1982). Moreover, it has been discussed that the shock thickness has to be fairly large compared to electron gyroradii to be consistent with the observation of electron heating at shocks (Lembege et al., 2004). More detailed studies using full particle simulations and hybrid simulations have been presented by Yang et al. (2009) and Wu et al. (2009).

Giacalone & Jokipii (1999) has demonstrated that the effect of large-scale mag-

netic turbulence can efficiently lower the injection velocity v_{inj} at perpendicular shocks by increasing the transport of charged particles normal to magnetic field direction. Recent numerical simulations for the acceleration of charged particles in the existence of large-scale magnetic fluctuations show very efficient acceleration, which indicates that there is *no* injection problem (Giacalone, 2005a,b). It should be noted that there is also an injection problem for electrons, which has been considered to be more difficult than that of ions. In Chapter 4 we will discuss the acceleration of electrons. The results suggest that the acceleration of electrons prefers perpendicular shocks.

3.3 A 3-D Hybrid Simulation on Particle Acceleration at Parallel Shocks

In order to examine the acceleration of charged particles at parallel shocks, we performed 3-D hybrid simulations to study the initial acceleration process. As pointed out by a few previous works (Jokipii et al., 1993; Giacalone & Jokipii, 1994), it is important to consider the motions of charged particles in 3-D to avoid the artificial restriction on their gyro-motions.

3.3.1 Numerical Methods

We perform 3-D hybrid simulations for particle acceleration at parallel shocks. In the hybrid simulation (e.g., Winske & Quest, 1988), the ions are treated fully kinetically and thermal electrons are treated as a massless fluid. It keeps ion-scale kinetic physics but neglect electron-scale kinetic physics. Therefore the relevant spatial scales are ion gyroradius v_{thi}/Ω_{ci} and ion inertial length c/ω_{pi} , and the relevant time scale is the ion gyroperiod Ω_{ci}^{-1} , where v_{thi} is the ion thermal speed, Ω_{ci} is the ion gyrofrequency, c is the light speed in *vacuum*, and ω_{pi} is the ion plasma frequency. This feature is well suited to describe supercritical collisionless shocks, in which the dynamics of ions is important.

In the simulation, the ions are treated as kinetic particles moving in the simulation domain by solving the equations of motion for each ion j :

$$m_j \frac{d\mathbf{v}_j}{dt} = q_j \left(\mathbf{E} + \frac{\mathbf{v}_j \times \mathbf{B}}{c} \right) - \eta \mathbf{J} \quad (3.4)$$

$$\frac{d\mathbf{x}_j}{dt} = \mathbf{v}_j. \quad (3.5)$$

The first two terms in the right-hand side of Equation 3.4 represent the Lorentz force, and the third term describes the effect of resistive coupling between electrons and ions where η is the resistivity and \mathbf{J} is the total current. The electric and magnetic fields are defined on grid points, and are interpolated to the locations of particles. After pushing the particles at each time step, the new particle positions \mathbf{x}_j and velocities \mathbf{v}_j are collected at the grid points to get the quantities such as ion density n_i , ion flow velocity \mathbf{V}_i and ion current $\mathbf{J}_i = q_i n_i \mathbf{V}_i$. Since the electrons in the simulation are assumed to be a massless neutralizing fluid. We solve the momentum equation of electron fluid:

$$n_e m_e \frac{d\mathbf{V}_e}{dt} = -en_e \left(\mathbf{E} + \frac{\mathbf{V}_e \times \mathbf{B}}{c} \right) - \nabla \cdot \vec{\mathbf{P}}_e + \eta \mathbf{J} = 0, \quad (3.6)$$

where \mathbf{V}_e is the electron fluid velocity and $\vec{\mathbf{P}}_e$ is the electron pressure tensor. The electron and ion charge density are equal $en_e = q_i n_i$, where n_e is the electron number density. The pressure tensor $\vec{\mathbf{P}}_e$ in the equation is usually taken to be a scalar $\vec{\mathbf{P}}_e = p_e \vec{\mathbf{I}}$. We assume the electron fluid is adiabatic $p_e \propto n_e^{5/3}$.

The electromagnetic fields are described by Ampere's law,

$$\nabla \times \mathbf{B} = \frac{4\pi}{c} \mathbf{J} = \frac{4\pi}{c} q_i n_i (\mathbf{V}_i - \mathbf{V}_e), \quad (3.7)$$

and Faraday's law

$$\frac{\partial \mathbf{B}}{\partial t} = -c(\nabla \times \mathbf{E}). \quad (3.8)$$

At each time step, we get \mathbf{V}_e from Equation 3.7. The electric field is obtained from Equation 3.6 and the magnetic field is updated using Equation 3.8.

We have improved the parallelization of the 1-D, 2-D, and 3-D hybrid simulation models (Giacalone et al., 2000; Giacalone, 2004, 2005b). The new versions of the codes have been implemented and tested on the NASA's Pleiades supercomputer using a few thousand CPU cores. In Figure 3.1 we use a 2-D example to illustrate the method of parallelization. The 2-D simulation domain is split into several sub-domains along the x and y directions. Each sub-domain is placed on a single CPU core, CPU 1, CPU 2, ... The sub-domain also has two labels that is determined by its location in the global simulation domain. For example, the sub-domain CPU 1 is labelled by $C_x = 0$ and $C_y = 0$, and the sub-domain of CPU 6 is labelled by $C_x = 1$ and $C_y = 1$. The dimension of each sub-domain is $d_x = L_x/n_{cx}$ and $d_y = L_y/n_{cy}$, where n_{cx} and n_{cy} are numbers of CPUs along the x and y directions, respectively. The information of the kinetic particles in numerical cells \mathbf{x}_j and \mathbf{v}_j and fields on grid points like \mathbf{B} , \mathbf{E} within each sub-domain is loaded on the corresponding CPU. At each time step, the fields at boundaries are transferred to and from its adjacent sub-domains $(C_x + 1, C_y)$, $(C_x - 1, C_y)$, $(C_x, C_y + 1)$ and $(C_x, C_y - 1)$. When a particle move across a sub-domain, it will be transfer to the corresponding adjacent CPU. The number of the CPU is determined by its label C_x and C_y .

For this work, we consider a three-dimensional Cartesian grid (x, y, z) . All the physical vectors have components in three directions and also spatially depend on x, y , and z . A shock is produced by using the so-called piston method, in which a plasma flow is injected continuously from one end ($x = 0$, in our case) of the simulation box, and reflected elastically at the other end ($x = L_x$). This boundary is also assumed to be a perfectly conducting barrier. The pileup of density and magnetic field creates a shock propagating in the $-x$ direction. In the y and z direction the boundary conditions are periodic for both particles and electromagnetic fields.

The size of the simulation box for each case is listed in Table 3.1. The Mach number of the plasma flow in the simulation frame is $M_{A0} = 4.0$. The electron and ion plasma betas are $\beta_e = 1.0$ and $\beta_i = 0.5$, respectively. The grid size is $\Delta x \times \Delta y \times \Delta z = 0.5c/\omega_{pi} \times 0.5c/\omega_{pi} \times 0.5c/\omega_{pi}$, where c/ω_{pi} is the ion inertial length, and c and

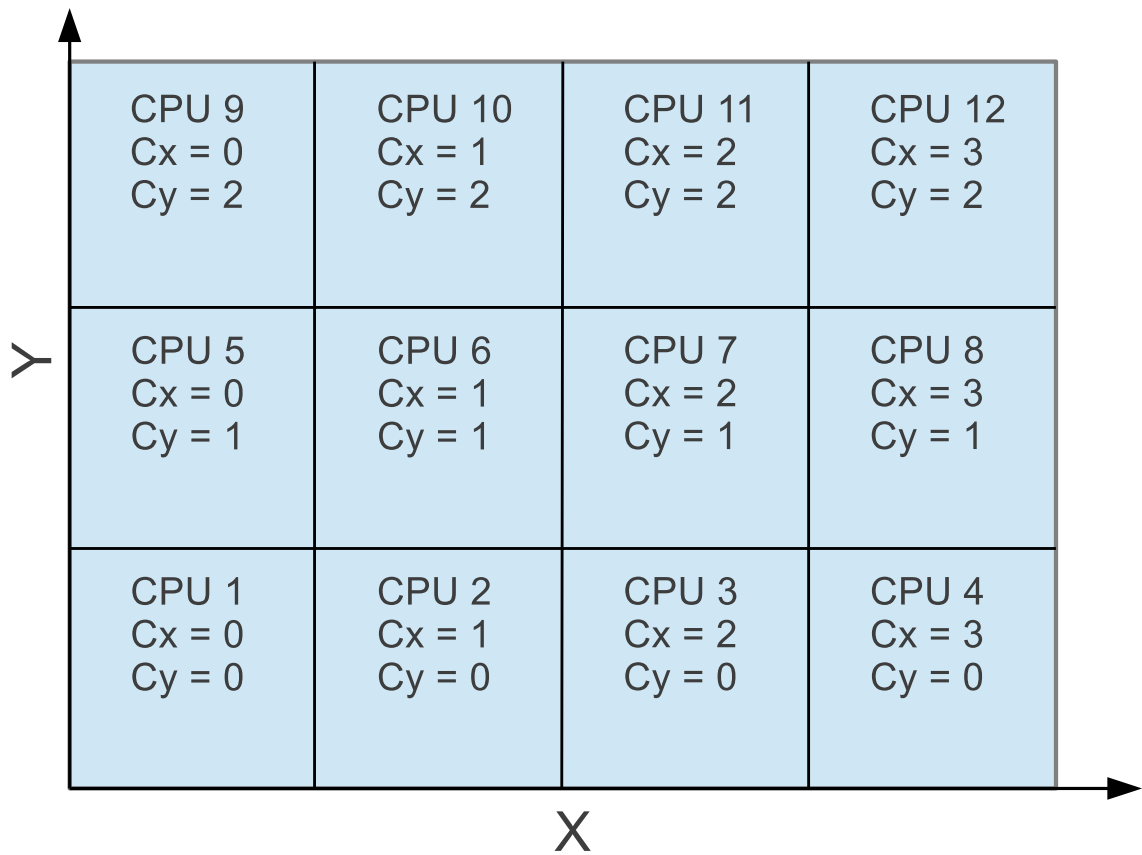


Figure 3.1: A 2-D example for the parallization of hybrid simulation.

ω_{pi} are the light speed in *vacuum* and proton plasma frequency in the simulation domain at the beginning of the simulation, respectively. The time step is taken to be $\Omega_{ci}\Delta t = 0.01$, where Ω_{ci} is the gyrofrequency. The ratio between light speed and upstream Alfvén speed is $c/v_{A0} = 6000.0$, and the anomalous resistivity is $\eta = 1 \times 10^{-6} 4\pi\omega_{pi}^{-1}$. The initial spatially uniform thermal ion distribution is represented using 25 particles per cell, which is enough to give a reasonable distribution.

Initially the average magnetic field is assumed to be $\mathbf{B}_0 = B_0\hat{x}$, i.e., the averaged shock normal angle is 0° . We examine four simulation cases with parameters listed in Table 3.1. The spatial sizes in the x direction are taken to be $300c/\omega_{pi}$ for all the cases. For the first two cases, the system is assumed to have *no* pre-existing magnetic fluctuation but the size of the simulation box in the y and z direction for Run 2 ($40c/\omega_{pi}$) are considerably larger than that for Run 1 ($10c/\omega_{pi}$). The fluctuations in the simulation box are self-consistently generated during the simulation. In Run 3 and Run 4, the sizes of the simulation boxes are the same as that in Run 2. Differently, we examine the effect of pre-existing magnetic fluctuations by superposing a random magnetic field on the mean field. The turbulent magnetic field is added at the beginning of the simulation and also injected continuously at the $x = 0$ boundary during the simulation. In Run 3, we assume the pre-existing magnetic fluctuation is one-dimensional and only depends on x , but the resulting field can depend on all three dimensions. The amplitude of the fluctuations at wave number k is determined from a Kolmogorov-like power spectrum. The largest and smallest wave lengths are taken to be $40c/\omega_{pi}$ and $2.5c/\omega_{pi}$. The total variance is taken to be $\sigma^2 = \delta B^2/B_0^2 = 0.1$. In Run 4 the magnetic power of the injected fluctuation is assumed to be isotropically distributed in three wave number vectors k_x , k_y , and k_z . The total variance is taken to be $\sigma^2 = 0.1$, the same as that in Run 3. The difference between Run 3 and Run 4 is that in Run 4 the pre-existing magnetic fluctuation is allowed to be variable in full three dimensions. As we will see below, this has an important effect on the motions of charged particles along the shock front.

Run	$L_x(c/\omega_{pi}) \times L_y(c/\omega_{pi}) \times L_z(c/\omega_{pi})$	$\sigma^2(\delta B^2/B_0^2)$	Model
1	$300 \times 10 \times 10$	0.0	-
2	$300 \times 40 \times 40$	0.0	-
3	$300 \times 40 \times 40$	0.1	1-D slab
4	$300 \times 40 \times 40$	0.1	3-D isotropic

Table 3.1: Some parameters for different cases in the 3-D hybrid simulations of parallel shocks: the size of the simulation domain in unit c/ω_{pi} , the variance of injected magnetic fluctuation σ^2 , and the model for the injected magnetic fluctuation.

3.3.2 Results of Numerical Simulations

In Figure 3.2 we present the simulation results for Run 1 at $\Omega_{ci}t = 120.0$. The figure shows the profiles of the magnetic field components in the x direction B_x/B_0 (a), y direction B_y/B_0 (b), and z direction B_z/B_0 (c) along $y = 5 c/\omega_{ci}$ and $z = 5 c/\omega_{ci}$, where B_0 is the initial upstream magnetic field. It is shown that the magnetic field fluctuations around the shock layer are mostly transverse to the initial magnetic field in the x direction. The fluctuations are circularly right-handed polarized if they propagate along upstream direction, indicating that they are excited by the reflected ions that flow upstream. This result is consistent with previous analytical theories and numerical simulations (e.g., Quest, 1988). Close to the shock layer, the magnetic fluctuations are steepened and enhanced. The fluctuations get compressed and amplified when they are passed by the shock. Different from 1-D simulations, the fluctuations in the x direction are also observed. In Figure 3.3 (a) the magnitude of magnetic field B/B_0 along $y = 5 c/\omega_{ci}$ and $z = 5 c/\omega_{ci}$ is plotted using a black line. The magnitude of magnetic field averaged over the y and z directions is overlapped on the plot using a blue line. It can be seen that although there is some small difference between the profile of the magnetic field and the averaged magnetic field, the 1-D cut is very close to the averaged value of the magnetic field, indicating that the fields are weakly dependent on the y and z directions. The same features can be seen in Figure 3.3 (b) and Figure 3.3 (c), which show the profiles and averaged values of plasma number density n/n_0 and flow velocity in the x direction V_x/V_{A0} , where n_0 is the initial upstream plasma number density and V_{A0} is the initial upstream

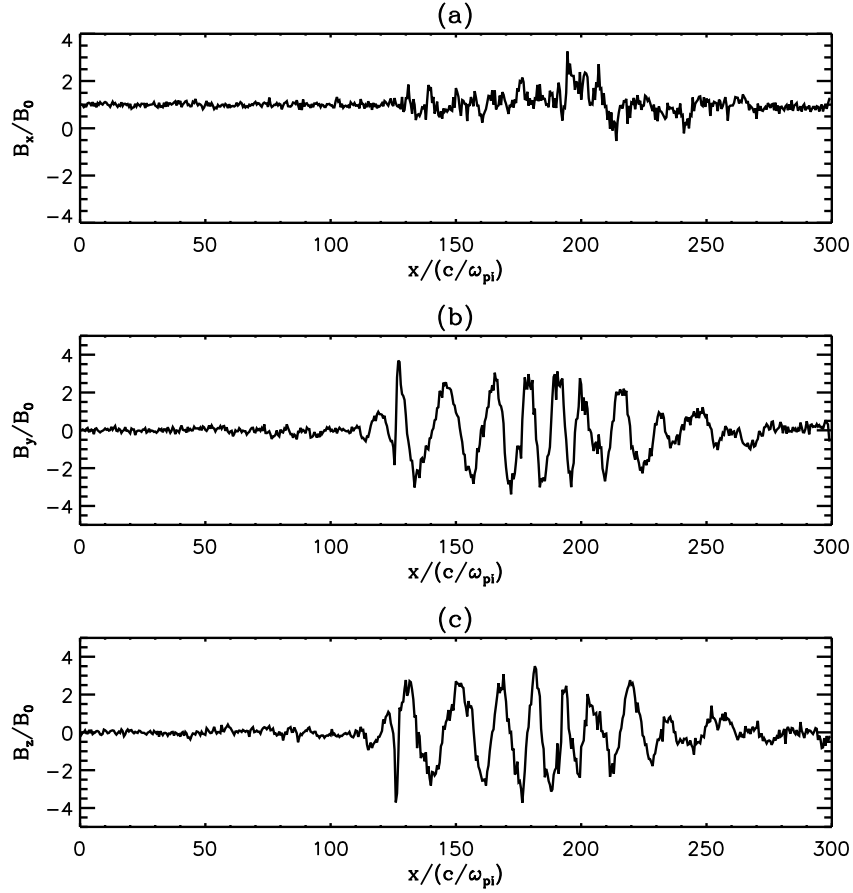


Figure 3.2: 1-D profiles of magnetic field components B_x/B_0 , B_y/B_0 , and B_z/B_0 for Run 1 (with a small simulation box in the y and z directions), where B_0 is the initial upstream magnetic field.

Alfven speed.

Figure 3.4 shows the simulation results for Run 2, which has a large simulation domain in the y and z directions than that of Run 1. The physical quantities are plotted in a way similar to Figure 3.2, except that the profile is selected at $y = 35 c/\omega_{ci}$ and $z = 35 c/\omega_{ci}$. One can see from Figure 3.4 (a) that the x -component of the magnetic field B_x/B_0 is more fluctuating compared to that for Run 1. This is probably due to the fact that a larger number of modes are allowed for the larger simulation domain and more obliquely propagating modes are excited. As shown in Figure 3.5, a very different feature for physical quantities in Run 2 compared

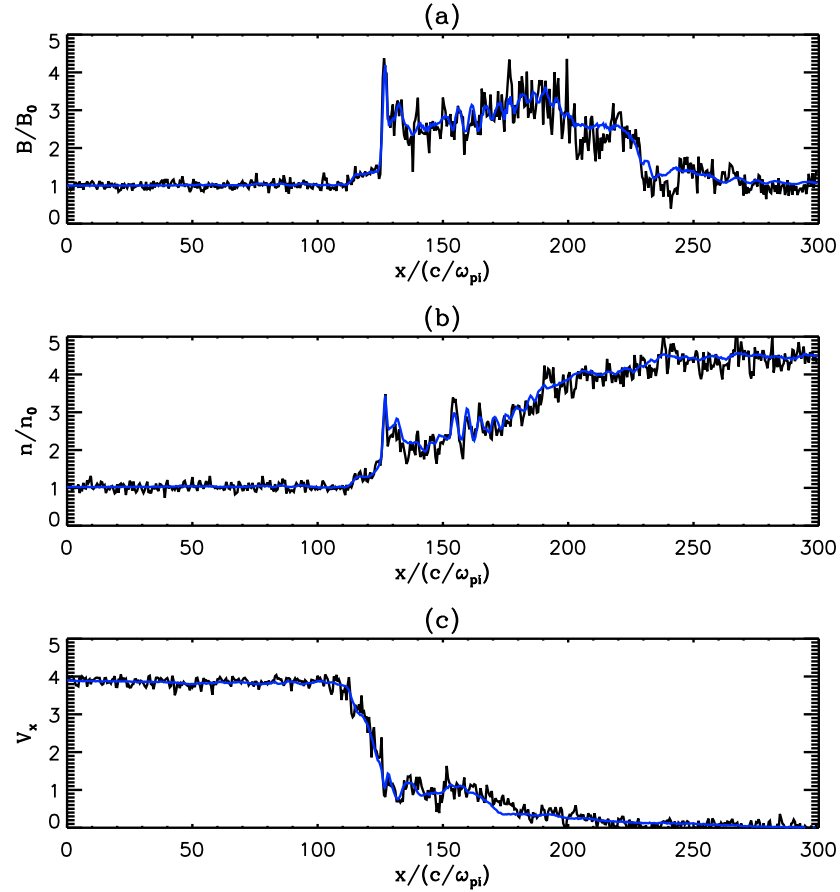


Figure 3.3: 1-D representation of magnetic-field magnitude, plasma density, and velocity for Run 1: (a) the profile of magnitude of magnetic field B/B_0 along the same line (black line) and the magnetic field magnitude averaged over the y and z directions (blue line); (b) the profile of plasma number density n/n_0 along the same line (black line) and the number density averaged over the y and z directions (blue line), where n_0 is the initial upstream plasma number density; (c) the profile of the x -component of the plasma flow speed V_x/V_{A0} along the same line (black line) and the plasma flow speed in the x direction averaged over the y and z directions (blue line), where V_{A0} is the initial upstream Alfvén speed.

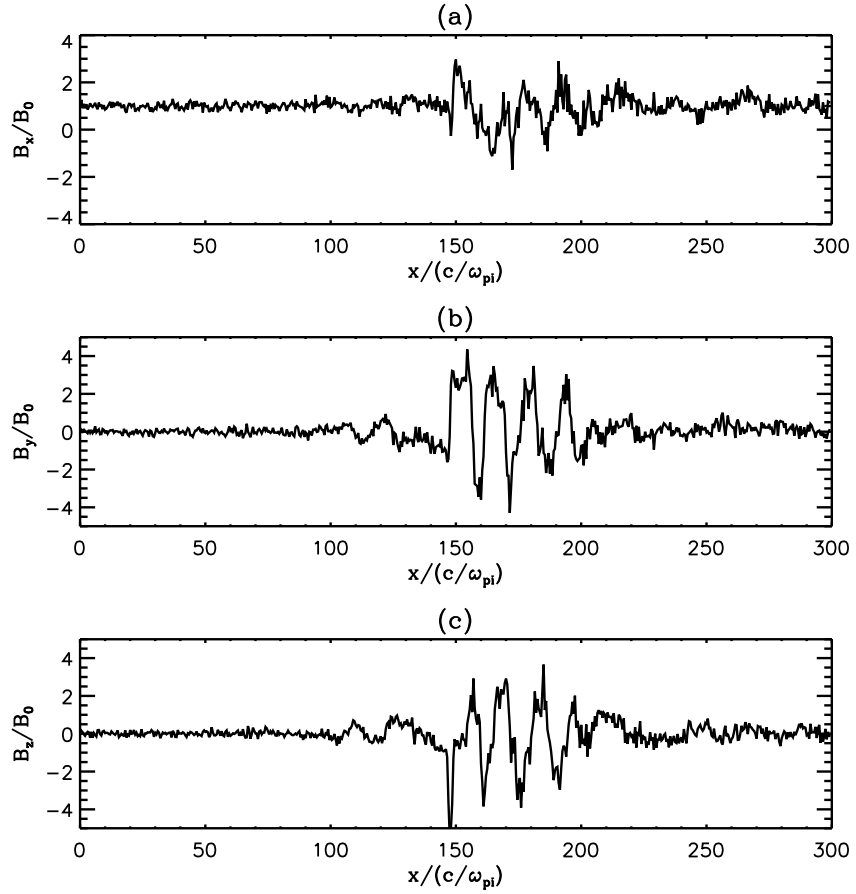


Figure 3.4: 1-D profiles of magnetic field components B_x/B_0 , B_y/B_0 , and B_z/B_0 for Run 2 (with a large simulation box in the y and z directions), where B_0 is the initial upstream magnetic field.

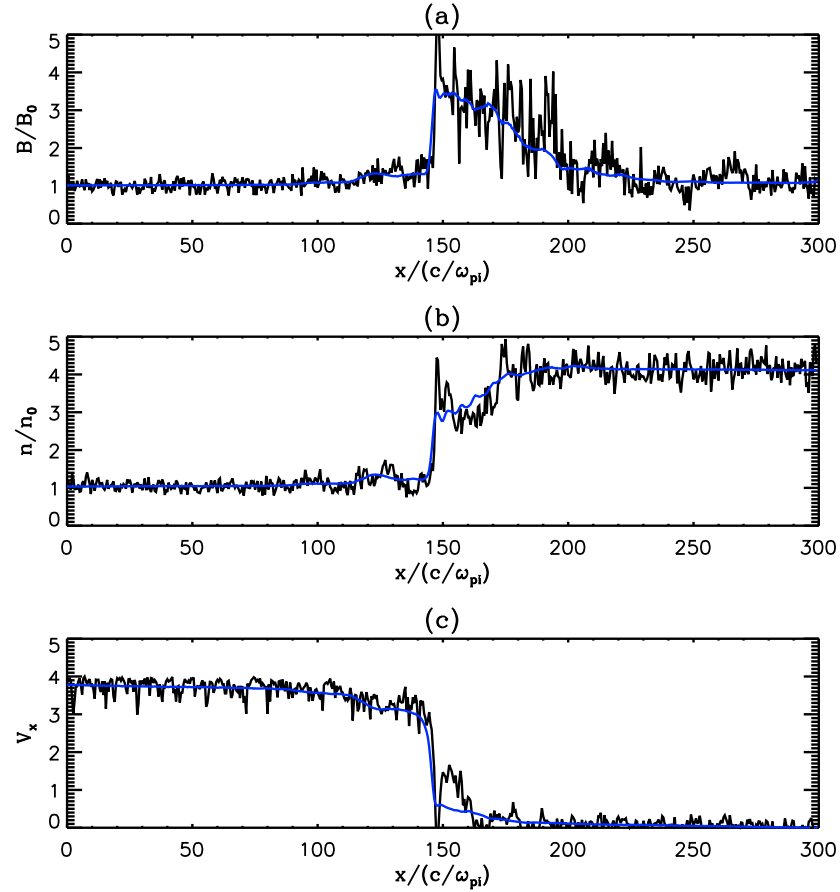


Figure 3.5: 1-D representation of magnetic-field magnitude, plasma density, and velocity for Run 2: (a) the profile of magnitude of magnetic field B/B_0 along $y = 35 c/\omega_{ci}$ and $z = 35 c/\omega_{ci}$ (black line) and the magnetic field magnitude averaged over the y and z directions (blue line); (b) the profile of plasma number density n/n_0 along the same line (black line) and the number density averaged over the y and z directions (blue line), where n_0 is the initial upstream plasma number density; (c) the profile of the x -component of the plasma flow speed V_x/V_{A0} along the same line (black line) and the plasma flow speed in the x direction averaged over the y and z directions (blue line), where V_{A0} is the initial upstream Alfvén speed.

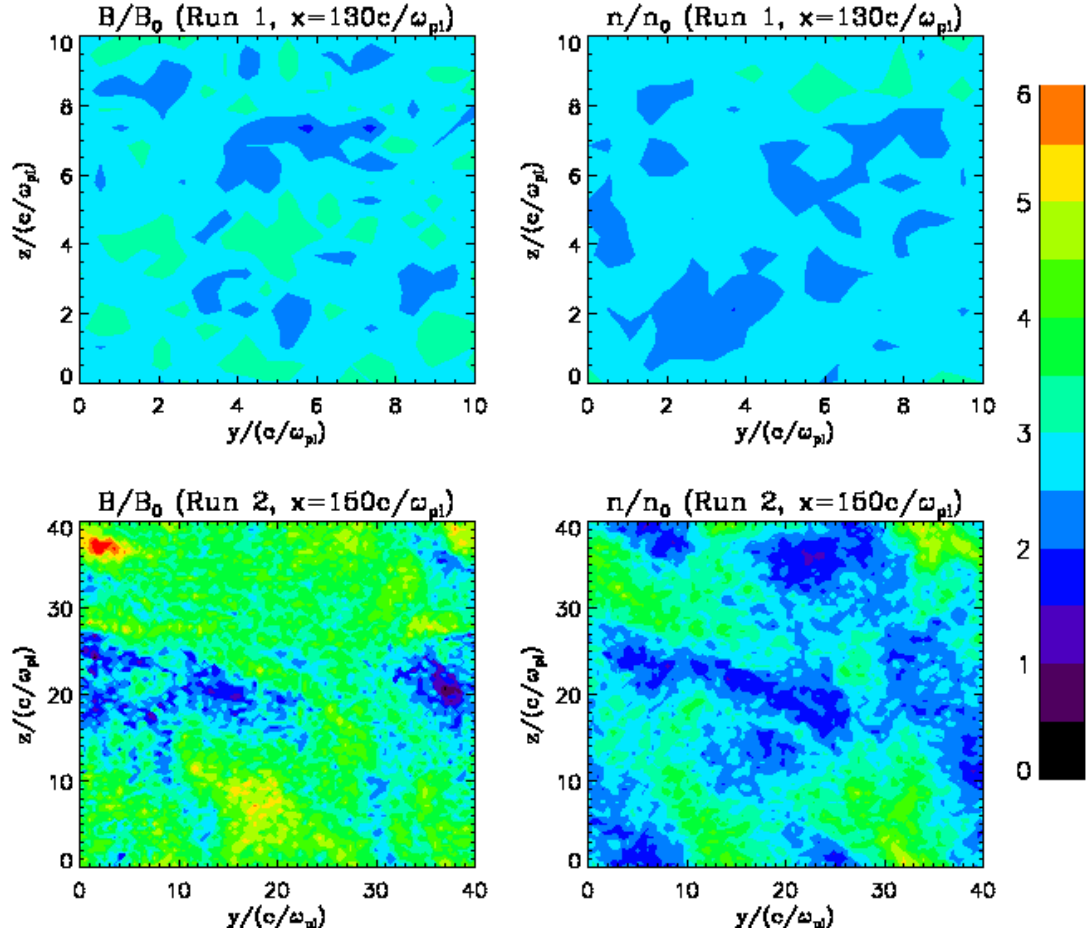


Figure 3.6: The cross sections of magnetic-field magnitude and density close to the shock fronts for Run 1 ($x = 130c/\omega_{pi1}$) and Run 2 ($x = 150c/\omega_{pi1}$) at $\Omega_{ci}t = 120$.

to that in Run 1 is that the 1-D profiles of physical quantities close to the shock front cannot be well represented by the average values over the y and z directions. This indicates that the physical quantities in Run 2 is dependent on three spatial dimensions, whereas those quantities in Run 1 is only weakly dependent on the y and z directions.

To better illustrate the difference between Run 1 and Run 2, in Figure 3.6 we plot the cross sections of magnetic-field magnitude around the shock front for Run 1 and Run 2. It can be seen that in Run 2 the magnetic-field fluctuation around the

shock front has a larger amplitude than that in Run 1. The difference between Run 1 and Run 2 can also be seen in 2-D contours. In Figure 3.7 we show the color-coded contours of the 2-D cuts of (a) the magnitude of the magnetic field B/B_0 (the $z = 5 c/\omega_{pi}$ plane and the $y = 5 c/\omega_{pi}$ plane), and (b) the flow velocity in the x -direction V_x/V_{A0} (the $z = 5 c/\omega_{pi}$ plane and the $y = 5 c/\omega_{pi}$ plane) for the case of Run 1. In Figure 3.8 we show color-coded contours of 2-D cuts of (a) the density of plasma n/n_0 (the $z = 5 c/\omega_{pi}$ plane and the $y = 5 c/\omega_{pi}$ plane), and (b) the density of accelerated particles with energy $3E_1 < E < 5E_1$ (the $z = 5 c/\omega_{pi}$ plane and the $y = 5 c/\omega_{pi}$ plane) for Run 1, where $E_1 = \frac{1}{2}m_p V_1^2$ is the upstream plasma ram energy in the shock frame. The simulation time for these figures is $\Omega_{ci}t = 120.0$. From these figures we can see that the shock front is approximately located at about $x = 125 c/\omega_{pi}$ where the physical quantities have a jump. Although the simulation is fully 3-D, because of the limited size of the simulation box, all the physical quantities appear to be close to 1-D and only depend on x . When the size of the simulation box is larger in the y and z directions, the restriction on the motion of the particle can be removed since the wave modes are allowed to grow in 3-D. This is indicated by Figure 3.9 and 3.10, which show the similar contours to Figure 3.7 and 3.8, but for Run 2. In this case the lengths of the simulation box in the y direction and the z direction are both $40c/\omega_{pi}$. In Figure 3.11 the region around the shock front is zoomed in to show the magnetic field structure close to the shock. One can see the 3-D features around the shock front.

In Figure 3.12 we show a trajectory of a representative particle that is accelerated at shock layer for the case of Run 1. The physical quantities for each panel are: (a) the energy versus the x position in the simulation frame, (b) the energy versus the x position in the shock frame, (c) the energy versus the time in the simulation, (d) the time versus the x position in the simulation frame, (e) the time versus the x position in the shock frame, and (f) the displacement along the z direction versus the displacement along the y direction. One can clearly see that the acceleration happens right at the shock front. The acceleration mechanism is due to the reflection at the shock layer. As shown in this figure, the particle can ride on the shock front

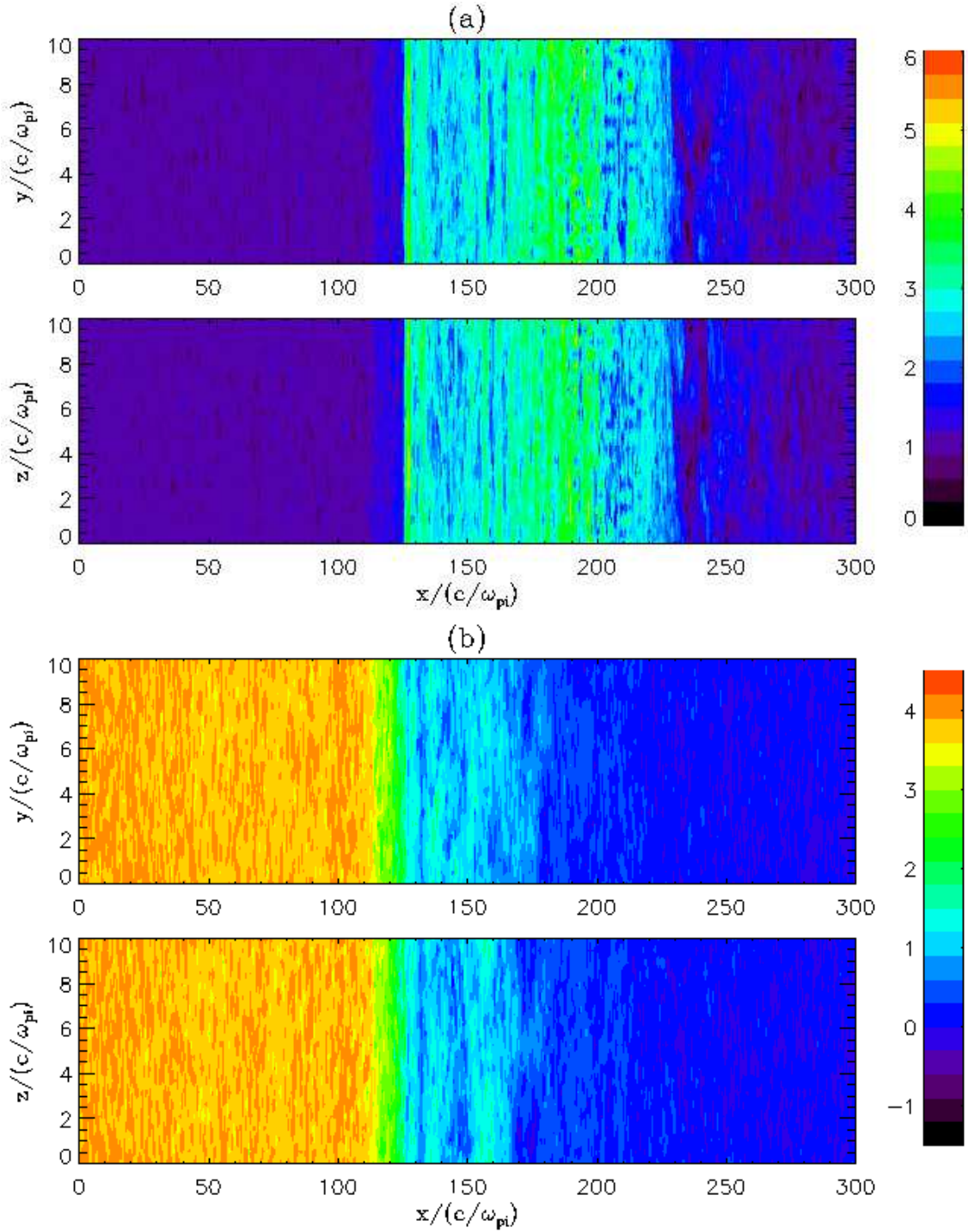


Figure 3.7: 2-D representation of (a) the magnitude of magnetic field B/B_0 (the $z = 5 c/\omega_{pi}$ plane and the $y = 5 c/\omega_{pi}$ plane) and (b) the velocity in the x -direction V_x/V_{A0} (the $z = 5 c/\omega_{pi}$ plane and the $y = 5 c/\omega_{pi}$ plane), for the case of Run 1.

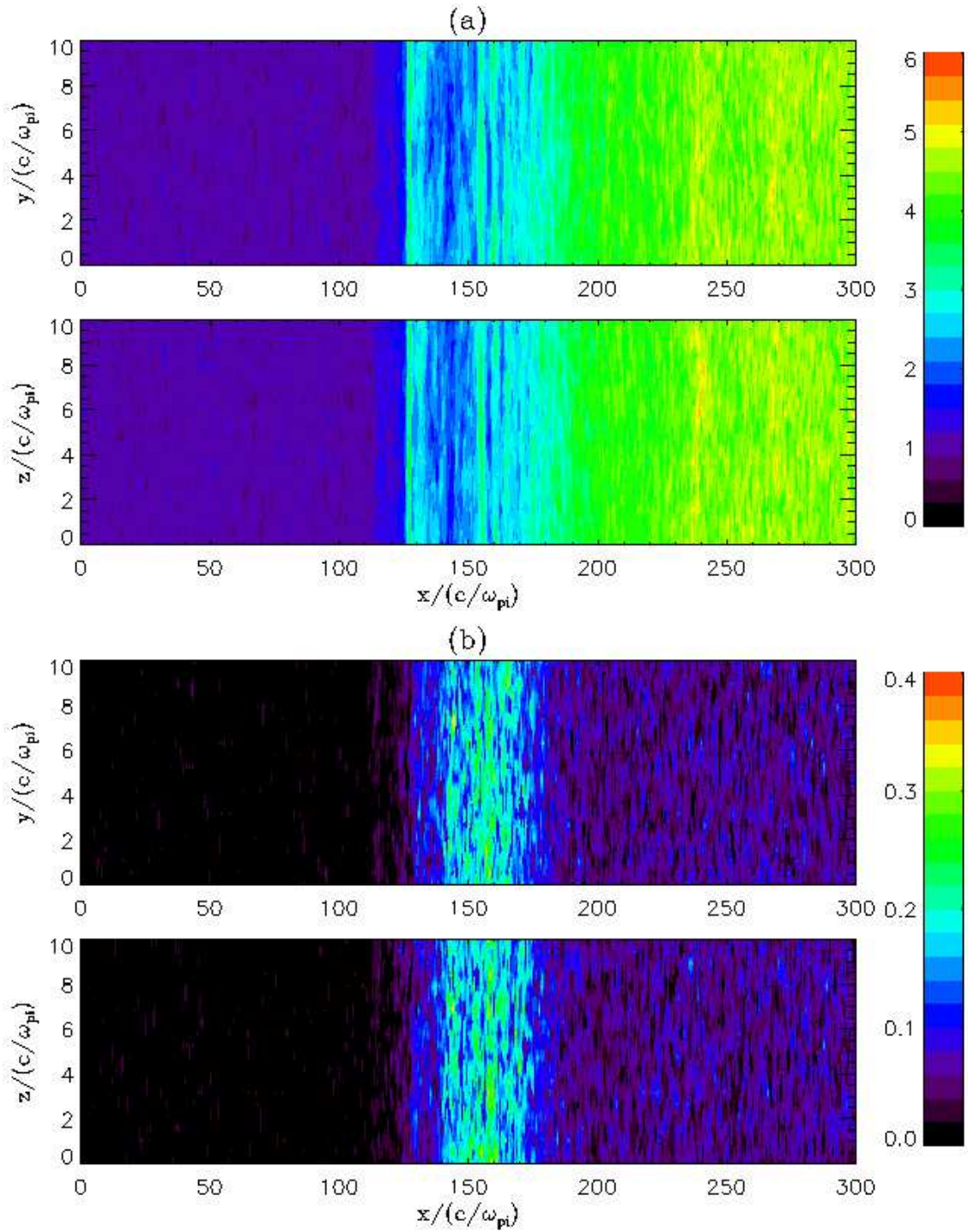


Figure 3.8: Similar to Figure 3.7. 2-D representation of (a) the density of the plasma flow and (b) the density of the accelerated particles with energy $3E_1 < E < 5E_1$, for the case of Run 1.

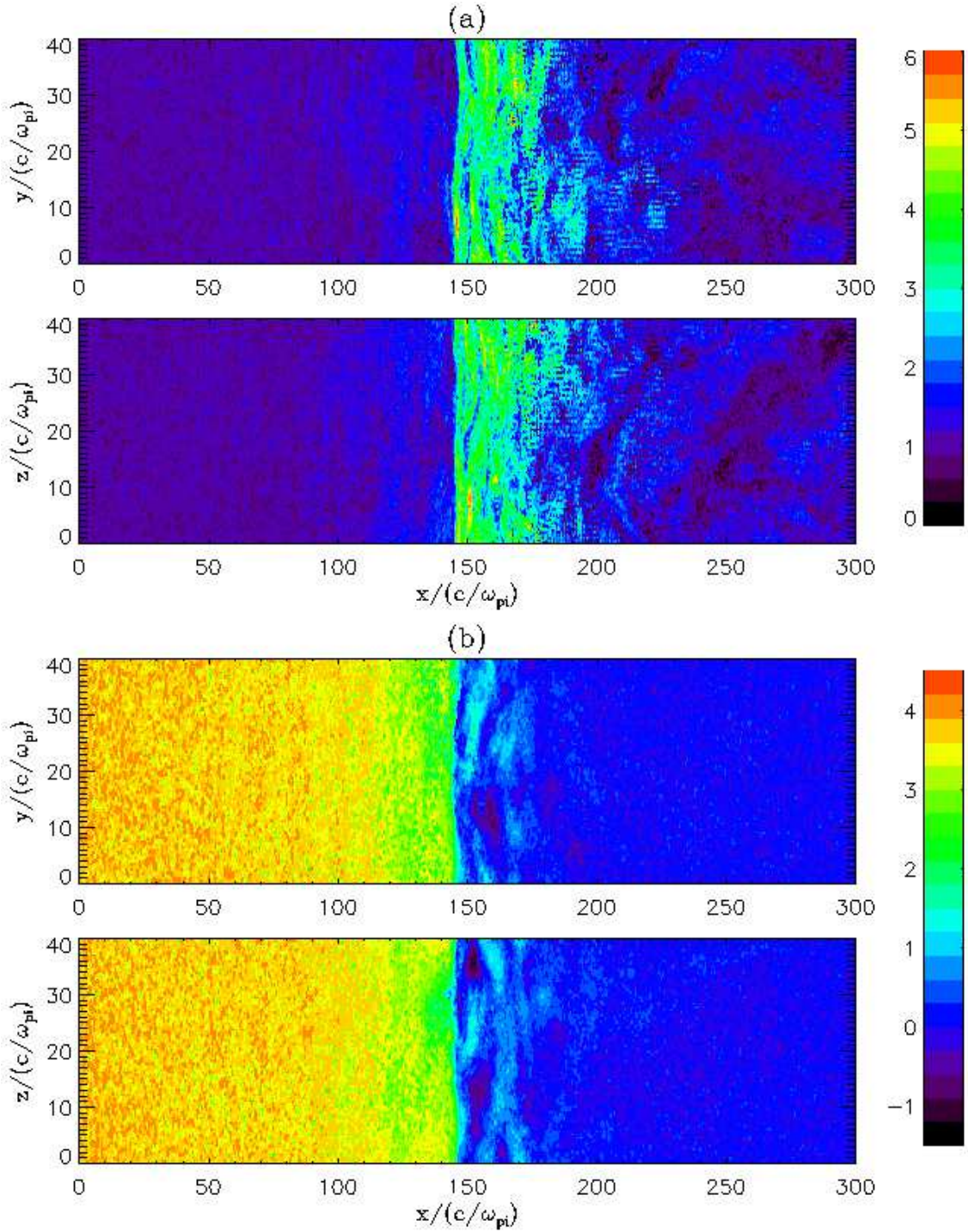


Figure 3.9: 2-D representation of (a) the magnitude of magnetic field B/B_0 (the $z = 20 c/\omega_{pi}$ plane and the $y = 20 c/\omega_{pi}$ plane) and (b) the velocity in the x -direction V_x/V_{A0} (the $z = 20 c/\omega_{pi}$ plane and the $y = 20 c/\omega_{pi}$ plane), for the case of Run 2.

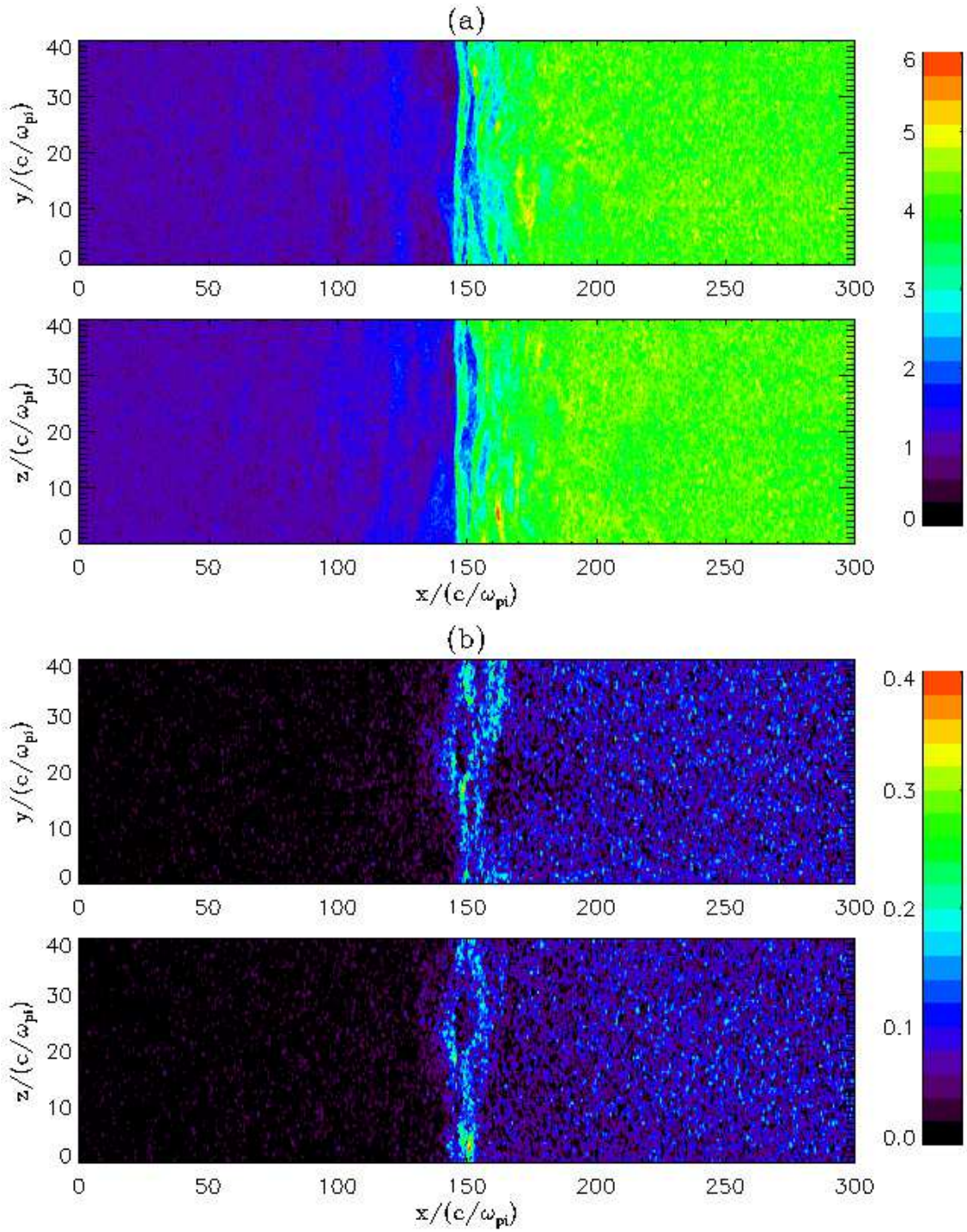


Figure 3.10: Similar to Figure 3.9. 2-D representation of (a) the density of the plasma flow and (b) the density of the accelerated particles with energy $3E_1 < E < 5E_1$, for the case of Run 2.

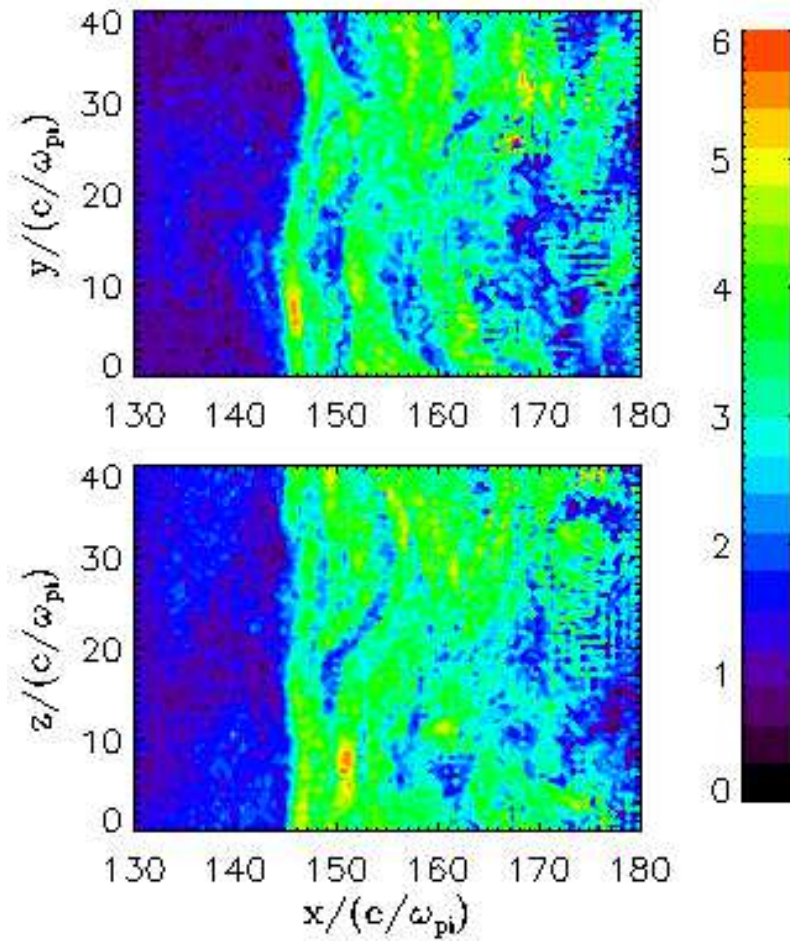


Figure 3.11: The magnitude of magnetic field around the shock front for Run 2.

and get accelerated for about 15 gyroperiods and the energy gain can be about 10 times of the plasma ram energy. This process has been discussed by previous authors (Quest, 1988; Scholer & Terasawa, 1990; Scholer, 1990; Kucharek & Scholer, 1991; Giacalone et al., 1992). Although we use the 3-D hybrid simulation, in this case the motion of the particle is still restricted by the limited size of the simulation box. This can be seen from Figure 3.12 (f), which shows that the guiding center of the particle did not move much during the acceleration process.

For the case of Run 2, it is expected that the trajectories of the accelerated particles could be different since the fluctuations around the shock layer have 3-D structures. Figure 3.13 shows an example of the trajectory of the accelerated particles for the case of Run 2. We find that the acceleration process is quite similar to what is found for the case of Run 1. The main difference is that the particle is allowed to cross its original field line in this 3-D electric and magnetic fields. This can be seen from Figure 3.13 (f), in which the guiding center of the charged particle is drifting in the y - z plane during the acceleration. The difference can be seen clearly in Figure 3.14, which shows the three-dimensional trajectories of the two representative particles from Run 1 and Run 2, respectively. It can be seen that the particle from Run 2 drift along the z direction during the acceleration at the shock front, whereas the guiding center of the particle from Run 1 does not move much during the acceleration.

The acceleration of thermal protons at the shock front creates a nonthermal population of energetic particles. Figure 3.15 shows the density of accelerated particles (Upper panel: $3.0E_1 < E < 4.5E_1$; Lower panel: $6.0E_1 < E < 10.0E_1$) averaged over the y and z directions at $\Omega_{ci}t = 120.0$, where $E_1 = 1/2m_iU_1^2$ and U_1 is taken to be $5.3V_{A0}$ for both cases. The black solid lines represent the results from Run 1 and the red dashed lines represent the results from Run 2. In Run 1 more accelerated particles are trapped around the shock front than in Run 2. The energetic particles in Run 2 can more efficiently escape upstream and downstream of shock. In Figure 3.16 we show downstream energy spectra in $200c/\omega_{pi} < x < 300c/\omega_{pi}$ at $\Omega_{ci}t = 120.0$. The black solid line shows the spectra for Run 1 and the red dashed

dot line represents the spectra for Run 2. In both of the two cases, a fraction of thermal protons are accelerated to several times of bulk energy. In the case of Run 2, more high-energy protons are concentrated in downstream region and their energy range is from several times of bulk energy to about 20 times of bulk energy.

We also consider the effect of the pre-existing upstream fluctuations. In Run 3 we examine the effect of a 1-D pre-existing magnetic fluctuation that only depends on x . Figure 3.17, 3.18, and 3.19 present analyses the same as the previous cases. We find that in this case all the physical quantities are close to 1-D. The wave excitation processes at the shock front seem to be strongly influenced by the injected 1-D fluctuations. Since the injected fluctuation is only dependent on x , it forces the motion of the reflected particle to have the one-dimensional dependence, therefore the fluctuations excited at the shock front are not strongly dependent on y and z . The trajectory analysis (Figure 3.19) of an accelerated particle also confirms this idea, which shows that the motion of the particle is close to 1-D and the guiding center is approximately localized at the same position in the $y - z$ plane compared with that at the beginning of the simulation.

We further examine the effect of pre-existing magnetic fluctuations in Run 4 by injecting a 3-D isotropic fluctuation. In Figure 3.20, 3.21, and 3.22 we present similar analyses to Figure 3.17, 3.18 and 3.19, but for the case that the injected magnetic fluctuation is isotropic in 3-D. The results show that in this case all the physical quantities is dependent on three spatial dimensions. From the analyses of the trajectory of a particle, the guiding center drifts in the $y-z$ plane. Note that although the guiding center can freely jump to another field line, the acceleration process is quite similar to the cases we discussed.

3.3.3 Summary and Discussion

The injection problem is a long standing problem for diffusive shock acceleration. The charged particles are required to be energetic enough and efficiently interact with magnetic fluctuations. In this section we focus on the mechanism for the pre-acceleration, in other words, how a population of thermal or low-energy particles get

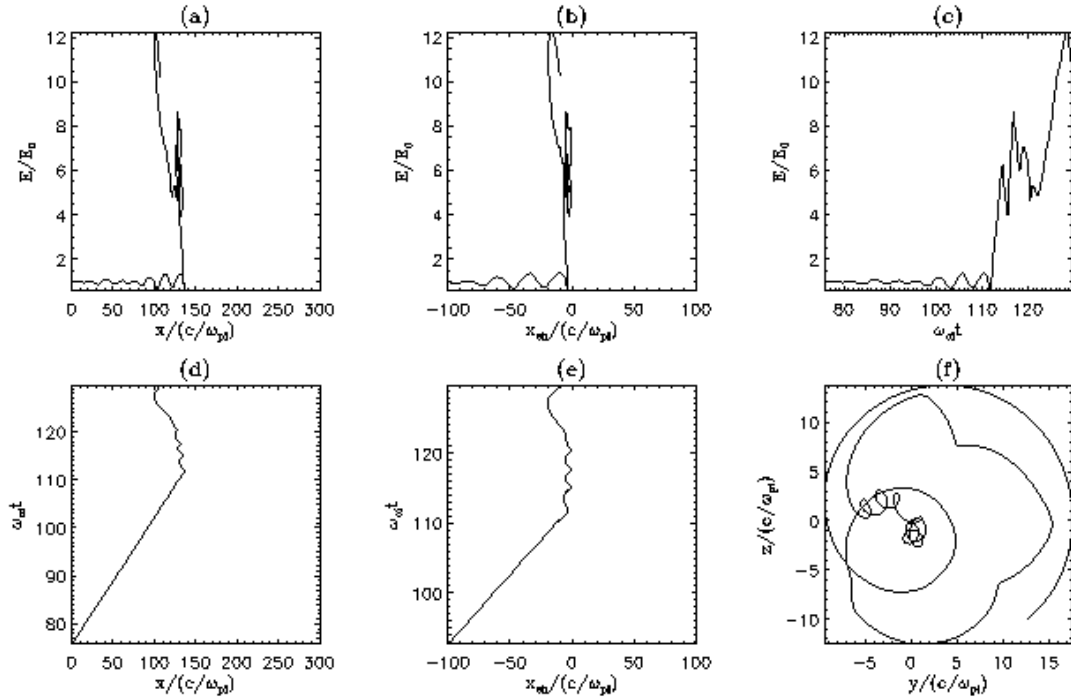


Figure 3.12: The trajectory of a representative particle accelerated at the shock layer for Run 1. The physical quantities for each panel are: (a) the energy versus the x position in the simulation frame, (b) the energy versus the x position in the shock frame, (c) the energy versus the time in the simulation, (d) the time versus the x position in the simulation frame, (e) the time versus the x position in the shock frame, and (f) the displacement along the z direction versus the displacement along the y direction.

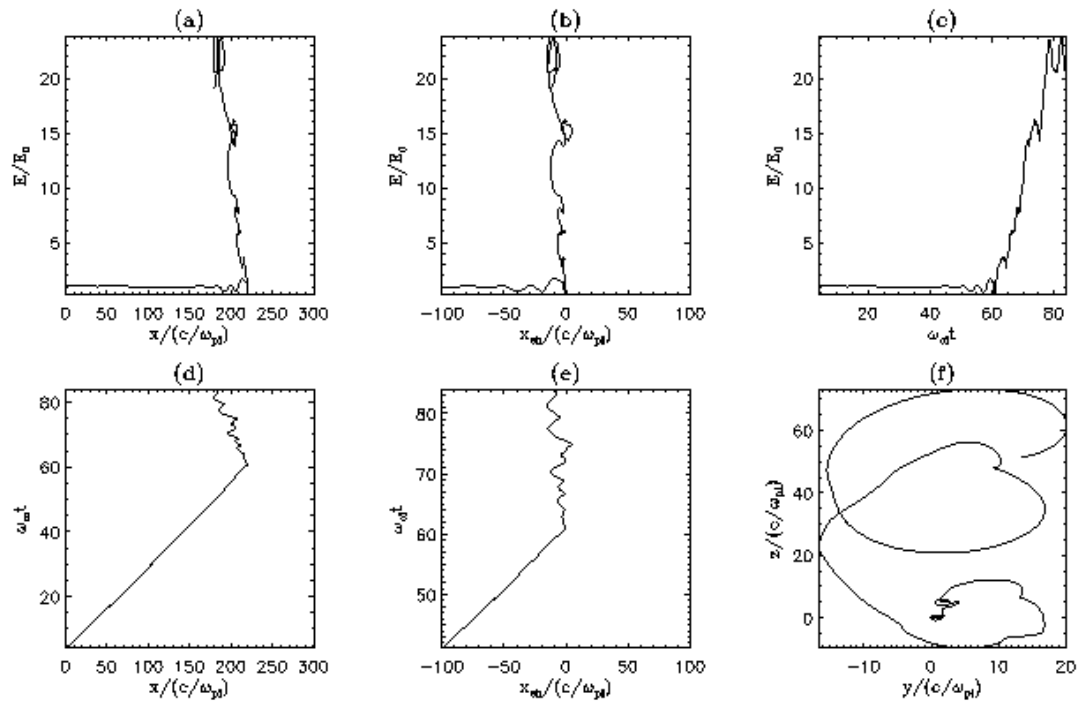


Figure 3.13: The trajectory of a representative particle accelerated at the shock layer for Run 2. The plotted physical quantities are similar to Figure 3.12.

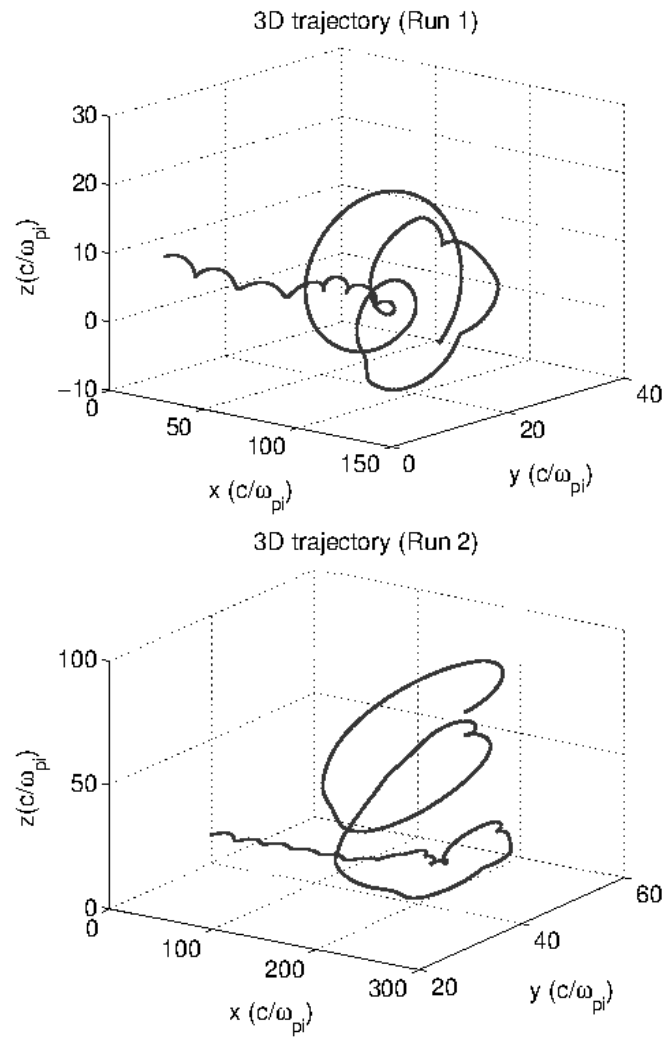


Figure 3.14: Three-dimensional plots of representative particle trajectories for Run 1 and Run 2. In the y and z directions, the displacements $y = \int v_y dt$ and $z = \int v_z dt$ are used instead of the locations of the charged particles.

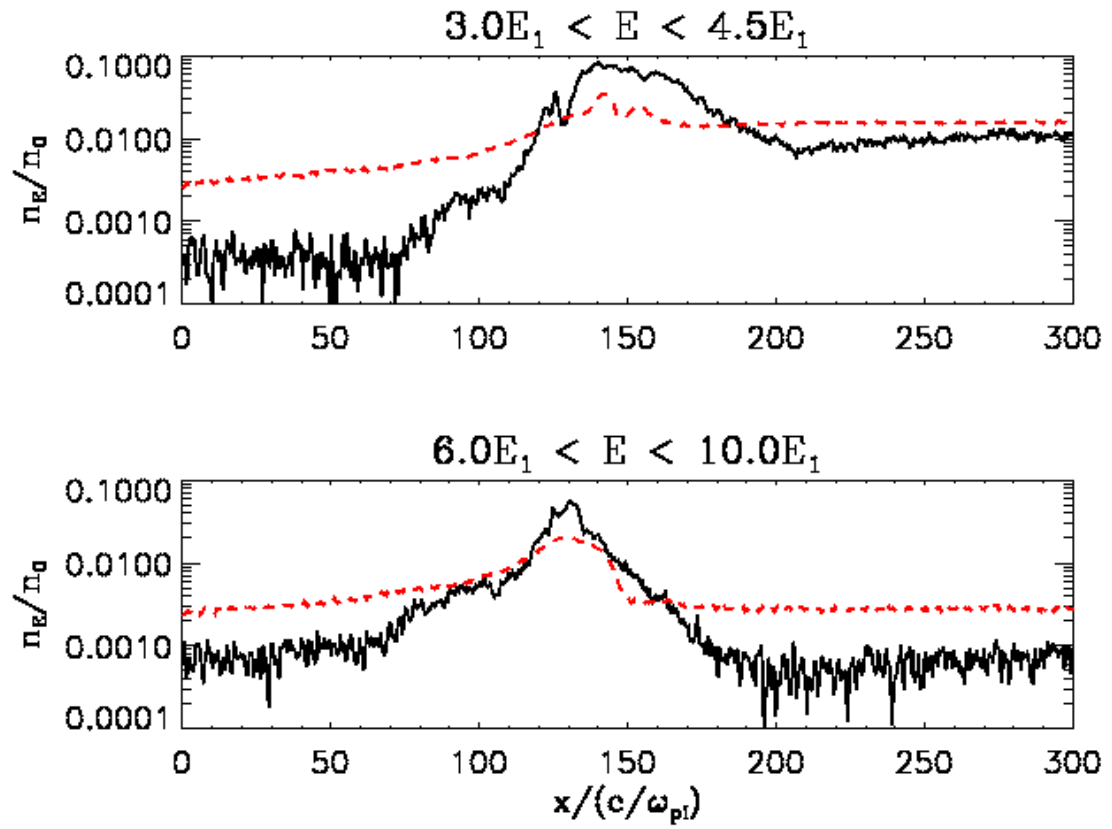


Figure 3.15: 1-D averages of the density of energetic particles in Run 1 and Run 2 at $\Omega_{cit} = 120.0$

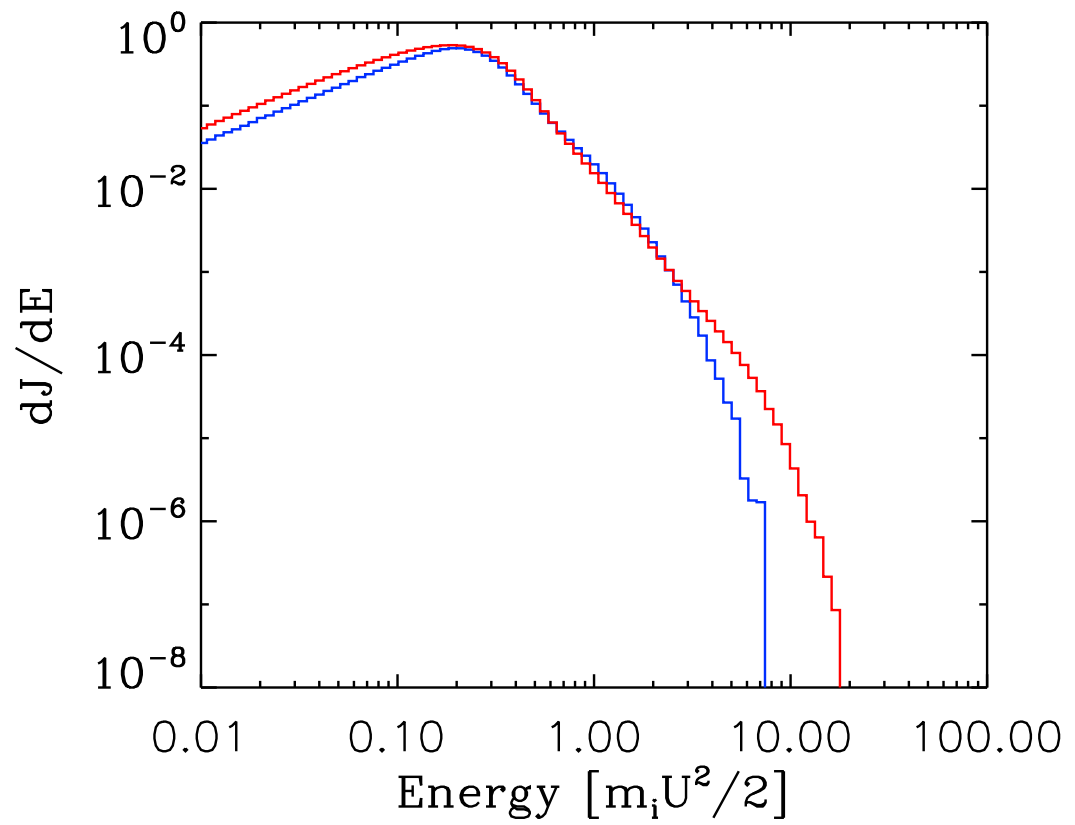


Figure 3.16: Downstream energy spectra for ions in Run 1 (blue) and Run 2 (red) at $\Omega_{cit} = 120.0$

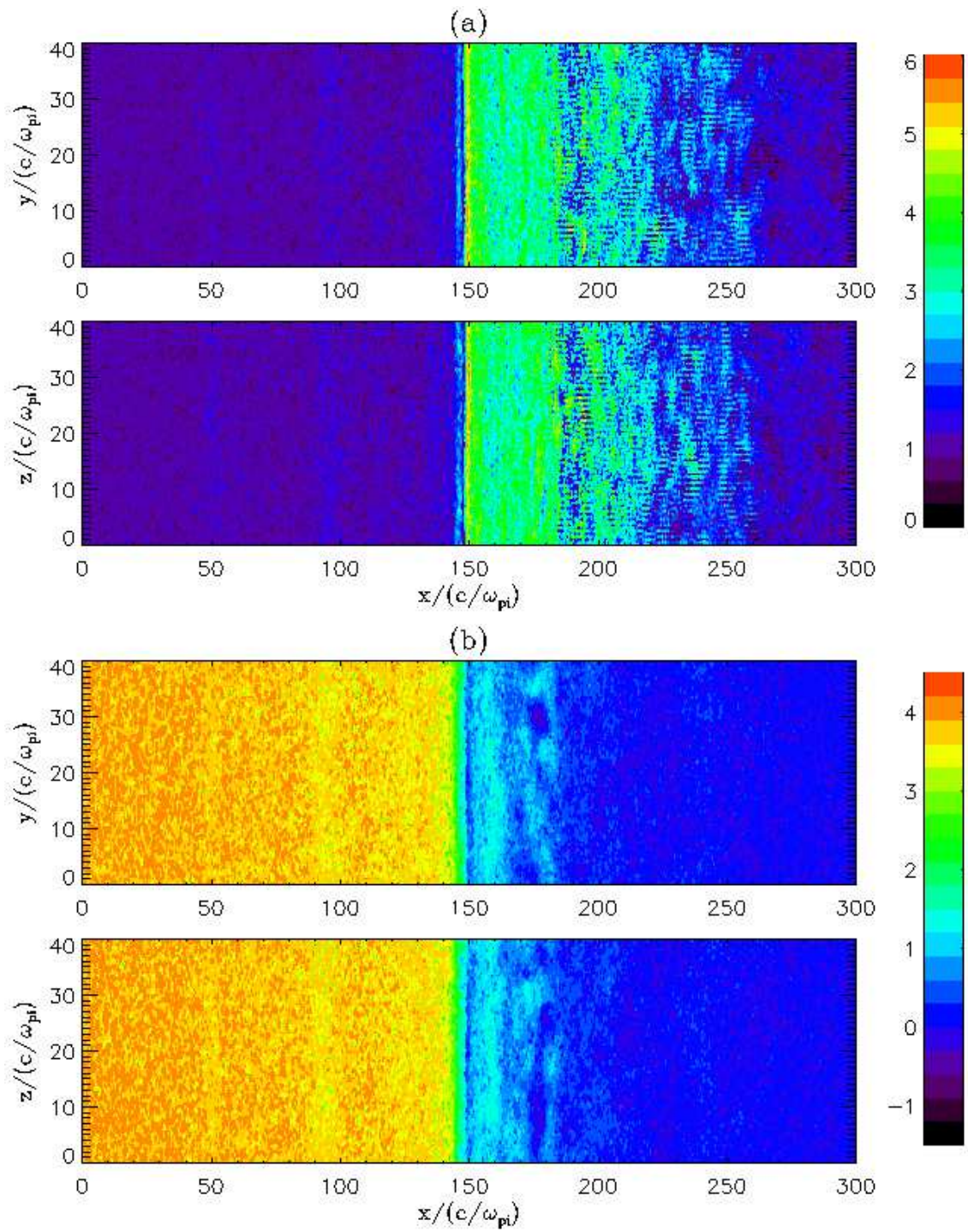


Figure 3.17: Similar to Figure 3.9, but for the case of Run 3.

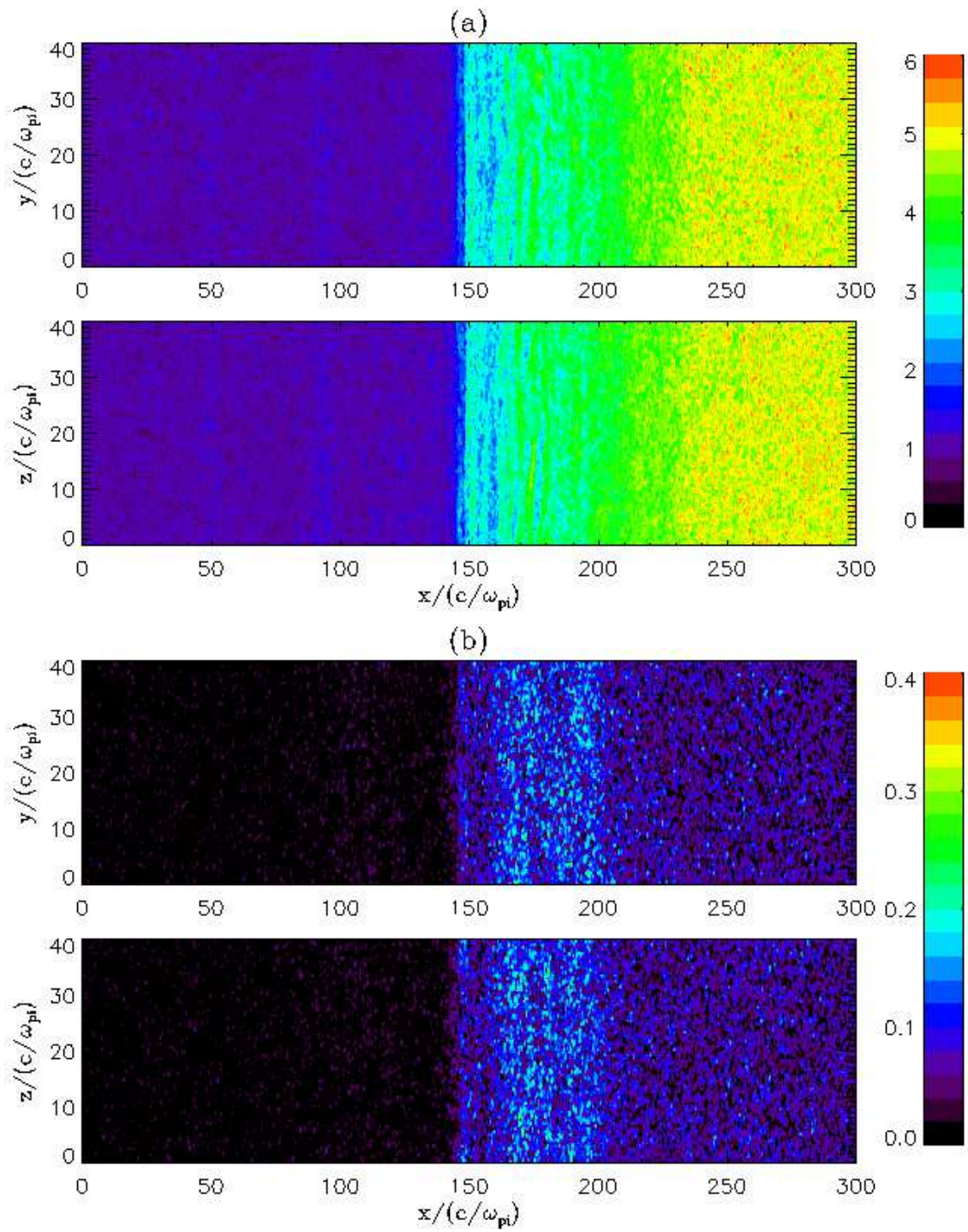


Figure 3.18: Similar to Figure 3.10, but for the case of Run 3.

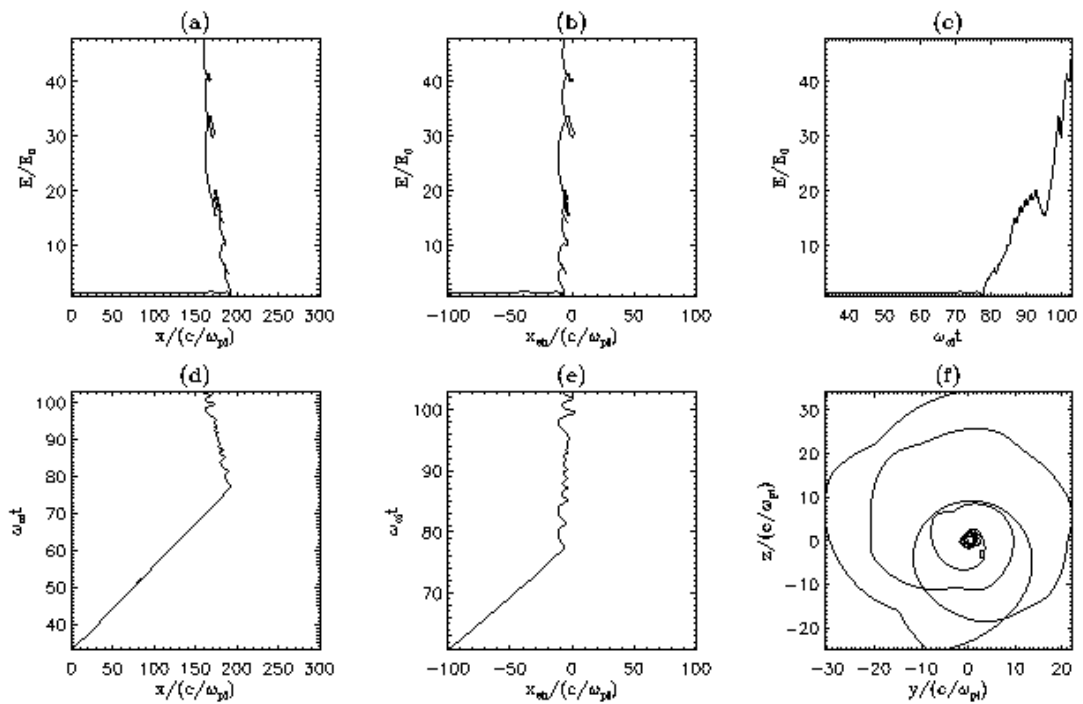


Figure 3.19: The trajectory of a representative particle accelerated at the shock layer for Run 3. The plotted physical quantities are similar to Figure 3.12.

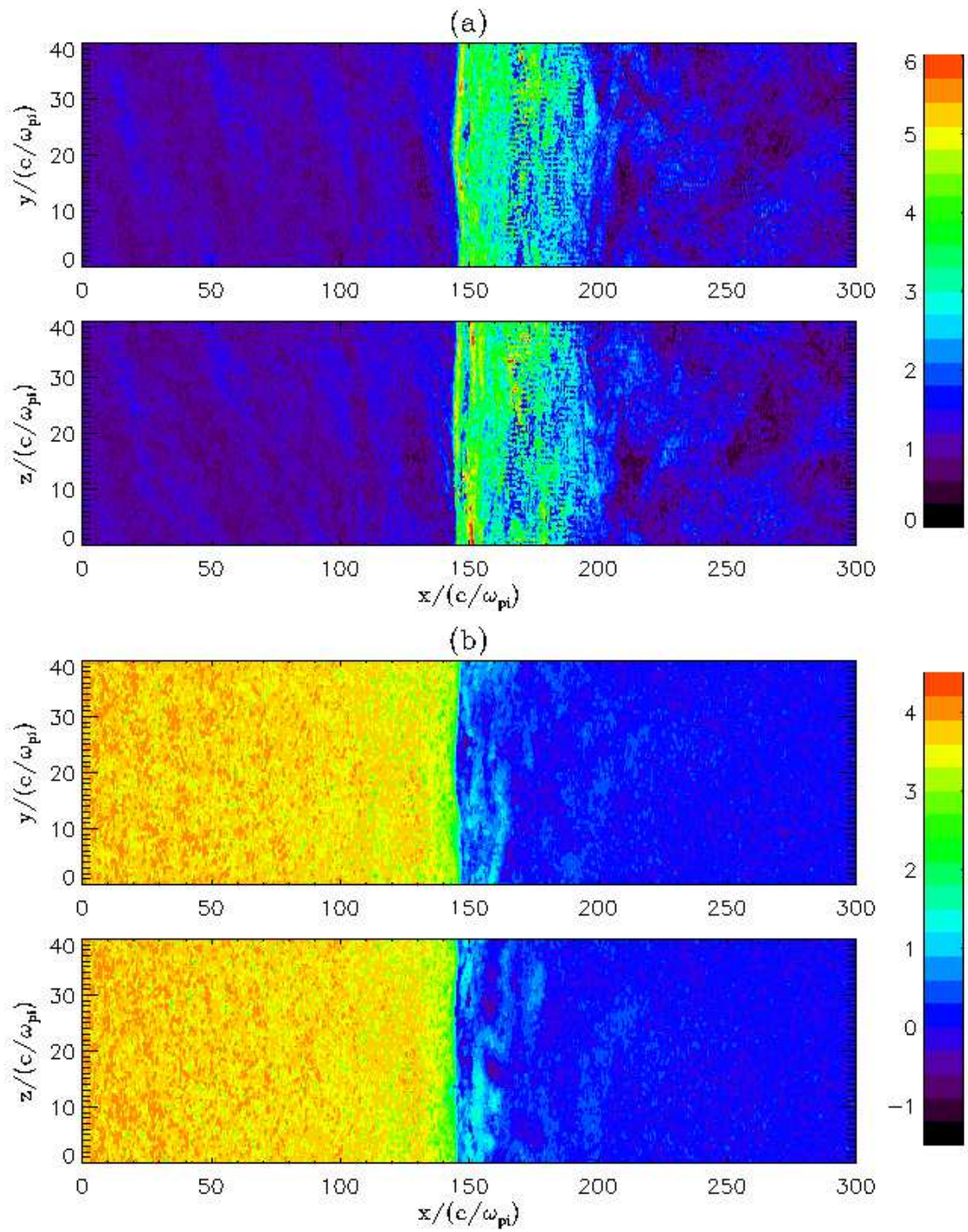


Figure 3.20: Similar to Figure 3.9, but for the case of Run 4.

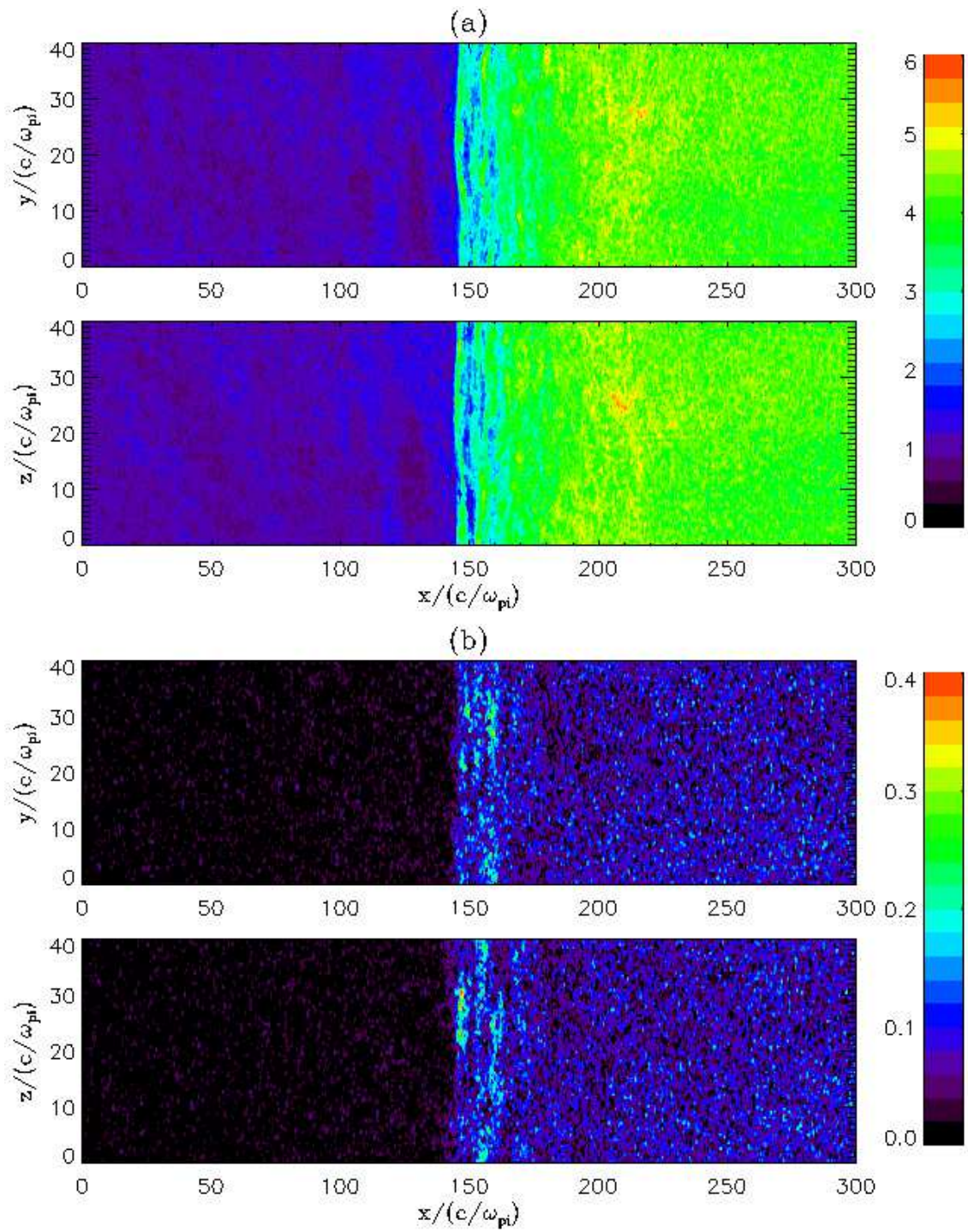


Figure 3.21: Similar to Figure 3.10, but for the case of Run 4.

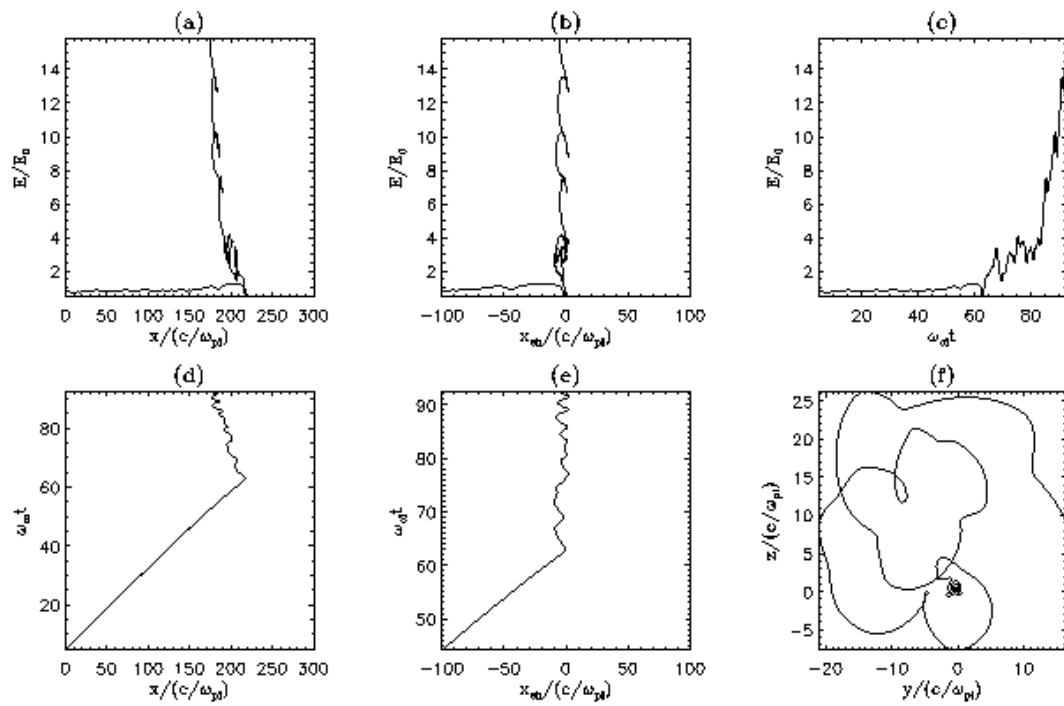


Figure 3.22: The trajectory of a representative particle accelerated at the shock layer for Run 4. The plotted physical quantities are similar to Figure 3.12.

accelerated at the shock front. Previous studies have proposed two different injection mechanisms for the injection of low-energy ions at parallel shocks, i.e., particle energization by downstream heating (Ellison, 1981) and by reflection at the shock layer (Quest, 1988; Scholer & Terasawa, 1990; Scholer, 1990; Kucharek & Scholer, 1991; Giacalone et al., 1992). Although previous self-consistent hybrid simulations have found that the initial energization is due to the ion reflection and acceleration at the shock layer, the results were obtained only for 1-D simulations and occasionally 2-D simulations. As pointed out by Jokipii et al. (1993), Giacalone & Jokipii (1994), and Jones et al. (1998), in a magnetic field that is spatially dependent only on 1-D or 2-D, the motions of charged particles are restricted on their original field lines of force. In this sense, the previous simulations are not conclusive.

In this study, we perform 3-D hybrid simulations to investigate the initial acceleration of thermal protons at parallel shocks. In the case of no pre-existing magnetic fluctuation, we find that the electric and magnetic fields can be generated by the plasma instabilities at the shock front (Quest, 1988). When the size of the simulation box normal to the initial magnetic field is large enough ($40 c/\omega_{pi}$ in our case), the electric and magnetic fields generated at the shock front show significant 3-D variations. By examining the trajectories of the accelerated particles, we find that the guiding center of the representative particle can move off its original place when the electric and magnetic fields are 3-D, meaning that the particles can move across field lines. We also examine if the effect of pre-existing magnetic fluctuations can modify this results. We find that for the case of the 1-D pre-existing magnetic fluctuations, the electric and magnetic fields close to the shock are weakly dependent on the y and z directions. Since the injected fluctuation is only dependent on x , it restricts the motion of the reflected ions and therefore the fluctuations excited at the shock front are not strongly dependent on y and z . When we consider a 3-D pre-existing magnetic fluctuation, this restriction is removed. The charged particles can move across field lines, as suggested by analysing the their trajectories. In all the simulation cases, we find that the charged particles can gain energy at the shock layer. The particle can ride on the shock front and gain a large amount of energy

(several decades of the plasma ram energy). The results confirm previous hybrid simulations that the initial acceleration of charged particles is right at the shock front (Quest, 1988; Scholer & Terasawa, 1990; Scholer, 1990; Kucharek & Scholer, 1991; Giacalone et al., 1992), even if in a 3-D electromagnetic field.

3.4 Beyond the 1-D Diffusive Shock Acceleration

Although the 1-D steady state DSA solution gives a very elegant description for the acceleration of charged particles at the shock front, some other effects could play a role during the acceleration. These effects may help explain the observed variability of energetic particles at shocks. For example, Ellison & Ramaty (1985) discussed the effects such as adiabatic cooling and limited acceleration time, which can cause turnovers in the power law energy spectra of shock-accelerated charged particles if the diffusion coefficient is proportional to energy. They suggest that the spectra have an exponential rollover $dJ/dE \propto \exp(-E/E_0)$. Recent observations indicate that the spectra are more similar to a double power law spectrum (Mewaldt, 2006), i.e., after the spectrum break the spectra still have a power law shape with a steeper slope. Tylka et al. (2005) and Tylka & Lee (2006) argue that the variable spectral and compositional characteristics in large SEP events can be produced by considering the effects of shock angles and different species of seed particles. Their model is based on the argument that the injection speed of particles for diffusive shock acceleration is much higher at perpendicular shocks than that at parallel shocks (see Equation 3.3). As a result, parallel shocks can accelerate charged particles from solar wind particles, whereas perpendicular shocks only accelerate superthermal particles pre-accelerated in solar flares. This model can qualitatively explain the high variable features of spectral characteristics and elemental composition in large gradual SEP events. However, recent numerical simulations show that perpendicular shocks can efficiently accelerate charged particles to high energy in existence of strong pre-existing magnetic fluctuation (Giacalone, 2005a,b). This questions the validity of the Tylka et al. (2005) model. Li et al. (2009) presented a model for

particle acceleration at oblique shocks that include both parallel diffusion and perpendicular diffusion. The results can roughly reproduce the observed dependence of break energy on the charge-to-mass ratio. It should be noted that most of these studies consider particle acceleration at a planar shock. In the real situation the particles can sample a range of shock structures with different shock normal angles as they move along shock surface.

Here we mainly discuss a different mechanism that can modify the 1-D solution of DSA. DSA is thought to be the mechanism that accelerates anomalous cosmic rays (ACRs) in the heliospheric termination shock and also galactic cosmic rays (GCRs) with energy up to at least 10^{15} eV in supernova blast waves. However, recent *in situ* observations at the termination shock and in the heliosheath by *Voyager 1* (Stone et al., 2005) found that the intensity of ACRs was not saturated at the place where *Voyager 1* crossed the termination shock and kept increasing after entering the heliosheath, which strongly indicates that the simple planar shock model is inadequate to interpret the acceleration of ACRs. Numerical and analytical studies suggest that the possible solution can be made by considering the temporary and/or spatial variation (Florinski & Zank, 2006; McComas & Schwadron, 2006; Jokipii & Kóta, 2008; Kóta & Jokipii, 2008; Schwadron et al., 2008). In particular, McComas & Schwadron (2006) discussed the importance of the magnetic geometry of a blunt shock on particle acceleration. The idea can be illustrated by Figure 3.23. They argued that the missing ACRs at the nose of the heliospheric termination shock is due to particle energization occurring primarily back along the flanks of the shock where magnetic field lines have had a longer connection time to the termination shock. Kóta & Jokipii (2008) presented a more sophisticated simulation that gives results similar to that described by McComas & Schwadron (2006). Schwadron et al. (2008) also developed a 3-D analytic model for particle acceleration in a blunt shock, including perpendicular diffusion and drift motion due to large-scale shock structure.

Large-scale magnetic field line meandering is ubiquitous in the heliosphere and other astrophysical environments (Jokipii, 1966; Jokipii & Parker, 1969; Parker,

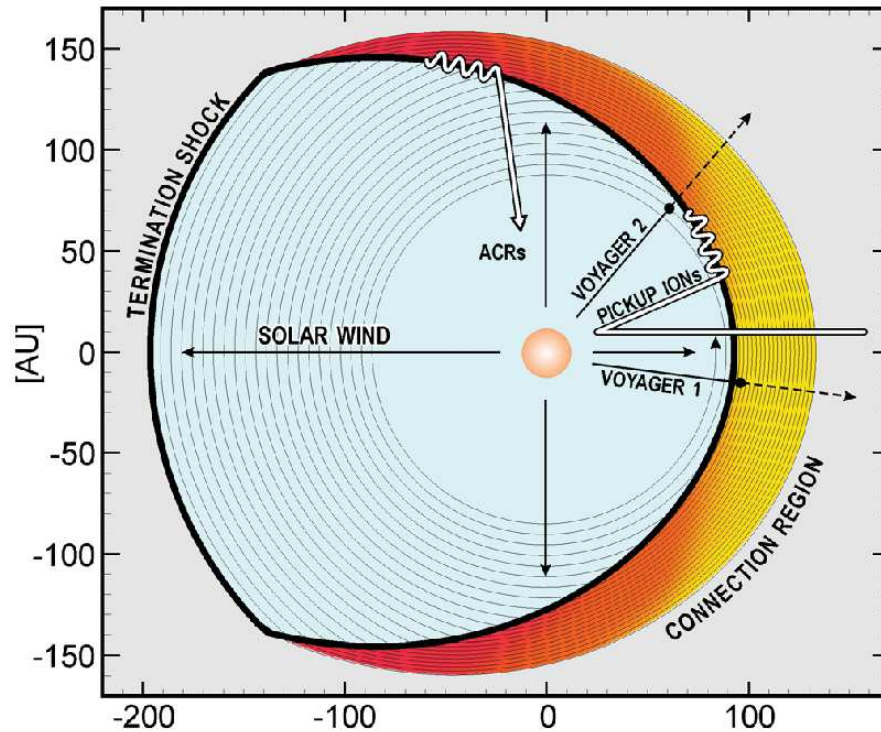


Figure 3.23: McComas & Schwadron (2006)'s idea on the acceleration of anomalous cosmic rays: The Cartoon shows an equatorial cut of the termination shock and the heliosphere. The Parker spiral magnetic field get compressed at the termination shock. Pickup ions can get accelerated at the termination shock in all directions but have different acceleration rate. Because charged particles mainly travel along field lines, pickup ions near the nose take a longer time to travel back to the shock than those close to the shock flanks. The figure is adapted from (McComas & Schwadron, 2006).

1979). The acceleration of charged-particles in collisionless shocks has been shown to be strongly affected by magnetic-field turbulence at different scales (Giacalone, 2005a,b; Giacalone & Neugebauer, 2008). The large-scale magnetic field variation will have important effects on the shock acceleration since the transport of charged particles is different in the direction parallel and perpendicular to the magnetic field, as shown in early work (Jokipii, 1982, 1987). Blunt shocks or shocks with fluctuating fronts (Li & Zank, 2006) that have a similar geometry, are also relevant to this problem. In this study we analyze the effect of the large-scale spatial variation of magnetic field on DSA by considering a simple system that captures the basic physical ideas.

3.5 A Study on Particle Acceleration at Shocks Containing Large-scale Magnetic Variations

In this section we present a study on the acceleration of particles at shocks containing large-scale magnetic variations. The main part of this section has been published in the *Astrophysical Journal* (Guo et al., 2010). Diffusive shock acceleration at collisionless shocks is thought to be the source of many of the energetic particles observed in space. Large-scale spatial variations of the magnetic field has been shown to be important in understanding observations. The effects are complex, so here we consider a simple, illustrative model. Here, we solve numerically the Parker transport equation for a shock in the presence of large-scale sinusoidal magnetic-field variations. We demonstrate that the familiar planar-shock results can be significantly altered as a consequence of large-scale, meandering magnetic lines of force. Because the perpendicular diffusion coefficient κ_{\perp} is generally much smaller than the parallel diffusion coefficient κ_{\parallel} , energetic charged particles are trapped and preferentially accelerated along the shock front in regions where the connection points of magnetic field lines intersecting the shock surface converge, and thus create “hot spots” of accelerated particles. For regions where the connection points are separated from each other, the acceleration to high energies will be suppressed.

Furthermore, the particles diffuse away from the “hot spot” regions and modify the spectra of downstream particle distribution. These features are qualitatively similar to the recent Voyager’s observation in the heliosheath. These results are potentially important for particle acceleration at shocks propagating in turbulent magnetized plasmas as well as those that contain large-scale nonplanar structures. Examples include anomalous cosmic rays accelerated by the solar wind termination shock, energetic particles observed in propagating heliospheric shocks, and galactic cosmic rays accelerated by supernova blast waves, etc.

3.5.1 Basic Considerations and Numerical Model

The diffusive shock acceleration (DSA) can be studied by solving the Parker transport equation (Parker, 1965). Here we consider a 2-D system, the Parker transport equation (1.13) can be written in Fokker-Planck form as:

$$\begin{aligned} \frac{\partial f}{\partial t} = & \frac{\partial^2}{\partial x^2} (\kappa_{xx} f) + \frac{\partial^2}{\partial z^2} (\kappa_{zz} f) + \frac{\partial^2}{\partial x \partial z} (2\kappa_{xz} f) \\ & - \frac{\partial}{\partial x} \left[\left(U_x + \frac{\partial \kappa_{xx}}{\partial x} + \frac{\partial \kappa_{xz}}{\partial z} \right) f \right] - \frac{\partial}{\partial z} \left[\left(\frac{\partial \kappa_{zz}}{\partial z} + \frac{\partial \kappa_{xz}}{\partial x} \right) f \right] \\ & + \frac{\partial}{\partial p^3} \left(\frac{\partial U_x}{\partial x} p^3 f \right) + Q, \end{aligned} \quad (3.9)$$

where $\kappa_{xx} = \langle \Delta x^2 \rangle / 2\Delta t$, $\kappa_{zz} = \langle \Delta z^2 \rangle / 2\Delta t$, and $\kappa_{xz} = \langle \Delta x \Delta z \rangle / 2\Delta t$. Following the usual approach in stochastic integration (Jokipii & Levy, 1977), the solution can be calculated by successively integrating the trajectories of the pseudo-particles:

$$\begin{aligned} \Delta x = & r_1 (2\kappa_{\perp} \Delta t)^{1/2} + r_3 (2(\kappa_{\parallel} - \kappa_{\perp}) \Delta t)^{1/2} \frac{B_x}{B} \\ & + U_x \Delta t + \left(\frac{\partial \kappa_{xx}}{\partial x} + \frac{\partial \kappa_{xz}}{\partial z} \right) \Delta t, \end{aligned} \quad (3.10)$$

$$\begin{aligned} \Delta z = & r_2 (2\kappa_{\perp} \Delta t)^{1/2} + r_3 (2(\kappa_{\parallel} - \kappa_{\perp}) \Delta t)^{1/2} \frac{B_z}{B} \\ & + \left(\frac{\partial \kappa_{zz}}{\partial z} + \frac{\partial \kappa_{xz}}{\partial x} \right) \Delta t, \end{aligned} \quad (3.11)$$

$$\Delta p = -\frac{p}{3} \frac{\partial U_x}{\partial x} \Delta t, \quad (3.12)$$

where r_1 , r_2 , and r_3 are different sets of random numbers that satisfy $\langle r_i r_j \rangle = 0$ and $\langle r_i^2 \rangle = 1$. It can be easily demonstrated that the ensemble average of stochastic differential equations 3.10, 3.11, and 3.12 is the solution of transport equation 3.9. In order to study diffusive shock acceleration, we approximate the shock layer as a sharp variation $U_x = (U_1 + U_2)/2 - (U_1 - U_2)\tanh(x/th)/2$ with a thickness th much smaller compared with the characteristic length of diffusion acceleration κ_{xx1}/U_1 . At the same time, we have to make sure that the time step Δt is small enough to resolve the motion in the shock layer.

Kóta & Jokipii (2008) and Kóta (2010) considered analytically a model in which the upstream magnetic field was in a plane (say, x, y), with average direction in the y direction. The x -component of the magnetic field was composed of uniform sections (straight field lines) alternating in sign, which were periodic in y . They find “hot spots” and spectral effects that illustrate the effect of an upstream meandering in the magnetic field.

Here, we consider a 2-D (x, z) system with a planar shock at $x = 0$, and a sinusoid magnetic field $\mathbf{B} = \mathbf{B}_0 + \sin(kz)\delta\mathbf{B}$. For most of the parts in this paper we discuss the case shown in Figure 3.24. In this figure, the magnetic lines of force are illustrated by blue lines. The shock is denoted by the red dashed line. Since, in the system of interest here, the magnetic field is small enough that its effects are very small (dynamic pressure/magnetic pressure $\sim \rho V_w^2/(B^2/8\pi) \sim 100$ in the solar wind at 1 AU). The system is periodic in the z direction, with the magnetic field convecting from upstream ($x < 0$) to downstream ($x > 0$). In the shock frame, the particles will be subjected to convection and diffusion due to the flow velocities U_1 (upstream) and U_2 (downstream) and diffusion coefficients parallel and perpendicular to large scale magnetic field ($\kappa_{1(\parallel, \perp)}$ and $\kappa_{2(\parallel, \perp)}$), respectively. The gradient and curvature drifts in this case are only in the direction out of the x - z plane and thus irrelevant to this study. Because of the steady velocity difference between upstream and downstream, charged particles that travel through the shock layer will be accelerated. However, since we consider the large-scale magnetic field variation, transport of energetic particles in the fluctuating magnetic field become

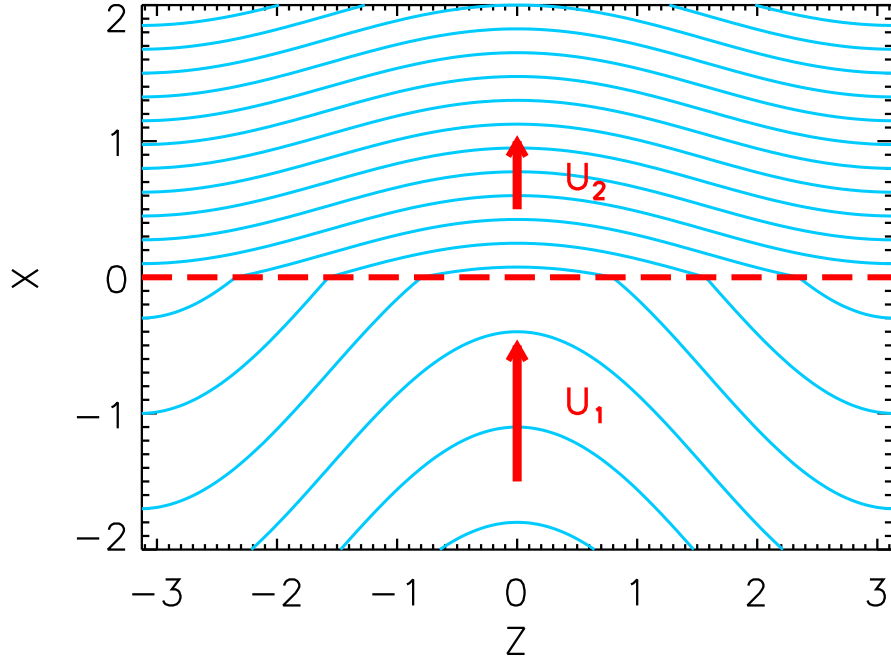


Figure 3.24: The shock and the magnetic field geometry for an upstream average magnetic field perpendicular to the shock normal. The blue lines represent the magnetic field lines and the red dashed line indicates the surface of shock wave. The flow velocities are U_1 (upstream) and U_2 (downstream).

important. The diffusion coefficient in the x - z system can be expressed as:

$$\kappa_{ij} = \kappa_{\perp} \delta_{ij} - \frac{(\kappa_{\perp} - \kappa_{\parallel}) B_i B_j}{B^2}. \quad (3.13)$$

The normalization units chosen in this study are: the spatial scale $X_0 = 10$ AU, the upstream velocity $U_1 = 500$ km/s, the time scale $T_0 = 3 \times 10^6$ sec, and the diffusion coefficients are in unit of $\kappa_0 = 7.5 \times 10^{21}$ cm²/s. The shock compression ratio $r = U_1/U_2$ is taken to be 4.0. The shock layer is considered to be a sharp variation $U_x = (U_1 + U_2)/2 - (U_1 - U_2) \tanh(x/th)/2$ with thickness $th = 1 \times 10^{-3} X_0$, which is required to be less than κ_{xx1}/U_1 everywhere in the upstream simulation domain, where κ_{xx1} is the upstream diffusion coefficient normal to the shock surface. The simulation domain is taken to be $[-2.0X_0 < x < 2.0X_0, -\pi X_0 < z < \pi X_0]$. The parallel diffusion coefficients upstream and downstream are assumed to be the same

and taken to be $\kappa_{\parallel 1} = \kappa_{\parallel 2} = 0.1X_0^2/T_0$ at $p = p_0$. The ratio between parallel diffusion coefficient and perpendicular diffusion coefficient is taken to be $\kappa_{\perp}/\kappa_{\parallel} = 0.05$, which is consistent with that determined by integrating the trajectories of test particles in magnetic turbulence models (Giocalone & Jokipii, 1999). The momentum dependence of the diffusion coefficient is taken to be $\kappa \propto p^{4/3}$, corresponding to non-relativistic particles in a Kolmogorov turbulence spectrum (Jokipii, 1971). We use the stochastic integration method to obtain the numerical solution of the transport equation. In the Equation 1.13, the source function $Q = \delta(p - p_0)\delta(x)$ is represented by injecting pseudo-particles at the shock $x = 0$ with initial momentum $p = p_0$. The trajectories of pseudo-particles are integrated each time step to obtain the numerical solution. The pseudo-particles will be accelerated if they crossing the shock as predicted by DSA. The time step is $1 \times 10^{-7}T_0$ and even reduce at the shock front to resolve the variation of U_x at the finite shock layer. Particles that move past the upstream or downstream boundaries will be removed from the simulation. The system is periodic in the z direction, so a pseudo-particle crossing the boundaries in the z direction will re-appear at the opposite boundary and continue to be followed. A particle splitting technique similar to (Giocalone, 2005a) is used in order to improve the statistics. Although we use very approximate parameters, we note that the results are insensitive to the precise numbers. Our results are also qualitatively unchanged after allowing the injection rate to vary as a function of shock normal angle and different downstream diffusion coefficients. We also note that our model is simplified to illustrate the physics of the magnetic-field variation. Other effects such as changes in plasma properties (density, temperature, etc.) is small for problems of current interest.

3.5.2 Results of Numerical Simulations

A shock propagating perpendicular to the average magnetic field

Consider first the case where the average magnetic field is in the z direction and the fluctuating magnetic field is $\delta B = B_0$. As shown in Figure 3.24, the magnetic

field is convected through the shock front and is compressed in the x direction, thus $B_{z2} = rB_{z1}$. For the sinusoid magnetic field considered in this paper, the local angle between upstream magnetic field and shock normal, θ_{Bn} , will vary along the shock surface. As a magnetic field line passes through the shock surface, its connection points (the points where the field lines intersect the surface of the shock) will be moving apart in the middle of the plane ($z = 0$) and approaching each other on the both sides of the system ($|z| = \pi X_0$). Since, $\kappa_{\parallel} \gg \kappa_{\perp}$, the particles tend to remain on the magnetic field lines. Because the acceleration only occurs at the shock front, as the magnetic lines of force convect downstream, the particles will be trapped and accelerated at places where the connection points converge toward each other, leading to further acceleration. For the regions where the field lines separate from each other, the particles are swept away from those regions. Figure 3.25 displays the spatial distribution contours of accelerated particles in three energy ranges: $3.0 < p/p_0 < 4.0$ (top), $8.0 < p/p_0 < 10.0$ (middle), and $15.0 < p/p_0 < 30.0$ (bottom). The density is represented by the number of particles in simulation and its unit is arbitrary. It can be seen that “hot spots” form in the regions that connection points approaching each other at all energy ranges, with lobes extend along the magnetic field lines. The density of the accelerated particles at the connection-point separating region (in the middle of the plane) is clearly much smaller, although there is still a concentration of low-energy accelerated particles there since the acceleration of low-energy particles is rapid and efficient at perpendicular shocks. At higher energy ranges (middle and bottom), the lack of accelerated particles may be interpreted as due to the fact that the acceleration to high energies takes time.

Figure 3.26 illustrates the profiles of the density of accelerated particles for different energy ranges at $z = 0$ (top) and $z = \pi X_0$ (bottom). In each panel, the black solid lines show the density of low-energy particles ($3.0 < p/p_0 < 4.0$), the blue dashed lines show the density of intermediate energy particles ($8.0 < p/p_0 < 10.0$), and red dot dashed lines show the density of particles with high energies ($15.0 < p/p_0 < 30.0$). In connection-point separating regions $z = 0$ (top), it can be seen that

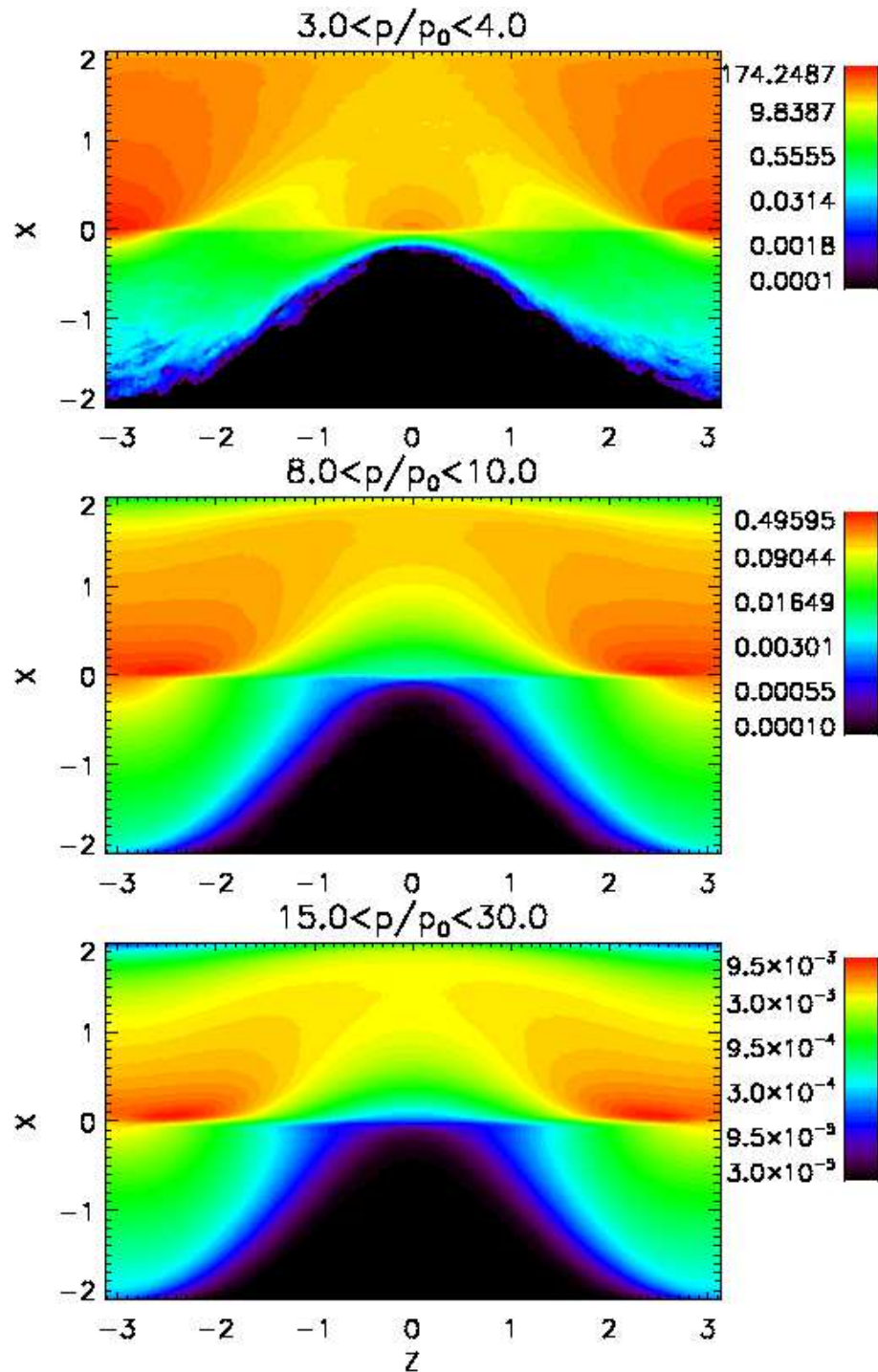


Figure 3.25: The representation of density contour of accelerated particles, for energy range: $3.0 < p/p_0 < 4.0$ (top), $8.0 < p/p_0 < 10.0$ (middle), $15.0 < p/p_0 < 30.0$ (bottom). It is shown that the hot spots form on the both side of the system. The acceleration at the center of the shock is suppressed.

while the downstream distribution of low-energy particles is roughly a constant, the density of particles with higher energies increase as a function of distance downstream from the shock. These particles are not accelerated at the shock layer in the center of the plane but in the “hot spots”. At $z = \pi X_0$ (bottom), the density of particles of all energies decreases as a function of distance, which indicates that the accelerated particles diffusive away from the “hot spots”. Since the high energy particles have larger diffusion coefficients than the particles with low energy, it is easier for them to transport to the middle of the plane. The profile at $z = 0$ is similar to *Voyager*’s observation of anomalous cosmic rays (ACRs) at the termination shock and the heliosheath (Stone et al., 2005; Cummings et al., 2008) that shows the intensity of the ACRs is still increasing and the energy spectrum is unfolding over a large distance after entering the heliosheath. The same physics has been discussed by Jokipii & Kóta (2008), where “hot spots” of energetic particles is produced by the spatial variation of the injection of the source particles. In our current work, the concentration of energetic particles are a consequence of particle accelerated in a shock containing large-scale magnetic variation.

The top panel in Figure 3.27 represents the positions in z direction and the times as soon as the particles reached a certain momentum $p_c = 3p_0$. We show that particles are accelerated mainly at the connection-point converging region. There are also particles accelerated at middle of the plane because the particles can gain energy rapidly at perpendicular or highly oblique shock due to the smallness of perpendicular diffusion coefficient (Jokipii, 1987). However, the further acceleration is suppressed by the effect that the charged particles travel away from the connection-point separating region (see also the top panel in Figure 3.28). It is clear that since the particles tend to follow the magnetic field lines, when the field line connection points separate from each other as field convects through the shock, the particles travel mainly along magnetic field and away from the middle of the plane. The characteristic time for a field line convect from upstream to downstream $\tau_c = D/U_1 \sim T_0$, therefore there is no significant acceleration in the middle of the plane after $t = \tau_c$. Some of the particles can get more acceleration traveling from other region to “hot

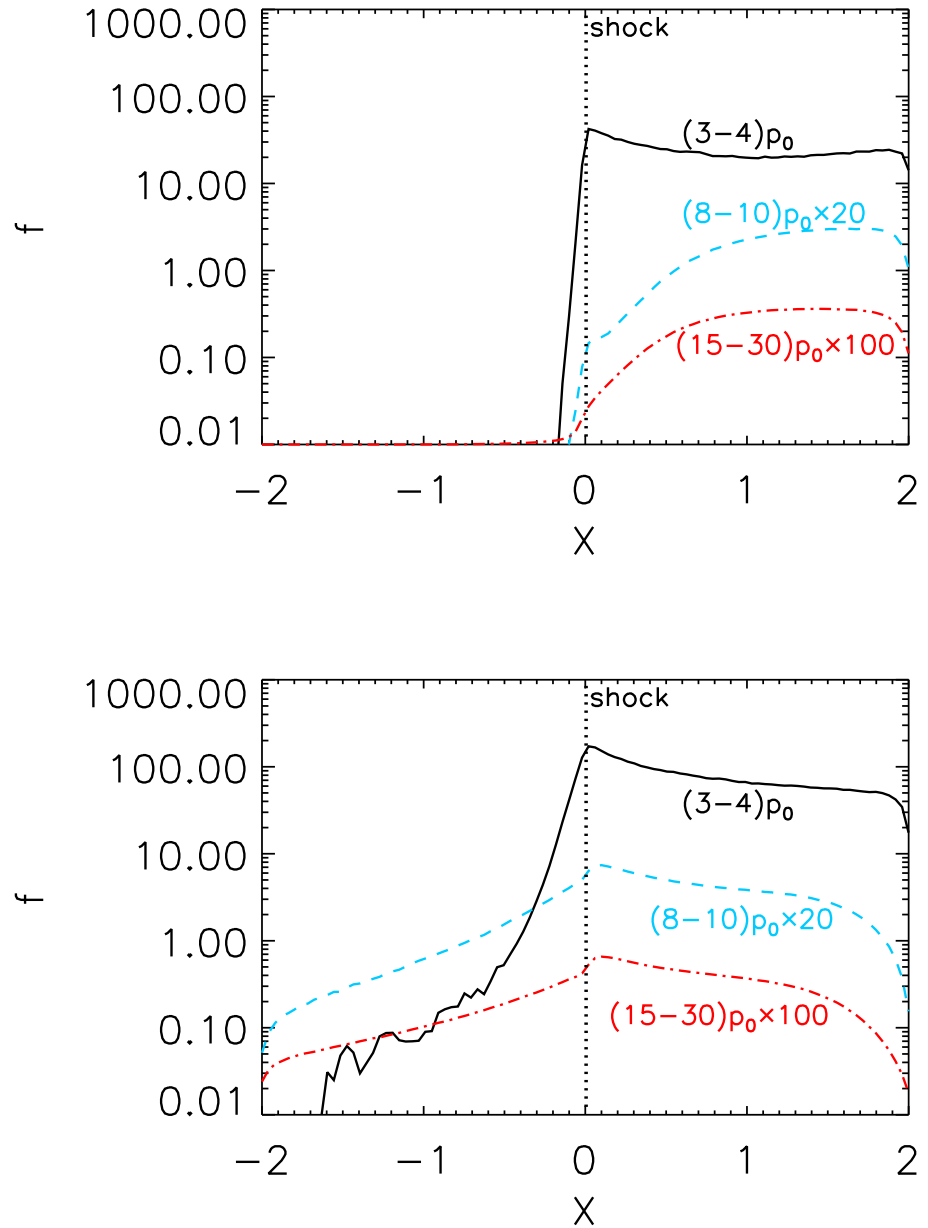


Figure 3.26: The profiles of density of the accelerated particles, for energy ranges: $3.0 < p/p_0 < 4.0$ (black lines), $8.0 < p/p_0 < 10.0$ (blue dashed lines), $15.0 < p/p_0 < 30.0$ (red dot dashed lines) at different locations $z = 0.0$ (top) and πX_0 (bottom), respectively.

spots”. Figure 3.27 *bottom* shows the distance particles traveled in the z direction from its original places $|z - z_0|$ versus time when particle get accelerated at a certain energy ($p_c = 3p_0$). It shows that many particles are accelerated close to their original position, which is related to the acceleration in the “hot spot”. Nevertheless, there are also a number of particles travel from the connection point separating region to “hot spot” and get further acceleration, which is represented by the particles that travel a large distance in the z direction.

Figure 3.28 shows the same plot as Figure 3.27, except here the critical momentum is $p_c = 10.0p_0$. It is shown again in Figure 3.28 *top* that most of particles are accelerated to high energy are in the hot spot. However, as opposite to Figure 3.27 *top*, there are very few particles accelerated at the center of plane since energetic particles more transport away from the middle region and the time available is not long enough. For a quick estimate, the acceleration time is approximately,

$$\begin{aligned}
 \tau_{acc} &= \frac{3}{U_1 - U_2} \int_{p_0}^p \left(\frac{\kappa_{xx1}}{U_1} + \frac{\kappa_{xx2}}{U_2} \right) d \ln p \\
 &> \frac{3}{U_1 - U_2} \int_{p_0}^{10p_0} \left(\frac{\kappa_{\perp}}{U_1} + \frac{\kappa_{\perp}}{U_2} \right) d \ln p \\
 &> \tau_c.
 \end{aligned} \tag{3.14}$$

Therefore for most of particles, they do not have sufficient time to be accelerated to high energies at the center. A number of particles accelerated at the center will travel to the “hot spot” and get more acceleration, as shown in Figure 3.28 *bottom*.

Clearly, the acceleration by the shock containing 2-D spatial magnetic field variations shows a different picture than the acceleration by a 1-D planar shock, indicating that the resulting distribution function is spatially dependent. In Figure 3.29 we show the steady state energy spectra obtained in the regions *top*: $[0.1X_0 < x < 0.3X_0, (\pi - 0.2)X_0 < z < \pi X_0]$ (black solid line), and $[0.1X_0 < x < 0.3X_0, -0.1X_0 < z < 0.1X_0]$ (green dashed line) and *bottom*: $[0.8X_0 < x < 1.0X_0, (\pi - 0.2)X_0 < z < \pi X_0]$ (black solid line), and $[0.8X_0 < x < 1.0X_0, -0.1X_0 < z < 0.1X_0]$ (green dashed line). It is shown that the spatial difference among distribution functions at different locations caused by large-scale magnetic field variation

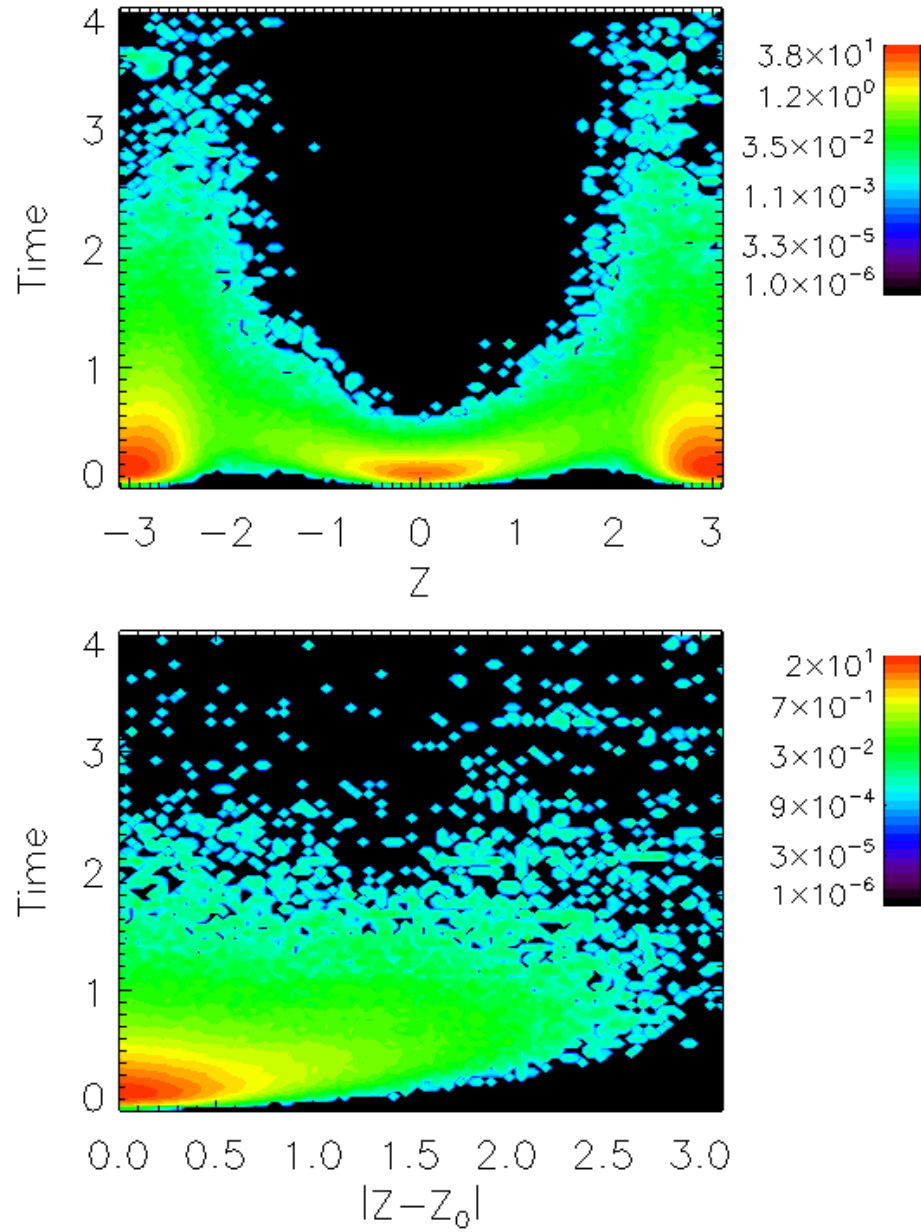


Figure 3.27: *top*: The position in the z direction and time when the particle momentum reached $p = 3.0p_0$; *bottom*: The travel distance in the z direction $|z - z_0|$ and time when the particle momentum reached $p = 3.0p_0$.

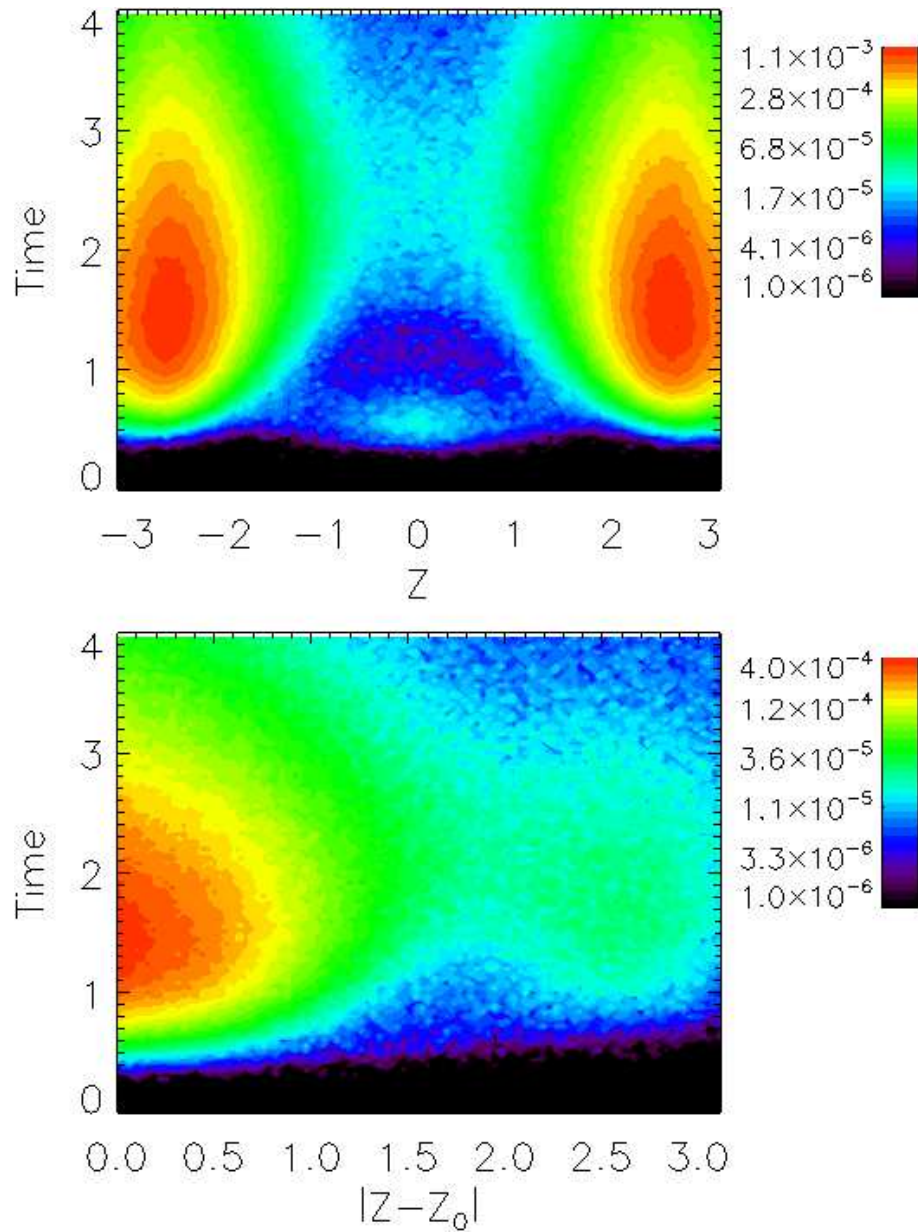


Figure 3.28: *top*: The position in the z direction and time when the particle momentum reached $p = 10.0p_0$; *bottom*: The travel distance in the z direction $|z - z_0|$ and time when the particle momentum reached $p = 10.0p_0$.

is considerable. The black lines in both top plot and bottom plot, which correspond to the “hot spots”, show power-law like distributions except at high energies. At high energies, the particles will leave the simulation domain before gain enough energy that causes the roll over in distribution function, this roll over is mainly caused by a finite distance to upstream boundary. For other locations, the 2-D effect we discussed will produce the modification in distribution functions. The most pronounced effect can be found at the nose of the shock (green lines), in the top panel the distribution of particles shows a suppression of acceleration at all the energies. This insufficient acceleration is most prominent in the range of $6 - 12p_0$. At these energies the acceleration time scales are longer than the time for the field line convection swipe the particles away from the connection-point separating region, as we discussed above. The bottom plot shows that deep downstream the spectrum of accelerated particles is similar at high energies since the mobility of these particles.

An oblique shock

The previous discussion has established the effect of a spatially varying upstream magnetic field on the acceleration of fast charged particles at a shock propagating normal to the average upstream magnetic field. We next consider the case where the shock propagation direction is *not* normal to the average magnetic field.

Clearly, if the varying direction of the upstream magnetic field is such that at some places the local angle of the magnetic field relative to the average field direction exceeds the angle of the average magnetic field to the shock plane, we will have situations similar to that discussed in the previous sections. There will be places where the connection points of the magnetic field to the shock move further apart or closer together. Hence we expect that the same physics can be applicable. An example is given in Figure 3.30. In this case the ratio of $\delta B/B_0$ is taken to be 0.5 and the averaged shock normal angle $\theta_{Bn} = 70^\circ$. It can be seen from this plot that the connection points can still move toward each other in some regions. Figure 3.31 shows the density contours of accelerated particles the same as Figure 3.25, but for the case of the oblique shock. We find that in this case the process we discussed

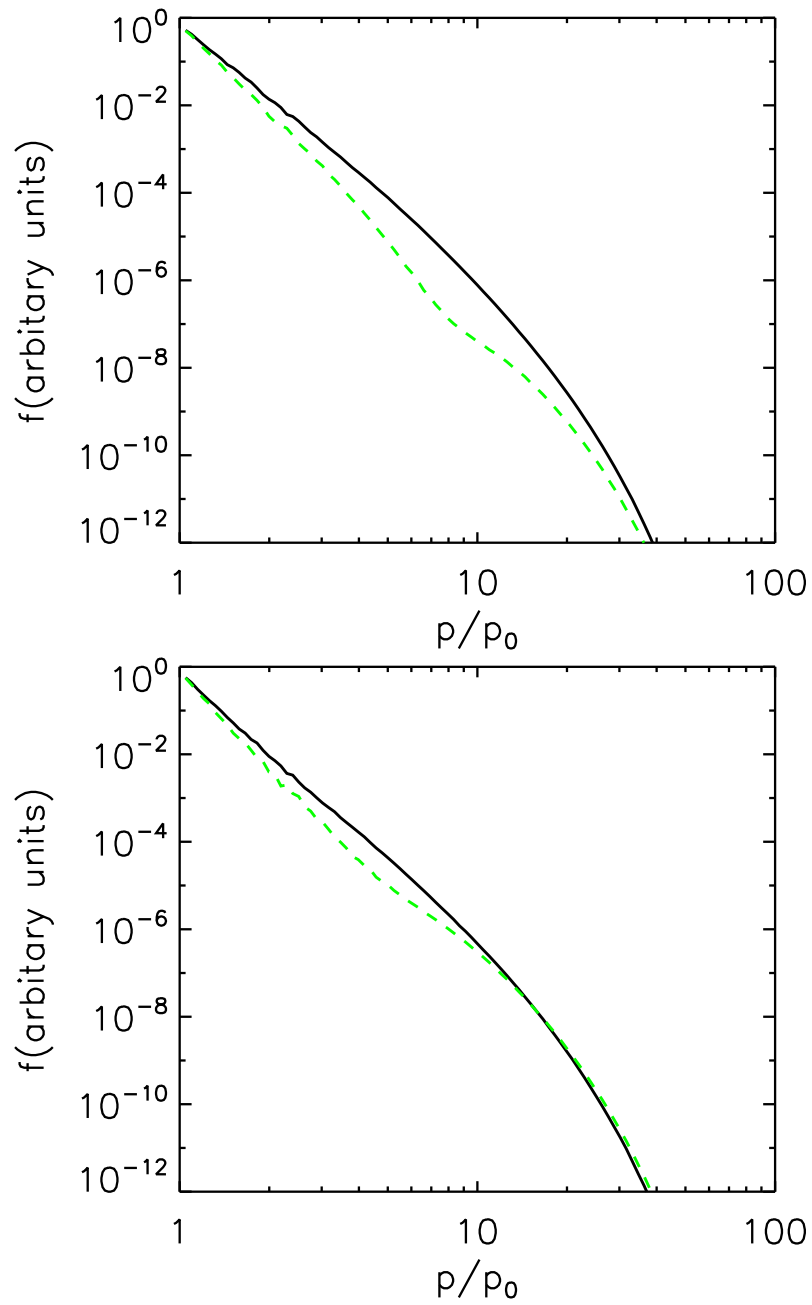


Figure 3.29: The steady state distribution functions at *top*: $[0.1X_0 < x < 0.3X_0, (\pi - 0.2)X_0 < z < \pi X_0]$ (black solid line), $[0.1X_0 < x < 0.3X_0, -0.1X_0 < z < 0.1X_0]$ (green dashed line) and *bottom*: $[0.8X_0 < x < 1.0X_0, (\pi - 0.2)X_0 < z < \pi X_0]$ (black solid line), $[0.8X_0 < x < 1.0X_0, -0.1X_0 < z < 0.1X_0]$ (green dashed line), respectively.

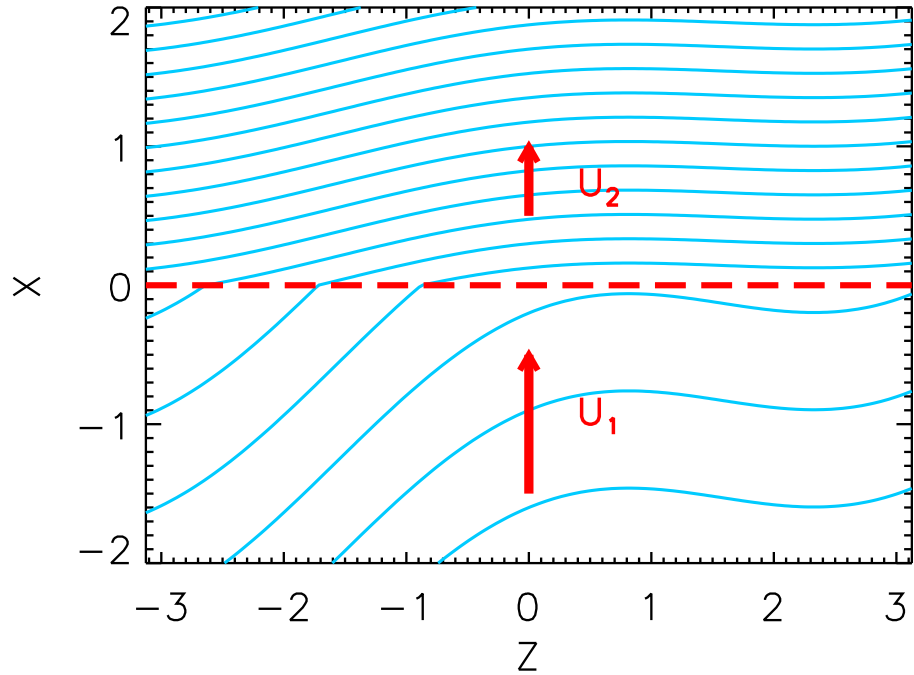


Figure 3.30: The shock and the magnetic field geometry considered for the case of an average magnetic field is 70° of the shock normal. The blue lines represent the magnetic field lines and red dashed line indicates the position of shock wave. The flow velocities are U_1 (upstream) and U_2 (downstream).

in the last section is still persistent, even for an oblique shock and relative smaller $\delta B/B_0$. The “hot spot” forms correspond to the converging magnetic connection points and particle acceleration is suppressed in the region where connection points separate from each other. We may conclude that, for a shock that is oblique, if some magnetic field lines can intersect the shock multiple times, we have “hot spots” of accelerated particles forms where the connection points converging together.

3.5.3 Summary and Discussion

The acceleration of charged particles in shock waves is one of the most important unsolved problems in space physics and astrophysics. Charged particle transport in turbulent magnetic field and acceleration in shock region are two inseparable problems. In this section we illustrate the effect of a large-scale sinusoidal magnetic

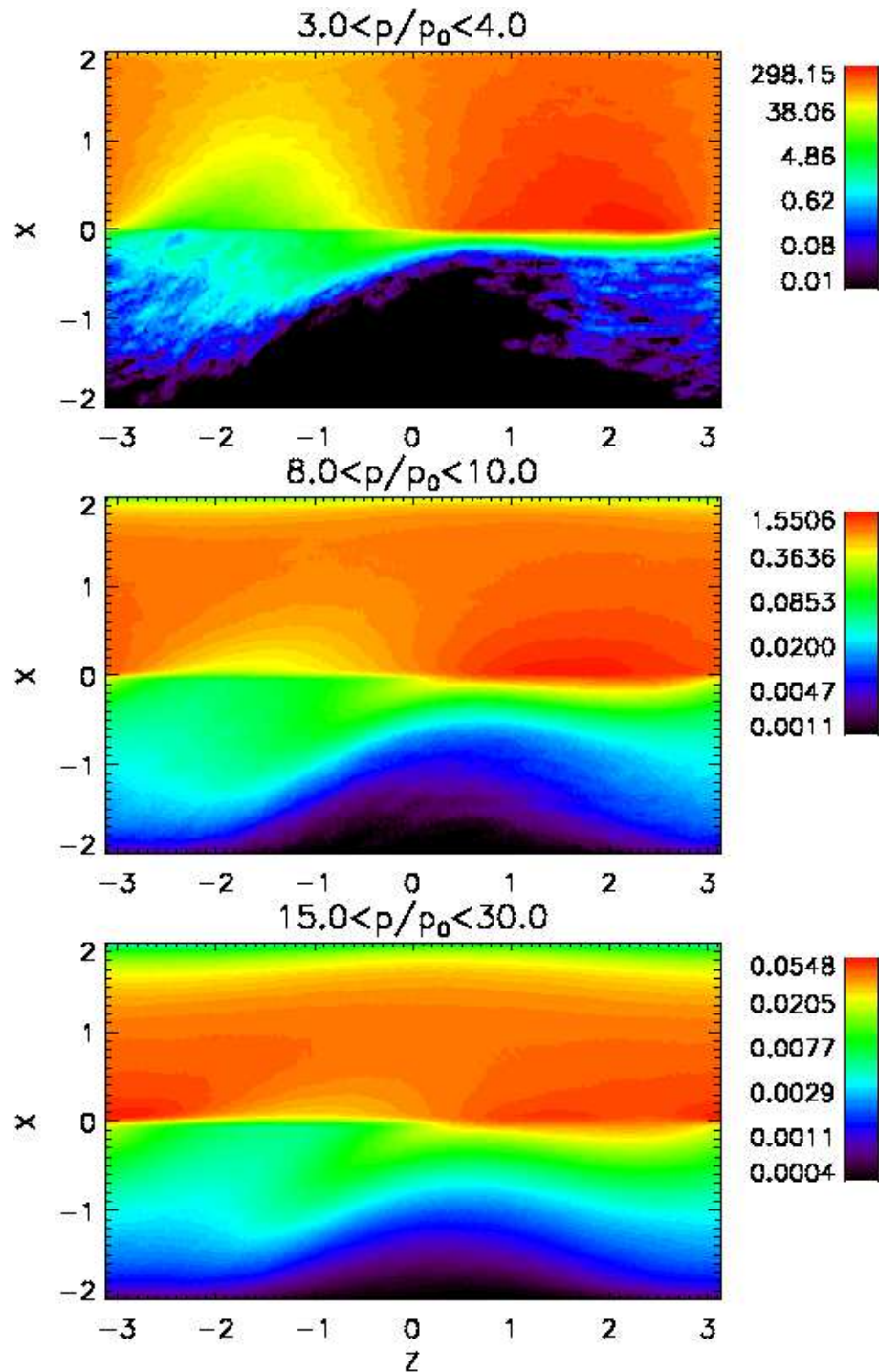


Figure 3.31: The density contour of accelerated particles for the case of oblique shock and $\delta B/B_0 = 0.5$, for energy range: $3.0 < p/p_0 < 4.0$ (top), $8.0 < p/p_0 < 10.0$ (middle), $15.0 < p/p_0 < 30.0$ (bottom).

field variation. This simple model allows a detailed examination of the physical effects. As the magnetic field lines pass through the shock, the connection points between field lines on the shock surface will move accordingly. We find that the region where connection points approaching each other will trap and preferentially accelerate particles to high energies and form “hot spots” along the shock surface, somewhat in analogy to the “hot spots” postulated by Jokipii & Kóta (2008). The shock acceleration will be suppressed at places where the connection points move apart each other. Some of the particles injected in those regions will transport to the “hot spots” and get further accelerated. The resulting distribution function is highly spatially dependent at the energies we studied, which could give a possible explanation to the *Voyager* observation of anomalous cosmic rays. Although we have discussed a simplified, illustrative model, the resulting spectra and radial distributions show qualitative similarities with the *in situ Voyager* observations. In Figure 3.32 we compare a spatial profile of energetic particle intensity obtained in our simulation and the time profile observed by *Voyager 1* as it passed the termination shock and entered into the heliosheath. One can see that our simulation qualitatively agree with the observation. This mechanism gives an interpretation for the observation that the ACR intensity did not saturate at the termination shock.

Thus, the intensities do not in general, peak at the the shock and the energy spectra are not power laws. We show that this process is robust even for the case of oblique shocks with relatively small magnetic field variations. Large scale magnetic field variation, which could be due to magnetic structures like magnetic clouds, or the ubiquitous large scale field line random walk, will strongly modify the simple planar shock solution. This effect could work in a number of situations for large scale shock acceleration including magnetic variations, for example, the solar wind termination shock and supernova blast waves.

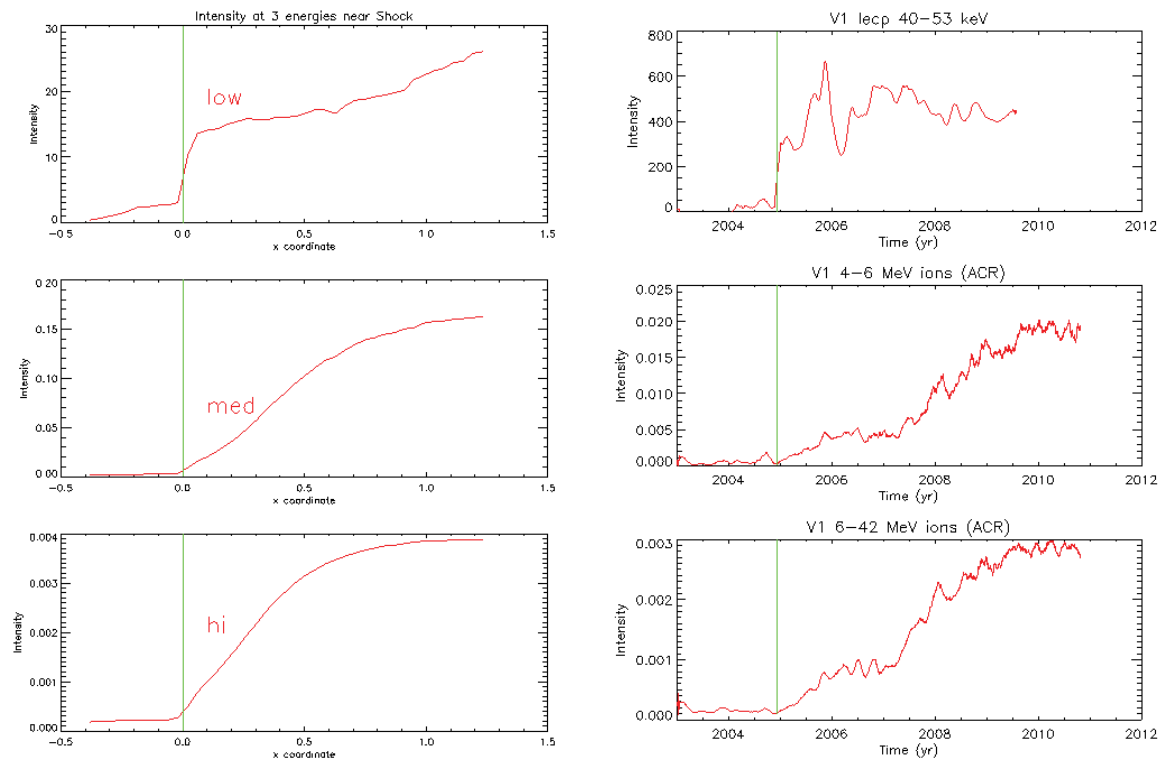


Figure 3.32: A comparison between a spatial profile for the density of energetic particles picked from the numerical simulation and observation made by *Voyager 1*.

CHAPTER 4

The Acceleration of Electrons at Collisionless Shocks

4.1 Overview

As we discussed in Section 1.2 and Section 3.1, collisionless shocks are efficient accelerators for a variety of energetic charged particles observed in the heliosphere. However, the acceleration of electrons at collisionless shocks is generally considered to be more difficult than that of ions. This is primarily due to the fact that the gyro-radii of non-relativistic electrons are much smaller compared with that of protons of the same energy (by a factor of $\sqrt{m_i/m_e} \sim 43$), therefore low-energy electrons cannot resonantly interact with the large-scale magnetic turbulence or ion-scale waves close to the shock front. Despite the theoretical difficulties, energetic electrons are commonly observed in SEP events. The accelerated electrons are usually observed to be associated with quasi-perpendicular shocks in interplanetary shocks and planetary bow shocks (e.g., Anderson et al., 1979). The acceleration of electrons remains poorly understood.

In this chapter we study numerically the acceleration of low-energy electrons at shocks that propagate through turbulent magnetized media, using a combination of hybrid simulations (kinetic ions, fluid electron) and test-particle electron simulations. We find that the acceleration of electrons is greatly enhanced due to the effect of large-scale magnetic turbulence, which provides a mechanism for accelerating electron to high energy and injecting electrons into the diffusive shock acceleration (DSA).

We first review the observations of energetic electrons related to collisionless shocks in Section 4.2. Then we give an introduction for the previous theoretical works on the acceleration of electrons in Section 4.3. In Section 4.4 we discuss the numerical method used in this study. Section 4.5 presents the results on elec-

tron acceleration at a shock propagating through a turbulent magnetic field. The parameters are similar to observations of electrons associated with interplanetary shocks and also the solar wind termination shock. The results can also be used to understand the acceleration of electrons at CME-driven shocks. Section 4.6 presents the numerical results with parameters similar to solar flare region. We discuss and conclude the results in Section 4.7.

4.2 Observations of Energetic Electrons Associated with Shock Waves

Energetic electrons are often observed to be associated with collisionless shocks. At the terrestrial bow shock and interplanetary shocks, electrons with energy up to ~ 100 keV are often observed close to quasi-perpendicular shocks (Fan et al., 1964; Anderson et al., 1979; Gosling et al., 1989; Oka et al., 2006), i.e., the angle between the incident magnetic field vector and the shock normal θ_{Bn} is larger than 45° . Anderson et al. (1979) showed the *ISEE* spacecraft measurements of upstream electrons (> 16 keV) at the Earth's bow shock that originated from a thin region close to the point of tangency between interplanetary magnetic field lines and the shock surface. Gosling et al. (1989) pointed out that the accelerated superthermal electrons were often seen close to perpendicular shocks or quasi-perpendicular shocks, rather than in the vicinity of parallel shocks. The energy spectra of electrons close to shocks appear to follow a power law with a slope index between -3 to -4 . Tsurutani & Lin (1985) reported the observations of energetic electrons associated with interplanetary shocks showing “spike-like” flux enhancements for energies > 2 keV. The spike events were observed at quasi-perpendicular shocks with $\theta_{Bn} \geq 70^\circ$. Some shock crossings had no enhancements of energetic electrons that were reported to be associated with low shock speeds and/or small θ_{Bn} . Simnett et al. (2005) have presented data showing that energetic electrons (~ 50 -100 keV) are accelerated close to interplanetary shocks. They also showed that some accelerated electrons can escape far upstream of a nearly perpendicular interplanetary shock. The clear evidence of electron acceleration at interplanetary shocks by DSA is rare, but a recent example

discussed by Shimada et al. (1999) shows evidence of the importance of whistler waves (a high frequency wave that can resonantly interact with low-energy electrons) close to a quasi-perpendicular shock. The observation by *Voyager 1* at the termination shock showed a spike-like enhancement of energetic electrons (Decker et al., 2005). *Voyager 2* observed an exponential increase upstream of the termination shock and roughly constant downstream in the heliosheath, similar to what is predicted from DSA (Decker et al., 2008). Both of the *Voyager* spacecraft have observed that electrons are accelerated to at least MeV range, indicating that the termination shock can efficiently accelerate electrons.

Bale et al. (1999) and Pulupa & Bale (2008) observed electron foreshocks and related Langmuir waves upstream of interplanetary shocks. These events appeared to be associated with irregular shock surfaces with spatial scales $\sim 2 \times 10^5$ km. They proposed that the complex upstream electron events result from large-scale irregularities in the shock surface. The large-scale ripples have been detected using multiple spacecraft observations (Neugebauer & Giacalone, 2005; Koval & Szabo, 2010) and the magnitude of radii of curvature is in the range of 3×10^5 to 10^7 km with an average of 3.5×10^6 km, similar to the correlation length of the interplanetary turbulence (e.g., Coleman, 1968).

In solar energetic particles (SEPs) that originate from CME-driven shocks or solar flares, electrons are frequently observed to be accelerated to 10 keV - 1 MeV. It is important to point out that in SEP events, the electrons and ions are often observed to have tight correlations (Posner, 2007; Cliver, 2009; Haggerty & Roelof, 2009). For example, Haggerty & Roelof (2009) reported that 175-315 keV electrons are well associated with 1.8-4.7 MeV protons. Cliver (2009) showed that the electrons (~ 0.5 MeV) and the protons (> 10 MeV) in large SEP events are strongly correlated. The correlation depends weakly on isotope ratio (Fe/O), which indicates that the effect of source regions on the electron-proton correlation is not important. The tight correlation between electrons and ions has also been found in ground base level events (Tylka, private communication), where both electrons and protons are accelerated to relativistic energies. These observations indicate that a common

mechanism may exist in the process of particle acceleration during SEP events. The accelerated electrons are believed to produce type II and type III radio bursts in the solar corona and interplanetary space (Nelson & Melrose, 1985), which provides a remote probe for electron acceleration. Herringbone structures featured by fast electron speeds are often observed in type II radio bursts, which indicates that electrons are accelerated to about 20 – 200 keV at CME-driven shocks (Roberts, 1959; Cairns & Robinson, 1987; Cane & White, 1989).

In solar flares, the acceleration of electrons can be observed remotely since the accelerated electrons are subjected to several radiation processes. Hard X-ray emissions produced by superthermal electrons above magnetic loops have been observed (Masuda et al., 1994; Krucker et al., 2010) and may be associated with flare termination shocks (Forbes, 1988; Shibata et al., 1995). Using the emissions from neutron-capture γ -ray line and electron bremsstrahlung, Shih et al. (2009) have shown that the emissions of > 30 MeV protons and that of > 0.3 MeV electrons are proportional to each other. Again, this indicates that the electrons and ions are accelerated by closely related mechanisms.

In astrophysical shocks, electrons are observed to be accelerated to very high energies (may reach 10^{15} eV) and produce strong synchrotron emissions in the existence of magnetic fields (Reynolds et al., 2011). At those energies, the electrons are ultra-relativistic and their gyroradii are virtually the same as protons of the same energy. In that situation, both the acceleration of electrons and that of protons may be considered to be DSA.

As a summary, there is plenty of evidence of energetic electrons associated with fast shock waves. Observations suggest that accelerated electrons are more associated with oblique shocks and rarely seen at parallel shocks. Compared to ions, energetic electrons are more-easily to excite electromagnetic radiation (radio bursts, bremsstrahlung emission, and synchrotron radiations, etc.), which can be used as remote tracers for energetic electrons. In many situations, electron acceleration and ion acceleration are observed to be correlated, which may give a constraint to the acceleration mechanism.

4.3 Review of Previous Theoretical Works

In order to explain the energization of electrons within the shock layer, Holman & Pesses (1983); Wu (1984) and Leroy & Mangeney (1984) developed analytic models for electron acceleration from thermal energies by adiabatic reflection off a quasi-perpendicular shock. This is usually referred to as shock drift acceleration (SDA) or fast-Fermi acceleration. The theory describes a scatter-free electron acceleration process in a planar, time-steady shock. It obtains a qualitative agreement with observations at Earth's bow shock in terms of the loss-cone pitch-angle distribution and energy range of accelerated electrons. Krauss-Varban et al. (1989) used the combination of electron test-particle simulation and 1-D hybrid simulation and verified Wu's basic conclusions. The main energy source of fast Fermi acceleration comes from the $-\mathbf{V} \times \mathbf{B}/c$ electric field that is the same as shock drift acceleration (Armstrong et al., 1985). It can be demonstrated that fast-Fermi acceleration and SDA are the same process in two different frames of reference (Krauss-Varban & Wu, 1989). Thus one would expect electrons to drift in the direction perpendicular to the flow and magnetic field during the acceleration at the shock front.

However it is commonly known that in this process both the fraction and attainable energy of the accelerated particles are limited (e.g., Ball & Melrose, 2001). This cannot explain the observed high-energy electron. For example, observations at Earth's bow shocks (Gosling et al., 1989) suggested that the accelerated electrons have a power law distribution with an exponential drop, which cannot be produced by this simple mechanism. In a recent work, Pulupa et al. (2012) presented a comparison between the STEREO measurements of electron acceleration at Earth's bow shock and the theory of adiabatic fast-Fermi acceleration (Wu, 1984). It is clear that the fast-Fermi acceleration fails to predict the observed energetic electrons in both the accelerated fraction and spectrum shape. Herringbone structures observed in Type II burst (Cairns & Robinson, 1987) require a high electron energy, and the energetic electrons cannot be produced by fast Fermi acceleration unless electrons are extremely hot.

Some recent progress in shock acceleration is the consideration of nonplanar effects such as shock ripples and magnetic turbulence. The simulations by Burgess (2006) and Umeda et al. (2009) show that small-scale shock ripples can be important in scattering the electrons and facilitating the acceleration. Savoini et al. (2010) discussed the non-adiabatic motion of electrons. Recently, Jokipii & Giacalone (2007) proposed a novel mechanism to solve the injection problem that does not require strong pitch-angle scattering from small-scale fluctuations. The low-energy particles can move along the meandering field lines of force, travel back and forth across a shock front, therefore gain energy from the difference between upstream and downstream flow velocities. In this study (Section 4.5 and Section 4.6), using self-consistent hybrid simulations combined with test-particle simulation for electrons, we have found that efficient electron acceleration can happen after considering large-scale pre-existing upstream magnetic turbulence. The turbulent magnetic field leads to field-line meandering that allows the electrons to get accelerated at a shock front multiple times. The shock surface becomes irregular on a variety of spatial scales from small-scale ripples due to ion-scale plasma instabilities (Lowe & Burgess, 2003), to large-scale structures caused by the interaction between the shock and upstream turbulence (Giacalone & Neugebauer, 2008; Lu et al., 2009). The rippled surface of the shock front also contributes to the acceleration by mirroring electrons between the ripples. The observational evidence of these large-scale ripples has been shown by a number of authors (Neugebauer & Giacalone, 2005; Bale et al., 1999; Pulupa & Bale, 2008; Koval & Szabo, 2010). These results, along with the previous work on acceleration of ions (Giacalone, 2005a,b), suggest that large-scale turbulence has an important effect on the acceleration of both electron and ions at shocks, which is consistent with the correlation between ions and electrons in solar energetic particle events (e.g., Haggerty & Roelof, 2009; Cliver, 2009).

Another scenario that solves this injection problem relies on small-scale waves excited close to the shock front. Levinson (1992, 1994) has proposed an analytical theory for thermal electron injection due to whistler waves excited by electrons streaming upstream. In this theory efficient electron acceleration requires large

Mach numbers $M_A \sim 43/\sqrt{\beta_e}$, where β_e is the ratio of thermal electron pressure to magnetic pressure inside the shock. This condition is rarely satisfied for shocks in the heliosphere. Amano & Hoshino (2007) proposed “electron surfing acceleration” where electron can reach efficient acceleration by being trapped in electrostatic solitary waves. This mechanism also requires a relative high mach number shock (Alfven mach number M_A is greater than 14). Recently, Riquelme & Spitkovsky (2011) used full particle simulations to study electron acceleration at oblique shocks. For the parameters they use, they find that efficient nonthermal electron acceleration when electrons are scattered by oblique whistler waves at a $M_A \sim 7$ quasi-perpendicular shock. However, these full particle simulations generally use unrealistic mass ratio m_i/m_e and the ratio between the speed of light and thermal speed c/V_{the} , which may produce some artificial effects. In fact in the simulations they find the electrons are heated at the shock layer to a temperature the same as that of protons (Riquelme & Spitkovsky, 2011). This is not consistent with in situ observations at interplanetary shocks and the relevant theoretical works (Thomsen et al., 1987; Schwartz et al., 1988; Scudder, 1995), in which the the heating of electrons at shocks is significantly less than that of ions (Thomsen et al., 1987; Schwartz et al., 1988; Scudder, 1995). The effect of whistler waves for electron acceleration at shocks still remains to be clarified.

4.4 Numerical Method

Investigating the motion of charged particles in the vicinity of a collisionless shock requires a spatial scale large enough for particles to travel back and forth across the shock, and a spatial resolution small enough to include the detailed physics for particle scattering and shock microstructure. We implement a combination of a 2-D hybrid simulation to model the fields and plasma flow and a test particle simulation to follow the orbits of a large number of energetic electrons. In the first step, we employ a two-dimensional hybrid simulation (Giacalone, 2005b) that includes pre-existing large-scale turbulence. In the hybrid simulation (e.g., Winske & Quest,

1988), the ions are treated fully kinetically and the thermal (i.e., non-energetic) electrons are treated as a massless fluid. This approach is well suited to resolve ion-scale plasma physics that is critical to describe supercritical collisionless shocks. We consider a two-dimensional Cartesian grid in the $x - z$ plane. All the physical vector quantities have components in three directions, but depend spatially only on these two variables. A shock is produced by using the so-called piston method (for a discussion, see Jones & Ellison, 1991), in which the plasma is injected continuously from one end ($x = 0$, in our case) of the simulation box, and reflected elastically at the other end ($x = L_x$). This boundary is also assumed to be a perfectly conducting barrier. The pileup of density and magnetic field creates a shock propagating in the $-x$ direction. To include the effect of large-scale magnetic fluctuations, a random magnetic field is superposed on a mean field at the beginning of the simulation and is also injected continuously at the $x = 0$ boundary during the simulation. The simplified one-dimensional fluctuations have the form $\mathbf{B}(z, t) = \delta\mathbf{B}(z, t) + \mathbf{B}_1$, where \mathbf{B}_1 is the averaged upstream magnetic field. The fluctuating component contains an equal mixture of right- and left-hand circularly polarized, forward and backward parallel-propagating plane Alfvén waves. The amplitude of the fluctuations at wave number k is determined from a Kolmogorov-like power spectrum:

$$P(k) \propto \frac{1}{1 + (kL_c)^{5/3}}, \quad (4.1)$$

in which L_c is the coherence scale of the fluctuations. For the simulations presented in this study, we take $L_c = L_z$, which is the size of simulation box in the z -direction. Note that in addition to magnetic fluctuations, there are also velocity perturbations with $\delta\mathbf{v} = v_{A1}\delta\mathbf{B}/B_1$ (Alfvén waves). Different from previous studies, the consideration of large-scale magnetic fluctuations enables us to consider the effect of pre-existing magnetic turbulence on electron acceleration, which has been shown to be important for low-energy ion acceleration (Giacalone, 2005a,b) since particle transport normal to the mean field is enhanced. However, particle transport in full 3-D turbulence cannot be properly treated in a self-consistent way using available

computation. As demonstrated by previous work (Jokipii et al., 1993; Giacalone & Jokipii, 1994; Jones et al., 1998), in the model with at least one ignorable coordinate, the center of gyration of particles is confined to within one gyroradius of the original magnetic field line. The test-electrons can still move normal to the mean field in our model because of the field-line random walk.

In the second part of our calculation we integrate the full motion equation of an ensemble of test-particle electrons in the electric and magnetic fields obtained in the hybrid simulations (see Figure 4.1). This part of the calculation is done separately from the main hybrid simulation as a post processing phase. As noted by Krauss-Varban et al. (1989), high-order interpolation of fields is required to ensure numerical accuracy and avoid artificial scattering in calculating electron trajectories. In this work we use a second-order spatial interpolation and a linear temporal interpolation, which ensure the smooth variations of the electromagnetic fields. The test-particle electrons are released uniformly upstream when the shock has fully formed and is far from the boundaries. The numerical technique used to integrate electron trajectories is the so-called Bulirsch-Stoer method, which is described in detail by Press et al. (1986). It is highly accurate and conserves energy well. It is fast when fields are smooth compared with the electron gyroradius. The algorithm uses an adjustable time-step method based on the evaluation of the local truncation error. The time step is allowed to vary between 5×10^{-4} and $0.1\Omega_{ce}^{-1}$, where Ω_{ce} is the electron gyrofrequency. The ratio Ω_{ce}/Ω_{ci} is taken to be the realistic value 1836. The total number of electrons in the simulation is 1.6×10^6 . The electrons that reach the left or right boundary are assumed to escape from the shock region and are removed from the simulation. The boundary condition in the z direction is taken to be periodic. The readers are referred to (Burgess, 2006) for more details on the numerical methods.

Magnetic field turbulence has already proved to have key effects on the particle acceleration in collisionless shocks. Unfortunately, solving the whole problem in three-dimensional space and resolving magnetic turbulence from coherence scale to electron scale are still limited by available computation in the near future. This

limitation motivates us to solve these problems approximately. We also note that in our model the electron test-particle simulation is not self-consistent since the hybrid simulation does not include the electron scale physics. The electron scale shock structure may be important but is neglected here.

4.5 The Effect of Large-Scale Magnetic Turbulence on the Acceleration of Electrons: Interplanetary Shocks

Much of this section has been published in the *Astrophysical Journal* (Guo & Giacalone, 2010).

4.5.1 Initial Condition and Parameters

In this section we use the numerical method described in Section 4.4 to study the acceleration of electrons at a shock that propagates through a turbulent magnetic field. The parameters are similar to interplanetary shocks and the solar wind termination shock. For most part of this study, we consider a turbulence variance $\sigma^2 = \delta B^2/B_1^2 = \delta v^2/v_{A1}^2 = 0.3$, where δv and v_{A1} are the magnitude of velocity perturbation and upstream Alfvén speed, respectively. We also discuss the effect of different values of turbulence variances. The size of the simulation box for most of situations is $L_x \times L_z = 400c/\omega_{pi} \times 1024c/\omega_{pi}$, where c/ω_{pi} is the ion inertial length. We also examine the effect of different size of simulation box. The Mach number of the flow in the simulation frame is $M_{A0} = 4.0$ and the averaged Mach number in the shock frame is about 5.6. Most of the results presented here are for the averaged shock normal angle $\langle \theta_{Bn} \rangle = 90^\circ$, but we also simulate the cases for $\langle \theta_{Bn} \rangle = 60^\circ$ and 75° to examine the dependence of the acceleration efficiency on shock normal angle. The other important simulation parameters include electron and ion plasma beta $\beta_e = 0.5$ and $\beta_i = 0.5$, respectively, grid sizes $\Delta x = \Delta z = 0.5c/\omega_{pi}$, time step $\Delta t = 0.01\Omega_{ci}^{-1}$, the ratio between light speed and upstream Alfvén speed $c/v_{A1} = 8696.0$, and the anomalous resistivity is taken to be $\eta = 1 \times 10^{-5}4\pi\omega_{pi}^{-1}$. The initial spatially uniform thermal ion distribution was generated using 40 particles

per cell. Under these parameters, the upstream Alfvén speed is about 34.5 km/s and the shock speed is about 193 km/s in upstream frame.

We assume non-relativistic motion that is reasonable because the highest energy electrons obtained in our study are still non-relativistic. We release a shell distribution of electrons with energy of 100 eV, which corresponds to an electron velocity $V_e = 30.7U_1 = 5.7v_{the}$ in the upstream frame, where U_1 is upstream bulk velocity in the shock frame and v_{the} is the thermal velocity of fluid electrons considered in the hybrid simulations. This energy is typical for the halo component of electron velocity distributions observed in the solar wind.

4.5.2 Simulation Results for the Acceleration of Electrons

Figure 4.1 shows a snapshot of the z component of the magnetic field, B_z/B_1 , at time $110\Omega_{ci}^{-1}$ in a color-coded contour. At this time, the shock is fully developed. In this case, the angle between the average magnetic field direction and shock normal, $\langle\theta_{Bn}\rangle$ is 90° . The position of the shock front is clearly seen from the boundary of the magnetic field jump. The shock is moving in the $-x$ direction at a speed dependent on z , which is about $1.6 v_{A1}$ on average. On the right bottom a small region of the simulation domain is zoomed in, which shows small-scale irregularities at shock front. Because of the effect of large-scale turbulence with the shock, the shock surface becomes irregular on a variety of spatial scales from small-scale ripples, which could be due to ion-scale plasma instabilities (Lowe & Burgess, 2003), to large-scale structure caused by the interaction between the shock and upstream turbulence (Neugebauer & Giacalone, 2005; Giacalone & Neugebauer, 2008; Lu et al., 2009). Locally, the structure of the shock, shown in top right panel, is still clearly a quasi-perpendicular shock. The upstream magnetic field is compressed and distorted as it passes through the shock into the downstream region. We note that the rippling of the shock and varying upstream magnetic field leads to a varying local shock normal angle along the shock front. As we will discuss later, the irregular shock surface and magnetic field geometry will efficiently accelerate electrons and produce a number of features similar to observations, such as the electron foreshock and

spike-like intensity increases at the shock front. The meandering of field lines close to the shock surface helps to trap the electrons at the shock, leading to efficient acceleration. The shock ripples also contribute to the acceleration by mirroring electrons between them.

Figure 4.2 shows a color-coded representation of the number of energetic electrons with energies higher than 10 times (i.e., 1 keV) the initial (at release) energy at three different times (a) $76\Omega_{ci}^{-1}$, (b) $81\Omega_{ci}^{-1}$, and (c) $90\Omega_{ci}^{-1}$. It is found that after the initial release, a fraction of the electrons are reflected and accelerated at the shock front, and then travel upstream along the turbulent magnetic field lines. These accelerated electrons are then taken back to the shock by the field line meandering, which provides even further acceleration. The number of energetic electrons close to the shock surface is highly irregular because the acceleration efficiency varies along the shock front depending on the local shock normal angle (Wu, 1984). Most of the electrons concentrate near the shock front since the global magnetic field is mostly perpendicular to the shock normal. As the field lines convect through the shock, the electrons eventually are taken downstream. Since the electrons are tied to individual field lines in 2-D magnetic field, once the electrons are no longer capable of crossing the shock, there will be no additional significant acceleration. At this point, once all electrons are downstream, the energy spectrum no longer changes with time.

Examination of the trajectories of some electrons shows that the rippling of the shock front also contributes to the acceleration by mirroring electrons between the ripples, as illustrated in Figure 4.3. In this figure, the top left plot displays the trajectory of a representative electron in the x - z plane, overlapped with the 2-D gray-scale representation of B_z at $\Omega_{ci}t = 89.0$, the gray scale is the same as in Figure 4.1. The upper right plot shows the position of this electron (in x) as a function of time. The electron bounces back and forth between the ripples for several times. For example, the reflections are labeled a - b , c , d , f - g , h , and j . The energy change as a function of position, x , corresponding to these reflections is shown in the bottom left panel. We find that there are jumps in energy at each of the reflections. The panel on the bottom right shows the electron energy as a function of time that also

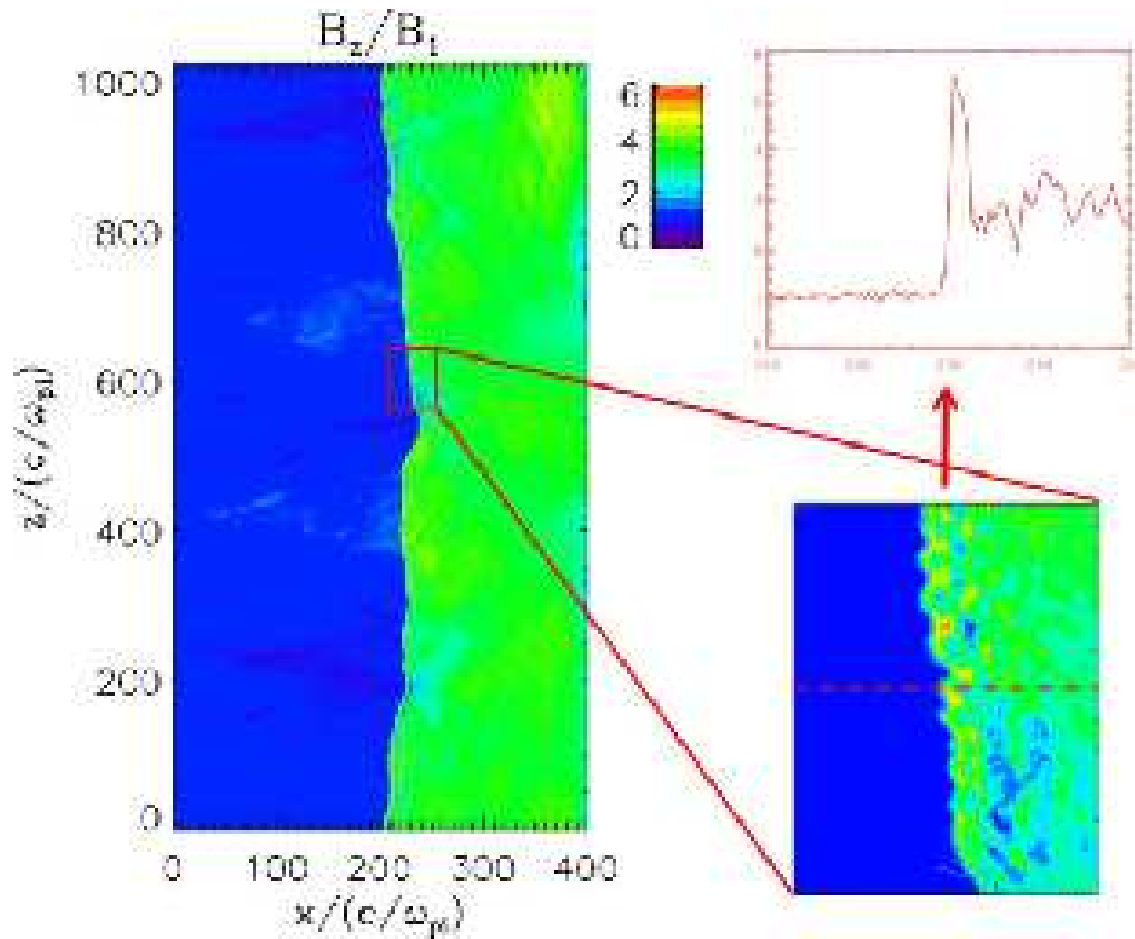


Figure 4.1: A snapshot of the magnetic field in the z -direction B_z/B_1 represented in color-coded scale at $t = 110\Omega_{ci}^{-1}$, where B_1 is the averaged upstream magnetic field strength. A region at the shock front is zoomed in on the right bottom and a profile is illustrated on the right upper panel. The shock surface is shown to be rippled and irregular in different scales.

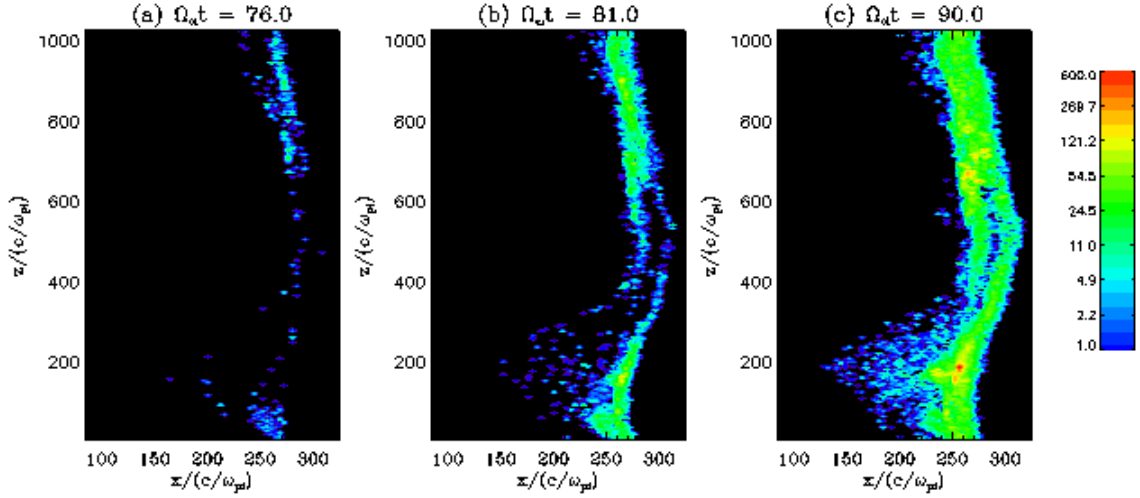


Figure 4.2: The number of energetic electrons with energies $E > 10E_0$, the initial release energy $E_0 = 100$ eV, at (a) $\Omega_{ci}t = 76$, (b) $\Omega_{ci}t = 81$, and (c) $\Omega_{ci}t = 90$, respectively. Initial electrons are released uniformly upstream at $\Omega_{ci} = 70$.

illustrates the features of multiple accelerations related to multiple reflections. The trajectory analysis shows that the electron will be mirrored between the ripples and get accelerated multiple times. Note that the shock does not move much during the time scale of this trajectory.

We now consider the effect of varying the angle between the mean magnetic field and shock-normal. Shown in Figure 4.4 are the resulting energy spectra for three different mean shock-normal angles ($\langle \theta_{Bn} \rangle = 60^\circ, 75^\circ$, and 90° , respectively) at the end of simulations ($\Omega_{ci}t = 120.0$). It is found that for $\langle \theta_{Bn} \rangle = 90^\circ$, the electrons can be readily accelerated to up to 200 – 300 times the initial energy within $50\Omega_{ci}^{-1}$. The spectrum is flat between about 0.1 keV to 0.7 keV. This shape is similar to the “plateau” structure discussed by Burgess (2006). Above 1 keV, the spectrum falls off with energy with a slope index about -3 . It can be found that both the number fraction and highest energy of accelerated particles decrease as $\langle \theta_{Bn} \rangle$ decreases. We have also tried different values of initial energies (not shown), and find that the acceleration efficiency decreases for electrons with higher initial energies, which is similar to the results of (Burgess, 2006).

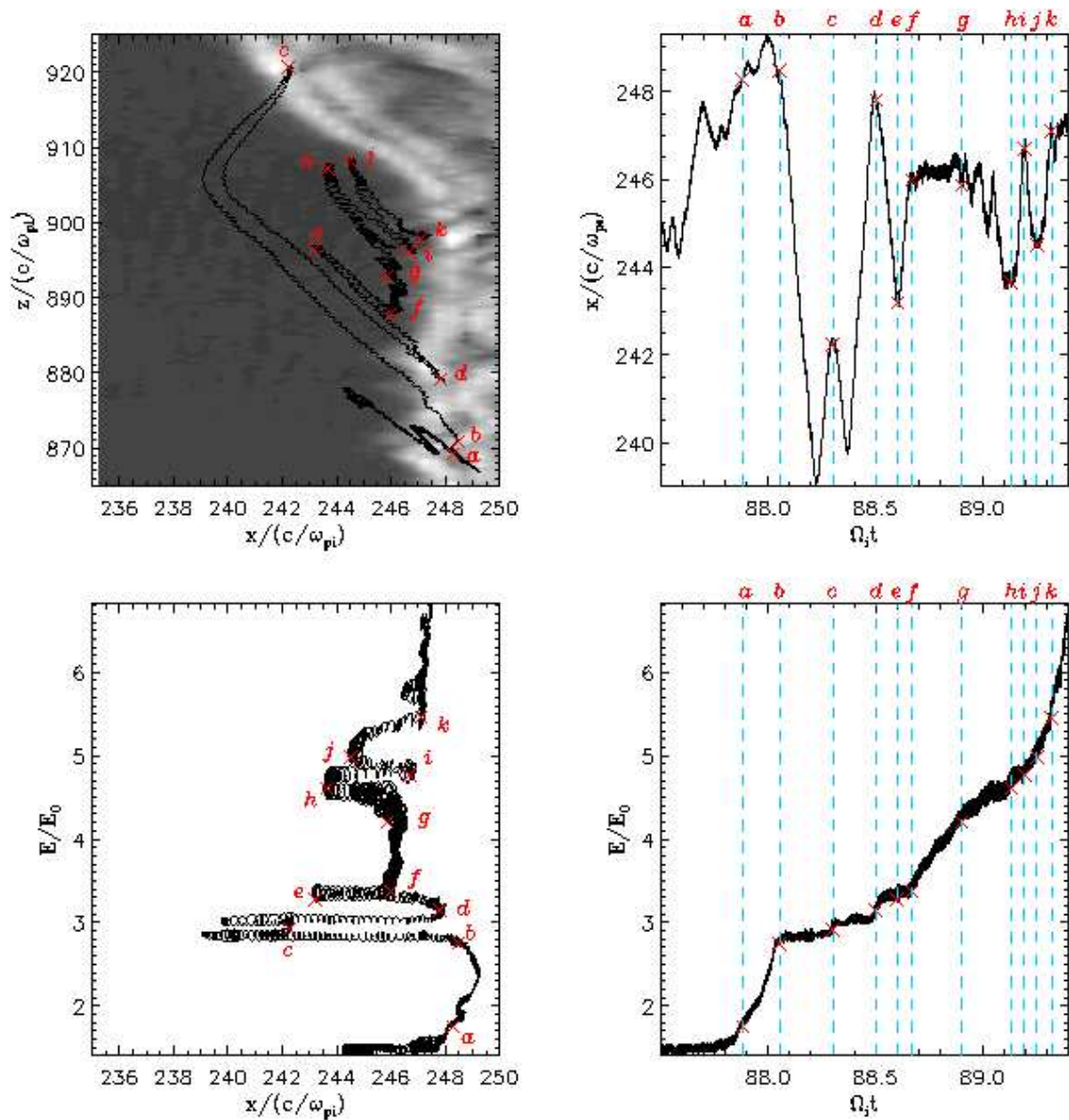


Figure 4.3: A typical electron trajectory analysis that shows acceleration by multiple mirroring between ripples. The top left panel displays the trajectory of the representative electron in x - z plane, overlapped with contour of B_z magnetic field where the gray-scale is the same as that in Figure 1; The top right panel shows the position of the electron in x coordinate as a function of time; The bottom left panel illustrates the energy of the representative electron E/E_0 as a function of x ; The bottom right panel shows the dependence of electron energy E/E_0 on time.

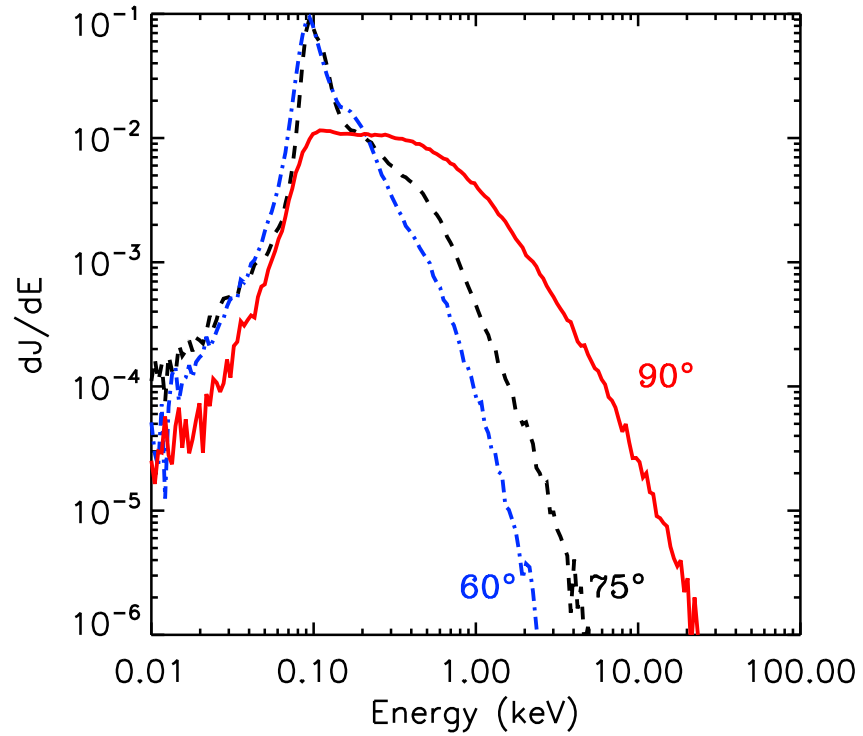


Figure 4.4: The energy flux spectrum of electrons at $\Omega_{ci}t = 120$ for different averaged shock normal angles. The red solid line is for the case with shock angle $\langle \theta_{Bn} \rangle = 90^\circ$, the blue dot dashed line and the black dashed line are for the cases with $\langle \theta_{Bn} \rangle = 60^\circ$ and 75° , respectively.

The effect of varying level of magnetic turbulence variance is examined in Figure 4.5. We compare three cases with different turbulence variances $\sigma^2 = 0.1, 0.3,$ and $0.5,$ respectively. At the end of simulations, the final energy spectra are similar at low energies, with significant variations in the spectra only at energies higher than 2 keV. It is found that the energy spectrum is hardened at high energies when the turbulence variance is largest, which indicates that the large-scale turbulence is more important for accelerating electrons to high energies. We argue that collisionless shocks that move through magnetic turbulence with significant power leads to efficient electron acceleration to high energies since the motion normal to the shock front is enhanced. The reason is that the meandering of field lines is enhanced, which allows the electrons to have a better chance to travel through the shock multiple times.

We examine the effect of different turbulence correlation lengths in Figure 4.6. We compare three cases with different sizes of simulation box $L_z = 2000, 1024,$ and $400c/\omega_{pi},$ respectively. In each case, the correlation length is made to be the same as the size of the simulation box in z -direction $L_c = L_z.$ It is shown that for the case $L_c = L_z = 2000c/\omega_{pi},$ more electrons are accelerated to high energy. In the case of $L_c = L_z = 400c/\omega_{pi},$ less electrons are accelerated and the highest energy is less than the other two cases. The more efficient acceleration for the case that L_c is larger can also be understood as the motion of particle normal to the shock front is more enhanced. As derived by Jokipii and Parker (1969), large-scale magnetic fluctuation dominate the random walk of magnetic field lines and can be expressed as

$$\frac{\langle \Delta x^2 \rangle}{\Delta z} = \frac{P(k=0)}{B_0^2}, \quad (4.2)$$

where Δx and Δz represent the displacement of a field line in the direction transverse and along the mean magnetic field, respectively. $P(k=0)$ represents spectral power at wave number $k=0.$ Although we use a restricted simulation box, our simulation is qualitatively consistent with this picture. In figure 4.7 we plot three magnetic field

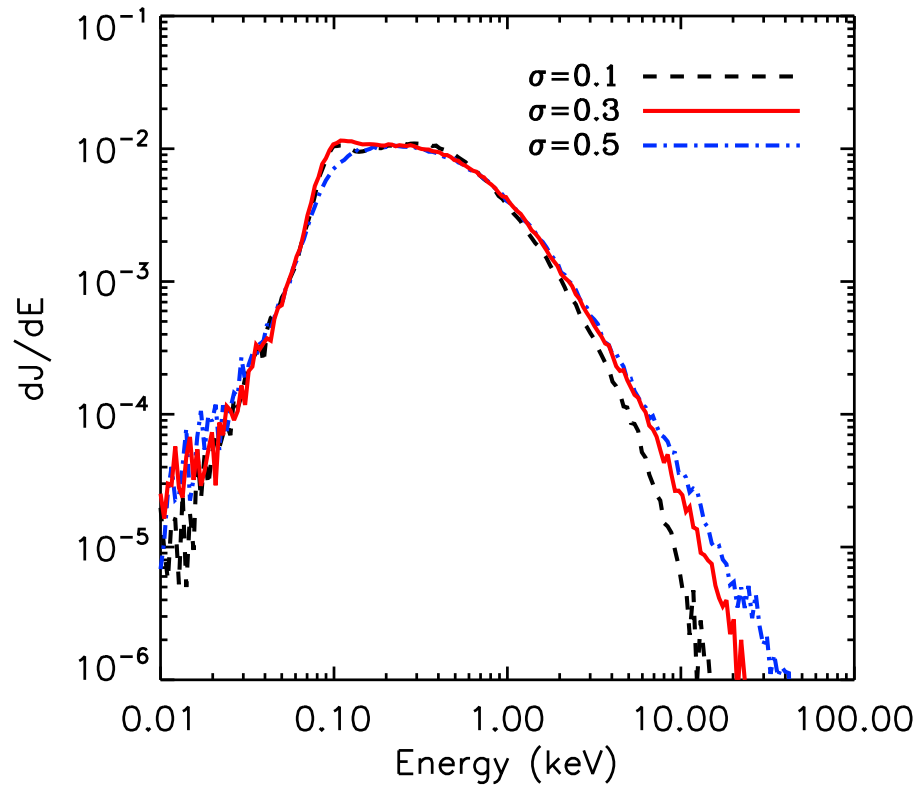


Figure 4.5: The energy flux spectra of electrons at $\Omega_{cit} = 120$ for an averaged perpendicular shock with different turbulence variances. The black dashed line, red solid line, and blue dot dashed line are in the cases that $\sigma^2 = 0.1, 0.3,$ and $0.5,$ respectively.

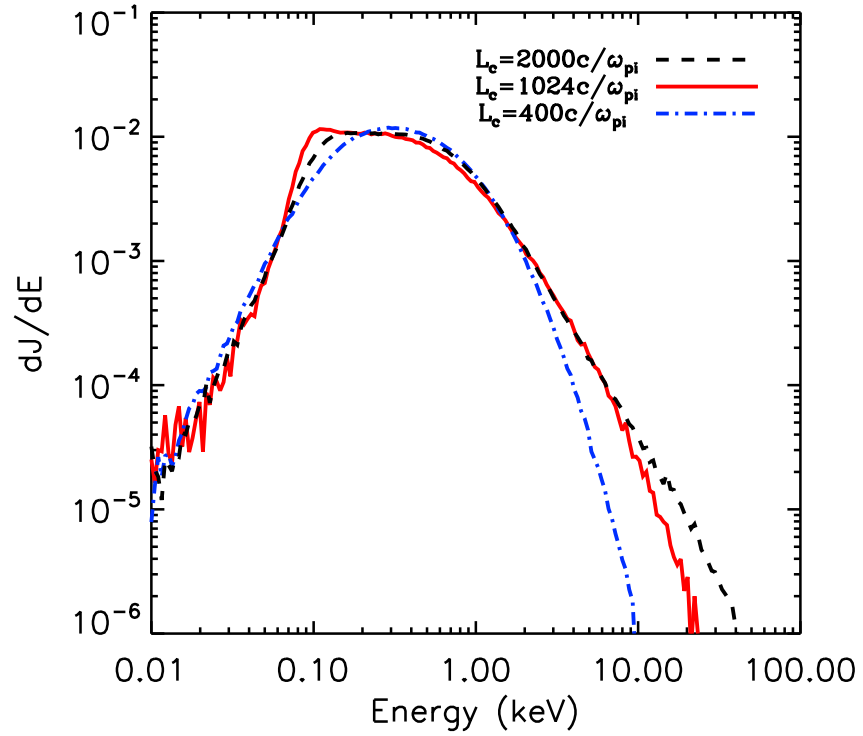


Figure 4.6: The energy flux spectrum of electrons at $\Omega_{pi}t = 120$ for averaged perpendicular shock with different turbulence coherence lengths. The black dashed line, red solid line, and blue dot dashed line are in the cases that $L_c = 2000c/\omega_{pi}$, $1000c/\omega_{pi}$, and $400c/\omega_{pi}$, respectively.

lines generated from magnetic turbulence in the cases of three different coherence lengths. In this plot the horizontal axis x represents the spatial distance transverse to mean magnetic field with a plot range from $-1000c/\omega_{pi}$ to $1000c/\omega_{pi}$, and the vertical axis z represents the spatial distance along the mean magnetic field. In order to show the difference between these field lines, the spatial range for z axis is changing for different field lines. In the three cases of $L_c = 14000c/\omega_{pi}$ (blue dashed line), $L_c = 2000c/\omega_{pi}$ (red dotted line) and $L_c = 400c/\omega_{pi}$ (black solid line), the spatial ranges in z direction are made to be $0 - 14000c/\omega_{pi}$, $0 - 2000c/\omega_{pi}$ and $0 - 400c/\omega_{pi}$, respectively. One can see that the x -direction displacement of the field line in the case of $L_c = 14000c/\omega_{pi}$ is much more enhanced compare to the case of $L_c = 400c/\omega_{pi}$. Because the limited computational resource, the largest simulation is made to be $L_c = L_z = 2000c/\omega_{pi}$, whereas for typical interplanetary parameters, this value is about $14000c/\omega_{pi}$ (0.01 AU).

The idea of field line random walk (and its related large-scale irregular shock surface) is also useful for interpreting the observation of energetic particles associated with shock waves. An example is shown in Figure 4.8, which shows the profiles of the number of energetic electrons at $\Omega_{ci}t = 100.0$ as a function of x , for the case of $\langle\theta_{Bn}\rangle = 90^\circ$. The black solid line is the profile at $z = 200c/\omega_{pi}$, and the red dashed line shows the profile at $z = 800c/\omega_{pi}$. The corresponding position of the shock front at each of these values of z are represented using dot lines. At $z = 200c/\omega_{pi}$, it is observed that the energetic electrons travel far upstream up to about $100c/\omega_{pi}$ from the shock. However, the profile at $z = 800c/\omega_{pi}$ shows no significant upstream energetic electron flux. The upstream energetic electron profiles show irregular features similar to *in-situ* observations reported by Simnett et al. (2005) (Figure 10). The irregular features are controlled by the global topology of the large-scale turbulent magnetic field lines, along which the accelerated electrons could travel far upstream. Additionally, energetic electron profiles in x direction generally show “spike-like” structure close to the shock front, which is usually observed in interplanetary shocks and Earth’s bow shock. This feature is relatively stable within the simulation time once the upstream electron structure is developed.

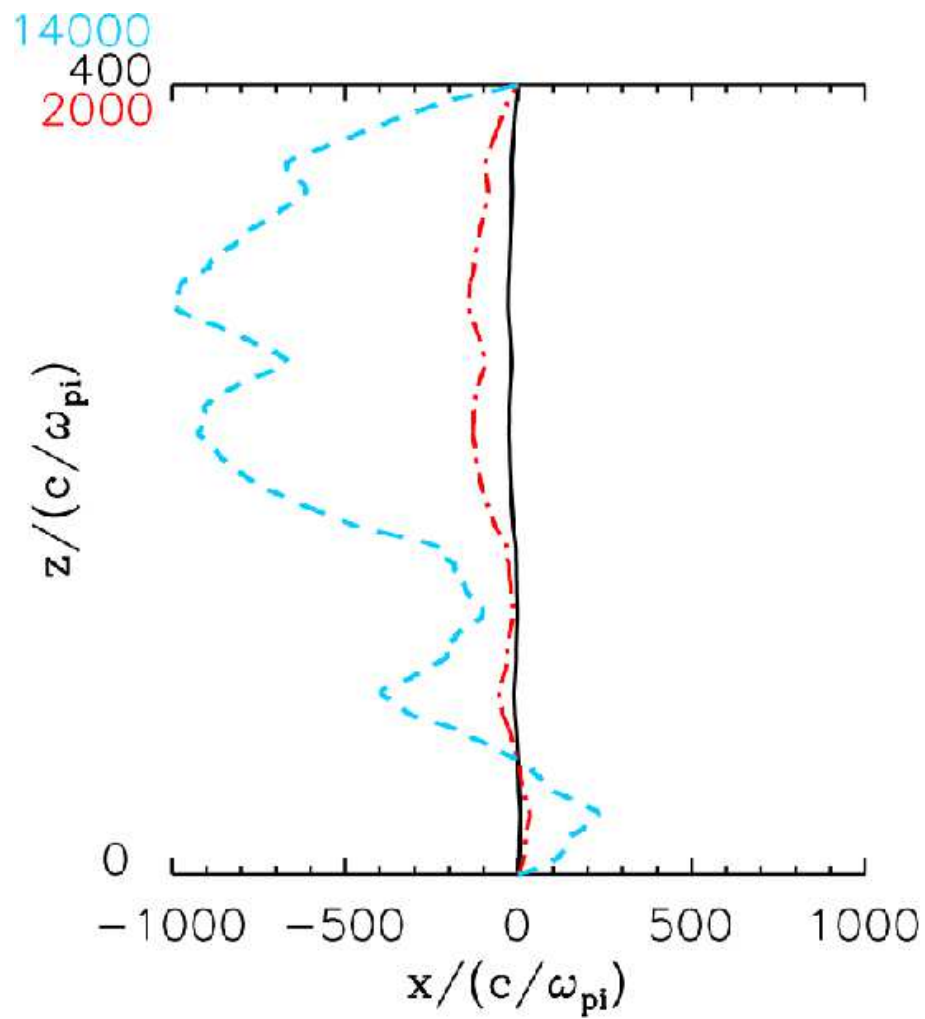


Figure 4.7: Three turbulent magnetic field lines for different correlation lengths. The blue dashed line, red dot dashed line, and black solid line are in the cases that $L_c = 14000c/\omega_{pi}$, $2000c/\omega_{pi}$, and $400c/\omega_{pi}$, respectively.

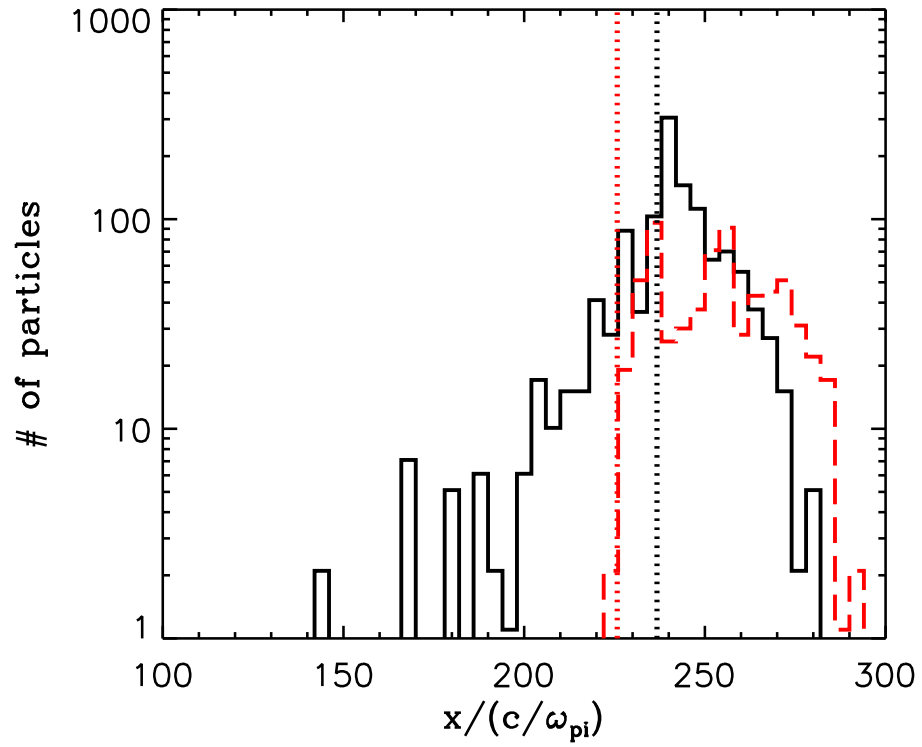


Figure 4.8: The profiles of the number of energetic electrons across the shock at $z = 200c/\omega_{pi}$ and $z = 800c/\omega_{pi}$ and time $\Omega_{ci}t = 100.0$, respectively. The red dot line and the black dot line label the corresponding positions of the shock fronts.

Since the temporal and spatial scales in our hybrid simulation is not large enough compared with the realistic scales of the magnetic turbulence in interplanetary space, we have to estimate how long the upstream electrons can be observed before the shock encounter in realistic parameters. We have carried out an order of magnitude calculation by assuming a planar perpendicular shock whose surface connects to meandering field lines of force at various places. The magnetic turbulence is assumed to be the two-component model (Matthaeus et al., 1990), discussed in Section 2.2. We take the value of coherence length in solar wind turbulence $L_c = 0.01$ AU and the total variance of turbulence is $\delta B^2/B_0^2 = 0.3$. One can estimate the diffusion of magnetic field lines transverse to the average direction of magnetic field $D_\perp = \Delta x^2/\Delta z$. We take the value from numerical simulation that $D_\perp = 0.14L_c$ (Giocalone & Jokipii, 1999). Then we can derive that the field line wandering along the shock normal is $\Delta x \sim 0.4L_c$. Using a shock speed of 800 km/s, we estimate that the electron foreshock region for a perpendicular shock propagating into a turbulent upstream is about 10 minutes. This rough order of magnitude estimate agrees with the *in-situ* observation by Simnett et al. (2005). The upstream energetic electrons have been also observed by Voyager spacecraft, in a much larger scale (Decker et al., 2005, 2008). Voyager II also observed the change of energetic electron intensity, presumably due to large-scale magnetic field change.

4.5.3 Comparison Between the Acceleration of Electrons and That of Ions and its Implication to SEP Events

The correlation between electrons and ions in SEP events has been reported and discussed by a number of authors (see Section 4.2). The correlation indicates that electrons and ions are accelerated close to the Sun by similar processes. We have shown that large-scale turbulence has important effects on accelerating electrons to high energy. The result, along with the previous work on the acceleration of ions (Giocalone, 2005a,b), suggests that perpendicular shocks may play an important role in the acceleration of both electron and ions at shocks, which is consistent with the correlation between ions and electrons in solar energetic particle events (e.g.,

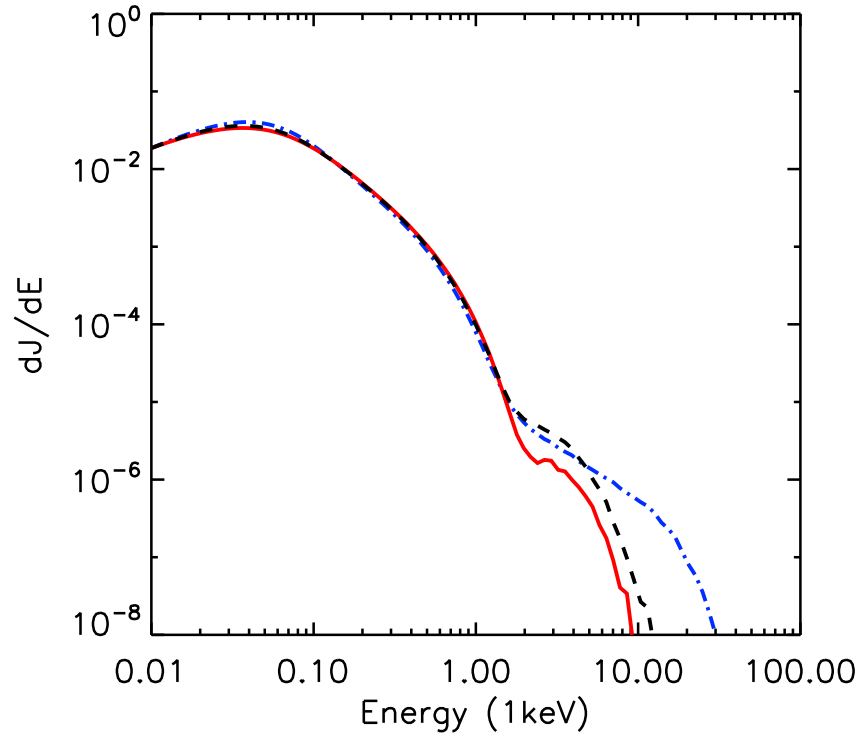


Figure 4.9: The energy flux spectra of protons at $\Omega_{ci}t = 120$ for different averaged shock normal angle. The red solid line is in the case that the shock angle $\langle\theta_{Bn}\rangle = 90^\circ$, the blue dot dashed line and the black dashed line are in the cases that $\langle\theta_{Bn}\rangle = 60^\circ$ and 75° , respectively.

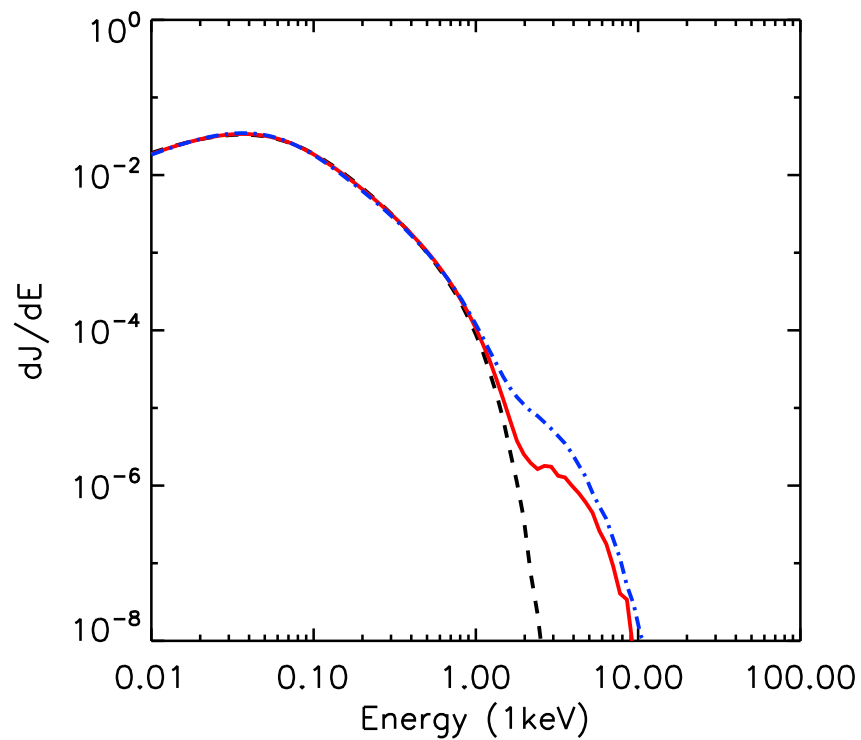


Figure 4.10: The energy flux spectra of protons at $\Omega_{ci}t = 120$ for an averaged perpendicular shock with different turbulence variances. The black dashed line, red solid line, and blue dot dashed line are in the cases that $\sigma^2 = 0.1, 0.3,$ and $0.5,$ respectively.

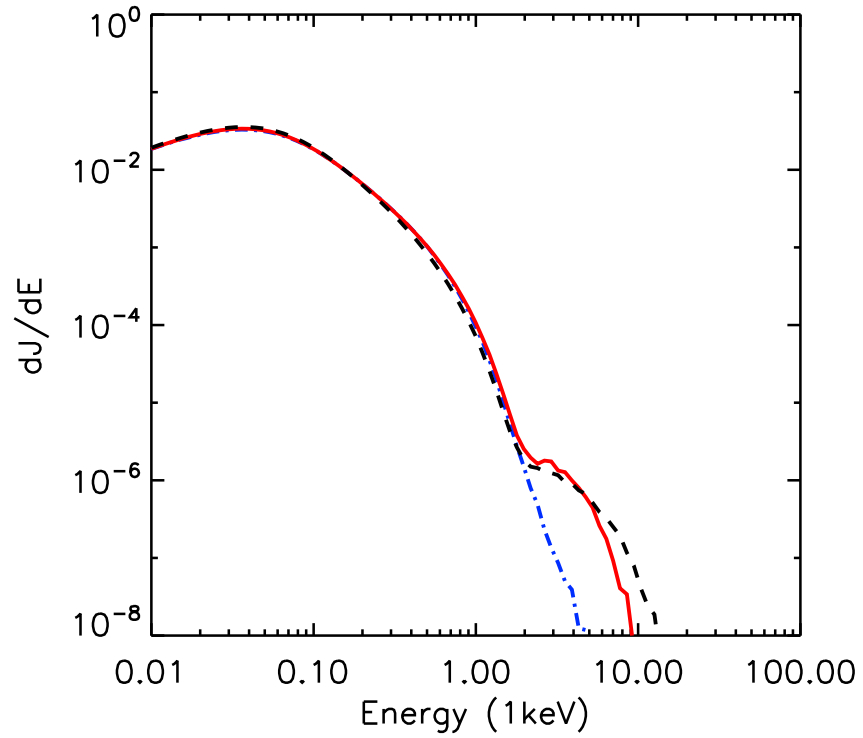


Figure 4.11: The energy flux spectrum of protons at $\Omega_{pi}t = 120$ for averaged perpendicular shock with different turbulence correlation lengths. The black dashed line, red solid line, and blue dot dashed line are in the cases that $L_c = 2000c/\omega_{pi}$, $1000c/\omega_{pi}$, and $400c/\omega_{pi}$, respectively.

Cliver, 2009).

Here we explicitly compare the energy spectra of electrons with that of protons. In Figure 4.9, 4.10, and 4.11, we show the energy spectra of downstream protons from the hybrid simulations, corresponding to the spectra of electrons in Figure 4.4, 4.5, and 4.6. We find that more efficient acceleration for protons can be obtained in the case of larger values of turbulence variances and correlation lengths. These agree well with the characteristics of the acceleration of electrons. In our simulations, the accelerated protons at the oblique shock with $\langle\theta_{Bn}\rangle = 60^\circ$ are found to reach higher energies, which is different from previous works (Jokipii, 1982, 1987; Giacalone, 2005a,b). This is probably due to the limited temporal and spatial scales of our simulations. As shown by Giacalone (2005b) using test-particle simulations, the energy spectra of protons reach the highest energy in perpendicular shock case in a longer time scale $\Omega_{ci}t \sim 50000$ (this corresponds to 5 – 10 minutes for typical parameters in solar corona). However the current results from hybrid simulations do show a population of thermal protons can be accelerated to high energies in perpendicular shocks, which supports the idea that both electrons and protons can be efficiently accelerated by shocks with large shock normal angles.

4.5.4 Summary

We have presented the results of the acceleration of electrons (and also protons) at a perpendicular shock that propagates through a turbulent magnetic field. The acceleration of electrons are enhanced due to the effect of large-scale turbulence. The accompanying results for protons qualitatively show the correlation between accelerated electrons and accelerated ions in oblique shocks with large shock normal angles. This indicates that quasi-perpendicular/perpendicular shocks play an important role in SEP events.

This study will help to explain the correlation between electrons and ions in solar energetic particles from both CME-driven shocks (Cliver, 2009) and solar flares (Shih et al., 2009). The result also poses a question on the contribution of parallel shocks in SEP events. Since it is difficult for parallel shocks to accelerate electrons, most

of SEPs are probably originated from perpendicular shocks. The acceleration of electrons has to be included in current scenario of SEP events (e.g., Tylka et al., 2005).

4.6 The Effect of Large-Scale Magnetic Turbulence on the Acceleration of Electrons: Flare Termination Shocks

In this section we use the combination of hybrid simulations and test-particle electron simulation (see Section 4.4) to study the acceleration of electrons at flare termination shocks predicted to exist in the vicinity of solar flares. Most of this section has been published in the *Astrophysical Journal* (Guo & Giacalone, 2012).

The existence of standing termination shocks has been examined by flare models and numerical simulations (e.g., Shibata et al., 1995; Forbes, 1986). Solar flares are observed to be strong sources of energetic charged particles (Aschwanden, 2002). The release of magnetic energy by magnetic reconnection is thought to be the driving process (Masuda et al., 1994). While several mechanisms have been proposed to explain the acceleration of charged particles in flares (see review by Miller et al., 1997; Zharkova et al., 2011, and references therein), there is still no general consensus and this remains an unsolved problem. Recent hard X-ray observations of the non-thermal electron bremsstrahlung emission by *Reuven Ramaty High Energy Solar Spectroscopic Imager (RHESSI)*; Lin et al., 2002) have provided more details of electron acceleration in solar flares. The observations indicate that a large fraction of released energy resides in high-energy electrons during a short amount of time. Hard X-ray sources above the top of magnetic loops have been detected (e.g., Masuda et al., 1994; Krucker et al., 2010), providing important clues to the acceleration process. For example, the loop-top source recently reported by Krucker et al. (2010) shows that a large number of electrons ($> 5 \times 10^{35}$) are accelerated to more than 16 keV and the highest energy reaches \sim MeV. Since the observed hard X-ray source requires very efficient acceleration, explaining how such a large number of electrons (probably also ions) are accelerated to high energy poses a challenge to theoretical

astrophysics.

The existence of fast shocks in the reconnection outflow region has been predicted in flare models (Shibata et al., 1995) and numerical simulations (e.g., Forbes, 1986, 1988; Shiota et al., 2003; Workman et al., 2011). Using MHD numerical simulations, Forbes (1986) studied the formation of a standing termination shock when a high-speed jet driven by reconnection encounters a closed magnetic loop. The geometry of the flare termination shocks can be represented by Figure 4.12. The high-speed jet created in the reconnection out-flow region collides with the top of the magnetic loop and produces a fast-mode, standing termination shock. The resulting flare termination shock has a unit normal to its surface that points nearly perpendicular to the magnetic field. This is a perpendicular shock (i.e., the angle between the upstream magnetic field and shock normal vector $\theta_{Bn} = 90^\circ$). Forbes (1986) predicts the existence of this shock with a compression ratio of 2.0 and an upstream Mach number as high as 2.3. A recent study by Workman et al. (2011) shows similar results. The observational evidence of the existence of flare shocks has been presented by Aurass et al. (2002).

Particle acceleration at flare termination shocks has been considered by a number of authors. It is usually thought that the injection of electrons is a problem at perpendicular shocks. We addressed this in previous sections. There has been some works on facilitating particle acceleration at flare termination shocks. Tsuneta & Naito (1998) considered electron heating by a slow-shock pair as a pre-energization process. Somov & Kosugi (1997) considered the role of plasma heating and collapsing magnetic trap at reconnecting magnetic field lines. In this paper we present results from a combination of hybrid simulations and test-particle electron simulations to study the electron energization at a flare termination shock in the existence of upstream magnetic fluctuations. We consider the nonlinear modification of a planar shock front by upstream Alfvénic fluctuations and its effect on electron acceleration. Although the plasma waves and turbulence in the reconnection outflow region could be considerably different from our simplified model, some intrinsic characteristics of this interaction, such as the braiding of magnetic field lines and shock rippling,

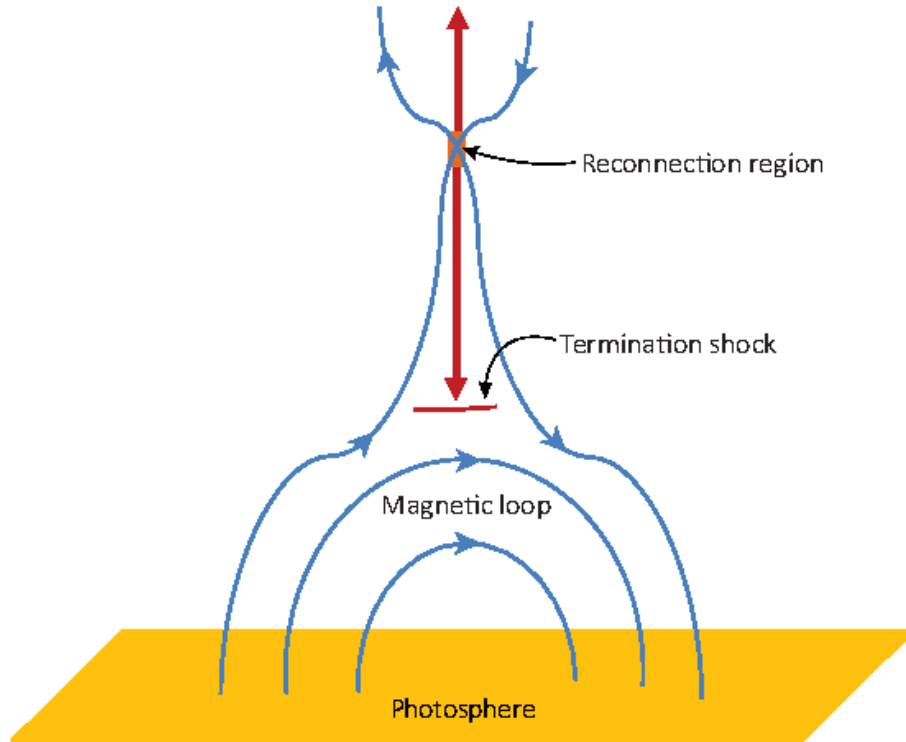


Figure 4.12: A cartoon illustration of the geometry of flare termination shocks.

should still be preserved. We show that after considering a fluctuating upstream region, the electron acceleration in flare termination shock is a rapid and efficient process. A large fraction of the initial thermal electrons is accelerated to hundreds of keV and even reaches MeV energies in a very short time. This indicates that collisionless shocks may play an important role in particle acceleration in solar flares. In Section 4.6.1 we describe the initial conditions and parameters used in this paper. Section 4.6.2 discusses the simulation results.

4.6.1 Initial Conditions and Parameters

The size of the simulation domain $L_x \times L_z$ for each case is listed in Table 4.1. The flare termination shock is modeled by injecting plasma continuously from one end ($x = 0$) of the simulation box and colliding the reflecting boundary at the other end ($x = L_x$). The total variance of magnetic turbulence in each case is listed in Table

1. In all the cases, we take $L_c = L_z$. We expect large-scale magnetic turbulence to exist in reconnection outflow plasma. These fluctuations can be triggered by reconnection, foot-point motion or other processes (see Krucker et al., 2008, for a detailed discussion). Although this simplified form of magnetic-field fluctuations may not be realistic, any turbulence with large variances should allow strong field-line wandering, which is essential in our particle acceleration model.

In order to produce a low Mach number shock as predicted by other numerical simulations, the inflow Alfvén Mach number is taken to be $M_{A0} = 1.0$. After reflection at the right boundary, this produces a shock with averaged Mach number of about 2.0 in the shock frame, consistent with the flare termination shock predicted by previous MHD simulations (Forbes, 1986; Workman et al., 2011). The grid sizes are $\Delta x = \Delta z = 0.5c/\omega_{pi}$ and the time step is taken to be $\Delta t = 0.01\Omega_{ci}^{-1}$, where c/ω_{pi} is the ion inertial length and Ω_{ci}^{-1} is the ion gyroperiod. The plasma beta β_i and β_e are taken to be 0.03 and the ratio between light speed and upstream Alfvén speed $c/V_{A0} = 410$, which roughly corresponds to an initial situation with temperature 2×10^6 K, number density $8 \times 10^9 \text{ cm}^{-3}$ and magnetic field $B_0 = 30$ G, similar to constraints from observations (Krucker et al., 2010). Under these parameters, the average shock speed in the shock frame (also the jet outflow speed) is about 1460 km/s. This speed is measurable because the outflow plasma from reconnection is moving at the Alfvén speed. The estimate from observations (Tsuneta et al., 1997) is roughly consistent with this value.

In the second step, we integrate the relativistic equations of motion for an ensemble of test-particle electrons in the two-dimensional time-dependent electric and magnetic fields obtained in the hybrid simulations. These test-particle electrons are treated as a different part from the electron fluid in the hybrid simulations. We use a second-order spatial interpolation and linear temporal interpolation to get the field at the particle position. Initially we release a Maxwellian distribution with $T_e = 2.0 \times 10^6$ K in the upstream frame. The test-particle electrons are released upstream at $\Omega_{ci}t = 30$ after the shock has fully formed and far from the boundaries. The simulation domain in the x -direction is large enough so that no test-particle

Run	$L_x(c/\omega_{pi}) \times L_z(c/\omega_{pi})$	$\delta B^2/B_0^2$	$\Gamma\%$ ($E \geq 15$ keV)
1	500×400	0.0	1.3
2	500×400	0.03	4.5
3	500×400	0.1	8.0
4	500×400	0.3	9.8
5	500×800	0.03	4.9
6	500×800	0.1	8.9
7	500×800	0.3	11.9

Table 4.1: Some parameters for different simulation runs. The size of the simulation domain, the variance of injected magnetic fluctuation, and the fraction of electrons whose energy is more than 15 keV at the end of simulation.

electrons escape from the system. Strictly speaking, this test-particle simulation is only valid when the influence of the accelerated electron to the background fluid is negligible. However, in the end of the simulation, the initial Maxwellian distribution of test-particle electrons has been considerably changed due to the energization process at the shock front. This indicates that our approach may not be suitable in studying the long-term evolution of the termination shock.

4.6.2 Simulation Results

In this work we discuss the electron acceleration in flare termination shocks, which have low Mach numbers and high shock speeds. The plasma in solar corona is in a high temperature and low plasma beta (strong magnetic field) regime, which is considerably different from that in interplanetary space. We focus on the modification of shock surface by upstream Alfvénic fluctuations and its effect on acceleration of electrons. Table 4.1 lists some key parameters for all the simulation runs including the size of the simulation domain, the variance of the injected magnetic fluctuation, and the fraction of electrons whose energy is more than 15 keV at the end of simulation. For runs 1-4 we consider the effect of different variances of magnetic turbulence. The turbulence variances are from 0.0 to 0.3 and the sizes of the simulation domain $L_x \times L_z = 500c/\omega_{pi} \times 400c/\omega_{pi}$ ($1.27 \text{ km} \times 1.02 \text{ km}$) for these four cases. For runs 5-7, the magnetic variances are the same as runs 2-4, but the size

of the simulation box is changed to $L_x \times L_z = 500c/\omega_{pi} \times 800c/\omega_{pi}$ (1.27 km \times 2.03 km) to examine the effect of changing the coherence length. In the flare region, the strong large-scale Alfvénic magnetic fluctuation can be triggered by reconnection, and cascade to small scales. This process is usually assumed to be the source of magnetic turbulence required in many acceleration models (e.g., Miller et al., 1996; Petrosian & Liu, 2004). Since the size of our largest simulation domain is still much smaller than the observed hard X-ray emission region ($L \sim 10^3$ km), we do not consider the realistic geometry of flare termination shock but approximate it locally as a perpendicular shock that propagates into a plasma containing magnetic fluctuations.

Figure 4.13 shows the color-coded contours of (a) magnetic field in the z direction B_z and (b) ion number density n_p from run 3 at $\Omega_{ci}t = 110.0$. The magnetic field and plasma density have been normalized using the average upstream magnetic field B_{10} and in-flow density n_0 . The averaged Alfvén Mach number in the shock frame is about 2.0 and the average compression ratio is about 2.1. As noted in the earlier works (Giacalone, 2005b; Guo & Giacalone, 2010), the shock surface becomes distorted due to the interaction between the shock front and the upstream turbulence. Meandering magnetic field lines cross the shock front at various locations along the shock, which allows the electrons to cross and/or get reflected at the shock front multiple times. The shock-front rippling has also been shown to contribute to particle acceleration by mirroring electrons between ripples (Guo & Giacalone, 2010).

Figure 4.14 presents the energy spectra dJ/dE of electrons. The green solid line shows the initial distribution of thermal electrons in the upstream region. The black solid line displays the energy distribution for all the electrons in downstream region at the end of simulation for run 1. In this case no pre-existing fluctuation is considered and the electron energization is primarily due to heating at shock layer. We have calculated that the effective electron kinetic temperature jump in the downstream region including the superthermal distribution is about 6 times of the upstream temperature. The simulated electron temperature jump is about 40%

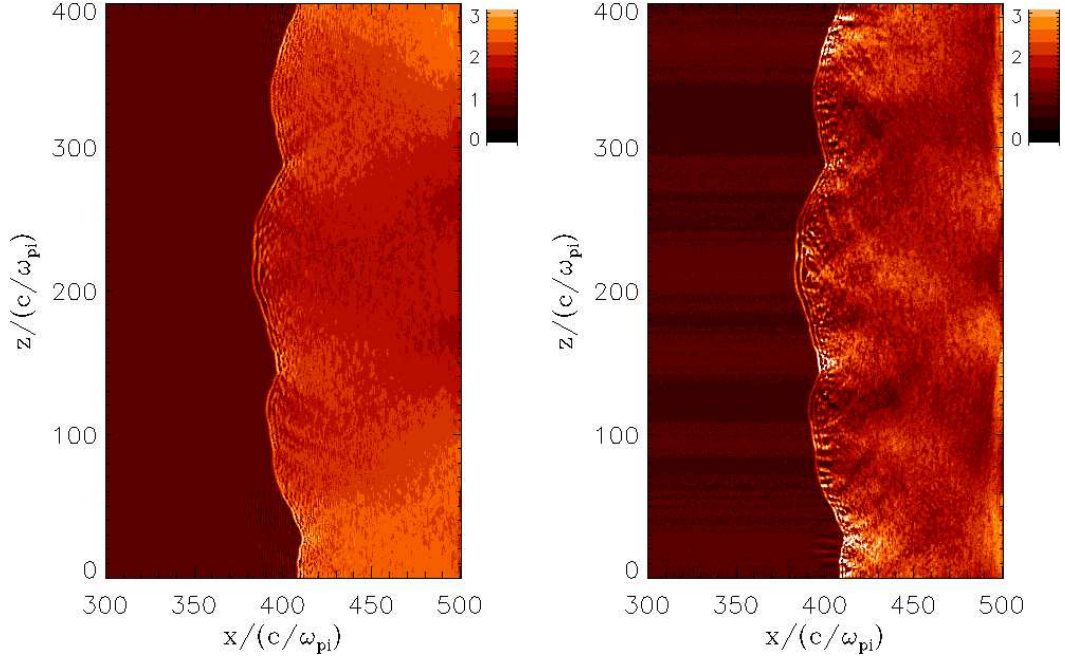


Figure 4.13: The color-coded images of (a) magnetic field B_z , (b) ion density n_p for run 3 at $\Omega_{ci}t = 110.0$.

of the proton temperature jump across the shock layer in our hybrid simulation. This is consistent with the theoretical prediction that the heating of electrons in fast shocks is less than that of ions (Goodrich & Scudder, 1984; Scudder, 1995) and the observational constraints from measurements at planetary bow shocks and interplanetary shocks (Thomsen et al., 1987; Schwartz et al., 1988). We note that in our simulation electron heating may not be determined very accurately since the test-particle electrons have no feedback to the electric and magnetic field at the shock layer. In the following we focus on the nonthermal acceleration of electrons at shocks after considering the pre-existing magnetic fluctuations. The blue solid, dot and dashed lines in Figure 4.14 represent energy distribution for all the electrons in downstream region at the end of simulation ($\Omega_{ci}t = 130.0$) for runs 2-4, respectively. At this time the energy spectra do not evolve anymore. It can be seen that the electrons are accelerated to high energy after considering the upstream magnetic turbulence. For higher variance of magnetic turbulence, there are more particles accelerated to high energy. For run 4 ($\delta B^2/B_0^2 = 0.3$), 9.8% of electrons are accelerated

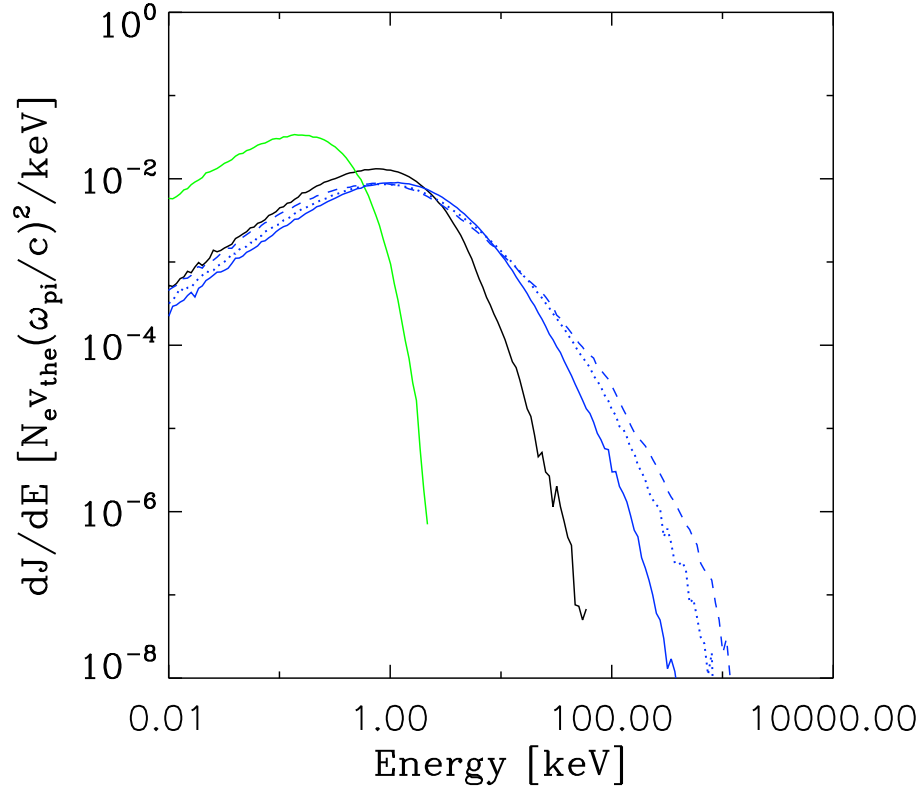


Figure 4.14: The energy spectra of electrons at the end of the simulation ($\Omega_i t = 130.0$). The energy spectra are normalized using $N_e v_{the} (\omega_{pi}/c)^2 / keV$, where N_e is the total number of electrons used in the simulations and v_{the} is the initial electron thermal speed. The green solid line shows the initial distribution of thermal electrons in the upstream region. The black solid line displays the energy distribution for all the electrons in downstream region at the end of simulation for run 1. The blue solid, dot and dashed lines represent results from runs 2, 3, and 4, respectively.

to more than 15 keV at the end of the simulation. The efficient electron acceleration can be understood as stronger magnetic turbulence allows stronger field-line meandering, and the electrons can be taken by field lines of force and therefore gain energy at a hock front multiple times.

In Figure 4.15 we examine the effect of changing the coherence length of the magnetic turbulence and focus on the high energy part of the energy spectra. It shows results from runs 5-7 (red lines, $L_z = 800c/\omega_{pi}$) along with corresponding runs 2-4 (blue lines, $L_z = 400c/\omega_{pi}$). It is shown that for larger coherence length, the

electrons could reach higher energy and the spectral slope tends to be flatter. The more efficient acceleration in runs 5-7 can be understood as the larger simulation domain in the direction of magnetic field allows more field line wandering normal to the shock ($\Delta x^2 \propto \Delta z$, where Δx is the field-line random walk normal to the averaged magnetic field and Δz is distance along the field) therefore the electrons move across the shock more easily. This dependence shows that long-wavelength fluctuations are important to accelerate electrons to high energy.

We also analyze the acceleration of protons, which are treated self-consistently in this problem (i.e., they are included in the hybrid simulation). Figure 4.17 shows the differential energy spectra of protons in the shock frame for runs 2-7. Similar to Figure 4.15, the results from runs 5-7 are represented by red lines and the results from runs 2-4 are displayed using blue lines. The accelerated protons show a similar dependence on turbulence variance and coherence length to that of electrons. This dependence has been found previously for the case of higher Mach number shock and larger correlation length (Giacalone, 2005b). These results show that both electrons and protons can get efficiently accelerated. However, for the parameters we use the slopes of the energy spectra of protons are considerably steeper than that of the spectra of electrons. This is probably due to the limited temporal and spatial scales of our simulations. As shown by Giacalone (2005b) using test-particle simulations, the energy spectra of protons reach the highest energy in perpendicular shock case in a longer time scale $\Omega_{ci}t \sim 50000$. However the current results from hybrid simulations do show a population of thermal protons can be accelerated to high energies in perpendicular shocks, which supports the idea that both electrons and protons can be efficiently accelerated by shocks with large shock normal angles.

4.7 Discussion and Conclusions

In this chapter we studied the acceleration of electrons at collisionless shocks by utilizing a combination of a 2-D hybrid simulation to obtain the shock structure and a test-particle simulation to determine the motion of electrons. The hybrid

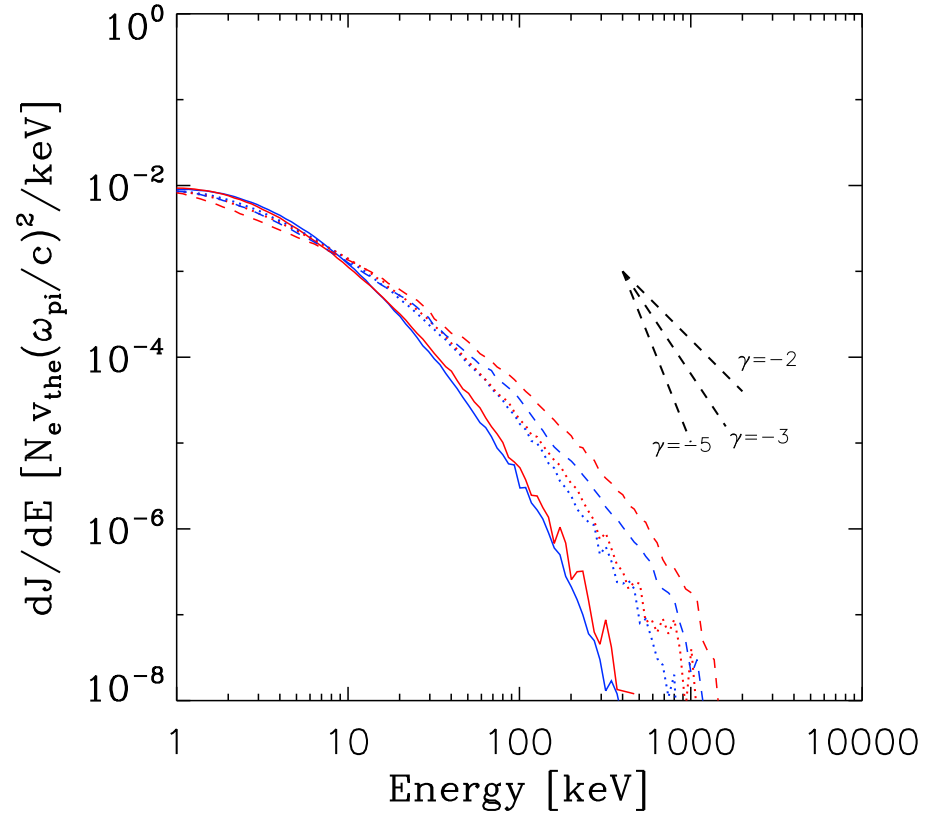


Figure 4.15: The energy spectra of electrons at the end of the simulation ($\Omega_i t = 130.0$). The energy spectra are normalized using $N_e v_{the} (\omega_{pi}/c)^2 / keV$, where N_e is the total number of electrons used in the simulations and v_{the} is the initial electron thermal speed. The red solid, dot and dashed lines represent the energy distributions for all the electrons in downstream region at the end of simulation for runs 5, 6, and 7 respectively. The blue solid, dot and dashed lines represent results from runs 2, 3, and 4, respectively.

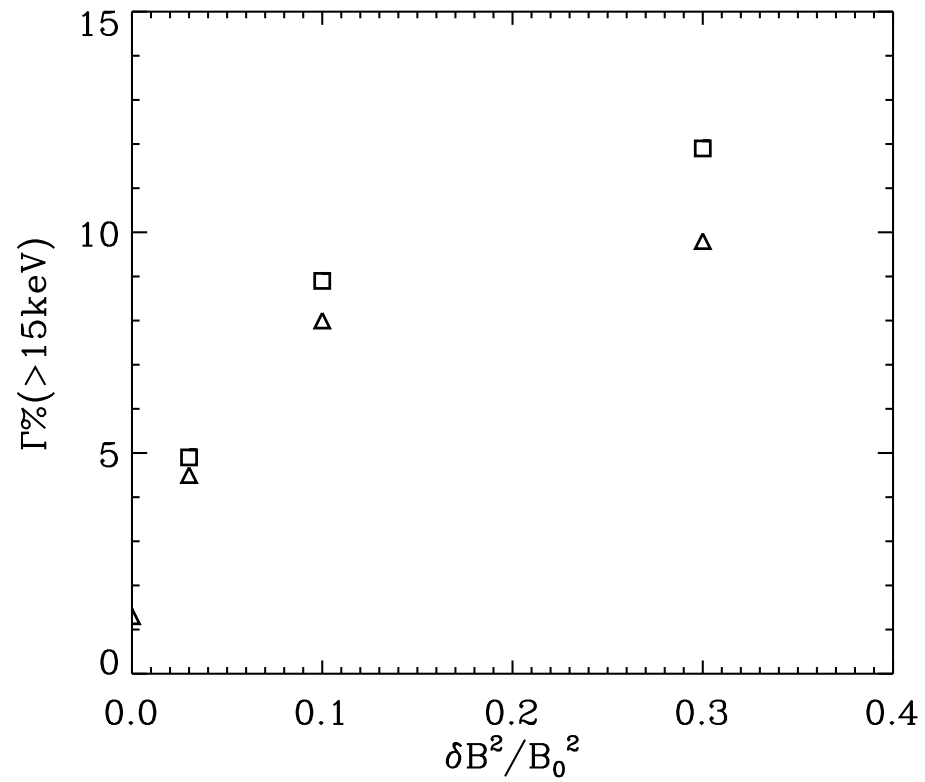


Figure 4.16: The relation between the turbulence amplitude $\delta B^2/B_0^2$ injected in hybrid simulation and the percentage of electrons eventually accelerated to more than 15 keV.

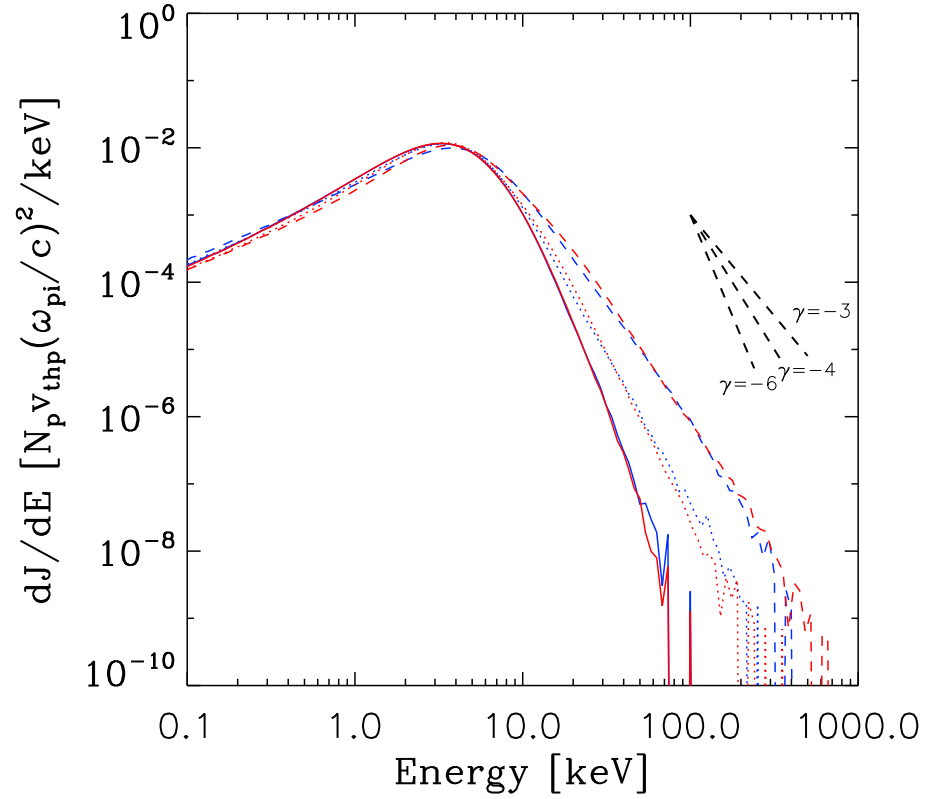


Figure 4.17: The energy spectra of protons downstream of the shock at the end of the simulation ($\Omega_i t = 130.0$), normalized using $N_p v_{thp} (\omega_{pi}/c)^2 / keV$, where N_p is the total number of protons used to plot the spectra and v_{thp} is the initial proton thermal speed. The red solid, dot and dashed lines represent the energy spectra for protons in downstream region at the end of simulation for runs 5, 6, and 7 respectively. The blue solid, dot and dashed lines represent results from runs 2, 3, and 4, respectively.

simulation provides realistic electric and magnetic fields within the transition layer of the shock that effect the motion of test-electrons, which is determined by solving the equation of motion. The interaction of the shock with pre-existing upstream fluctuations, and other nonlinear processes occurring in the hybrid simulation lead to a “rippling” of shock surface that also effects the transport of the electrons. We find that the electrons are efficiently accelerated by a nearly perpendicular shock. The turbulent magnetic field leads to field-line meandering that allows the electrons to cross the shock front many times. The rippling of the shock front also contributes to the acceleration by mirroring electrons between the ripples. This acceleration process is more efficient at perpendicular shocks. As $\langle \theta_{Bn} \rangle$ decreases from 90° , both the number fraction and highest achievable energy of accelerated particles decreases. Based on our calculations, we conclude that perpendicular shocks are the most important for the acceleration of electrons. The current study is helpful in understanding the injection problem for electron acceleration by collisionless shocks. It is also found that different values of variances and correlation lengths of the injected magnetic turbulence also strongly affect the attainable maximum energy and accelerated fraction of electrons. The cases with larger turbulence variances or larger turbulence correlation lengths have a flatter energy spectrum than that with smaller turbulence variance, which suggests the enhanced motion of electrons normal to the shock front, due to enhanced field-line random walk, is of importance for the acceleration of electrons to high energies.

Here we discuss the applications of this process to interplanetary shocks and SEP events (Section 4.7.1) and particle acceleration in solar flares (Section 4.7.2).

4.7.1 Application to Interplanetary Shocks and SEP events

We presented the results of electron acceleration at shocks under parameters similar to interplanetary shocks. The results can also be useful for considering acceleration of electrons by shocks in SEP events. For the case that the averaged shock normal angle $\langle \theta_{Bn} \rangle = 90^\circ$ and turbulence variance $\sigma^2 = 0.3$, the electrons can be readily accelerated to up to 200 – 300 times the initial energy. The resulting spectrum is

flat between about 0.1 keV to 0.7 keV. At higher energies, the spectrum falls off with energy following a power law with a spectral slope of about -3 . We found that the energetic electron density upstream and downstream of collisionless shocks show filamentary structures (Figure 4.2). This could help explain electron spike-like events observed upstream and downstream of terrestrial and interplanetary shocks (Anderson et al., 1979; Tsurutani & Lin, 1985; Simnett et al., 2005). Observation by Voyager 1 at the termination shock and in the heliosheath also show the evidence of electron spike-like enhancements at the shock front (Decker et al., 2005). The upstream spatial distribution of energetic electrons shows irregular features that depend on both the irregularity in the shock surface and the global topology of magnetic field lines. At first the electrons are accelerated and reflected at the shock front, and then they travel upstream along the magnetic field lines. The electrons could be taken far upstream by field line random walk. This result can possibly lead to an interpretation to the complex electron foreshock events recently observed to be associated with interplanetary shocks (Bale et al., 1999; Pulupa & Bale, 2008). Bale et al. (1999) and Pulupa & Bale (2008) proposed that the complex upstream electron events result from large-scale irregularities in shock surface. In this paper we have demonstrated that the upstream electron flux may be controlled by both an irregular shock surface and by large-scale meandering magnetic field lines.

We have also presented the accompanying results for protons that qualitatively show the correlation between accelerated electrons and accelerated ions in oblique shocks with large shock normal angles. The shocks can efficiently accelerate both electrons and ions. This indicates that quasi-perpendicular/perpendicular shocks play an important role in SEP events.

4.7.2 Application to Particle Acceleration in Solar Flares

Understanding particle acceleration in solar flares is a challenge since only remote observations are available and it is hard to identify the main mechanism. While it is commonly thought that magnetic reconnection drives the energy release, the detailed physical process involved in accelerating the electrons and ions is still not

clear. We studied electron acceleration at flare termination shocks that have been predicted by numerical simulations and flare models. We find that electrons are rapidly and efficiently accelerated at a flare termination shock in the presence of pre-existing magnetic fluctuations. Electrons are accelerated to a few MeV in 100 ion gyroperiod (of the order of a millisecond) and more than 10% of thermal electrons are accelerated to more than 15 keV given a sufficiently strong magnetic turbulence. We also show that electron acceleration is more efficient for larger turbulence variance $\delta B^2/B_0^2$ and/or a larger turbulence coherence length L_c . Both of these indicate that large-scale field-line meandering plays an essential role in accelerating electrons at a shock front. Our simulations show that after considering the magnetic turbulence the flare termination shock could accelerate electrons to much higher energies than usual drift shock acceleration (e.g., Mann et al., 2009). We note that the similar mechanism has been shown to efficiently accelerate ions and has similar dependence on the turbulence properties. This correlation between ions and electrons is actually commonly observed in solar energetic particle events. For the parameters used in our simulations, the accelerated protons have energy spectra steeper than that of electrons. This is different from the previous results for parameters similar to interplanetary space (Giacalone, 2005b; Guo & Giacalone, 2010). We note that these results are carried out for energies lower than the injection energy for diffusive shock acceleration. When the pitch-angles of charged particles are scattered sufficiently as to be trapped near the shock, the energy spectra of the accelerated particles are presumably close to that predicted by diffusive shock acceleration.

We also note that for the situation we study, the resulting distribution of electrons is non-Maxwellian. The structure of collisionless shocks may be considerably modified by accelerated particles. While this effect is not considered in our test-particle simulations, it may be important. Due to the limitation of computation, a full particle simulation of collisionless shock with realistic mass ratio $m_i/m_e = 1836$ that includes the influence of turbulent upstream magnetic field is not available so far. The evolution of this flare termination shock remains to be explored. Also, other plasma effects like emission process in flare region may need to be considered

to directly compare with the observations.

CHAPTER 5

Conclusions and Future Work

5.1 Summary and Conclusions for the Dissertation

In this dissertation, we studied the effects of magnetic fluctuations on the acceleration and transport of charged particles in the heliosphere. We started by reviewing the basics of the acceleration and transport of charged particles and relevant physics in the heliosphere. We discussed the Parker's transport equation (Parker, 1965), which has been the fundamental equation to study the transport and acceleration of energetic charged particles. Then we focused on the limitation of the transport equation and discussed the possible solutions. Since Parker's transport equation assumes a quasi-isotropic distribution function in momentum space, in the case that the distribution function of energetic particles is highly anisotropic, the evolution of the distribution function cannot be properly described by the transport equation. The examples are the initial release of solar energetic particles and the acceleration of low-energy particles at the shock front. In addition, the observations of impulsive SEP events show fine structures in intensity-time plots on small temporal scales (hours) that cannot be easily described by a large-scale spatial diffusion.

In Chapter 2 we presented numerical simulations for the propagation of SEPs in the inner heliosphere. We numerically integrated the trajectories of energetic charged particles in the turbulent magnetic field generated from two commonly used magnetic turbulence models (the foot-point random motion model and the two-component model). The observations of SEP events are simulated by collecting charged particles which reached 1 AU. We study the velocity dispersion of SEPs in the turbulent magnetic field and estimate the error involved in the onset analysis. We find that the the velocity dispersion can be well produced by this model. For a typical turbulence variation $\delta B^2/B_0^2 \sim 0.1$ observed at 1 AU and a large source

region, we find that the difference between the apparent release time inferred from the onset analyses and the actual release time is less than a few minutes, but the apparent path length can be significantly different than the real path length along the average magnetic field line. For the foot-point random motion model, the error for the inferred release time is smaller than that of the two-component model. We have also reproduced SEP dropouts in the numerical simulations using the foot point random motion model, assuming the SEP source region is smaller than the correlation scale. The widths of these dropout are typically several hours, similar to the time scales of dropouts observed in space. The velocity dispersion of the energetic particles appears to have different path lengths, which indicates that the energetic particles travel along different field lines. We have also attempted to use the two-component model to numerically simulate the dropouts of energetic particles. However, we rarely find the evidence of SEP dropouts in our simulation for the two-component model. This is because the parallel diffusion coefficient of particles in the two-component model is considerably smaller than that in the foot-point random model. This result questions the popular used two-component model in that it gives more pitch-angle scattering than that constrained by the observation of SEP dropouts.

In Chapter 3 we studied two processes for particle acceleration at shock waves. The first problem is associated with the acceleration of low-energy particles at shocks. We presented a numerical study on the acceleration of thermal protons at parallel shocks using 3-D hybrid simulations. The 3-D simulations removed the artificial restriction of the motion of charged particles in previous 1-D and 2-D simulations. The results confirmed the injection mechanism at parallel shocks that the accelerated particles are originated from reflected particles. In the second study we illustrate the effect of a large-scale sinusoidal magnetic field variation. This simple model allows a detailed examination of the physical effects. As the magnetic field lines pass through the shock, the connection points between field lines on the shock surface will move accordingly. We find that the region where connection points approaching each other will trap and preferentially accelerate particles to high energies

and form “hot spots” along the shock surface. The shock acceleration will be suppressed at places where the connection points move apart each other. Some of the particles injected in those regions will transport to the “hot spots” and get further accelerated. The resulting distribution function is highly spatial dependent at the energies we studied, which could give a possible explanation to the *Voyager* observation of anomalous cosmic rays (ACRs). This mechanism gives an interpretation for the observation that the ACRs did not saturate at the termination shock.

In Chapter 4 we studied the acceleration of electrons at collisionless shocks by utilizing a combination of a 2-D hybrid simulation to obtain the shock structure and a test-particle simulation to determine the motion of electrons. We find that the electrons are efficiently accelerated by a nearly perpendicular shock when the large-scale pre-existing magnetic fluctuations are considered. The turbulent magnetic field leads to field-line meandering that allows the electrons to cross the shock front many times. The rippling of the shock front also contributes to the acceleration by mirroring electrons between the ripples. This acceleration process is more efficient at perpendicular shocks. As $\langle\theta_{Bn}\rangle$ decreases from 90° , both the number fraction and highest achievable energy of accelerated particles decreases. Based on our calculations, we conclude that perpendicular shocks are the most important for the acceleration of electrons. The current study is helpful in understanding the injection problem for electron acceleration by collisionless shocks. It is also found that different values of variances and correlation lengths of the injected magnetic turbulence also strongly affect the attainable maximum energy and accelerated fraction of electrons. The cases with larger turbulence variances or larger turbulence correlation lengths have flatter energy spectra than the cases with smaller turbulence variances, which suggests that the enhanced motion of electrons normal to the shock front, due to enhanced field-line random walk, is of importance for the acceleration of electrons to high energies. We discussed the applications of this process to interplanetary shocks and SEP events (Section 4.7.1) and particle acceleration in solar flares (Section 4.7.2). We also discussed the implication of this study to solar energetic particles (SEPs) by comparing the acceleration of electrons with that of

protons. The intensity correlation of electrons and ions in SEP events indicates that perpendicular or quasi-perpendicular shocks play an important role in accelerating charged particles.

5.2 Future Work

5.2.1 Effect of Shock Geometry on the Acceleration of Charged Particles in Gradual SEP Events

The acceleration of solar energetic particles (SEPs) remains to be one of the most important unsolved problems in heliospheric physics. Observations indicate that the acceleration at high energies is highly variable in spectral properties and elemental composition. Many recent works suggest that effects like seed particles, shock geometries and/or the generation of self-excited waves can play an important role on the observed variable energy spectra (e.g., Tylka et al., 2005).

In Section 3.5 we have considered the effect of large-scale shock geometry on the diffusive shock acceleration (DSA) of anomalous cosmic rays at the termination shock. The results show that this effect can significantly modify the well-known 1-D steady state solution of DSA. Similarly, we plan to study numerically the acceleration of particles in CME-driven shocks, including the effect of shock geometry. Since the CME-driven shocks are known to have large-scale non-planar shapes, we expect that the particles can sample shock fronts with various shock normal angles during the acceleration. This effect has not been considered by previous works, which usually assume a planar shock or no cross-field diffusion (e.g., Lee, 2005; Tylka et al., 2005; Sandroos & Vainio, 2007; Li et al., 2009). This work will treat particle acceleration in CME-driven shocks in a more realistic way.

5.2.2 Understanding the Physical Processes in the Acceleration of Low-Energy Particles at Shocks

Solving the acceleration of energetic particles in the heliosphere requires the knowledge of the acceleration of low-energy particles. Since the DSA is not concerned with

low-energy particles that has high anisotropies, most of DSA models do not include the acceleration of low-energy particles or treat it in a *ad hoc* way (e.g., Ellison, 1981; Ellison et al., 1990). To fully understand the observed energetic particles, we need to model the acceleration of low-energy protons, electrons, and also heavy ions.

a) Recent observations have indicated that the pre-accelerated particles from solar flares or other source may be important in acceleration of SEPs. In Chapter 3 we have used 3-D hybrid simulations to study the acceleration of low-energy protons at collisionless shocks. We plan to further explore the injection problem using the self-consistent hybrid simulations including the seed particle population pre-accelerated in solar flares or other sources.

b) We also plan to use full particle simulations (kinetic ions and kinetic electrons) to study the acceleration of electrons at collisionless shocks. In Chapter 4 we have shown that low-energy electrons can be efficiently accelerated when a shock propagates normal to a magnetic field that contains pre-existing large-scale magnetic turbulence. The simulation model include a combination of a hybrid model (kinetic ions and fluid electron) and a test-particle electron model. Since the model does not consider the electron-scale plasma physics and the feedback of accelerated electrons on the shock front, we need to use a full particle simulation model to consider the effects in order to fully solve the problem of acceleration of electrons at collisionless shocks. This work will consider the interplay between large-scale effects (large-scale magnetic fluctuations and shock ripples) and small-scale effects (whistler waves at shock fronts).

5.2.3 The Application of the Hybrid Simulations in the Heliospheric Plasma Processes

During the doctoral study, we have improved the parallelization of the 1-D, 2-D and 3-D hybrid simulation models (Giacalone et al., 2000; Giacalone, 2004, 2005b). The new version of the code has good scalability and has been tested on NASA's Pleiades supercomputer using a few thousand CPU cores. The high performance of the code on supercomputers allows us to study a variety of problems using multi-dimensional

simulations or 1-D simulations with large simulation boxes and long simulation times. While we have presented some results using the new code, plenty of other plasma physics problems in the heliosphere can be studied using this numerical tool. We have plans to study numerically the ion cyclotron waves excited by fresh pickup ions (Florinski et al., 2010) using 2-D hybrid simulations, plasma instabilities and waves upstream and downstream of shocks, and the acceleration of charged particles by multiple shocks (Li et al., 2012).

REFERENCES

- Amano, T., & Hoshino, M. 2007, *ApJ*, 661, 190
- Anderson, K. A., Lin, R. P., Martel, F., Lin, C. S., Parks, G. K., & Reme, H. 1979, *Geophys. Res. Lett.*, 6, 401
- Armstrong, T. P., Pesses, M. E., & Decker, R. B. 1985, *Shock Drift Acceleration, Collisionless Shocks in the Heliosphere: A Tutorial Review*, AGU Geophysical Monograph Series, 35, 271
- Aschwanden, M. J. 2002, *Space Sci. Rev.*, 101, 1
- Aurass, H., Vršnak, B., & Mann, G. 2002, *A&A*, 384, 273
- Axford, W. I. 1972, *NASA Special Publication*, 308, 609
- Axford, W. I., Leer, E., & Skadron, G. 1977, in *Proc. 15th Int. Cosmic-Ray Conf. (Plovdiv)*., Vol. 11, , 273
- Bale, S. D., Mozer, F. S., & Horbury, T. S. 2003, *Physical Review Letters*, 91, 265004
- Bale, S. D., Reiner, M. J., Bougeret, J., Kaiser, M. L., Krucker, S., Larson, D. E., & Lin, R. P. 1999, *Geophys. Res. Lett.*, 26, 1573
- Ball, L., & Melrose, D. B. 2001, *PASA*, 18, 361
- Balogh, A., Smith, E. J., Tsurutani, B. T., Southwood, D. J., Forsyth, R. J., & Horbury, T. S. 1995, *Science*, 268, 1007
- Belcher, J. W., & Davis, Jr., L. 1971, *J. Geophys. Res.*, 76, 3534
- Bell, A. R. 1978, *MNRAS*, 182, 147
- Bieber, J. W., Matthaeus, W. H., Smith, C. W., Wanner, W., Kallenrode, M.-B., & Wibberenz, G. 1994, *ApJ*, 420, 294
- Bieber, J. W., Wanner, W., & Matthaeus, W. H. 1996, *J. Geophys. Res.*, 101, 2511
- Blandford, R. D., & Ostriker, J. P. 1978, *ApJ*, 221, L29
- Boyd, T. J. M., & Sanderson, J. J. 2003, *The Physics of Plasmas*

- Burgess, D. 1995, *Collisionless Shocks*, in *Introduction to Space Physics*, Edited by Margaret G. Kivelson and Christopher T. Russell, Cambridge, UK: Cambridge University Press.
- . 2006, *ApJ*, 653, 316
- Burlaga, L. F. 1967, *J. Geophys. Res.*, 72, 4449
- Cairns, I. H., & Robinson, R. D. 1987, *Sol. Phys.*, 111, 365
- Cane, H. V., & White, S. M. 1989, *Sol. Phys.*, 120, 137
- Chollet, E. E. 2008, PhD thesis, The University of Arizona
- Chollet, E. E., & Giacalone, J. 2008, *ApJ*, 688, 1368
- . 2011, *ApJ*, 728, 64
- Chollet, E. E., Giacalone, J., Mazur, J. E., & Al Dayeh, M. 2007, *ApJ*, 669, 615
- Chuychai, P., Ruffolo, D., Matthaeus, W. H., & Meechai, J. 2007, *ApJ*, 659, 1761
- Cliver, E. W. 2009, in *IAU Symposium*, Vol. 257, *IAU Symposium*, ed. N. Gopalswamy & D. F. Webb, 401–412
- Cohen, C. M. S., Mewaldt, R. A., Leske, R. A., Cummings, A. C., Stone, E. C., Wiedenbeck, M. E., Christian, E. R., & von Roseninge, T. T. 1999, *Geophys. Res. Lett.*, 26, 2697
- Coleman, Jr., P. J. 1968, *ApJ*, 153, 371
- Cummings, A. C., Stone, E. C., McDonald, F. B., Heikkila, B. C., Lal, N., & Weber, W. R. 2008, in *American Institute of Physics Conference Series*, Vol. 1039, *American Institute of Physics Conference Series*, ed. G. Li, Q. Hu, O. Verkhovlyadova, G. P. Zank, R. P. Lin, & J. Luhmann, 343–348
- Damiano, P. A., & Wright, A. N. 2005, *Journal of Geophysical Research (Space Physics)*, 110, 1201
- Decker, R. B., Krimigis, S. M., Roelof, E. C., Hill, M. E., Armstrong, T. P., Gloeckler, G., Hamilton, D. C., & Lanzerotti, L. J. 2005, *Science*, 309, 2020
- . 2008, *Nature*, 454, 67
- Diaz, I., Zhang, M., Qin, G., & Rassoul, K. H. 2011, in *International Cosmic Ray Conference*, Vol. 10, *International Cosmic Ray Conference*, 40
- Drake, J. F., Opher, M., Swisdak, M., & Chamoun, J. N. 2010, *ApJ*, 709, 963

- Dwyer, J. R., Mason, G. M., Mazur, J. E., Jokipii, J. R., von Rosenvinge, T. T., & Lepping, R. P. 1997, *ApJ*, 490, L115
- Ellison, D. C. 1981, *Geophys. Res. Lett.*, 8, 991
- Ellison, D. C., Moebius, E., & Paschmann, G. 1990, *ApJ*, 352, 376
- Ellison, D. C., & Ramaty, R. 1985, *ApJ*, 298, 400
- Fan, C. Y., Gloeckler, G., & Simpson, J. A. 1964, *Physical Review Letters*, 13, 149
- Fisk, L. A., Kozlovsky, B., & Ramaty, R. 1974, *ApJ*, 190, L35
- Florinski, V., Decker, R. B., le Roux, J. A., & Zank, G. P. 2009, *Geophys. Res. Lett.*, 36, 12101
- Florinski, V., & Zank, G. P. 2006, *Geophys. Res. Lett.*, 33, 15110
- Florinski, V., Zank, G. P., Heerikhuisen, J., Hu, Q., & Khazanov, I. 2010, *ApJ*, 719, 1097
- Forbes, T. G. 1986, *ApJ*, 305, 553
- . 1988, *Sol. Phys.*, 117, 97
- Geiss, J., Gloeckler, G., Fisk, L. A., & von Steiger, R. 1995, *J. Geophys. Res.*, 100, 23373
- Giacalone, J. 2004, *ApJ*, 609, 452
- . 2005a, *ApJ*, 624, 765
- . 2005b, *ApJ*, 628, L37
- Giacalone, J., Burgess, D., Schwartz, S. J., & Ellison, D. C. 1992, *Geophys. Res. Lett.*, 19, 433
- Giacalone, J., & Jokipii, J. R. 1994, *ApJ*, 430, L137
- . 1999, *ApJ*, 520, 204
- . 2012, *ApJ*, 751, L33
- Giacalone, J., Jokipii, J. R., & Matthaeus, W. H. 2006, *ApJ*, 641, L61
- Giacalone, J., Jokipii, J. R., & Mazur, J. E. 2000, *ApJ*, 532, L75
- Giacalone, J., & Neugebauer, M. 2008, *ApJ*, 673, 629

- Gloeckler, G., & Geiss, J. 1998, *Space Sci. Rev.*, 86, 127
- Gloeckler, G., Hovestadt, D., Ipavich, F. M., Scholer, M., Klecker, B., & Galvin, A. B. 1986, *Geophys. Res. Lett.*, 13, 251
- Gloeckler, G., Schwadron, N. A., Fisk, L. A., & Geiss, J. 1995, *Geophys. Res. Lett.*, 22, 2665
- Goldreich, P., & Sridhar, S. 1995, *ApJ*, 438, 763
- Goldstein, M. L., Roberts, D. A., & Matthaeus, W. H. 1995, *ARA&A*, 33, 283
- Goodrich, C. C., & Scudder, J. D. 1984, *J. Geophys. Res.*, 89, 6654
- Gosling, J. T., Thomsen, M. F., Bame, S. J., & Russell, C. T. 1989, *J. Geophys. Res.*, 94, 10011
- Guo, F., & Giacalone, J. 2010, *ApJ*, 715, 406
- . 2012, *ApJ*, 753, 28
- Guo, F., Jokipii, J. R., & Kota, J. 2010, *ApJ*, 725, 128
- Haggerty, D. K., & Roelof, E. C. 2009, in *American Institute of Physics Conference Series*, Vol. 1183, *American Institute of Physics Conference Series*, ed. X. Ao & G. Z. R. Burrows, 3–10
- Hilchenbach, M., Sierks, H., Klecker, B., Bamert, K., & Kallenbach, R. 2003, in *American Institute of Physics Conference Series*, Vol. 679, *Solar Wind Ten*, ed. M. Velli, R. Bruno, F. Malara, & B. Bucci, 106–109
- Hill, M. E., Haggerty, D. K., McNutt, R. L., & Paranicas, C. P. 2009, *Journal of Geophysical Research (Space Physics)*, 114, 11201
- Holman, G. D., & Pesses, M. E. 1983, *ApJ*, 267, 837
- Hundhausen, A. J. 1972, *Coronal Expansion and Solar Wind*, ed. Hundhausen, A. J.
- Ipavich, F. M., Galvin, A. B., Gloeckler, G., Hovestadt, D., Klecker, B., & Scholer, M. 1986, *Science*, 232, 366
- Isenberg, P. A., & Jokipii, J. R. 1979, *ApJ*, 234, 746
- Jokipii, J. R. 1966, *ApJ*, 146, 480
- . 1971, *Reviews of Geophysics*, 9, 27
- . 1982, *ApJ*, 255, 716

- . 1987, *ApJ*, 313, 842
- Jokipii, J. R., & Giacalone, J. 2007, *ApJ*, 660, 336
- Jokipii, J. R., & Kota, J. 1989, *Geophys. Res. Lett.*, 16, 1
- Jokipii, J. R., & Kóta, J. 2008, in *American Institute of Physics Conference Series*, Vol. 1039, *American Institute of Physics Conference Series*, ed. G. Li, Q. Hu, O. Verkhoglyadova, G. P. Zank, R. P. Lin, & J. Luhmann, 390–396
- Jokipii, J. R., Kota, J., & Giacalone, J. 1993, *Geophys. Res. Lett.*, 20, 1759
- Jokipii, J. R., Kóta, J., Giacalone, J., Horbury, T. S., & Smith, E. J. 1995, *Geophys. Res. Lett.*, 22, 3385
- Jokipii, J. R., & Levy, E. H. 1977, *ApJ*, 213, L85
- Jokipii, J. R., & Parker, E. N. 1969, *ApJ*, 155, 777
- Jones, F. C., & Ellison, D. C. 1991, *Space Sci. Rev.*, 58, 259
- Jones, F. C., Jokipii, J. R., & Baring, M. G. 1998, *ApJ*, 509, 238
- Kahler, S., & Ragot, B. R. 2006, *ApJ*, 646, 634
- Kahler, S. W., Sheeley, Jr., N. R., Howard, R. A., Michels, D. J., Koomen, M. J., McGuire, R. E., von Roseninge, T. T., & Reames, D. V. 1984, *J. Geophys. Res.*, 89, 9683
- Kang, H., Ryu, D., & Jones, T. W. 2012, *ApJ*, 756, 97
- Kennel, C. F., Coroniti, F. V., Scarf, F. L., Livesey, W. A., Russell, C. T., & Smith, E. J. 1986, *J. Geophys. Res.*, 91, 11917
- Kóta, J. 2010, *ApJ*, 723, 393
- Kóta, J., & Jokipii, J. R. 2008, in *American Institute of Physics Conference Series*, Vol. 1039, *American Institute of Physics Conference Series*, ed. G. Li, Q. Hu, O. Verkhoglyadova, G. P. Zank, R. P. Lin, & J. Luhmann, 397–403
- Koval, A., & Szabo, A. 2010, *Journal of Geophysical Research (Space Physics)*, 115, A12105
- Krall, N. A., & Trivelpiece, A. W. 1973, *Principles of plasma physics*
- Krauss-Varban, D., Burgess, D., & Wu, C. S. 1989, *J. Geophys. Res.*, 94, 15089
- Krauss-Varban, D., & Wu, C. S. 1989, *J. Geophys. Res.*, 94, 15367

- Krucker, S., Hudson, H. S., Glesener, L., White, S. M., Masuda, S., Wuelser, J.-P., & Lin, R. P. 2010, *ApJ*, 714, 1108
- Krucker, S., & Lin, R. P. 2000, *ApJ*, 542, L61
- Krucker, S., et al. 2008, *A&A Rev.*, 16, 155
- Krymsky, G. F. 1977, *Akademiia Nauk SSSR Doklady*, 234, 1306
- Kucharek, H., & Scholer, M. 1991, *J. Geophys. Res.*, 96, 21195
- Lee, M. A. 1982, *J. Geophys. Res.*, 87, 5063
- . 1983, *J. Geophys. Res.*, 88, 6109
- . 2005, *ApJS*, 158, 38
- Lee, M. A., Shapiro, V. D., & Sagdeev, R. Z. 1996, *J. Geophys. Res.*, 101, 4777
- Lembege, B., et al. 2004, *Space Sci. Rev.*, 110, 161
- Leroy, M. M., & Mangeney, A. 1984, *Annales Geophysicae*, 2, 449
- Leroy, M. M., Winske, D., Goodrich, C. C., Wu, C. S., & Papadopoulos, K. 1982, *J. Geophys. Res.*, 87, 5081
- Levinson, A. 1992, *ApJ*, 401, 73
- . 1994, *ApJ*, 426, 327
- Li, G., Moore, R., Mewaldt, R. A., Zhao, L., & Labrador, A. W. 2012, *Space Sci. Rev.*, 1
- Li, G., & Zank, G. P. 2006, in *American Institute of Physics Conference Series*, Vol. 858, *Physics of the Inner Heliosheath*, ed. J. Heerikhuisen, V. Florinski, G. P. Zank, & N. V. Pogorelov, 183–189
- Li, G., Zank, G. P., Verkhoglyadova, O., Mewaldt, R. A., Cohen, C. M. S., Mason, G. M., & Desai, M. I. 2009, *ApJ*, 702, 998
- Lin, R. P., et al. 2002, *Sol. Phys.*, 210, 3
- Lintunen, J., & Vainio, R. 2004, *A&A*, 420, 343
- Lowe, R. E., & Burgess, D. 2003, *Annales Geophysicae*, 21, 671
- Lu, Q., Hu, Q., & Zank, G. P. 2009, *ApJ*, 706, 687
- Lyu, L. H., & Kan, J. R. 1990, *Geophys. Res. Lett.*, 17, 1041

- Malkov, M. A. 1998, *Phys. Rev. E*, 58, 4911
- Mann, G., Warmuth, A., & Aurass, H. 2009, *A&A*, 494, 669
- Mason, G. M., Mazur, J. E., & Dwyer, J. R. 1999, *ApJ*, 525, L133
- Masuda, S., Kosugi, T., Hara, H., Tsuneta, S., & Ogawara, Y. 1994, *Nature*, 371, 495
- Matthaeus, W. H., Ghosh, S., Oughton, S., & Roberts, D. A. 1996, *J. Geophys. Res.*, 101, 7619
- Matthaeus, W. H., & Goldstein, M. L. 1982, *J. Geophys. Res.*, 87, 6011
- Matthaeus, W. H., Goldstein, M. L., & Roberts, D. A. 1990, *J. Geophys. Res.*, 95, 20673
- Matthaeus, W. H., Qin, G., Bieber, J. W., & Zank, G. P. 2003, *ApJ*, 590, L53
- Mazur, J. E., Mason, G. M., Dwyer, J. R., Giacalone, J., Jokipii, J. R., & Stone, E. C. 2000, *ApJ*, 532, L79
- Mazur, J. E., Mason, G. M., Looper, M. D., Leske, R. A., & Mewaldt, R. A. 1999, *Geophys. Res. Lett.*, 26, 173
- McComas, D. J., Elliott, H. A., Schwadron, N. A., Gosling, J. T., Skoug, R. M., & Goldstein, B. E. 2003, *Geophys. Res. Lett.*, 30, 100000
- McComas, D. J., & Schwadron, N. A. 2006, *Geophys. Res. Lett.*, 33, 4102
- Mewaldt, R. A. 2006, *Space Sci. Rev.*, 124, 303
- Mewaldt, R. A., et al. 2003, in *International Cosmic Ray Conference*, Vol. 6, *International Cosmic Ray Conference*, 3313
- Meyer-Vernet, N. 2007, *Basics of the Solar Wind* (Cambridge University Press)
- Miller, J. A., Larosa, T. N., & Moore, R. L. 1996, *ApJ*, 461, 445
- Miller, J. A., et al. 1997, *J. Geophys. Res.*, 102, 14631
- Nelson, G. J., & Melrose, D. B. 1985, *Type II bursts*, ed. McLean, D. J. & Labrum, N. R., 333–359
- Neugebauer, M., & Giacalone, J. 2005, *Journal of Geophysical Research (Space Physics)*, 110, 12106
- Oka, M., et al. 2006, *Geophys. Res. Lett.*, 33, L24104

- Palmer, I. D. 1982, *Reviews of Geophysics and Space Physics*, 20, 335
- Parker, E. N. 1958, *ApJ*, 128, 664
- . 1965, *Planet. Space Sci.*, 13, 9
- . 1979, *Cosmical magnetic fields: Their origin and their activity*, ed. Parker, E. N.
- Pei, C., Jokipii, J. R., & Giacalone, J. 2006, *ApJ*, 641, 1222
- Pesses, M. E., Eichler, D., & Jokipii, J. R. 1981, *ApJ*, 246, L85
- Petrosian, V., & Liu, S. 2004, *ApJ*, 610, 550
- Posner, A. 2007, *Space Weather*, 5, 5001
- Press, W. H., Flannery, B. P., & Teukolsky, S. A. 1986, *Numerical recipes. The art of scientific computing*, ed. Press, W. H., Flannery, B. P., & Teukolsky, S. A.
- Pulupa, M., & Bale, S. D. 2008, *ApJ*, 676, 1330
- Pulupa, M., Bale, S. D., Opitz, A., Fedorov, A., Lin, R. P., & Sauvaud, J.-A. 2012, *ArXiv e-prints*
- Qin, G., Matthaeus, W. H., & Bieber, J. W. 2002, *ApJ*, 578, L117
- Quest, K. B. 1988, *J. Geophys. Res.*, 93, 9649
- Reames, D. V. 1999, *Space Sci. Rev.*, 90, 413
- . 2009, *ApJ*, 693, 812
- Reynolds, S. P., Gaensler, B. M., & Bocchino, F. 2011, *Space Sci. Rev.*, 269
- Richardson, J. D., & Stone, E. C. 2009, *Space Sci. Rev.*, 143, 7
- Riquelme, M. A., & Spitkovsky, A. 2011, *ApJ*, 733, 63
- Roberts, J. A. 1959, *Australian Journal of Physics*, 12, 327
- Roelof, E. C., Decker, R. B., & Krimigis, S. M. 1983, *J. Geophys. Res.*, 88, 9889
- Ruffolo, D., Matthaeus, W. H., & Chuychai, P. 2003, *ApJ*, 597, L169
- Sáiz, A., Evenson, P., Ruffolo, D., & Bieber, J. W. 2005, *ApJ*, 626, 1131
- Sandroos, A., & Vainio, R. 2007, *ApJ*, 662, L127

- Savoini, P., Lembége, B., & Stienlet, J. 2010, *Journal of Geophysical Research (Space Physics)*, 115, 9104
- Scholer, M. 1990, *Geophys. Res. Lett.*, 17, 1821
- Scholer, M., & Terasawa, T. 1990, *Geophys. Res. Lett.*, 17, 119
- Schwadron, N. A., Geiss, J., Fisk, L. A., Gloeckler, G., Zurbuchen, T. H., & von Steiger, R. 2000, *J. Geophys. Res.*, 105, 7465
- Schwadron, N. A., Lee, M. A., & McComas, D. J. 2008, *ApJ*, 675, 1584
- Schwartz, S. J., Thomsen, M. F., Bame, S. J., & Stansberry, J. 1988, *J. Geophys. Res.*, 93, 12923
- Scudder, J. D. 1995, *Advances in Space Research*, 15, 181
- Shibata, K., Masuda, S., Shimojo, M., Hara, H., Yokoyama, T., Tsuneta, S., Kosugi, T., & Ogawara, Y. 1995, *ApJ*, 451, L83+
- Shih, A. Y., Lin, R. P., & Smith, D. M. 2009, *ApJ*, 698, L152
- Shimada, N., Terasawa, T., Hoshino, M., Naito, T., Matsui, H., Koi, T., & Maezawa, K. 1999, *Ap&SS*, 264, 481
- Shiota, D., Yamamoto, T. T., Sakajiri, T., Isobe, H., Chen, P.-F., & Shibata, K. 2003, *PASJ*, 55, L35
- Simnett, G. M., Sakai, J., & Forsyth, R. J. 2005, *A&A*, 440, 759
- Somov, B. V., & Kosugi, T. 1997, *ApJ*, 485, 859
- Stone, E. C., Cummings, A. C., McDonald, F. B., Heikkila, B. C., Lal, N., & Webber, W. R. 2005, *Science*, 309, 2017
- Stone, E. C., Frandsen, A. M., Mewaldt, R. A., Christian, E. R., Margolies, D., Ormes, J. F., & Snow, F. 1998, *Space Sci. Rev.*, 86, 1
- Stone, R. G., & Tsurutani, B. T. 1985, *Washington DC American Geophysical Union Geophysical Monograph Series*, 34
- Thomsen, M. F., Stansberry, J. A., Bame, S. J., Gosling, J. T., & Mellott, M. M. 1987, *J. Geophys. Res.*, 921, 10119
- Tidman, D. A., & Krall, N. A. 1971, *Shock waves in collisionless plasmas*
- Treumann, R. A. 2009, *A&A Rev.*, 17, 409

- Tsuneta, S., Masuda, S., Kosugi, T., & Sato, J. 1997, *ApJ*, 478, 787
- Tsuneta, S., & Naito, T. 1998, *ApJ*, 495, L67+
- Tsurutani, B. T., & Lin, R. P. 1985, *J. Geophys. Res.*, 90, 1
- Tu, C.-Y., & Marsch, E. 1995, *Space Sci. Rev.*, 73, 1
- Tylka, A. J., Cohen, C. M. S., Dietrich, W. F., Lee, M. A., MacLennan, C. G., Mewaldt, R. A., Ng, C. K., & Reames, D. V. 2005, *ApJ*, 625, 474
- Tylka, A. J., & Lee, M. A. 2006, *ApJ*, 646, 1319
- Tylka, A. J., et al. 2003, in *International Cosmic Ray Conference*, Vol. 6, *International Cosmic Ray Conference*, 3305
- Umeda, T., Yamao, M., & Yamazaki, R. 2009, *ApJ*, 695, 574
- Vasyliunas, V. M., & Siscoe, G. L. 1976, *J. Geophys. Res.*, 81, 1247
- Wiedenbeck, M. E., et al. 2010, *Twelfth International Solar Wind Conference*, 1216, 621
- Winske, D., & Quest, K. B. 1988, *J. Geophys. Res.*, 93, 9681
- Workman, J. C., Blackman, E. G., & Ren, C. 2011, *Physics of Plasmas*, 18, 092902
- Wu, C. S. 1984, *J. Geophys. Res.*, 89, 8857
- Wu, C. S., & Davidson, R. C. 1972, *J. Geophys. Res.*, 77, 5399
- Wu, C. S., Gaffey, Jr., J. D., & Winske, D. 1986, *Geophys. Res. Lett.*, 13, 865
- Wu, C. S., et al. 1984, *Space Sci. Rev.*, 37, 63
- Wu, P., Winske, D., Gary, S. P., Schwadron, N. A., & Lee, M. A. 2009, *Journal of Geophysical Research (Space Physics)*, 114, 8103
- Yang, Z. W., Lu, Q. M., Lembège, B., & Wang, S. 2009, *Journal of Geophysical Research (Space Physics)*, 114, 3111
- Zank, G. P. 1999, *Space Sci. Rev.*, 89, 413
- Zank, G. P., Pauls, H. L., Cairns, I. H., & Webb, G. M. 1996, *J. Geophys. Res.*, 101, 457
- Zhang, M., Jokipii, J. R., & McKibben, R. B. 2003, *ApJ*, 595, 493
- Zharkova, V. V., et al. 2011, *Space Sci. Rev.*, 159, 357

